Investigation of the promotional effect of Cu and Ag on iron-based Fischer-Tropsch catalysts using ferrites as model catalysts

by

Zandile Hlengiwe Chonco

BSc. Chemistry (Distinction), University of the Western Cape, South Africa
BSc. Honors Chemistry, University of the Western Cape, South Africa
MSc. Chemistry, University of Johannesburg, South Africa

Thesis presented to the University of Cape Town
in the fulfilment of the requirements
for the degree of

Doctor of Philosophy

Centre for Catalysis Research
Department of Chemical Engineering
University of Cape Town

Cape Town
January 2014

“My presence will go with you.

I’ll see the journey to the end”

Exodus 33:14

Declaration

I, Zandile Hlengiwe Chonco certify that this submission is my own, unaided work, except for the information obtained from literature sources and my prescribed supervisors. All sources of information have been adequately acknowledged and referenced. I have not received assistance from any other source in completing this submission.

Signature:……

Acknowledgements

To **God** the almighty, you helped me keep the fire burning and my hope alive. Without you this thesis would have not been possible and because you knew I could not do it on my own you brought into life amazing people to assist me in achieving this dream, Thank you God.

To my supervisor, Prof. Eric van Steen, there are not enough words to express my gratitude for the support that you have given me through my PhD studies. I will forever be grateful for the science knowledge that you **patiently** instilled in me. For always having a minute to answer a silly question (which I probably asked a lot), and answered them so profoundly. I thank you for all the thesis corrections. I am sure I speak for all students (past, present and future) when I say, 'for all the motivation as well as giving us a 'can do' attitude in all we do, WE THANK YOU, Prof. Eric van Steen. May God continue to immensely bless you, guard and guide you in all you do.

To my co-supervisor, Prof. M. Claeys, your advice and help throughout my thesis was highly appreciated.

To Kobus van de Merwe, Waldo Koorts and Rachel Cupido: fixing and finding stuff around the lab would have been a daunting task without you all, I thank you for making working around the lab so much easier.

To my mentor, Dr Alta Ferreira, I don't ever remember hearing a no (as an answer) coming from you. Thank you for always saying yes or I will see what I can do (which always ended up being a yes). Thank you for the support and encouraging words whenever we saw each other. Special thanks for connecting me with the right scientists to characterise my samples at Sasol.

To the scientist, Sasol-Mössbauer spectroscopy team, Dr Lonzeche Lodya, Dr Stanely Manzini and Jeanette Ngubane for analysing a lot of my samples and assisting me with the interpretation of the data. As well as, teaching me about the Mössbauer technique. To Dr Esna du Plessis, Sasol-XRD, thank you for all the XRD and Topas Retieveld refinement training. You always assisted with a smile, which was highly appreciated. Because of all of you, I know a little bit more today.

To Nothando Mungwe, you made this journey so much more memorable. The long hours in the lab were not felt when you were around. We encouraged each other, and knew that no matter how tough it was this day would come. Most of all I thank you for the laughter. Doreen Nabaho, for the encouragement at all times. You and Ntando were my lunch-time science problem solving buddies, at the UCT cafe. To Nozonke and Rukaya, thanks for bringing fun moments in the lab. To Miss Eudorah Maswanganyi and Dr Nishlan Govender, they say the darkest hour is just before the dawn, thank you for the last push.

Last but definitely not least, my one and only love 'family' Mum, Dad, Bhekizenzo, Magambushe, Muziwandile, Zamachonco, Phumzile and my nephew (my little brother) Lindela Chonco, thank you all for your never ending support through this chapter of my life. You have lived through my PhD emotional journey, with so much understanding and love. Your abundant love and encouraging words kept me going. Muziwandile, Zamachonco and Phumzile, you can probably write this thesis after the numerous times I had to practice my presentations on you, thank you for not getting tired of me (or at least not showing it). I love you too much. *'Gambushe, shayimamba, mfomubi, nyonganda ziy'emhlubulweni'*

Presentations and Publications

Presentations

1. CATSA Conference 2009, Worcester, South Africa
   Investigating the promotional effect of Cu in iron-based Fischer-Tropsch catalyst using copper ferrite as a model system

2. CATSA Conference 2010, Bloemfontein, South Africa
   Mössbauer characterization of copper ferrite as a model system for the Fischer-Tropsch synthesis

3. CATSA Conference 2011, Johannesburg, South Africa
   (a) Comparative study of the promotional effect of Cu or Ag on iron-based FT catalysts using Cu and Ag ferrites as model catalysts

   (b) Copper ferrites as model catalysts to investigate Cu promotion of Fischer-Trospch synthesis

4. Syngas convention 2012, Cape Town, South Africa
   Investigating the promotional effect of Cu in iron-based Fischer-Tropsch catalyst using copper ferrite as a model system

Publications resulting from this work

1. Zandile H. Chonco, Alta Ferreira, Lonzeche Lodya, Michael Claeys and Eric van Steen (2013), ' Ferrites - a model structure to study group 11 promoters in Fe-based Fischer-Tropsch catalysts', *Journal of Catalysis* **307**, 283.

2. Zandile H. Chonco, Lonzeche Lodya, Michael Claeys and Eric van Steen (2013), 'Copper ferrites: a model for investigating the role of copper in the dynamic iron-based Fischer-Tropsch catalyst', *Journal of Catalysis* **308**, 363.

Synopsis

The Fischer-Tropsch synthesis is regarded as a stepwise polymerisation reaction between adsorbed hydrogen, carbon monoxide and monomers formed from the reaction of hydrogen and carbon monoxide. The catalytically active metals for industrial application are cobalt and iron. The commercially used iron-based Fischer-Tropsch catalyst is supported on silica (Si), to improve the dispersion of the active metal and is promoted with small amounts of potassium to enhance the activity and selectivity of the catalyst and copper to enhance the reducibility of the iron oxide. However, the effect of copper on the iron catalyst on the product activity and selectivity remains elusive. A number of studies that have been conducted on the promotional effect of copper on iron-based Fischer-Tropsch catalysts have mainly been focused on fully promoted iron-based FT catalyst (Fe/Cu/K/Si), thus making it difficult to exclusively study the effect of the overall promotional effect of copper on the FT performance of iron-based catalysts. Additionally, minimal work has been conducted on the promotional effect of metals (i.e. silver) in the same group in the periodic table as copper. A previous study further showed that silver had no effect on the FT performance of the iron catalysts. These results were ascribed to the lack of intimate contact between the promoter and the catalytically active phase.

In this study, copper and silver ferrites which are model iron catalysts composed of Cu or Ag as promoters ($CuFe_2O_4$, $CuFeO_2$ and $AgFeO_2$) will be prepared via the co-precipitation method. The model catalysts will then be activated in H_2 and CO reaction environment and exposured to Fischer-Tropsch conditions in an attempt to understand the influence of the copper (Cu) as well as silver (Ag) on the iron catalyst. The results are compared to maghemite (γ-Fe_2O_3) and hematite (α-Fe_2O_3). The presence of group 11 metals in the crystal structure facilitates the reduction of trivalent iron into magnetite during catalyst activation in either hydrogen or carbon monoxide and the consecutive conversion of Fe_3O_4 to α-Fe under H_2-activation implying the ability of these metals to spillover hydrogen to Fe_3O_4. The conversion of Fe_3O_4 to predominantly χ-Fe_5C_2 under CO-treatment is not facilitated by the presence of the promoter element. The amount of carbide in the catalyst under Fischer–Tropsch conditions is dependent on the presence of the promoter (Cu and Ag) in close proximity to the iron phases. An increase in the FT activity is observed for the promoted iron catalysts, and this is primarily attributed to the increased carbide surface area within the catalyst. Carbon dioxide (CO_2) in the Fischer-Tropsch synthesis is formed either in the

oxygen removal from the catalytic surface or in the carburization of particularly superparamagnetic Fe_3O_4. It is further shown that the olefin selectivity in the Fischer-Tropsch synthesis over the catalyst $AgFeO_2$ (ex) is higher than that obtained over the catalyst $CuFe_2O_4$ (ex) and $CuFeO_2$ (ex), which can be ascribed to a lower hydrogenation activity of silver in comparison to copper ((ex) is in reference to the model catalyst after Fischer-Tropsch synthesis). Furthermore, copper seems to facilitate secondary olefin hydrogenation.

Contents

List of Figures

Chapter 2

Chapter 4

Chapter 5

Chapter 6

Chapter 7

List of Tables

Chapter 2

Chapter 4

Chapter 5

Chapter 6

List of Schemes

Chapter 2

Chapter 4

Chapter 7

Nomenclature

AAS	Atomic absorption spectroscopy
APG	Associated petroleum gas
ASF	Anderson-Schlz-Flory
BET	Brunauer-Emmett-Teller
BPR	Back pressure regulator
d	Desorption
EDX	Energy dispersive X-ray spectroscopy
fcc	Face centered cubic
FID	Flame ionisation detector
FT	Fischer-Tropsch
FTIR	Fourier transformed infra-red spectroscopy
FTS	Fischer-Tropsch synthesis
g	Growth
GC	Gas chromatography
HCNs	Hydrocarbons
hcp	hexagonal
HTFT	High Temperature Fischer-Tropsch synthesis
JCPDS	Joint Committee for Powder Diffraction Standards
LTFT	Low Temperature Fischer-Tropsch synthesis
MFC	Mass flow controller
Ol	Olefins
P	Paraffins
Pr	Producs
SEM	Scanning electron microscope
Sp	Surface species
STP	Standard temperature and pressure
TCD	Thermal conductivity detector
TPR	Temperature programmed reduction
WGS	Water gas shift
XRD	X-ray diffraction

Chemical formulas

Ag	Silver
$AgFeO_2$	Delaffosite silver ferrite
$AgNO_3$	Silver nitrate
Al_2O_3	Alumina oxide
Ar	Argon
C	Carbon
CH_2	Alkenyl group
CH_3	Alkyl group
CH_4	Methane
CO	Carbon monoxide
CO_2	Carbon dioxide
Cu	Copper
$CuFeO_2$	Delaffosite copper ferrite
$CuFe_2O_4$	Spinel copper ferrite
$Cu(NO_3)_2{\cdot}3H_2O$	Copper nitrate trihydrate
CuO	Copper oxide
Fe	Iron
ε -Fe_2C/ε-Fe_2C	Pseudo-hexagonal carbide
θ-Fe_3C	Cementite carbide
χ-Fe_5C_2	Hägg carbide
Fe_7C_3	Eckström-Adcock carbide
$Fe(NO_3)_3{\cdot}.9H_2O$	Iron nitrate nonahydrate
FeO	Wüstite
Fe_2O_3	Hematite
Fe_3O_4	Magnetite
H_2	Hydrogen
H_2O	Water
K	Potassium
NaOH	Sodium hydroxide
Ni	Nickel
O_2	Oxygen
OH	Hydroxyl

Rh	Rhodium
Ru	Ruthenium
Si	Silica
SiO_2	Silica oxide
TiO_2	Titanium oxide

Chapter 1

Introduction

This chapter is aimed at providing the reader with a reasonable background on the Fischer-Tropsch synthesis as well as the studies that have been reported on the group 1b promoted iron-based Fischer-Tropsch catalyst, in the process showing the relevance of the current study.

In the 1920s Frans Fischer and Hans Tropsch proposed a 'synthol process' which produced under high pressure (>100 bar) mainly oxygen containing products. At a lower pressure (~ 7 bars) the product consisted of mainly olefinic and paraffinic hydrocarbons. This process became known as the Fischer-Tropsch synthesis (FTS). The Fischer-Tropsch synthesis consists of a network of catalytic surface polymerisation reactions between adsorbed hydrogen and carbon monoxide to produce a non-selective product distribution [1,2,3,4]. The products that are formed during the Fischer-Tropsch synthesis include olefins, n-paraffins and the main by-product water. Other reported products include carboxylic acids, aldehydes, primary alcohols, branched hydrocarbons and aromatic compounds. A number of transition metals such as ruthenium (Ru), nickel (Ni), cobalt (Co) and iron (Fe) have shown significant activity for the Fischer-Tropsch synthesis [5]. However, due to cost, availability, level of activity as well as selectivity differences on Ru and Ni catalysts, only cobalt and iron are used industrially [6,7,8].

The industrially used iron catalyst for the low temperature Fischer-Tropsch synthesis (i.e., the ARGE catalyst) is usually promoted by a number of promoters such as potassium (K), silica (SiO_2) and copper (Cu) [4]. The effect of the K and SiO_2 has been well established in the open literature. Potassium acts as a chemical promoter by enhancing the FT activity and selectivity of the catalyst during the Fischer-Tropsch synthesis, and the structural promoter (SiO_2, Al_2O_3) acts as a binder to minimize chemical attrition and also assists in dispersing the catalytically active material. Additionally, it has been recently shown that silica may act as a chemical promoter [9,10].

The role of copper has been reported to assist in the reduction of the iron oxide when activated in H_2. This occurs via the facile reduction of CuO to metallic copper. Hydrogen dissociated on

metallic copper may spill-over to the iron oxide phase facilitating its reduction. The addition of copper to the iron catalyst has been associated with an increase in the activity for the Fischer-Tropsch synthesis as well as affecting the product selectivity [11,12]. However, the reason as to how the presence of copper in the iron catalyst affects the FT performance remains elusive. Iglesia et al. [13] stated that intimate contact between group 1b metals (copper or silver) and the iron phase was required for any promotional effect to occur. Further research conducted by Jin et al. [14] and Lee et al. [15] reached similar conclusions.

In this study we attempt to investigate the promotional effect of group 1b metals (Cu, Ag) on iron-based FT catalysts using ferrites as model catalysts ($CuFe_2O_4$, $CuFeO_2$ and $AgFeO_2$). The use of these ferrites eliminates the issues associated with the lack of intimate contact between metals, since the metals are initially in intimate contact in the ferrite system. Furthermore, the use of ferrites as model catalysts allows the evaluation of the promoter effect without the complicating effect of other promoters such as potassium (chemical promoter) and silica or alumina (structural promoter).

References

1. Claeys, M. and van Steen, E. (2004), 'Fischer-Tropsch Technology', *Studies in Surface Science and Catalysis* **152**, 601.

2. Gaube, J. and Klein, H. F. (2008), 'Studies on the reaction mechanism of the Fischer-Tropsch synthesis on iron and cobalt', *Journal of Molecular Catalysis A: Chemical* **283**, 60.

3. Schulz, H. (2003), 'Major and minor reactions in Fischer-Tropsch synthesis on cobalt catalysts', *Topics in Catalysis* **26**, 73.

4. Dry, M.E. (1990), 'Fischer-Tropsch synthesis over iron catalysts', *Catalysis Letters* **7**, 241.

5. Vannice, M. A. (1977), 'The catalytic synthesis of hydrocarbons from H_2/CO mixtures over the group VIII metals', *Journal of Catalysis* **50**, 228.

6. Dry, M. E. and Steynberg, A. P. (2004), 'Chapter 5-Commercial FT process application', *Studies in Surface Science and Catalysis* **152**, 406.

7. Schulz, H. (1999), 'Short history and present trends of Fischer-Tropsch synthesis', *Applied Catalysis A: General* **186**, 3.

8. Dry, M.E. (2002), 'The Fischer-Tropsch process: 1950-2000', *Catalysis Today* **71**, 227.

9. Mogorosi, R.P., Fischer, N., Claeys, M. and van Steen, E. (2012), 'Strong-metal-support interaction by molecular design: Fe-silicate interactions in Fischer-Tropsch catalysts', *Journal of Catalysis* **289**, 140.

10. Wan, H.J., Wu, B.S., Tao, Z.C., Li, T.Z., Xiang, H.W. and Li, Y.W. (2006), 'Study of an iron-based Fischer-Tropsch synthesis catalyst incorporated with SiO_2', *Journal of Molecular Catalysis A: General* **260**, 255.

11. O'Brien, R.J., Xu, L., Spicer, R.L., Bao, S., Milburn, D.R. and Davis, B.H. (1997), 'Activity

and selectivity of precipitated iron Fischer-Tropsch catalysts', *Catalysis Today* **36**, 325.

12. Bukur, D.B., Mukesh, D. and Patel, S.A. (1990), 'Promoter effects on precipitated iron catalysts for Fischer-Tropsch synthesis', *Industrial Engineering Chemistry Research* **29**, 194.

13. Wachs, I.E., Dwyer, D.J. and Iglesia, E. (1984), 'Characterization of Fe, Fe-Cu, and Fe-Ag Fischer-Tropsch catalyst', *Applied Catalysis* **12**, 201.

14. Jin, Y. and Datye, A.K. (2000), 'Phase transformations in iron Fischer-Tropsch catalysts during temperature-programmed reduction', *Journal of Catalysis* **196**, 8.

15. Li, S., Li, A., Krishnamoorthy, S. and Iglesia, E. (2001), 'Effects of Zn, Cu, and K promoters on the structure and on the reduction, carburization, and catalytic behavior of iron-based Fischer-Tropsch synthesis catalysts', *Catalysis Letters* **77**, 197.

Chapter 2

Literature Review

This chapter is aimed at providing the reader with reasonable background on the Fischer-Tropsch synthesis process as well as the iron-based Fischer-Tropsch catalysts, mainly focusing on the copper- or silver- promoted iron-based catalysts.

2.1. Fischer-Tropsch synthesis (FTS)

Fischer-Tropsch synthesis is the catalytic hydrogenation of carbon monoxide yielding higher molecular weight organic product compounds. Carbon monoxide hydrogenation over nickel and cobalt catalysts was first reported in 1902 by Sabatier and Senderens [1]. This captured the interest of many catalysis researchers and provided a platform for rigorous and intense research into this reaction. However, it was not until 1923 that the true significance of the carbon monoxide hydrogenation reaction was realized by two German scientists, Franz Fischer and Hans Tropsch, while working at the Kaiser Wilhelm Institute for Coal Research at Mülheim ad Ruhr, Germany [2]. This was the beginning of what is known today as the Fischer-Tropsch synthesis. In 1955, SASOL in South Africa began using the Fischer-Tropsch synthesis (FTS) to produce fuel and chemicals from coal, since it had large coal reserves and coal could be obtained cheaply. At present, the limited crude oil reserves, resulting in sky-scraping oil prices, increasing environmental constraints as well as the awareness that less expensive transportation fuels can be obtained from coal, natural gas or biomass has substantially increase interest in Fischer-Tropsch synthesis [3,4]. The development of new large industrial FT plants in Qatar (SASOL and Shell) and Nigeria (Chevron), in addition to the existing plants in South Africa (SASOL and PetroSA) and Malaysia (Shell), as well as, the proposed plants in China, Australia and Indonesia, confirm this interest.

2.2. Fischer-Tropsch reaction

The Fischer-Tropsch synthesis is the hydrogenation of carbon monoxide to produce clean transportation fuels and chemicals [5,6]. The surface chemistry can be conceptualized by equation 2.1.

$$CO + 2H_2 \Longrightarrow (-CH_2-) + H_2O \qquad (2.1)$$

with ΔH_{rxn} (240 °C) = –158 kJ/mol

The Fischer-Tropsch synthesis yields a broad spectrum of products. These include the main products, which are linear α-olefins and paraffins, as well as water as a by-product. Other products that are formed include branched compounds and oxygenates such as alcohols, acids, aldehydes and ketones. The Fischer-Tropsch synthesis product spectrum is strongly influenced by the reaction conditions (i.e., temperature, pressure, and the inlet H_2/CO-ratio) and the type of catalysts used. It is typically divided into two operating modes, the low temperature (LTFT) and the high temperature Fischer-Tropsch (HTFT) (although nowadays SYNFUEL China seems to have coined the medium temperature Fischer-Tropsch synthesis). The low temperature Fischer-Tropsch (220–250 °C) process is used for the production of long chain hydrocarbons in the boiling range of diesel to hard waxes [7] while high temperature Fischer-Tropsch (320–350 °C) process produces lighter products including associated petroleum gas (APG), petrol and chemicals [8]. Several metals, such as nickel, ruthenium, rhodium, cobalt and iron have been reported as active catalysts for FTS [9,10,11]; however, only iron and cobalt are used commercially. Depending on the catalysts used further side reactions may accompany the Fischer-Tropsch synthesis namely the water-gas shift (WGS) and the Boudouard reaction [9].

2.3. Formation of carbon dioxide (CO_2)

Carbon dioxide formation is typically observed over iron-based catalysts. This is typically ascribed to the water gas shift (WGS) activity of the catalyst, which would then involve the reaction of water (by-product of the FTS) with carbon monoxide yielding hydrogen (H_2) and carbon dioxide (CO_2), as shown in equation 2.2.

$$CO + H_2O \Leftrightarrow H_2 + CO_2 \qquad (2.2)$$

with ΔH_{rxn} (240 °C) = –39.7 kJ/mol

A further side reaction is the Boudouard reaction (shown in equation 2.3). This reaction involves the disproportionation of carbon monoxide (CO) to carbon and carbon dioxide as products.

$$2CO \Leftrightarrow C + CO_2 \qquad (2.3)$$

with ΔH_{rxn} (270 °C) = –172.9 kJ/mol

2.4. Fischer-Tropsch product distribution

The Fischer-Tropsch synthesis is a polymerization reaction [12], which occurs through a step-wise growth process. At each stage of growth, the hydrocarbon surface species may either desorb to form the primary Fischer-Tropsch products, or continue in a chain growth as shown in Figure 2.1 [13]. The probability of chain growth continuing is described by α, which is also known as the chain growth probability.

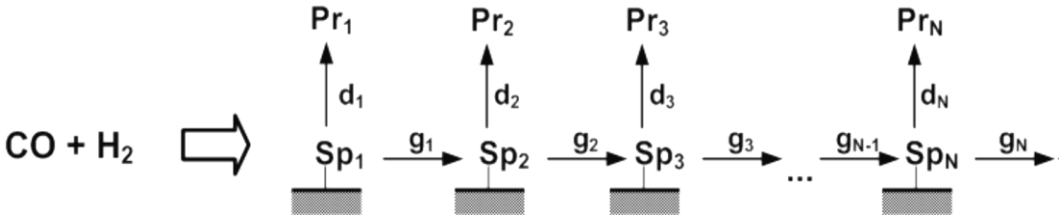

Figure 2.1: Fischer-Tropsch step-wise growth process with a surface species (Sp_i), products (Pr_i) (g: growth, d: desorption)

The chain growth probability (α) can also be defined in terms of the rate of chain propagation (r_g) and the sum of the chain propagation and termination (r_d) as shown below.

$$\alpha = \frac{r_g}{(r_g + r_d)}$$

The product distribution can then be predicted if the chain growth probability, α, is independent of carbon number. The rate of formation of a product Pr^n with n carbon atoms is given by:

$$r_{Pr_n} = r_{d_n} = \alpha^{n-1} \cdot (1 - \alpha) \cdot r_{f,1}$$

Here, $r_{f,1}$ is the rate at which the species with 1 carbon atom is formed. All product compounds are formed via the formation of Sp_1 (see Fig. 2.1). At steady state the total molar rate of formation of all products must be equal to the rate at which the species with 1 carbon atom is formed.

$$\frac{r_{Pr_n}}{\sum_{i=1}^{i=\infty} r_{Pr_i}} = x_n = \alpha^{n-1} \cdot (1 - \alpha)$$

From a commercial view point the mass or weight fraction of a certain product is of more interest. The relative weight fraction of the product with n carbon atoms is given by:

$$W_n = \frac{n \cdot r_{Pr_n}}{\sum_{i=1}^{i=\infty} i \cdot r_{Pr_i}},$$

which can also be linked to the Anderson-Schulz-Flory distribution:

$$\frac{W_n}{n} = \frac{r_{Pr_n}}{\sum_{i=1}^{i=\infty} i \cdot r_{Pr_i}},$$

$$\log\left(\frac{W_n}{n}\right) = \log\left(r_{Pr_n}\right) - \log\left(\sum_{i=1}^{i=\infty} i \cdot r_{Pr_i}\right) = \log\left(\alpha^{n-1} \cdot (1-\alpha)\right) - \log\left(\frac{1}{1-\alpha}\right),$$

$$\log\left(\frac{W_n}{n}\right) = 2 \cdot \log(1-\alpha) + (n-1) \cdot \log(\alpha)$$

Plotting the logarithm of the relative weight fraction ($\log(W_n/n)$) as a function of carbon number should thus yield a straight line, if the chain growth probability is independent of carbon number. The chain growth probability (α) can be determined from the slope of the straight line. Furthermore, the maximum selectivity of the different product classes that can be formed can be estimated by plotting the selectivity in mass or weight percent as a function of the chain growth probability α. The change in the product weight fraction as the chain growth probability increases is shown in Figure 2.2. An increase in the chain growth probability results in increase in the average the molecular weight of the product. Theoretically, only methane can be produced with 100 % selectivity (when the chain growth probability, α, equals zero). The only other product produced with high selectivity is heavy paraffin wax. The gasoline product fraction has a maximum selectivity of 48 %. The maximum diesel product fraction selectivity is closer to 40 % and varies depending on the range of carbon numbers in the product cut.

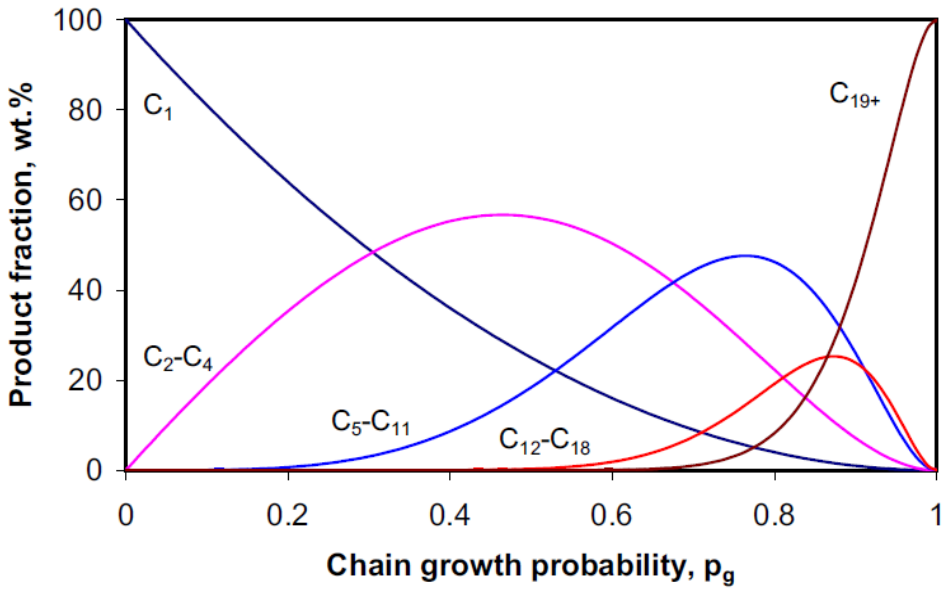

Figure 2.2: Theoretical product distribution as a function of the chain growth probability assuming ideal ASF kinetics [14]

The product distribution and composition of the products are dependent on the reaction variables, such as, temperature, pressure and H_2 to CO ratio [15]. Table 2.1 shows the effect of these variables on product selectivity. Methane selectivity increases with increasing temperature and increasing hydrogen to carbon monoxide ratio.

Table 2.1: Effect of process conditions on Fischer-Tropsch synthesis product selectivity (adapted from [15])

	Temperature	**Pressure**	**H_2: CO**
Methane selectivity	+	-	+
Olefin selectivity	~	~	-
Oxygenate selectivity	-	+	-
Chain growth	-	+	-
Chain branching	+	-	~
Carbon deposition	+	~	-

\+ increase with increasing parameter
\- decrease with increasing parameter
~ no clear effect

The formation of long chain linear products is favoured at low temperature where chain growth probabilities exceeding 0.9 can be achieved. Increasing the total pressure generally leads to

higher chain growth probabilities. The H_2 to CO ratio has a pronounced effect on the average chain length and the composition of the products. A high H_2 to CO ratio leads to the formation of lighter products which can be explained by enhanced product desorption with respect to chain growth in the kinetic Fischer-Tropsch mechanism. At hydrogen rich conditions, low olefin and oxygenates contents are found, which to an extent is due to increased secondary conversion of these valuable products facilitated by hydrogen.

The formation of various Fischer-Tropsch products has been proposed to form via a number of different mechanisms.

2.5. Proposed mechanisms in Fischer-Tropsch synthesis

The Fischer-Tropsch products are thought to form via a surface polymerisation reaction which is characterized by a series of key steps, these steps include [16,17,18];

- Reactant adsorption onto the surface of the catalyst
- Generation of a chain starter
- Chain growth (propagation step)
- Product desorption from the catalyst surface (termination step)
- Re-adsorption of reactive products and further reaction

Numerous pathways have been suggested for the Fischer-Tropsch synthesis mechanisms, however, 'alkyl', 'alkenyl', 'enol' and 'CO-insertion' mechanisms [13,19] are the most accepted.

2.5.1. Alkyl mechanism

The alkyl mechanism (schematically presented in scheme 2.1) was developed from the so-called "carbide"-mechanism, which was the first proposed FT reaction mechanism [20,21]. The chain initiation involves the dissociative CO-chemisorption to form carbon and oxygen atoms on the metal surface. The surface oxygen reacts either with adsorbed hydrogen to form water or with adsorbed carbon monoxide to form carbon dioxide. In a sequential reaction the surface carbon ("carbide") is hydrogenated to CH, CH_2 and CH_3 hydrocarbon species. The CH_2 and CH_3 species are considered the monomer and the chain initiator, respectively. Chain growth then takes place via incorporation of the monomer into surface alkyl species. The primary termination step includes either H-elimination to form an olefin or H-addition to form paraffin. Formation of oxygenates cannot be explained by the alkyl-mechanism, although, there has been a suggested

involvement of surface hydroxyl groups in their generation [22], via the coupling of a surface hydroxyl group with an alkyl group.

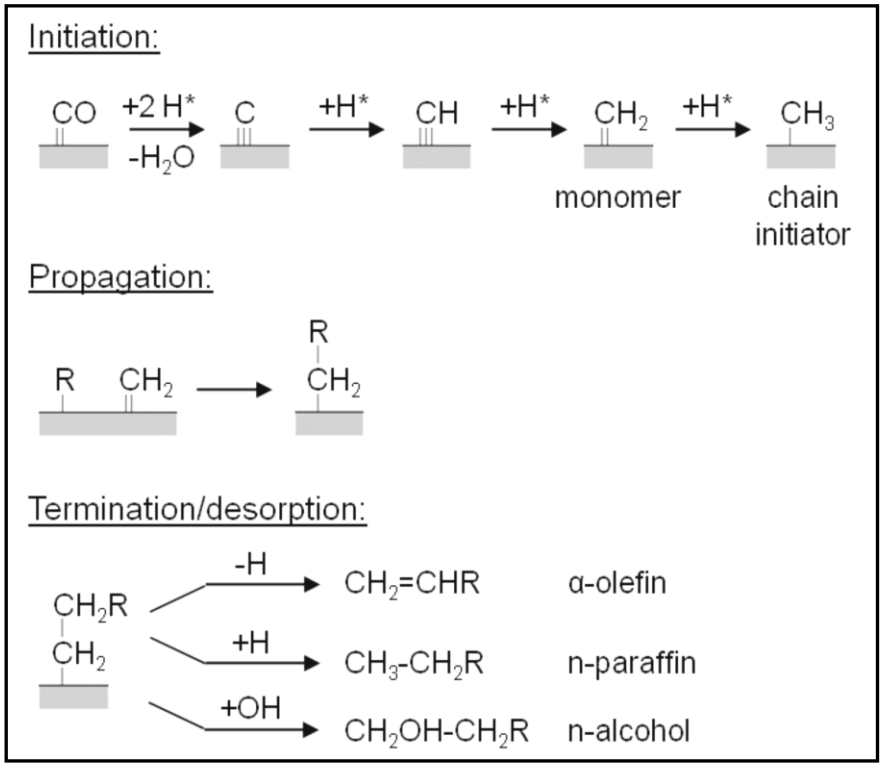

Scheme 2.1: Schematic representation of the alkyl mechanism

However, experimental evidence for the participation of surface hydroxyl groups in the formation of oxygenates is still lacking. Furthermore, the formation of branched hydrocarbons could not be explained by the alkyl mechanism shown in Scheme 2.1. Lee and Anderson [23] proposed a mechanism based on the experimentally proven re-adsorption and subsequent secondary reaction of primarily formed α-olefins [24], as shown in Scheme 2.2. This mechanism was also experimentally confirmed by Schulz et al. [25]. The other reaction involved the combination of an alkylidene surface species with the methyl species as shown in Scheme 2.2.

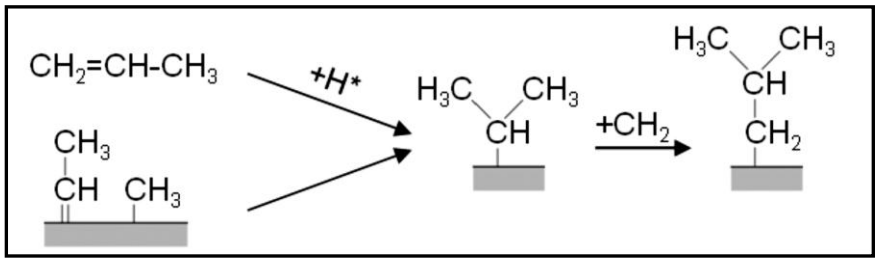

Scheme 2.2: Schematic representation of the formation of branched hydrocarbons

2.5.2. Alkenyl Mechanism

The alkenyl mechanism which is based on organometallic model system studies was proposed by Maitlis et al. [26,27,28], the schematic presentation in shown in Scheme 2.3. The first step involves the generation of a surface CH_x species, this step is the same as in the alkyl mechanism (Scheme 2.1).

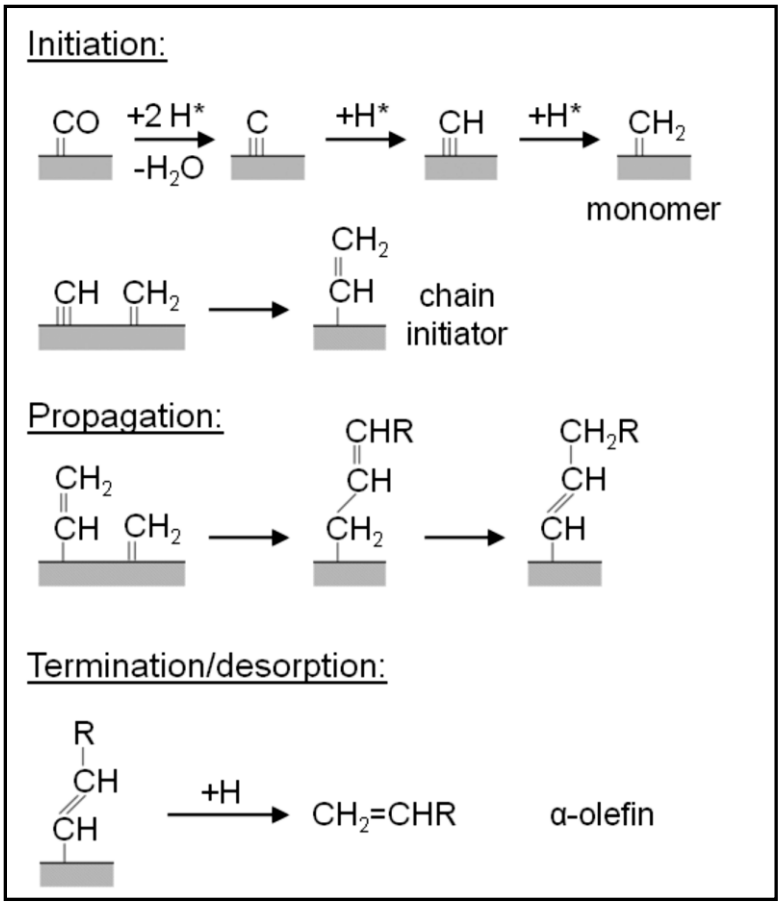

Scheme 2.3: Schematic representation of the alkenyl mechanism

The surface CH_x species, viz. methylidene (CH) and methylene (CH_2) species, reacts in a first C-C carbon bond formation to form the chain initiator, a vinyl surface species ($CH=CH_2$). Chain propagation involves the addition of a methylene species to a surface vinyl species yielding a surface allyl species, followed by isomerisation to a surface alkenyl species. The termination step involves the addition of hydrogen which leads to desorption of the product as α-olefin.

2.5.3. Enol Mechanism

The enol mechanism was proposed by Storch et al. [29]. The chain initiator is an enol species (M=CHOH). It is generated through the surface H-addition to chemisorbed carbon monoxide on

the metal surface as shown in Scheme 2.4. Through the condensation reactions of two neighbouring enol species, chain growth is initiated. Termination of those species can then yield oxygenates or olefins. The formation of n-paraffins is described as a secondary reaction by hydrogenation of primarily formed α-olefins. The primary formation of n-paraffins would require an alternative reaction pathway.

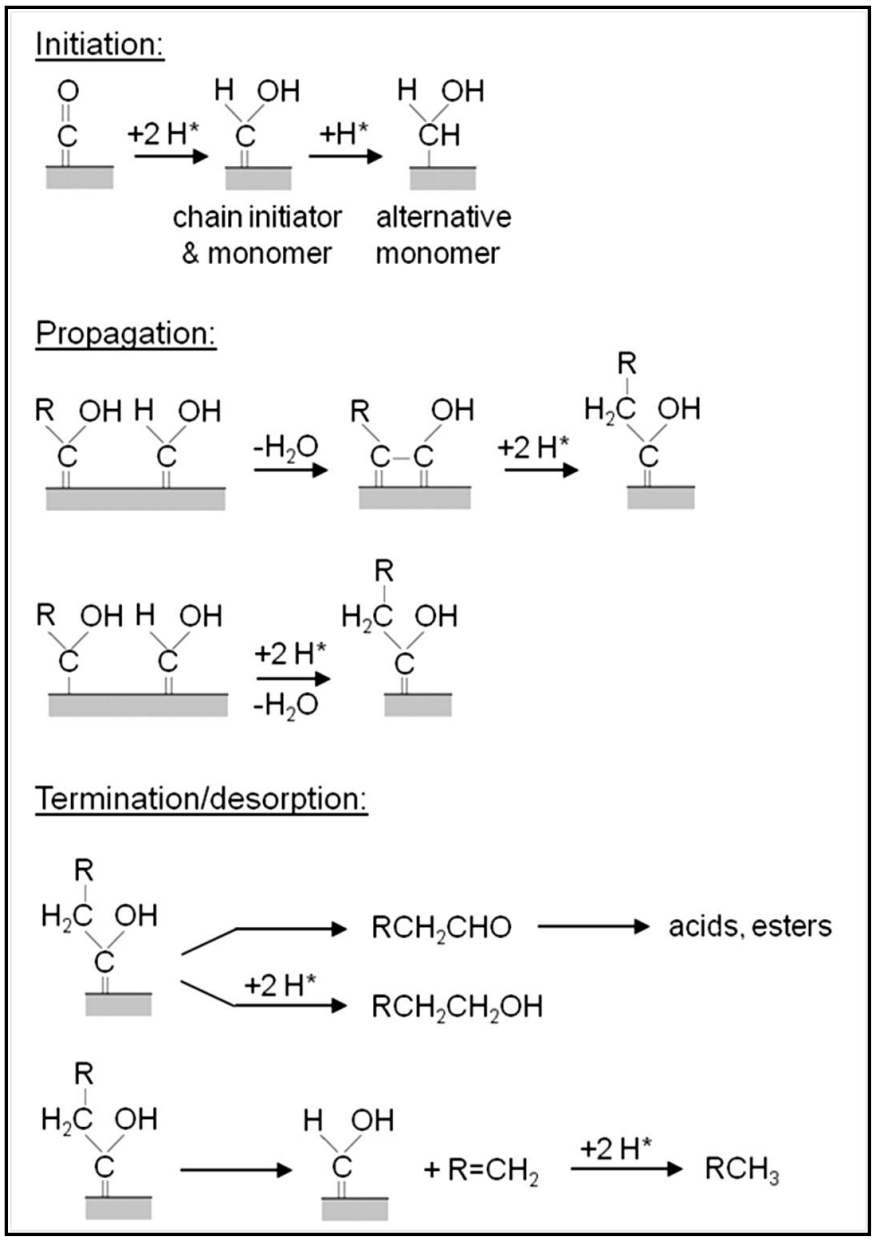

Scheme 2.4: Schematic representation of the enol mechanism

2.5.4. CO-insertion mechanism

The CO-insertion mechanism is often believed to be the main reaction pathway leading to the formation of oxygenates in Fischer-Tropsch synthesis [30,31,32]. It was originally formulated by

Sternberg and Wender [33] and Roginski [34] and further refined by Pichler and Schulz [35]. In this mechanism chemisorbed carbon monoxide is considered the monomer. Reaction of the monomer with activated hydrogen leads to the formation of the chain initiator, viz. a surface alkyl species.

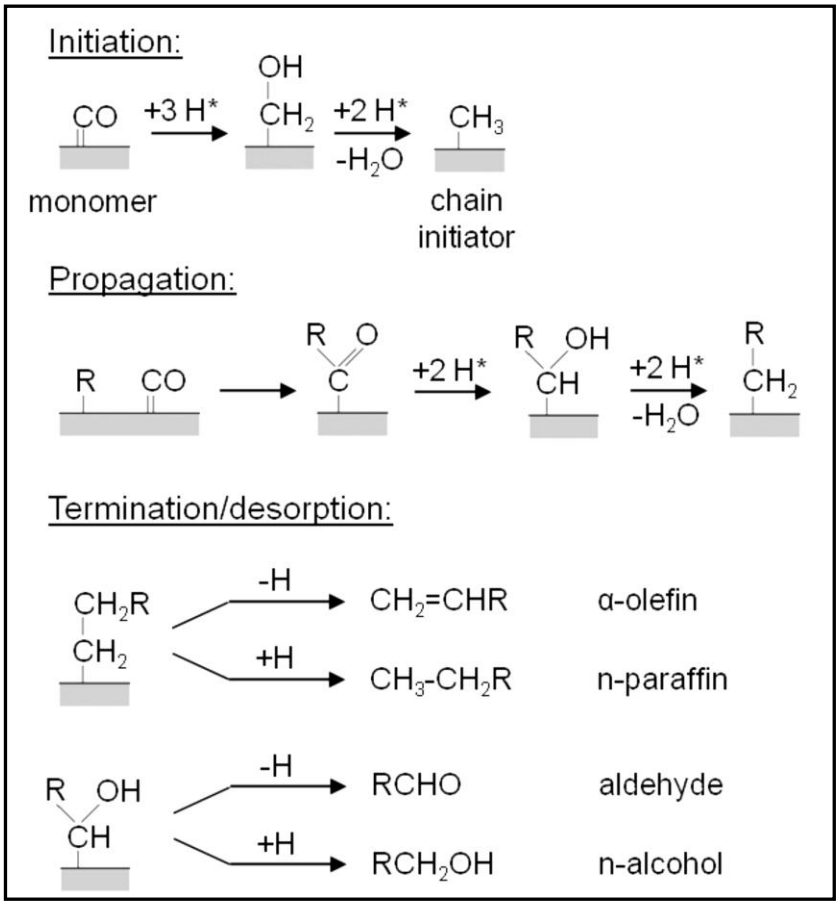

Scheme 2.5: Schematic representation of the CO-insertion mechanism

Chain growth takes place via CO-insertion in a methyl-alkyl bond leading to a surface acyl species. The C-O bond cleavage generates the longer chain surface alkyl species. Desorption of these species can either lead to the formation of α-olefins or n-paraffins, as already proposed in the alkyl-mechanism, or to the formation of aldehydes and alcohols from oxygen containing surface species as shown in Scheme 2.5.

2.6. Fischer-Tropsch synthesis catalysts

Group VIII metals; iron, cobalt, nickel and ruthenium have been shown to be active for the Fischer-Tropsch synthesis [36)], however, the low availability and high cost of ruthenium eliminates its viable for large-scale Fischer-Tropsch synthesis application, nickel catalyst are

reported to produce high methane yields due to its hydrogenating ability; in addition, at low temperatures, high pressure volatile nickel carbonyls are formed and the catalytically active material is lost from the reactor [37]. This leaves cobalt and iron catalysts as economically feasible on an industrial scale [38]. Table 2.2 show the approximate relative prices of the active metals for the Fischer-Tropsch synthesis. Iron is the cheapest material, while ruthenium is the most expensive metal.

Table 2.2: Approximate relative price of metals for Fischer-Tropsch synthesis [8,38,39]

Metal	**Price**
Fe	1
Co	1000
Ni	250
Ru	48000

Iron and cobalt are industrially used as Fischer-Tropsch catalysts. These two catalyst types differ amongst others in the purchase cost, in the manner in which oxygen present in CO is removed and temperature sensitivity of (in particular) methane formation. With cobalt-based catalysts, oxygen is mainly removed as water. However, with iron-based catalysts oxygen is removed as water and carbon dioxide. Hence, the feed gas for cobalt-based catalysts must have an inlet H_2 to CO ratio of approximately 2.0-2.3, since cobalt catalysts show little to no activity towards the water-gas-shift reaction [10,40,41]. A significant fraction of the oxygen removal over iron-based catalysts proceeds via CO_2-formation (typically assigned to the water-gas shift activity), thus allowing the use of feedstock with a lower inlet H_2 to CO ratiofeed gas i.e., 0.5-1.3, which is typically produced from coal [42].

The methane selectivity increases with increasing reaction temperature [43]. However, the increase over iron-based catalysts is rather modest over a temperature range spanning 100^oC. Hence, iron catalysts can be used in both the low temperature and high temperature Fischer-Tropsch synthesis. The methane selectivity increases strongly with increasing reaction temperature over cobalt-based catalysts, thus restricting the use of cobalt-based catalysts to the low temperature Fischer-Tropsch synthesis. The flexibility with respect to temperature together with some of the other advantages mentioned above makes the iron catalyst the preferred catalyst for the present study.

2.7. Iron-based Fischer-Tropsch catalysts

Iron-based Fischer-Tropsch catalysts are one of the oldest industrially used FT catalysts. The iron FT catalysts may be un-promoted (e.g., Fe_2O_3) or promoted (e.g., Arge catalyst). In a promoted iron–based catalyst, one or more promoters may be present, such as, potassium (K), silica (Si) and copper (Cu). Addition of these promoters assists the iron catalyst in achieving high Fischer-Tropsch synthesis performance (i.e., activity, selectivity and stability). In an attempt to understand the behaviour of the iron catalyst during the Fischer-Tropsch synthesis, it is vital to first understand the role of the individual promoters (i.e., K, Si, Cu) on the iron-based Fischer-Tropsch catalysts. A number of researchers have shown that promoters can be classified into different categories such as chemical, structural and reduction, depending on the overall performance of the promoter on the iron-based catalyst during Fischer-Tropsch synthesis.

2.7.1. Chemical promoters (e.g., potassium, K) have been reported to provide effective change in catalyst activity and product selectivity [44,45], by promoting CO chemisorption and facilitating CO dissociation while inhibiting H_2 chemisorption [46,47,48].

2.7.2. Structural promoters such as SiO_2, Al_2O_3 and TiO_2 [49], are added to iron-based FT catalysts to enhance the mechanical stability of the catalyst (and in particular with respect to chemical attrition). They may also serve to reduce sintering, thereby enhancing the performance (i.e., stability) of the iron-based catalysts during Fischer-Tropsch synthesis [50,51,52]. Silica has also been reported to act as a chemical promoter [49].

2.7.3. Reduction promoters are reported to affect the reducibility of the iron-based catalysts by increasing the rate of reduction of Fe_2O_3 to α-Fe (in H_2 atmosphere) [53]. Copper is commonly used as a reduction promoter for the iron-based FT catalysts. It is added to the iron oxide catalyst to increase the rate of Fe_2O_3 reduction to α-Fe. This occurs via a process known as the hydrogen spillover, involving the hydrogen dissociation on metallic copper and migration to the iron phase. This may thus provide a source of atomic hydrogen to assist in the reduction of the iron oxide to metallic iron in a hydrogen atmosphere or iron carbide in a carbon monoxide containing atmosphere [40,53,54,55,56].

2. 8. Iron oxide phases

Iron in the iron-based Fischer-Tropsch catalyst may be present as a number of different oxide phases prior, during and post Fischer-Tropsch synthesis; these include hematite, maghemite, magnetite and wüstite. The structure of iron oxides is dominated by the arrangement of oxygen or hydroxide anions. The cations occupy different positions relative to these layers of anions. Table 2.3 shows the crystallographic information and chemical properties of the iron oxides that are reported to be important in the Fischer-Tropsch synthesis. The selected iron oxides consist of close packed arrays of anions (O^{2-} or OH^-) (hexagonal (hcp) or face centered cubic (fcc) close packing) in which the iron cations, in either the trivalent or the divalent state, occupy the octahedral and sometimes tetrahedral spaces. The main structural differences between the different oxides arise from the way the octahedral and tetrahedral building units are organised.

Table 2.3: Crystallographic and chemical property information on the listed iron oxides

	Chemical Composition	**Crystallographic system**	**Space group**	**Density ($g.cm^{-3}$)**	**Type of magnetism**
Hematite	α-Fe_2O_3	Hexagonal	R3c	5.26	Weakly Ferromagnetic or anti-ferromagnetic
Maghemite	γ-Fe_2O_3	Cubic	Fd3m	4.87	Ferrimagnetic
Magnetite	Fe_3O_4	Cubic	$P4_332$	5.18	Ferrimagnetic
Wüstite	FeO	Cubic	Fm3m	5.90	Anti-ferrimagnetic

Hematite and maghemite: are formed from iron hydroxide precursors. Hematite (α-Fe_2O_3) is a mineral form of iron(III) oxide. It crystallizes in the rhombohedral system and it is usually brownish red to red in colour. The crystal structure of hematite is shown in Figure 2.3. Maghemite (γ-Fe_2O_3) is a hematite and magnetite related oxide mineral and it is blue with a gray shade in colour. Maghemite has the same structure as magnetite (i.e., spinel ferrite). Maghemite can be considered as an Fe(II)-deficient magnetite with formula $(Fe_8^{III})_A[Fe_{40/3}^{III}\square_{8/3}]_BO_{32}$, where $\square$ represents a vacancy, A indicates tetrahedral positioning and B octahedral. Depending on the preparation conditions only hematite or maghemite may be produced or may co-exist. Hematite is the thermodynamically more stable phase conditions for bulk material [58]. However, the surface energy contribution modifies the relative phase stability significantly [58,59,60,61] and maghemite becomes the more stable phase for nano-sized crystallites [58,59], which transforms

into hematite upon sintering. The transformation of maghemite to hematite has to obey the thermodynamic constraint that the Gibbs free energy of the system is at a minimum. Hence, the critical diameter for maghemite ($d_{maghemite,c}$) beyond which the transformation to hematite is thermodynamically allowed, is given by:

$$\mu_{hematite} - \mu_{maghetite} = 0$$

$$\mu^0_{hematite} - \mu^0_{maghetite} + \frac{6 \cdot \gamma_{hematite} \cdot M_{Fe_2O_3}}{d_{hematite,c} \cdot \rho_{hematite}} - \frac{6 \cdot \gamma_{maghemite} \cdot M_{Fe_2O_3}}{d_{maghemite,c} \cdot \rho_{maghemite}} = 0$$

$$d_{maghemite,c} = \frac{6 \cdot \gamma_{maghemite} \cdot M_{Fe_2O_3}}{\left(\mu^0_{maghetite} - \mu^0_{hematite}\right) \cdot \rho_{maghemite}} \cdot \left(\frac{\gamma_{hematite}}{\gamma_{maghemite}} \cdot \left(\frac{\rho_{maghemite}}{\rho_{hematite}}\right)^{2/3} - 1\right)$$

Here, μ is the chemical potential (in J/mol; with μ^0 the chemical potential at standard conditions), $d_{maghemite}$ is the diameter of the maghemite crystallite (in m), γ is the surface energy (in J/m^2), M is the molar mass of Fe_2O_3 (in g/mol), and ρ is the density of the respective phases (in mol/m^3). It can be estimated using a non-size dependent surface energy that for non-hydrated surfaces this transition occurs for crystallites of ca. 16 nm at 300 K and 18.5 nm at 700 K. For hydrated surfaces, this transformation may occur for much smaller maghemite crystallites, but the accurate transition size requires the incorporation of size dependent surface energies.

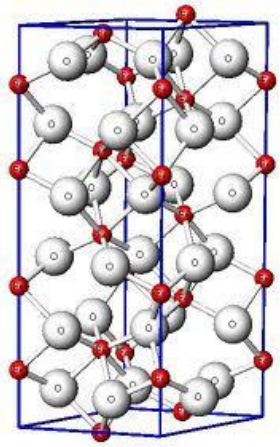

Figure 2.3: Crystal structure of hematite (α-Fe_2O_3)
(red atoms represent Fe^{3+} and white atoms represent oxygen)

Magnetite: is formed during activation of Fe_2O_3 and may also be present during the Fischer-Tropsch synthesis. Magnetite (Fe_3O_4) has a chemical formula of iron(II, III) oxide; which may

also be written as $FeO.Fe_2O_3$, it is one part wüstite and the other part hematite. Magnetite is a member of the spinel ferrite group. It is black or brownish black in colour. The crystal structure of magnetite is shown in Figure 2.4.

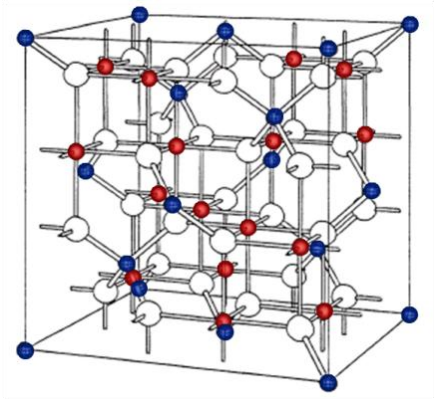

Figure 2.4: Crystal structure of magnetite (Fe_3O_4)
(blue atoms: tetrahedrally coordinated Fe^{2+} ; red atoms; octahedrally coordinated, 50/50 Fe^{2+}/Fe^{3+}; white atoms: oxygen)

Wüstite: is the unstable iron(II) oxide phase against disproportion with Fe_3O_4 and α-Fe, at temperatures less than 570^{o}C, although promoters may stabilize this phase [49]. It may be formed during catalyst activation or Fischer-Tropsch synthesis. Wüstite (FeO) is gray in colour. The crystal structure of wüstite is given in Figure 2.5.

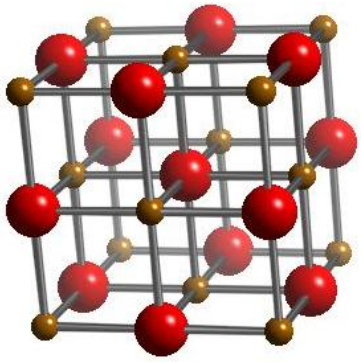

Figure 2.5: Crystal structure of wüstite (FeO)
(brown atoms: Fe^{2+}; red atoms: oxygens)

The various iron carbides (Fe_xC) formed can be classified into stable TP-carbides (carbides with carbon atoms in trigonal prismatic interstices) and the less stable O-carbides (carbides with carbon atoms in octahedral interstices) [62,63,64], as given in Table 2.4.

Table 2.4: List of the different iron carbides

		Formula	Structural name	Crystal lattice
Fe_xC	**Trigonal prismatic (TP) carbides**	Fe_7C_3	Eckström-Adcock	Orthorhombic
		χ-Fe_5C_2	Hägg	Monoclinic
		θ-Fe_3C	cementite	Orthorhombic
	Hexagonal (O) carbides	ε-Fe_2C	pseudo-hexagonal	Hexagonal to monoclinic
		$\acute{\varepsilon}$-$Fe_{2.2}C$		Hexagonal

2.9. Factors affecting the performance of the iron-based FT catalyst

Factors influencing the performance of iron-based FT catalysts include: catalyst preparation method, activation and Fischer-Tropsch synthesis conditions as well as addition of promoters to the iron catalysts.

2.9.1. Conventional catalyst preparation methods

Commercially, the preparation of iron catalysts varies depending on the process temperatures at which the catalyst will be operated. Low temperature Fischer-Tropsch catalysts are prepared by precipitation or co-precipitation while catalysts used in high temperature Fischer-Tropsch synthesis are prepared by fusing magnetite together with promoters [65]. Catalysts preparation techniques can assist in gaining new insights and give way to new and improved catalyst development of existing syntheses.

In the precipitation method, the catalyst precursor of the active metal is dissolved in a solvent such as water, and thereafter, precipitated on the support [66]. This precipitation step can be forced by changing the pH value of the solution. The pH adjustment can either be done in the presence of a support material or the support material can be formed via a simultaneous precipitation with the corresponding precursor or metal salt (co-precipitation). After drying and calcination, the oxidic catalyst precursors are obtained. The advantages of the precipitation method as compared to impregnation techniques are that;

- the composition obtained in homogenous,
- the crystallite size distribution is typically much narrower; and

- it is possible to prepare catalysts with a high metal loading on the support in one single preparation step [67,68,69].

2.9.2. Effect of activation conditions on iron-based FT catalysts

The term "activation" refers to the transformation of an inert catalyst precursor into a composition and structure that causes the reaction between hydrogen and carbon monoxide to take place thereby producing hydrocarbons. The use of hydrogen (H_2), carbon monoxide (CO) and synthesis gas (H_2/CO) as activation gases has been well documented in the open literature [47,70,71,72,73]. The phase transformation of Fe_2O_3 during H_2 activation is shown in Figure 2.6. The reduction of Fe_2O_3 occurs in a two-step reduction process via Fe_3O_4; the first reduction step corresponds to $Fe_2O_3 \rightarrow Fe_3O_4$ and the second reduction step corresponds to $Fe_3O_4 \rightarrow \alpha$-Fe [74]. The activation of Fe_2O_3 in CO or H_2/CO (see Figure 2.6) also proceeds in a two-step process, the reductive decomposition of the iron oxide and the carburization of the iron oxide (Fe_3O_4) to the iron carbide. The first step corresponds to the reduction of $Fe_2O_3 \rightarrow Fe_3O_4$ and the second carburization step corresponds to $Fe_3O_4 \rightarrow Fe_xC$, resulting in a number of different iron carbides. The term carburization will therefore be used to describe the transformation of the iron oxide to the iron carbide phase. Hence, irrespective of the activation gas used Fe_3O_4 is always an intermediate step in the reduction process [73]. Moreover, depending on the extent of reduction FeO may also form as an intermediate step, altering the overall reduction to a three step process: $Fe_2O_3 \rightarrow Fe_3O_4 \rightarrow FeO \rightarrow \alpha$-Fe (during H_2 activation) or Fe_xC (during CO activation). The formation of various iron carbides is dependent on the activation condition employed as well as the nature of the catalyst. For instance, the hexagonal carbide (ε-Fe_2C) has been reported to form by carburizing of the iron oxide or iron powder at temperatures as low as 170 ^oC in a flow of CO [75]. By increasing the temperature to 250 ^oC ε-Fe_2C may transform into the Hägg carbide (χ-Fe_5C_2), which at temperatures above 450 ^oC may eventually decompose into cementite (θ-Fe_3C). Cohn et al. [76], reported that θ-Fe_3C could also be formed by the reaction of iron with χ-Fe_5C_2 at temperatures above 260 ^oC.

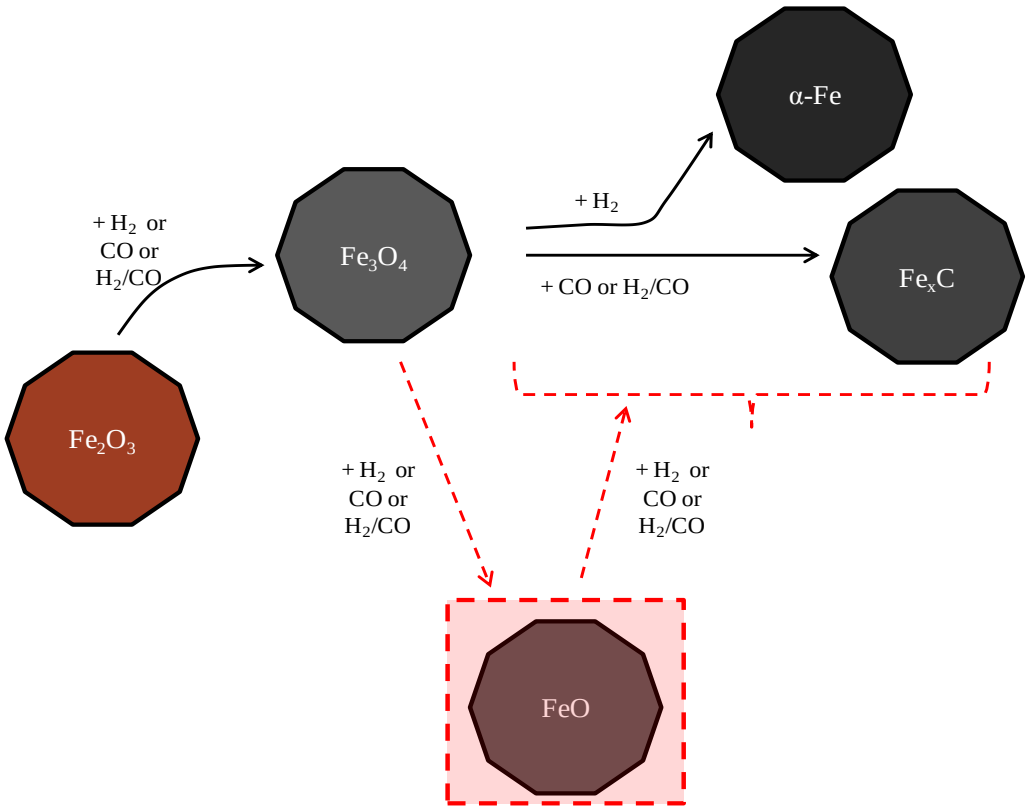

Figure 2.6: Phase(s) transformation of the iron-based Fischer-Tropsch catalyst during H_2, CO or H_2/CO activation.

2.9.3. Effect of the iron phase(s) (Fe_3O_4, Fe_xC) on performance of the iron-based FT catalyst

The nature of the final phase(s) formed after the activation process plays a vital role in the Fischer-Tropsch synthesis performance [77]. The fact that under FT reaction conditions iron can exist as a mixture of magnetite, metallic iron or several iron carbides phases creates part of the confusion as to which phase is responsible for the Fischer-Tropsch synthesis performance. A number of researchers have attempted to understand the effect of different pretreatment as well as correlate the phase(s) with the FTS activity observed [77,78,79]:

- *Iron oxide (Fe_3O_4) as the active phase for the Fischer-Tropsch synthesis:*

  Loaiza-Gil et al. [80] studied the formation of carbonaceous deposits in carbon monoxide hydrogenation on iron catalysts, focusing specifically on the effect of pressure. The catalysts were reduced in hydrogen. The results showed that increasing the pressure led to high carbon monoxide conversion (under steady state conditions). Furthermore, the bulk composition of the catalyst as determined by Mössbauer spectroscopy was Fe_3O_4, α-

Fe and χ-Fe_5C_2. They concluded that Fe_3O_4 was the active phase for Fischer-Tropsch synthesis, as it appeared that a correlation between the phase composition and the FT activity existed. Teichner et al. [81,82] also proposed that Fe_3O_4 was the active phase for the Fischer-Tropsch synthesis.

- *Iron carbide as the active phase for the Fischer-Tropsch synthesis:*

  Bukur et al. [83], investigated the effect of activation conditions on the iron catalysts performance during Fischer-Tropsch synthesis. A promoted iron catalyst (100Fe/5Cu/4.2K/25SiO_2) was activated at 280^{o}C, for various times (1-12 hrs) in H_2 and CO gases, respectively. They reported that the H_2 activated catalyst showed a gradual increase in FTS activity. The increase activity coincided with the conversion of metallic iron to pseudo-hexagonal ε-carbide. The initial activity obtained over the CO activated catalyst was higher than that of the H_2 activated catalyst. Furthermore, the CO activated catalyst showed a decrease in FT activity with time on stream, due to the partial conversion of χ-Fe_5C_2 to less active magnetite, in agreement with the hypothesis that an iron carbide is the active phase for the Fischer-Tropsch synthesis [84,85,86]. In another study, Ding and co-workers [87] investigated the effect of reducing agents on microstructure and catalytic performance of precipitated iron-manganese catalyst for the Fischer-Tropsch synthesis. The iron catalyst was activated in H_2, CO and H_2/CO at 265^{o}C for 24 hrs. They reported that the CO activated catalyst showed the highest initial activity compared with the H_2 and H_2/CO activated catalysts. A slight deactivation of the CO activated catalyst was also observed. This was attributed to the conversion of χ-Fe_5C_2 to Fe_3O_4. The activity of the H_2 activated catalyst increased gradually with the conversion of metallic iron to χ-Fe_5C_2 and ε-carbide upon exposure to syngas. The relationship between iron phases and FTS activity indicated that the formation of χ-Fe_5C_2 on the surface layers had a higher activity for the Fischer-Tropsch synthesis than ε-carbide. The formed Fe_3O_4 had a negligible effect on the Fischer-Tropsch synthesis activity. Similar, results have been reported by Bell and Dictor [63], Datye et al. [88].

2.9.4. Effect of Fischer-Tropsch synthesis conditions

Fischer-Tropsch synthesis conditions such as temperature, pressure, H_2: CO ratios play a crucial role in the FT activity. It is of general knowledge that the Fischer-Tropsch synthesis can be operated in the temperature range of 150-300 ^{o}C. At high temperatures, the reaction is faster and

higher conversion rates may be obtained, but methane formation may also be favored [92]. For this reason, the temperature is usually maintained at the low to middle part of the range. Furthermore, product selectivity may be varied by varying the temperature, when using iron-based FT catalysts. With higher temperature FT synthesis, the product selectivity is shifted towards shorter chain products, while in the low temperature FT synthesis longer chain products are produced. Increasing the pressure also leads to higher conversion as well as favoring the formation of long-chained product compounds. A variety of synthesis gas compositions (ranging from H_2/CO = 2 to 2.3) can be used in the iron-based Fischer-Tropsch synthesis. Iron-based catalysts can tolerate low H_2: CO ratios, since they promote the removal of oxygen as CO_2 (typically viewed as the ability of iron-based Fischer-Tropsch catalysts to catalyze the water gas shift reaction). This is important for synthesis gas derived from coal or biomass, which tend to have relatively low H_2: CO ratios (<2).

2.9.5. Effect of copper on iron-based FT catalyst

2.9.5.1. During different activation experiments

Hexana et al. [93] studied the promotional effect of copper on iron-based catalysts during H_2 activation using Temperature-Programmed Reduction (TPR). They compared the un-promoted (100Fe) catalyst to the copper promoted catalysts (100Fe/1Cu and 100Fe/3Cu). They observed that copper lowered the temperature of the first reduction peak (shown in Figure 2.8; also shown by other researchers [94,95]) via the initial facile reduction of CuO to Cu. Metallic copper thereafter assists in hydrogen dissociation thus providing a source of atomic hydrogen to assist in the reduction of the iron oxide to metallic iron. They concluded that copper acted as a reduction promoter.

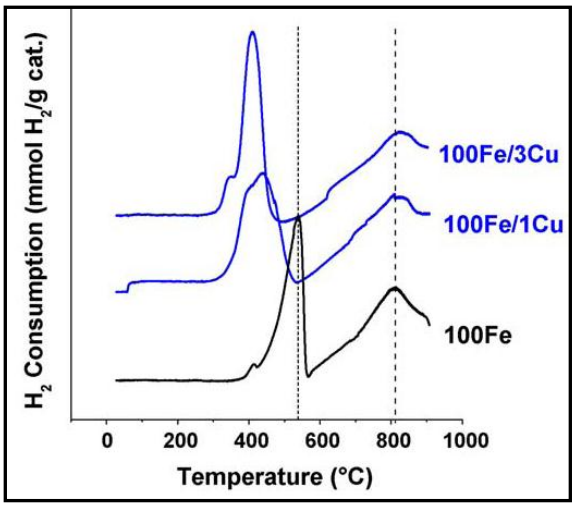

Figure 2.7: H_2-TPR profile of the copper promoted iron catalysts [93]

Hexana et al. [96] also studied the interaction of CO with the catalysts using DRIFTS in order to gain information about the strength of adsorption of CO on Fe, and the number and types of adsorbed CO molecules. CO adsorption performed on the un-promoted iron catalyst (100Fe) showed two peaks at 2033 and 2013 cm^{-1} (see Figure 2.8), indicative of CO linearly adsorbed on Fe^0. The introduction of Cu to Fe produced a slight red shift of the peak at 2013 to ~2011 cm^{-1} indicating a slight increase in the back-donation from the d-orbital of Fe.

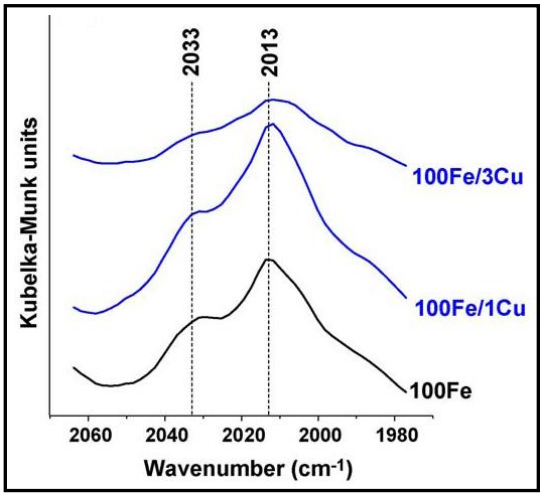

Figure 2.8: CO adsorption spectra of the copper promoted iron catalysts [93]

Jin and Datye [97] also investigated the effect of CO activation on the phase transformation in copper promoted iron catalysts using TPR. They reported that the presence of copper in the iron catalyst assisted the reduction of the iron oxide to metallic iron. The effect was however to a

lesser extent as compared to H_2 activation. Furthermore, while a simultaneous reduction of CuO to Cu and Fe_2O_3 to Fe_3O_4 was observed during H_2 activation, it was not the case during CO activation where the copper oxide seemed to reduce first followed by the iron phase. They concluded that intimate contact between copper and the iron oxide (during CO activation) was required to facilitate the reduction of Fe_2O_3 to Fe_3O_4.

2.9.5.2. Possible chemical promoter by reduction promoter

Several researchers have also shown that copper may also influence the performance of the iron catalyst during Fischer-Tropsch synthesis, claiming that copper acts as a chemical promoter. In earlier studies, Kölbel and Ralek [98,99] investigated the promotional effect of copper on the FT activity. They reported that addition of 0.1 wt% of copper (relative to iron) resulted in successful activation of Fe/Cu/K catalysts with H_2/CO. Moreover, H_2/CO activation at elevated pressure (>0.80 MPa) required the iron catalysts be promoted with copper in order to achieve reasonable activity. O'Brien et al [100] conducted a study on the activity and selectivity of the un-promoted and copper-promoted precipitated iron Fischer-Tropsch catalysts. The results showed that promotion with copper lowered the reduction temperature during activation and increased the FTS activity, regardless of the activation gas used (see Figure 2.9).

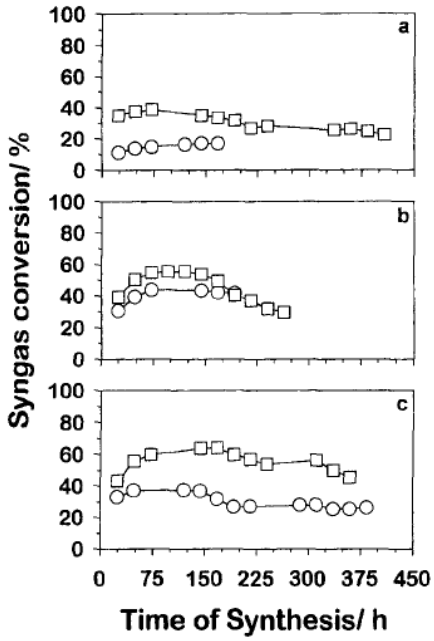

Figure 2.9: Syngas conversion for un-promoted (circle) and the copper-promoted (square) iron catalysts: Activation conditions: (a) H_2, (b) CO and (c) H_2: CO=0.7; Synthesis conditions: H_2: CO=0.7, T=230 ^oC and P=1.31 MPa

Furthermore, the selectivity of the FTS product was not affected by the activation gas employed or copper promotion. Bukur et al. [101] investigated the effect of copper on the precipitated iron-based catalyst using various promoted iron–based catalysts. The comparison of the un-promoted iron catalyst (100Fe) with the copper promoted iron catalyst (100Fe/3Cu) clearly showed an increase in the rate of Fischer-Tropsch synthesis for the copper promoted iron catalyst (see Figure 2.10). The increase in activity with copper addition was in agreement with the results observed by Kölbel and Ralek [98]. The copper promoted iron catalyst also showed a shift in the hydrocarbon distribution towards heavier products, which was accompanied by a slight enhancement in secondary reactions (olefin hydrogenation and isomerisation). The water-gas shift activity was analysed using the CO_2 selectivity (see Figure 2.11). The copper promoted iron catalyst had higher CO_2 selectivity than the un-promoted iron catalyst. The high CO_2 selectivity was attributed to the enhanced activity of the water gas shift reaction, which has been reported by other researchers to be promoted by the presence of copper [101].

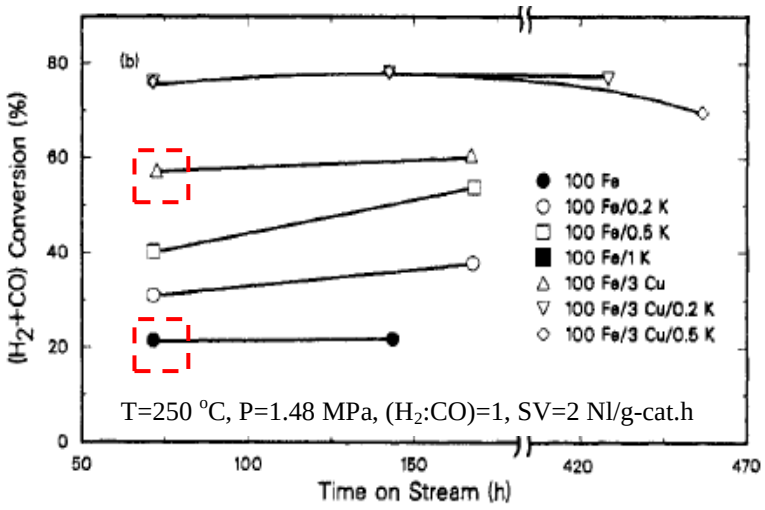

Figure 2.10: Promoter effects on the activity and stability: Synthesis gas (H_2/CO) conversion (%) vs time on stream (hr) at 250 °C [101].

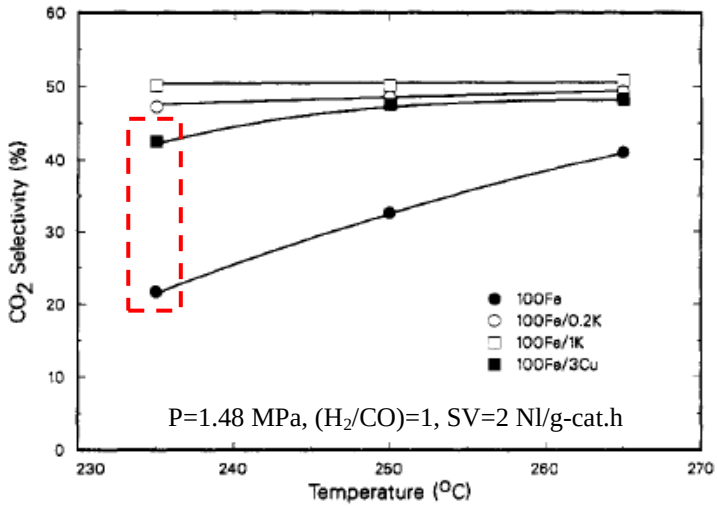

Figure 2.11: Effect of promoter and temperature on the water-gas shift reaction activity [101]

However, there is still an uncertainty as to how copper assists in the FT activity. In a recent study Cairns [94], investigated the promotional effect of copper on iron catalyst. He reported an increase in the overall oxygenate selectivity with increasing copper loadings as well as a slight change in the paraffin formation, these findings were attributed to a slight shift of primary product selectivity and the effects of secondary hydrogenation. Cairns [94] reported that copper had no effect on the FT activity. Wachs et al. [56] stated that in-order to achieve a promotional effect intimate contact between metals was required. Li et al. [47] also observed that for any promotional effect by copper on iron catalyst to occur, intimate contact between the metals was a prerequisite. This was further confirmed by Cairns [94] in the study conducted on the promotional effect of copper on iron catalysts. He further observed that intimate contact between metals was favoured by the use of the co-precipitation method.

2.9.6. Promotional effect of other group 1b metals on iron-based FT catalysts

Elements in the same group in the periodic table have similar properties and thus behave in a similar manner. If this rule is followed, then metals such as Cu, Ag and Au would behave similarly under similar reaction conditions. Hence, it might be assumed that group 1b metals such as Ag and Au may also act as a reduction promoter.

The promotional effect of silver on iron-based FT catalysts has not been well documented. To our knowledge the only study conducted was by Wachs et al. [56], in which the promotional effect of silver on iron catalysts was investigated and Jacobs et al. [102], in which they investigated that promotional effect of Cu, Ag and Au on Co/Al_2O_3 FT catalysts. The catalysts

were prepared by incipient wetness method and activated in H_2. They reported that silver had 'no effect' on the reduction behaviour of the iron catalyst and showed 'no effect' on the Fischer-Tropsch synthesis performance. They concluded that silver acted neither as a reduction promoter nor as a chemical promoter, because of the 'lack of intimate' contact between silver and iron during the activation and Fischer-Tropsch synthesis.

2.9.7. Overview of the promotional effect of copper and silver on iron-based FT catalysts

The effects of copper on iron-based FT catalysts can be summarized as follows:

- assists in the reduction of the iron oxide,
- may influence the activity of the iron-based FT catalyst during Fischer-Tropsch synthesis
- may affect the activity of the water-gas shift reaction,
- may affect Fischer-Tropsch product selectivity.

However, most of the studies conducted on the promotional effect of copper on iron-based FT catalysts have been done on multi-component catalysts. Thus, making it difficult to distinguish which component is responsible for the observed promotional effect. Furthermore, silver is in the same group in the period table as copper and thus, may show similar promotional effect. The lack of documented work on the silver promotional effect on iron-based catalysts makes silver a good candidate for evaluation as a promoter for iron-based FT catalyst. Previous work conducted on the promotional effect of metals (Cu, Mn) on the iron-based FT catalysts articulate that for any promotional effect to occur the promoter and the active phase need to be in intimate contact. Therefore, in order to eliminate the interference of the other components (such as K, SiO_2), and ensure intimate contact of the promoter (Cu and Ag) with iron, ferrites are used as model catalysts to investigate the promotional effect of Cu and Ag on iron-based catalysts.

2.10. Ferrites

Ferrites are defined as a material composed of Fe^{3+} ions as the main cationic component. Ferrite systems have received enormous attention due to their importance as magnetic materials, and semiconductors [103] and catalysts for a number of catalytic processes such as methane reforming, treatment of automotive exhausted gases and hydrogen production by steam reforming of DME as well as water-gas shift [104,105,106,107,108,109]. A number of preparation methods have been used to prepare pure phases of the ferrite systems, viz. ball-milling [110,111], solid state reaction [112], co-precipitation [113,114] and combustion

synthesis [115]. Great importance should be taken when choosing the preparation method, since the magnetic properties of the ferrite samples are governed by cation distribution between the two sublattices, which can be altered by the synthesis method, heat treatment temperature, heat duration time and cooling rate. Ferrites are further sub-divided into spinels and delaffosites, depending on the orientation of the cations within a ferrite crystal structure.

2.10.1. Spinel ferrites (AB_2O_4)

Spinel ferrites belong to a sub-group of ferrites and have a formula AB_2O_4, where A is a divalent metal (e.g., Cu, Mn , etc.) and B is a trivalent metal (e.g., Fe, Al, etc.). In spinel ferrite the metal ions are situated in two different lattice positions, the tetrahedral (A) and octahedral (B) sites according to the geometrical configuration of the oxygen nearest neighbours [116]. Spinel copper ferrite belongs to the spinel-type ferrite group. This material has a molecular formula of $CuFe_2O_4$. However, a whole range of distribution of cations is possible in $CuFe_2O_4$ and it can be represented generally by the formula $(Cu^{2+})_{1-x}(Fe^{3+})_x[(Cu^{2+})_x(Fe^{3+})_{2-x}]O_4^{2-}$ (the ions inside the brackets occupy the octahedral (B) sites and the ions outside the bracket occupy the tetrahedral (A) sites; x represents the so-called degree of inversion as defined as the fraction of A-sites occupied by Fe^{3+} cations). In the above formula when x=0, it is called normal spinel (Figure 2.12 (a)). When x=1 it is called inverse spinel (see Figure 2.12 (b)) and when $0<x<1$ it is called mixed spinel [117,111]. The cation distribution of the $CuFe_2O_4$ is significantly altered by the preparation method, calcination temperature, calcination duration and cooling rate. The normal spinel (cubic) forms during calcination at temperatures higher than 350 ^oC, with Cu^{2+} ions in the tetrahedral (A) sites and Fe^{3+} ions found on the A-sites and octahedral (B) sites [118,119,120]. While the inverse spinel (tetragonal) forms at temperature below 350 ^oC [121,122], where the Cu^{2+} ions mainly the on the B-sites, whereas, the Fe^{3+} ions are found on A- and B-sites with approximately equal occupancy. Weil et al. [123] reported a copper ferrite structure that was neither cubic nor inverse spinel, which was referred to as a disordered structure, with both kinds of ions in both sites. Earlier studies have also demonstrated that crystal distortion (tetragonal to cubic) may be induced due to the Jahn-Teller effect in partial inverse, bulk $CuFe_2O_4$ samples. The distortion depends on the Cu^{2+} ion distribution in the sublattices [124]. Since Cu^{2+} is a Jahn-Teller ion (J-T), it gives the anomalous favourable properties and also exhibits phase transition from tetragonal to cubic, depending on the temperature. The J-T transition is argued to be order-disorder in character, but exact nature is still not fully understood [125,126].

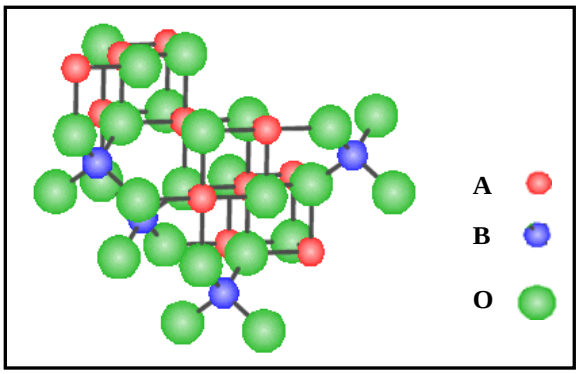

(a)

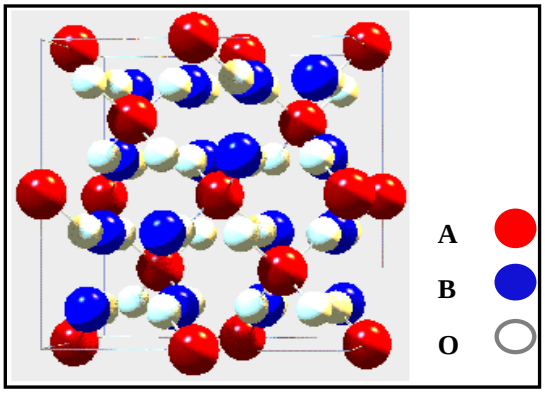

(b)

Figure 2.12: The spinel crystal structure of (a) tetragonal (inverse spinel) and (b) cubic spinel $CuFe_2O_4$ [127] (where A is the monovalent cation, B is the trivalent cation and O is oxygen)

2.10.2. Delafossite ferrites (CBO_2)

Delafossite is a ternary oxide with a general formula CBO_2, where C is a monovalent metal and B a trivalent metal. Examples of the delafossite systems include copper ferrite ($CuFeO_2$) and silver ferrite ($AgFeO_2$). The delafossite structure can be viewed as the stacking of $[B^{3+}O^{2-}{}_2]$ layers made of two closely-packed oxygen planes having all octahedral sites occupied by B^{3+} cations, which are connected by planes of C^+ cations arranged as a triangular network. Each C^+ cation is linearly coordinated with two oxygen ions from the oxygen planes above and below. The stacking sequence of successive oxygen compact layers along the *c* axis leads to various polytypes of the delafossite structure; the hexagonal layered structure can either belong to hexagonal 2H (space group: $P6_3/mmc$) or rhombohedral 3R (space group: $R3m$) structures as shown in Figure 2.13 (a) and (b) [128], respectively. The delafossite structure can be visualized

as consisting of two alternating layers: a planar layer of edge-sharing BO_6 octahedra flattening with respect to the *c*-axis. By stacking the double layers with alternating C layers oriented 180 ^{o}C relative to each other, the hexagonal 2H type is formed. The rhombohedral *3R* type is formed, if the double layers are stacked with the C layers oriented the same direction relative to one another but offset from each other in a three layer sequence.

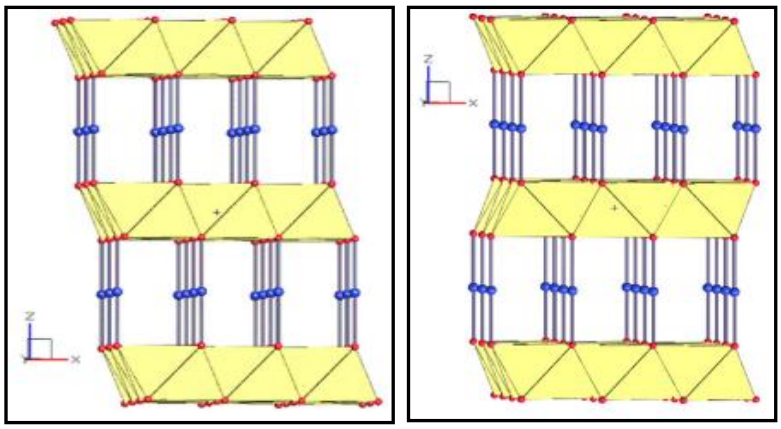

(a) (b)

Figure 2.13: The delafossite structure (yellow octahedra with coordinated Fe sites (red) and Cu/Ag sites (blue))

(a) rhombohedral (*R*3*m*)

(b) hexagonal (*$P6_3/mmc$*)

References

1. Sabatier, P. and Senderens, J. (1902), 'New syntheses of methane', *Journal of Society Chemical Ind.*, **21**, 504.

2. Schulz, H. (1999), 'Short history and present trends of Fischer-Tropsch synthesis', *Applied Catalysis A: General* **186**, 3.

3. Takeshita, T, and Yamaji, K. (2008), 'Important roles of Fischer-Tropsch synfuels in the global energy future', *Energy Policy*, doi:10.1016/j.enpol.2008.02.044

4. Dry, M.E. (1999), 'Fischer-Tropsch reactions and the environments', *Applied Catalysis A: General* **189**, 185.

5. Lozano-Blanco, G., Thybaut, J.W., Surla, K., Galtier, P. and Marin, G.B. (2006), 'Fischer-Tropsch synthesis: development of a microkinetic model for metal catalysis', *Oil and Gas Science and Technology – Review IFP* **61**, 489.

6. Dry, M.E. (1990), 'Fischer-Tropsch synthesis over iron catalysts', *Catalysis Letters* **7**, 241.

7. Dry, M.E. (1982), 'Catalytic aspects of industrial Fischer-Tropsch synthesis', *Journal of Molecular Catalysis* **17**, 133.

8. Dry, M.E. (2004), Chemical concepts used for engineering purposes. In A. Stenyberg & M. Dry (Ed.), *Fischer-Tropsch Technology, Studies in Surface Science and Catalysis* **152**, 196.

9. Luo, M. and Davis, B.H. (2003),'Fischer-Tropsch synthesis: Group II alkali-earth metal promoted catalysts' *Applied Catalysis A: General* **246**, 171.

10. Adesina, A.A. (1996), 'Practical and theoretical aspects of the catalytic Fischer-Tropsch process: Travails and Triumphs', *Applied Catalysis A: General* **138**, 345.

11. Vannice, M.A. (1975), 'The catalytic synthesis of hydrocarbons from H_2:CO mixtures over

the group VII metals: I. The specific activities and product distributions of supported metals', *Journal of Catalysis* **37**, 449.

12. Schulz, H., Beck, K. and Erich, E. (1988), In: Chang, C., Howe, R. and Yurchak, S. (Ed.), *Studies in Surface Science and Catalysis* **36**, 457

13. Claeys, M. and van Steen, E. (2004), 'Fischer-Tropsch Technology', *Studies in Surface Science and Catalysis* **152**, 601.

14. Mbileni, C.N. (2006), 'Applications of meso-structured carbonaceous materials as supports for Fischer-Tropsch metal catalyst', PhD Thesis, University of the Witwatersrand, Johannesburg

15. Mabaso, I. (2005), 'Nanosized iron crystallites for Fischer-Tropsch synthesis', PhD Thesis, University of Cape Town, Cape Town.

16. Lox, E.X. and Froment, G.F. (1993), 'Kinetics of the Fischer-Tropsch reaction on a precipitated promoted iron catalyst. 1. Experimental procedures and results', *Industrial and Engineering Chemistry Research* **32**, 61.

17. Lox, E.X. and Froment, G.F. (1993), 'Kinetics of the Fischer-Tropsch reaction on a precipitated promoted iron catalyst. 2. Kinetic modeling', *Industrial and Engineering Chemistry Research* **32**, 71.

18. Wang, Y-N., Ma, W-P., Lu, Y-J., Yang, J., Xiang, H.W, Xu, Y.Y., Li, Y.W., Zhang, B.J. and Zhao, Y.L. (2003), 'Kinetic modelling of Fischer-Tropsch synthesis over an industrial Fe-Cu-K catalyst', *Fuel* **82**, 195.

19. Anderson, R. (1984), 'The Fischer-Tropsch synthesis', New York: Academic Press.

20. Fischer, F. and Tropsch, H. (1926), 'The synthesis of petroleum at atmospheric pressures from gasification products of coal', *Brennstoff-Chemie* **7**, 97.

21. Craxford, S. and Rideal, E. (1939), 'Reactions of the Fischer-Tropsch synthesis of hydrocarbons and some related reactions', *Transactions of the Faraday Society* **35**, 946.

22. Johnson, B., Bartholomew, C. and Goodman, D. (1991), 'The role of surface structure and dispersion in CO hydrogenation on cobalt', *Journal of Catalysis* **128**, 231.

23. Lee, C.B. and Anderson, R.B, Proceedings of the 8th International Congress on Catalysis, Bruxelles, Belgium, (1985) II15.

24. Tau, M.L., Dabbagh, H.A., Chawla, B. and Davis, B.H. (1990), 'Fischer-Tropsch synthesis with an iron catalyst: incorporation of ethene into higher carbon number alkanes', *Catalysis Letters* **7**, 141.

25. Schulz, H., Erich, E., Gorre, H. and van Steen, E. (1990), 'Regularities of selectivity as a key for discriminating FT-surface reactions and formation of the dynamic system', *Catalysis Letters* **7**, 157.

26. Maitlis, P.M. (1989), 'A new view of the Fischer-Tropsch polymerization reaction', *Pure Applied Chemistry* **61**, 1747.

27. Maitlis, P., Long, H., Quyoum, R., Turner, M. and Whang, Z.Q. (1996), 'Heterogeneous catalysis of C-C bond formation: black art or organometallic science', *Journal of Chemical Society: Chemical Communication* **1**, 1.

28. Maitlis, P., Quyoum, R., Long, H. and Turne, M. (1999), 'Towards a chemical understanding of the Fischer-Tropsch reaction: Alkene formation', *Applied Catalysis A: General* **186**, 363.

29. Storch, H., Golumbic, N. and Anderson. R: 1951, The Fischer-Tropsch and related synthesis. New York: John Wiley and Sons.

30. Anderson, K. and Ekerdt, J. (1985), 'Study of Fischer-Tropsch synthesis over Fe/SiO_2: effect of diethylamine on hydrocarbon and alcohol production', *Journal of Catalysis* **95**, 602.

31. Dry, M.E (1990). 'The Fischer-Tropsch process - Commercial aspects', *Catalysis Today* **6**, 183.

32. Hindermann, J., Hutchings, G. and Kiennemann, A. (1993), 'Mechanistic aspects of the formation of hydrocarbons and alcohols from CO hydrogenation'. *Catalysis Reviews Science Engineering* **35**, 1.

33. Sternberg, A. and Wender, J, Proc. Intern. Conf. Coordination Chem., The Chemical Society, London, (1959) pp. 53

34. Roginski, S. (1965), In: Proceedings of 3rd Congress on Catalysis Amsterdam, pp. 939.

35. Pichler, H. and Schulz, H. (1970), 'Neue Erkenntnisse auf dem Gebiet der Synthese von Kohlenwasserstoffen aus CO und H_2', *Chemical Engineering and Technology* **42**, 1162.

36. Dry, M. (2002), 'The Fischer-Tropsch process: 1950 – 2000', *Catalysis Today* **71**, 227.

37. Shen, W., Dumesic, J. and Hill, C.J. (1981), 'Criteria for stable Ni particle size under methanation reaction conditions: Nickel transport and particle size growth via nickel carbonyl', *Journal of Catalysis* **68**, 152.

38. Rao, V.U.S., Stiegel, G.J., Cinquegrane, G.J. and R.D. Srivastava, R.D. (1992), 'Iron-based catalysts for slurry-phase Fischer-Tropsch process: Technology review', *Fuel Process Technology* **30**, 83.

39. Dry, M.E. (2004), 'FT catalysts', In: Steynberg, A. and Dry. M.E. (eds.): *Fischer-Tropsch Technology, Studies in Surface science and catalysis* **152**, 533.

40. O'Brien, R.J., Xu, L., Spicer, R.L., Bao, S., Milburn, D.R. and B.H. Davis, B.H. (1997), 'Activity and selectivity of precipitated iron Fischer-Tropsch catalysts', *Catalysis Today* **36**, 325.

41. Panpranot, J., Kaewkun, S., Praserthdam, P. and Goodwin Jr, J.G. (2003), 'Effect of cobalt precursors on the dispersion of cobalt on MCM-41' *Catalysis Letters* **91**, 95.

42. Davis, B.H. (2003), 'Fischer-Tropsch synthesis: relationship between iron catalyst composition and process variables', *Catalysis Today* **84**, 83.

43. Schulz, H. (2003), 'Fischer-Tropsch principles of CO-hydrogenation on iron catalysts', *Prepr. Pap. American Chemical Society., Div. Fuel Che.***48**, 557.

44. Dry, M.E. (1981), 'The Fischer-Tropsch synthesis", *In: Catalysis Science and Technology*, vol 1. Springer Verlag: New York: J.R Anderson, M. Boudart, pp. 159.

45. Anderson, R.B., Seligman, B., Schultz, J.F. and Elliot, M.A. (1952), 'Fischer-Tropsch synthesis: Some important variables of the synthesis of iron catalysts', *Industrial Engineering Chemistry* **44**, 391.

46. Arakawa, H. and Bell, A.T. (1983), 'Effect of potassium promotion on the activity and selectivity of iron Fischer-Tropsch catalysts', *Industrial Engineering Chemistry Process Design and Development* **22**, 97.

47. Li, S., Krishnamoorthy, S. Meitzner, G.D. and Iglesia, E. (2002), 'Promoted iron-based catalysts for the Fischer-Tropsch synthesis: Design, synthesis, site densities and catalytic properties', *Journal of Catalysis* **206**, 202.

48. Luo, M., O'Brien, R.J., Bao, S. and Davis, B.H. (2003), 'Fischer-Tropsch synthesis: induction and steady-state activity of high alpha potassium promoted iron catalysts', *Applied Catalysis A: General* **239**, 111.

49. Mogorosi, R.P., Fischer, N., Claeys, M. and van Steen, E. (2012), 'Strong-metal-support interaction by molecular design: Fe-silicate interactions in Fischer-Tropsch catalysts', *Journal of Catalysis* **289**, 140.

50. Wan, H.J., Wu, B.S., Tao, Z.C., Li, T.Z., Xiang, H.W. and Li, Y.W. (2006), 'Study of an iron-based Fischer-Tropsch synthesis catalyst incorporated with SiO_2', *Journal of Molecular Catalysis A: General* **260**, 255.

51. van den Berg, F.R., Craje, M.W.J., van der Kraan, A.M. and Geus, J.W. (2003), 'Influence of H_2/H_2O pre-treatment and H_2 pressure on the reduction behavior of Fe/ZrO_2 and $Fe/K/ZrO_2$ Fischer-Tropsch catalysts', *Applied Catalysis A: General* **251**, 347.

52. Duvenhage, D.J. and Coville, N.J. (2005), 'Effect of K, Mn and Cr on the Fischer-Tropsch activity of $Fe:Co/TiO_2$ Catalysts', *Catalysis Letters* **104**, 129.

53. Li, S., Li, A., Krishnamoorthy, S. and Iglesia, E. (2001), 'Effects of Zn, Cu, and K promoters on the structure and on the reduction, carburization, and catalytic behaviour of iron-based Fischer-Tropsch synthesis cataylsts', *Catalysis Letters* **77**, 197.

54. O'Brein, R.J. and Davis, B.H. (2004), 'Impact of copper on an alkali promoted iron Fischer-Tropsch catalyst', *Catalysis Letters* **94**, 1.

55. Jin, Y. and Datye, A. (2000), 'Phase transformations in iron Fischer-Tropsch catalysts during temperature-programmed reduction', *Journal of Catalysis* **196**, 8.

56. Wachs, I.E., Dwyer, D.J. and Iglesia, E. (1984), 'Characterization of Fe, Fe-Cu, and Fe-Ag Fischer-Tropsch catalyst', *Applied Catalysis* **12**, 201.

58. Yen, F.S., Chen, W.C., Yang, J.M. and Hong, C.T. (2002), 'Crystallite size variations of nanosized Fe_2O_3 powders during γ- and α- phase transformation', *Nanotechnology Letters* **2**, 245.

59. Navrotsky, A., Mazeina, L. and Majzlan, J. (2008),'Size-driven structural and thermodynamic complexity in iron oxides', *Science* **319**, 1635.

60. van Steen, E., Claeys, M., Dry, M.E., van de Loosdrecht, J., Viljoen, E.L. and Visagie, J.L. (2005),'Stability of nanocrystals: Thermodynamic analysis of oxidation and re-reduction of cobalt in water/hydrogen mixtures', *Journal of Physical Chemistry B* **109**, 3575.

61. van Steen, E. and Claeys, M. (2008), 'Fischer-Tropsch catalysts for the biomass-to-liquid process', *Chemical Engineering Technology* **31**, 655.

62. Shultz, J.F., Hall, W.K., Dubs, T.A. and Anderson, R.B. (1956), 'The Fischer-Tropsch

synthesis. XV. Cementite as catalyst', *Journal of American Chemical Society* **78**, 282.

63. Dictor, R.A. and Bell, A.T. (1986), 'Fischer-Tropsch synthesis over reduced iron oxide catalyst', *Journal of Catalysis* **97**,121.

64. Rao, K.R.P.M., Huggins, F.E., Mahajan, V., Huffman, G.P., Rao, V.U.S., Bhatt, B.L., Bukur, D.B., Davis, B.H. and O' Brien, R.J. (1995), 'Mössbauer spectroscopy study of iron-based catalysts used in Fischer-Tropsch synthesis', *Topics in Catalysis* **2**, 71.

65. Dry, M. (2002), 'The Fischer-Tropsch process: 1950-2000', *Catalysis Today* **71**, 227.

66. Geus, J. and van Dillen, A. (1997), 'Preparation of supported catalysts by deposition precipitation', In Ertl, G., Knözinger, H. and Weitkamp, J., editors, *Handbook of Heterogeneous Catalysis* Weinheim, Germany.

67. Reul, R.C. and Bartholomew, C.H. (1984), 'Effects of support and dispersion on the CO hydrogenation activity/selectivity properties of cobalt', *Journal of Catalysis* **85**, 78.

68. Reuel, R.C. and Bartholomew, C.H. (1984), 'The stoichiometries of H_2 and CO adsorption on cobalt: Effect of support and preparation', *Journal of Catalysis* **85**, 63.

69. Nijs, H. and Jacobs, P.A. (1980), 'Metal particle size distributions and Fischer-Tropsch selectivity. An extended Schulz-Flory model', *Journal of Catalysis* **65**, 328.

70. Davis, B.H. (2003), 'Fischer-Tropsch synthesis: relationship between iron catalyst composition and process variables', *Catalysis Today* **84**, 83.

71. Bukur, D.B., Lang, X. and Ding, Y.J. (1999), 'Pre-treatment effect studies with a precipitated iron Fischer-Tropsch catalyst in a slurry reactor ', *Applied Catalysis A: General* **186**, 255.

72. Hao, Q., Liu, F., Wang, H., Chang, J., Bai, L., Xiang, H., Li, Y., Yi, F. and Xu, B. (2007), 'Effect of reduction temperature on a spray-dried iron-based catalyst for slurry Fischer-Tropsch synthesis', *Journal of Molecular Catalysis A: Chemical* **261**, 104.

73. Herranz, T., Rojas, S., Pèrez-Alonso, F.J., Ojeda, M., Terreros, P. and Fierro, J.L.G. (2006), 'Genesis of iron carbides and their role in the synthesis of hydrocarbons from synthesis gas', *Journal of Catalysis* **243**, 199.

74. Wang, H., Yang, Y., Wu, B., Xu, J., Ding, M., Wang, H., Fan, W., Xiang, H. and Li, Y. (2009), 'Hydrogen reduction kinetics modelling of a precipitated iron Fischer-Tropsch catalyst', *Journal of Molecular Catalysis A: General* **308**, 96.

75. Shultz, J.F., Hofer, L.J.E., Cohn, E.M., Stein, K.C. and Anderson, R.B. (1959) *Bulletin – U. S. Bureau of Mines* **578**, 50.

76. Cohn, E.M. and Hofer, L.J.E. (1950), 'Preparation of iron carbides', *US Pat.*, 2,535,042.

77. Bukur, D.B., Koranne, M., Lang, X., Rao, K.R.P.M. and Huffman, G.P. (1995), 'Pretreatment effect studies with a precipitated iron Fischer-Tropsch catalyst', *Applied Catalysis A: General* **126**, 85.

78. Huffman, G.P. and Rao, K.R.P. (1996), 'Mössbauer study of iron Fischer-Tropsch catalysts during activation and synthesis', *Energy and Fuels* **10**, 546.

79. Bukur, D.B., Nowicki, L., Manne, R.K. and Lang, X. (1995), 'Activation studies with a precipitated iron catalyst for Fischer-Tropsch synthesis: II Reaction studies', *Journal of Catalysis* **155**, 366.

80. Loaiza-Gil, A., Fontal, B. and Rueda, F. (1999), 'On carbonaceous deposit formation in carbon monoxide hydrogenation on a natural iron catalyst', *Applied Catalysis A: General* **177**, 193.

81. Blanchard, F., Reymond, J.P., Pommier, B. and Teichner, J.J. (1982), 'On the mechanism of the Fischer-Tropsch synthesis involving unreduced iron catalyst', *Journal of Molecular Catalysis* **17**, 171.

82. Reymond, J.P., Mérlaudeau, O. and Teichner, S.J. (1982), 'Changes in the surface structure and composition on an iron catalyst of reduced or unreduced Fe_2O_3 during the reaction of

carbon monoxide and hydrogen', *Journal of Catalysis* **75**, 39.

83. Bukur, D.B., Nowicki, L., Manne, R.K., and Lang, X. (1995), 'Activation studies with as precipitated iron catalyst for Fischer-Tropsch synthesis 2: Reaction studies', *Journal of Catalysis* **155**, 366.

84. Amelse, J.A., Butt, J.B. and Schwartz, L. (1978), 'Carburization of supported iron synthesis catalysts', *Journal of Physical Chemistry* **82**, 558.

85. Raupp, G.B. and Delgass, W.N. (1979), 'Mössbauer investigation of supported Fe catalysts: III. *In situ* kinetics and spectroscopy during Fischer-Tropsch synthesis', *Journal of Catalysis* **58**, 361.

86. Bukur, D.B., Lang, X., Rossin, J.A., Zimmerman, W.H., Rosynek, M.P., Yeh, E.B. and Li, C. (1989), 'Activation studies with a promoted precipitated iron Fischer-Tropsch catalyst', *Industrial and Engineering Chemistry Research* **28**, 1130.

87. Ding, M., Yang, Y., Wu, B., Wang, T., Xiang, H. and Li, Y. (2011), 'Effect of reducing agents on microstructure and catalytic performance of precipitated iron-manganese catalyst for Fischer-Tropsch synthesis', *Fuel Processing Technology* **92**, 2353.

88. Datye, A.K., Shroff, M.D., Harrington, M.S., Coulter, K.E., Sault, A.G. and Jackson, N.B. (1995), 'Activation of precipitated iron Fischer-Tropsch synthesis catalysts', *Journal of Catalysis* **156**, 185.

92. 'Process conditions', en.wikipedia.org/wiki/Fischer-Tropsch_process.

93. Hexana, W.M. and Coville, N.J. (2010), 'Indium as a chemical promoter in Fe-based Fischer-Tropsch synthesis', *Applied Catalysis A: General* **377**, 150.

94. Cairns,P., 'Oxygenates in Iron Fischer-Tropsch Synthesis: is Copper a selectivity promoter?', PhD Thesis, University of Cape Town, Cape Town, 2008.

95. O'Brien, R.J., Xu, L., Spicer, R.L., Bao, S., Milburn, D.R. and Davis, B.H. (1997), 'Activity and selectivity of precipitated iron Fischer-Tropsch catalysts', *Catalysis Today* **36**, 325.

96. Hexana, W.M. and Coville, N.J. (2010), 'Indium as a chemical promoter in Fe-based Fischer-Tropsch synthesis', *Applied Catalysis A: General* **377**, 150.

97. Jin, Y. and Datye, A.K. (2000),'Phase transformations in iron Fischer-Tropsch catalysts during temperature-programmed reduction', *Journal of Catalysis* **196**, 8.

98. Kölbel, H., Ackermann, P., Ruschenburg, E., Langheim, R. and Engelhardt, F. (1951), 'Beitrag zur Fischer-Tropsch synthese on Eisenkontakten', *Chem. Ing. Tech.*, **23**, 153.

99. Kölbel, H. and Ralek, M. (1980), 'The Fischer-Tropsch synthesis in the liquid phase', *Catalysis Reviews, Science and Engineering* **21**, 225.

100. O'Brien, R.J., Xu, L., Spicer, R.L., Bao, S., Milburn, D.R. and Davis, B.H. (1997), 'Activity and selectivity of precipitated iron Fischer-tropsch catalysts', *Catalysis Today* **36**, 325

101. Bukur, D.B., Mukesh, D. and Patel, S.A. (1990), 'Promoter effects on precipitated iron catalysts for Fischer-Tropsch synthesis', *Industrial Engineering Chemistry Research* **29**, 194.

102. Jacobs, G., Ribeiro, M.A., Ma, W., Ji, Y., Khalid, S., Sumodjo, P.T.A. and Davis, B.H. (2009), 'Group 11 (Cu, Ag, Au) promotion of 15%Co/Al_2O_3 Fischer-Tropsch synthesis catalysts', *Applied Catalysis A General* **361**, 137.

103. Kodama, R.H., Berkowitz, A.E., McNiff, E.J. and Foner, S. (1996), 'Surface spin disorder in $NiFe_2O_4$ nanoparticles', *Physical Review Letters* **77**, 394.

104. Sterwart, S.J., Tueros, M.J., Cernicchiaro, G., Scorzelli, R.B. (2004), 'Magnetic size growth in nanocrystalline copper ferrite', *Solid State Communications* **129**, 347.

105. Ponhan, W. and Maensiri, S. (2009), 'Fabrication and magnetic properties of electrospun copper ferrite ($CuFe_2O_4$) nanofibers', *Solid State Sciences* **11**, 479.

106. Kang, K.-S., Kim, C.-H., Cho, W.-C., Bae, K.-K., Woo, S.-W. and Park, C.-S. (2008),

'Reduction characteristics of $CuFe_2O_4$ and Fe_3O_4 by methane; $CuFe_2O_4$ as an oxidant for two-step thermochemical methane reforming', *International Journal of Hydrogen energy* **33**, 4560.

107. Faungnawakij, K., Tanaka, Y., Shimoda, N., Fukunaga, T., Kikuchi, R. and Eguchi, K. (2007), 'Hydrogen production from dimethyl ether steam reforming over composite catalysts of copper ferrite spinel and alumina', *Applied Catalysis B: Environmental* **74**, 144.

108. Eguchi, K., Shimoda, N., Faungnawakij, K., Matsui, T., Kikuchi, R. and Kawashima, S. (2008), 'Transmision electron microscopic observation on reduction process of copper-iron spinel catalyst for steam reforming of dimethyl ether', *Applied Catalysis B: Environmental* **80**, 156.

109. Faungnawakij, K., Kikuchi, R., Fukunaga, T. and Eguchi, K. (2008), 'Catalytic hydrogen production from dimethly ether over $CuFe_2O_4$ spinel-based composites: Hydrogen reduction and metal dopants effects', *Catalysis Today* **138**, 157.

110. Goya, G.F. and Rechenberg, H.R. (1998), 'Superparamagnetic transition and local disorder in $CuFe_2O_4$ nanoparticles', *Nanostructure Materials* **10**, 1001.

111. Jiang, J.Z., Goya, G.F. and Rechenberg, H.R. (1999), 'Magnetic properties of nanostructured $CuFe_2O_4$', *Journal of Physics: Condensed Matter* **20**, 4063.

112. Pandya, P.B., Joshi, H.H. and Kulkarni, R.G. (1991), 'Magnetic and structural properties of $CuFe_2O_4$ prepared by the co-precipitation method', *Journal of Materials Science Letters* **8**, 474.

113. Tao, S., Lu, X. and Toftsorensen, O. (2000), 'Preparation and gas sensing properties of $CuFe_2O_4$ at reduced temperature', *Materials Science and Engineering B* **77**, 172.

114. Despax, C., Tailhades, P., Baubet, C., Villette, C. and Rousset, A. (1997), '$CuFe_2O_4$ thin-films – elaboration process, microstructural and magneto optical properties', *Thin Solid Films* **293**, 22.

115. Zhang, Y.S. and Stangle, G.C. (1994), 'Preparation of fine multicomponent oxide ceramic powder by a combustion synthesis process', *Journal Material Research* **9**, 1997.

116. Selvan, R.K., Augustin, C.O., Berchmans, L.J. and Saraswathi, R. (2003), 'Combustion synthesis of $CuFe_2O_4$', *Materials Research Bulletin* **38**, 41.

117. Goya, G.F., Rechenberg, H.R. and Jiang, J.Z. (1998), 'Structural and magnetic properties of ball milled copper ferrite', *Journal of Applied Physics* **84**, 1101.

118. Villette, C., Tailhades, Ph. and Rousset, A. (1995), 'Thermal behaviour and magnetic properties of acicular copper-cobalt ferrite particles', *Journal of Solid State Chemistry* **117**, 64.

119. Evans, B.J. and Hafner, S. (1968), 'Mössbauer resonance of Fe^{57} in oxidic spinel containing Cu and Fe', *Journal of Physical Chemical Solids* **29**, 1573.

120. Tang, X.X., Manthiram, A. and Goodenough, J.B. (1989), 'Copper ferrite revisited', *Journal of Solid State Chemistry* **79**, 250.

121. Thapa, D., Kulkarni, N., Mishra, S.N., Paulose, P.L. and Ayyub, P. (2010), 'Enhanced magnetization in cubic ferromagnetic $CuFe_2O_4$ nanoparticles synthesized from a citrate precursor: the role of Fe^{2+}', *Journal of Physics D: Applied Physics* **43**, 195004.

122. Kučera, M., V. Kolinskỳ, V., Višňovskỳ, S., Chvostová, D., Venkataramani, N. and Prasad, S. (2007), 'Faraday effect in cubic and tetragonal copper ferrite $CuFe_2O_4$ films-Comparative studies', *Journal of Magnetism and Magnetic Materials* **316**, e688.

123. Weil, L., Bertaut, F. and Bochirol, L. (1950), 'Propriétés magnétiques et structure de la phase quadratique du ferrite de cuivre', *Journal de Physique et le Radium* **11**, 208.

124. Ohnishi, H. and Teranishi, T. (1961), 'Crystal distortion in copper ferrite-chromite series', *Journal of Physical Society of Japan* **16**, 35.

125. Gajbhiye, N.S., Balaji, G., Bhattacharyya, S. and Ghafari, M. (2004), 'Mössbauer study of nanosize $CuFe_2O_4$ particles', *Hyperfine Interactions* **57**, 156.

126. Selvan, R.K., Krisham, V., Augustin, O., Bertagnolli, Kim, S. and Gedanken, A. (2008), 'Investigations on the structural, morphological, electrical and magnetic properties of $CuFe_2O_4$-NiO nanocomposites', *Chemistry of Material* **20**, 429.

127. http://www.unizar.es/gfgoya/index_archivos/image30431.jpg

128. Li, Jun., Yokochi, A.F.T. and Sleight, A.W. (2004), 'Oxygen intercalation of two polymorphs of $CuScO_2$', *Solid State Sciences* **6**, 831.

Chapter 3

Scope of the Thesis

This chapter is aimed at providing the reader with a brief discussion of the work that will be covered in the study.

Copper is added to the industrially used iron-based Fischer-Tropsch catalysts, to assist in the reducibility of the iron oxide during H_2 activation [1,2,3]. Furthermore, the presence of copper in iron-based Fischer-Tropsch catalysts may affect the Fischer-Tropsch performance of the catalyst [4,5]. Previous studies [6,7,8] have shown that in order for any promotional effect to occur, intimate contact between the promoter and the catalytically active phase is required. To achieve the intimate contact between the metals, ferrite systems were used. Ferrites are a group of metal oxides or mixed metal oxides in which intimate contact between metals exists. In this study the promotional effect of group 1b metals (copper and silver) on iron-based Fischer-Tropsch catalysts was investigated using ferrites (spinel copper ferrite ($CuFe_2O_4$), delofassite copper ferrite ($CuFeO_2$) and silver ferrite ($AgFeO_2$) as model catalysts. To our knowledge, no studies have been conducted using ferrites as model catalysts for investigating the promotional effect of copper (Cu) and silver (Ag) on iron-based Fischer-Tropsch catalysts.

The model catalysts were preparation via the co-precipitation method of their respective nitrates. No additional promoters (chemical or structural promoters) were added in order to minimise any additional promotional effects by other promoters. The nature, composition, reducibility of the calcined, H_2 and CO activated, spent model catalysts was characterized using several methods. These techniques include X-ray diffraction (XRD), Mössbauer absorption spectroscopy (MAS), Scanning electron microscopy-electron dispersive x-ray analysis (SEM-EDX), Atomic absorption spectroscopy (AAS), H_2-Temperature-programmed reduction (TPR) and *in-situ* X-ray diffraction (XRD). *In-situ* XRD analysis was conducted in order to gain better understanding of the phase transformation and changes in the average crystallite sizes in the model catalysts during the H_2 and CO activation. The Fischer-Tropsch performance of the model catalysts were tested in a slurry bed reactor at low temperature Fischer-Tropsch conditions (250 ^oC, 20 bar, H_2: CO in a ratio of 2.1: 1 and argon as an internal standard).

References

1. Cairns,P., 'Oxygenates in Iron Fischer-Tropsch Synthesis: is Copper a selectivity promoter?', PhD Thesis, University of Cape Town, Cape Town, 2008.

2. Bukur, D., Okabe, K., Rosynek, P., Li, C., Wang, D., Rao, K. & Huffman, G. (1995), 'Activation studies with a precipitated iron catalyst for Fischer-Tropsch synthesis', *Journal of Catalysis* **155**, 353.

3. Dry, M. (1981), Catalysis - Science and Technology. In John R. Anderson and Michel Boudart (Ed.), **1**, 159. Berlin Heidelburg:Springer-Verlag.

4. O'Brien, R.J., Xu, L., Spicer, R.L., Bao, S., Milburn, D.R. and Davis, B.H. (1997), 'Activity and selectivity of precipitated iron Fischer-Tropsch catalysts', *Catalysis Today* **36**, 325.

5. Bukur, D.B., Mukesh, D. and Patel, S.A. (1990), 'Promoter effects on precipitated iron catalysts for Fischer-Tropsch synthesis', *Industrial Engineering Chemistry Research* **29**, 194.

6. Wachs, I.E., Dwyer, D.J. and Iglesia, E. (1984), 'Characterization of Fe, Fe-Cu, and Fe-Ag Fischer-Tropsch catalyst', *Applied Catalysis* **12**, 201.

7. Li, S., Li, A., Krishnamoorthy, S. and Iglesia, E. (2001), 'Effects of Zn, Cu, and K promoters on the structure and on the reduction, carburization, and catalytic behaviour of iron-based Fischer-Tropsch synthesis catalysts', *Catalysis Letters* **77**, 197.

8. Jin, Y. and Datye, A.K. (2000), 'Phase transformations in iron Fischer-Tropsch catalysts during temperature-programmed reduction', *Journal of Catalysis* **196**, 8.

Chapter 4

Experimental Section

This chapter is aimed at providing the reader with a detailed discussion on the method of preparation of the selected model catalysts, characterization techniques used and the Fischer-Tropsch synthesis reaction conditions, also included is the analysis method of the Fischer-Tropsch synthesis products.

4.1. Model catalysts preparation

Maghemite (γ-Fe_2O_3) and hematite (α-Fe_2O_3) which were used as reference materials were prepared using the precipitation method while the co-precipitation method was used in the preparation of the spinel copper ferrite ($CuFe_2O_4$), delafossite copper ferrite ($CuFeO_2$) and silver ferrite ($AgFeO_2$). All the model catalysts were prepared following modified literature methods, and are discussed below.

4.1.1. Reagents

The reagents used in the preparation of the model catalysts were iron nitrate ($Fe(NO_3)_3{\cdot}9H_2O$, 98.0 %), copper nitrate ($Cu(NO_3)_2{\cdot}3H_2O$, 98.0 %) and silver nitrate ($AgNO_3$, 99.9 %). An aqueous ammonia solution (25 wt.-%) and an aqueous sodium hydroxide solution (45 wt.-%) were used as precipitating agents. All reagents were purchased from Kimix and were used as received.

4.2. Precipitation Method

4.2.1. Preparation of maghemite (γ-Fe_2O_3)

An aqueous solution of 25 wt.-% ammonia hydroxide (20 ml) was added drop-wise to 150 ml solution of 0.3 M $Fe(NO_3)_3{\cdot}9H_2O$ under constant stirring until pH of ~10. The solution was stirred for 4 hrs at room temperature. Thereafter, the precipitate was recovered by filtration and washed six times by adding 250 ml of de-ionized water to the precipitate. The recovered precipitate was dried in an oven at 120 ^oC for 16 hrs and subsequently calcined at 350 ^oC for 6 hrs (heating rate from room temperature to 350 ^oC of 10 $^oC.min^{-1}$) in a fluidised bed reactor in air with a flowrate of 150 ml(STP).min^{-1} [1].

4.2.2. Preparation of hematite (α-Fe_2O_3)

An aqueous solution of 25 wt.-% ammonium hydroxide (20 ml) was added drop-wise to 150 ml solution of 0.3 M $Fe(NO_3)_3 \cdot 9H_2O$ under constant stirring until pH of ~10. The resulting suspension was stirred for 4 hrs at room temperature. Thereafter, the precipitate was recovered by filtration and washed six times by adding 250 ml of de-ionized water to the precipitate. The recovered precipitate was dried in an oven at 120 ^oC for 16 hrs and subsequently calcined at 950 ^oC for 8 hrs (heating rate from room temperature to 950 ^oC of 10 $^oC.min^{-1}$) in a fluidised bed reactor, in air with a flowrate of 150 ml(STP).min^{-1} [2].

4.2.3. Preparation of copper oxide (CuO)

Copper oxide was prepared by drop-wise addition of (25 ml) of a 4M aqueous NaOH solution to 15 ml of a 0.7 M aqueous solution of $Cu(NO_3)_2 \cdot 3H_2O$ with constant stirring until pH of ~10. The precipitate was washed five times with 25 ml of de-ionized water. Thereafter, the sample was dried in an oven at 120 ^oC for 16 hrs and subsequently calcined in a fluidized bed in air at 450 ^oC (heating rate of 10 $^oC.min^{-1}$) for 4 hrs [3].

4.3. Co-precipitation Method

4.3.1. Preparation of copper ferrite ($CuFe_2O_4$)

An aqueous solution of 16.6 M sodium hydroxide (25 ml) was added drop-wise to 150 ml mixed-metal nitrate (0.1 M $Cu(NO_3)_2 \cdot 3H_2O$ (90 ml) and 0.3 M $Fe(NO_3)_3 \cdot 9H_2O$ (60 ml)) solution with a molar ratio of Cu: Fe = 1: 2, while stirring at a constant temperature of 70 ^oC. The final pH of the solution was 12. The mixture was heated under reflux at 70 ^oC for 6 hrs. The precipitate was recovered by filtration and washed 6 times with 250 ml of de-ionized water. Thereafter, the precipitate was dried in an oven at 120 ^oC for 16 hrs and subsequently calcined a fluidized bed reactor at 950 ^oC (heating ramp rate of 10 $^oC.min^{-1}$) for 8 hrs in air with a flowrate of 200 ml(STP).min^{-1} [4,5].

4.3.2. Preparation of the delafossite ferrite systems

4.3.2.1. Preparation of copper ferrite ($CuFeO_2$)

An aqueous solution of 16.6 M sodium hydroxide (25 ml) was added drop-wise to 150 ml of a 0.3 M mixed-metal nitrate (ratio of $Cu(NO_3)_2 \cdot 3H_2O$ and $Fe(NO_3)_3 \cdot 9H_2O$ of 1 : 2), while stirring at 70 ^oC until pH of ~12. The mixture was refluxed at 70 ^oC for 6 hrs. The resulting precipitate was recovered by filtration and washed 6 times with 250 ml of de-ionized water.

The precipitate was dried in an oven at 120 ^{o}C for 16 hrs and subsequently calcined at 950 ^{o}C (heating ramp rate of 15 ^{o}C.min^{-1}) for 48 hrs in a fluidised bed reactor under argon (flowrate of 100 ml(STP).min^{-1}), with intermediate grinding every 12 hrs in an agate mortar [6].

4.3.2.2. Preparation of silver ferrite ($AgFeO_2$)

An aqueous solution of 16.6 M sodium hydroxide (25 ml) was added drop-wise to a 150 ml mixed-metal nitrate (0.8 M $AgNO_3$ and 2.2 M $Fe(NO_3)_3{\cdot}9H_2O$) solution under stirring until a pH of ~12. An excess of iron was used to ensure incorporation of all silver as delafossite [7]. The mixture was heated under reflux at 70 ^{o}C for 6 hrs. The resulting ruby-brown precipitate was recovered by filtration and washed 6 times with 250 ml of de-ionized water. The ruby-brown precipitate was dried in an oven at 120 ^{o}C for 16 hrs and subsequently calcined at 400 ^{o}C (heating ramp rate of 10 ^{o}C.min^{-1}) for 8 hrs in a fluidised bed reactor under argon with a flowrate of 100 ml(STP).min^{-1}, [8]. A relatively low temperature was chosen since sliver ferrite decomposes in air to metallic silver and hematite at temperatures above 700 ^{o}C.

4.4. Characterization Techniques

The elemental composition of the calcined model catalysts was determined using atomic absorption spectroscopy (AAS) and scanning electron microscopy - energy dispersive X-ray analysis (SEM-EDX). The phases present, relative abundances and the average crystallite sizes of the calcined, activated and spent model catalysts were confirmed using X-ray diffraction (XRD). Mössbauer absorption spectroscopy (MAS) was used to study the iron phase(s) present i.e., the valence state of the iron present and relative abundance in the calcined, activated and spent model catalysts. Infrared spectroscopy (IR) was also used to study the iron and copper phases present in the calcined model catalysts. H_2-temperature programmed reduction (H_2-TPR) was used to study the reducibility and reduction behaviour of the model catalysts in hydrogen atmosphere. The phase transformation, relative abundance of the respective present phase(s) and the changes in the average crystallite sizes during H_2 and CO activation were studied using *in-situ* X-ray diffraction (*in-situ* XRD).

4.4.1. Atomic Absorption spectroscopy (AAS)

The sample (0.10 g) was digested in a mixture of 8 ml of 30 % hydrochloric acid (HCl) and 2 ml of 40 % hydrofluoric acid (HF). The slurry was brought to boiling in a 250 ml Erlenmeyer flask. Once boiling, 10 ml of 60 % nitric acid (HNO_3) was added and the resulting solution

was reduced to a volume of approximately 2 ml of concentrated perchloric acid (5 ml) was added and the resulting solution was reduced again to 2 ml. The sample was quantitatively transferred to a 100 ml volumetric flask and made up to a volume of 100 ml with distilled water. The liquid sample was then filtered and the filtrate was analysed on a Varian SpectrAA-30 spectrometer attached to a DS-15 station to determine the concentrations of iron, copper, silver and sodium on the respective calcined model catalysts.

4.4.2. Scanning electron microscopy - energy dispersive x-ray analysis (SEM- EDX)

The morphology of the calcined and spent model catalysts was determined using SEM. A scanning electron microscope (Nova NanoSEM 230) equipped with a Four Quadrant Back Scatter Detector and an energy dispersive Fissons Kevex X-ray spectrometer (EDXA) operating at 20 keV and a working distance of 6 mm from the sample. The INCA software was used to determine the amount of iron, copper, silver and sodium in the model catalyst. Sample preparation involved sprinkling the sample on an aluminium stub coated with glue containing graphite. Graphite is used to conduct electrons, thereby preventing charge build up. The samples are then coated with carbon, which does not interfere with the elemental analysis.

4.4.3. X-ray diffraction (XRD)

The crystalline phases present, relative abundances of the phases and the average crystallite sizes in the calcined, reduced and spent model catalysts were determined by X-ray diffraction (XRD) using a Bruker, D8 Advanced X-ray diffractometer (Germany) with a Co-K_α radiation source (λ = 1.78897 Å) and a position sensitive detector (Bruker Vantec) operating at 35 kV and 40 mA. For all the samples the optics were set to parallel beam geometry so as to counteract possible peak shifts due to sample height difference (sample displacement). The XRD patterns of the samples were measured in 0.0057 ^{o} steps from 10 ^{o} to 90 ^{o} (in 2θ) and were identified by matching experimental patterns to entries in the Diffrac^{plus} Version 6.0 indexing software. The average crystallite sizes in nanometers (nm) were calculated using Topas Rietveld refinement software.

4.4.4. Mössbauer absorption spectroscopy (MAS)

Mössbauer absorption spectroscopy (MAS) measurements of the calcined, reduced and spent model catalysts were performed at room temperature (298 K), at liquid helium temperature

(4.2 K) and at liquid helium temperature (4.2 K) in an applied magnetic field of 10 T using conventional constant acceleration spectrometers designed to operate in the absorption mode (MAS). The measurements in the absence or presence of an applied magnetic field were performed using the Spectromag SM4000-10 system. The individual absorption features of various doublets and sextets were then attributed to specific crystalline phases based on their isomer shift (δ), quadrupole splitting (Δ) and magnetic hyperfine field (B_{hf}). The quantity of each phase present was determined from their relative contribution to the absorption spectra. Metallic iron foil (α-Fe) was used to calibrate the velocity scale and the isomeric shift values are reported relative to it.

4.4.5. Fourier-Transform Infrared spectroscopy (FT-IR)

The Fourier-Transform Infrared technique was used to record the interaction of IR radiation with the sample by measuring the frequencies at which the sample absorbs the radiation. IR measurements were done on a Perkin-Elmer 1000 FT-IR spectrometer (Perkin-Elmer, USA). The samples were prepared by mixing pre-dried samples (50 mg) of the catalyst and potassium bromide (KBr, 1 g). The IR spectra were recorded between 400 and 4000 cm^{-1} with a resolution of 4 cm^{-1}. A 1000 scans were averaged to obtain the spectrum.

4.4.6. H_2-Temperature programmed reduction (H_2-TPR)

The reduction behaviour of the model systems was determined by H_2-temperature programmed reduction (H_2-TPR). The calcined model catalyst sample (m = 0.030 g) was placed in a quartz reactor of a Micromeritics AutoChem 2950 (Micromeritics Instrument Corp., USA). Hydrogen (5 %) in argon (Ar) was used as the reducing gas. The sample was dried in argon (flowrate of 50 $ml.min^{-1}$) for 2 hrs at 120 ^oC. Subsequently, the sample was heated in the reduction gas from 60 to 900 ^oC using a linear temperature ramp of 10 $^oC.min^{-1}$. The hydrogen consumption was measured with a thermal conductivity detector (TCD) which was calibrated at regular intervals using materials with known reduction behaviour (i.e., Ag_2O, NiO). The samples were heated with a regulated furnace and the temperature was measured by a thermocouple placed 2 mm above the sample.

4.4.7. *In-situ* X-ray diffraction (*in-situ* XRD)

The crystalline phases present, relative abundances of the phases and the average crystallite sizes of the model catalysts during H_2 and CO activation, respectively, were determined by

XRK-900 reaction chamber (Anton-Paar, Austria) attached to the X-ray diffraction (XRD) using a Bruker, D8 Advanced X-ray diffractometer (Germany) with a Co-K_α irradiation source (λ = 1.78897 Å) operating at 35 kV and 40 mA. The model catalyst (0.50 g) was loaded onto an alumina sample holder. A reducing gas was passed through the sample at a flowrate of 50 ml(STP).min^{-1}. The sample was heated from 50 to 270 ^{o}C with a heating rate of 1^{o}C.min^{-1}, while acquiring XRD data after every 30 minutes. Subsequently, the temperature was kept for 16 hours at 270 ^{o}C, while acquiring XRD data after every hour. The XRD patterns of the samples were measured in 0.011 ^{o} steps from 20 ^{o} to 84 ^{o} (in 2θ) and were identified by matching experimental patterns to entries in the Diffrac^{plus} Version 6.0 indexing software. The average crystallite sizes in nanometers (nm) were calculated using Topas Rietveld refinement software.

4.5. Fischer-Tropsch synthesis (FTS) experiments

4.5.1. Test unit set-up

The physical set-up of the rig for the Fischer-Tropsch synthesis is shown in Scheme 3.1. Gases are supplied from cylinders (Air Products, H_2, CO, CO_2, Ar) and were fed via mass flow controllers (Brooks 5850S, Brooks Instruments, The Netherlands). During normal operation, argon (used as an internal standard for the sample analysis), hydrogen (H_2) and carbon monoxide (CO) was fed to the system via mass flow controllers (MFC-1–3), straight to the reactor. The feed composition was measured with an on-line GC-TCD taken off the stream at the ampoule sampling point SP-1. The reactor is a 1L slurry bed micro reactor (E-1), equipped with a stirrer. A back-pressure regulator (BPR) is used to maintain and control the total pressure of the system. Heavy liquid hydrocarbon products from the Fischer-Tropsch synthesis were collected in the hot wax trap (E-2). The hot wax trap temperature was set at 210 ^{o}C, to ensure efficient collection of the heavy reaction products. Samples of the reactor effluent were taken at the ampoule sampling point SP-2. The effluent was sampled using the ampoule sampling technique [10] and with an online-GC-TCD. Water and oil products were collected in the cold trap (E-3), at room temperature. The temperature of all the lines after the reactor to the condenser was kept at 210 ^{o}C.

4.5.2. Reactor start-up

Commercially available hydrogenated hard wax (supplied by Sasol) was used as start-up slurry medium. The weighed model catalyst (5.00 g) was slowly added to the molten wax

(300 g) in a 1 dm^3 reactor vessel. The reaction vessel was then closed by attaching the reactor to the top flange by using the jaws. The temperature and pressure were subsequently increased to the reaction conditions under argon flowrate of 100 ml(STP).min^{-1}. The stirrer was set to 350 rpm. The activation gas was slowly introduced into the reactor vessel to prevent turbulence.

4.5.2.1. Model catalysts activation

Prior to the Fischer-Tropsch synthesis the model catalysts were activated *in-situ* at a temperature of 270 ^oC and atmospheric pressure, for 16 hrs, at a heating rate of 1 ^oC min^{-1}. Hydrogen (H_2) or carbon monoxide (CO) gas was passed through the stirred reactor at a flowrate of 500 ml(STP).min^{-1}. The activation conditions are summarized in Table 4.1.

Table 4.1: Activation conditions for model catalysts prior to the Fischer-Tropsch synthesis

Reduction conditions	
Activation gas	Hydrogen (H_2) / carbon monoxide (CO)
Mass of catalyst	5.00 g
Pressure	Atmospheric
Temperature	270 ^oC
Flow rate	500 ml(STP).min^{-1}

4.5.2.2. Fischer-Tropsch synthesis and conditions

After activation, the reactor was switched to bypass and cooled under argon (Ar) to the Fischer-Tropsch synthesis temperature of 250 °C. Once at reaction temperature the reactor system was pressurised to 20 bar (absolute). The synthesis gases were introduced into the reactor in a H_2: CO ratio of 2.1: 1. Argon was added to the synthesis gas in a ratio of Ar: CO of 0.6: 1 as an internal standard. The detailed Fischer-Tropsch synthesis conditions are given in Table 4.2.

Table 4.2: Fischer-Tropsch synthesis conditions for model catalysts

Fischer-Tropsch synthesis (FTS) conditions	
$Mass_{cat.}$	5.00 g
H_2: CO: Ar ratio	2.1: 1: 0.6
Temperature	250 ^{o}C
Pressure	20 bar (absolute)
Space velocity (SV)[1]	190 ml(STP).min^{-1}.g^{-1}
$F_{CO,0}$/W	0.14 mol.hr^{-1}.g^{-1}
Internal standard gas	Argon (Ar)

[1]: space velocity based on total gas flow in

The flow rates of hydrogen and carbon monoxide relative to the internal gas standard (Ar) were confirmed by on line gas chromatographic analysis over several consecutive feed analyses. The flow of the synthesis gas through the reactor system defined the start of the Fischer-Tropsch synthesis reaction. The progression of the reaction was monitored by regular sampling using a combination of online-TCD and offline-FID (via ampoule sampling) analytical techniques. Once the reaction was completed, the reactor was flushed with argon; thereafter, the stirred stopped and the temperature dropped to 150 ^{o}C. After 16 hrs the catalyst was allowed to settle at the bottom of the reactor, while, argon (50 ml(STP).min^{-1}) was passed through the reactor. Once the catalyst had settled at the bottom of the reactor, the temperature was further dropped to room temperature. Thereafter, the wax embedded sample was removed from the reactor and characterized.

4.6.1. Reactor set-up

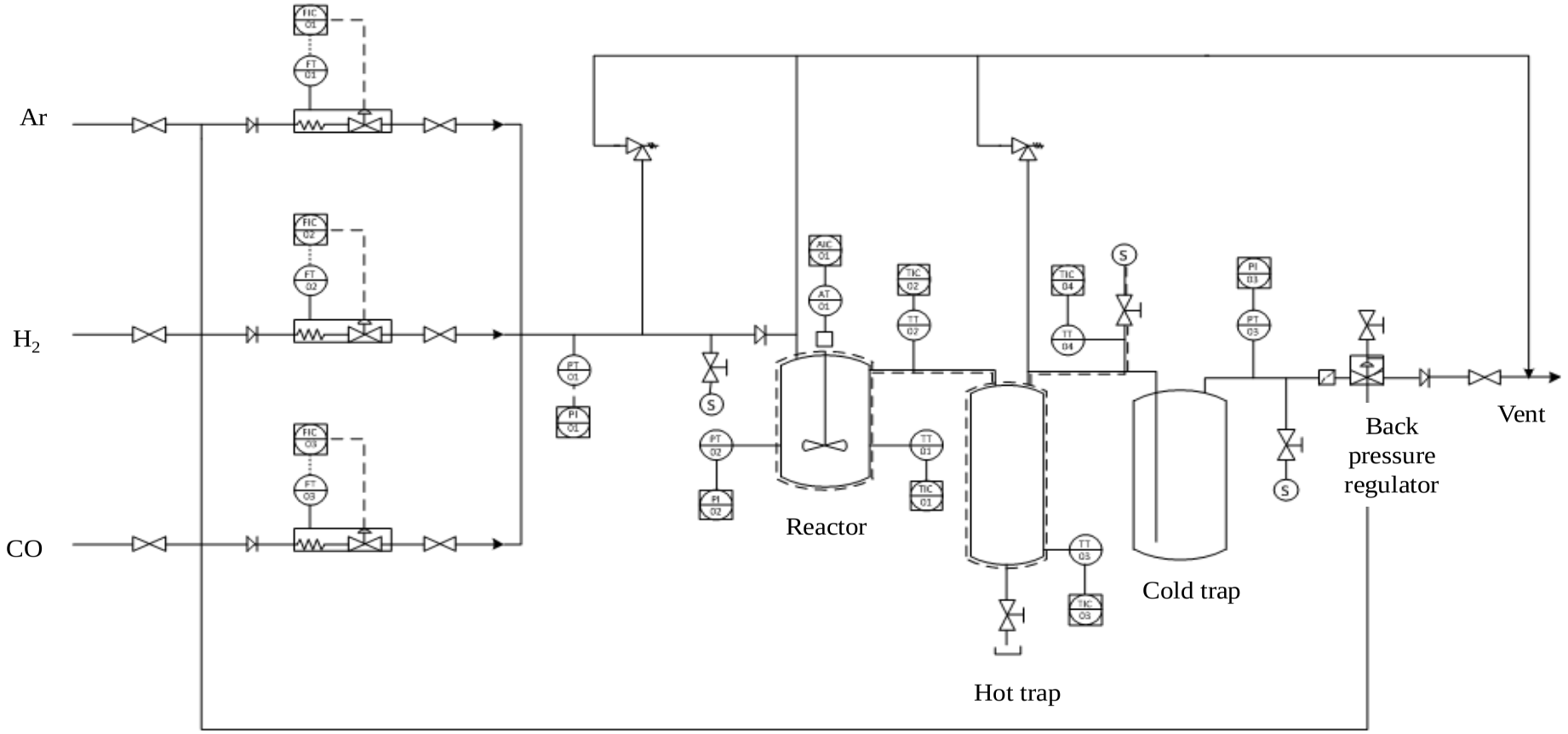

Scheme 4.1: Experimental set-up for Fischer-Tropsch synthesis using a slurry rig

4.7. Analytical procedures: Product analysis

4.7.1. Analysis of inorganic compound and methane

A gas chromatograph (GC) equipped with a thermal conductivity detector (TCD) was used for online analysis of H_2, CO, CO_2, Ar and CH_4 in the feed gas and the effluent gas from the Fischer-Tropsch synthesis. The use of this technique allowed for monitoring of reactant conversions and rate of product formation. Figure 4.1 shows a typical chromatogram obtained from the online GC-TCD analysis during the Fischer-Tropsch synthesis. The TCD peak areas of the respective gases were related to the peak area for argon (internal gas standard) in the chromatogram. The conditions under which the gas chromatographic analysis took place are tabulated in Table 4.3. A calibration gas mixture with known composition was used for the calibration of the TCD set-up. The peak areas (A_i) obtained from the TCD analysis of the calibration gas were then used to calculate the relative calibration factors ($f_{TCD,i}$), normalised for Arfollowing equation 3.1.

$$\left(\frac{\dot{n}_i}{\dot{n}_{Ar}}\right) = f_{TCD,i}\left(\frac{A_i}{A_{Ar}}\right) \qquad (4.1)$$

with $\dot{n}_i$: molar flow rate of compound i;

$\dot{n}_{Ar}$: molar flow rate of Ar.

$f_{TCD,i}$: response factor for compound i relative to the reference argon (Ar);

A_i : peak area of compound i in the TCD chromatogram;

A_{Ar} : peak area of Ar in the TCD chromatogram;

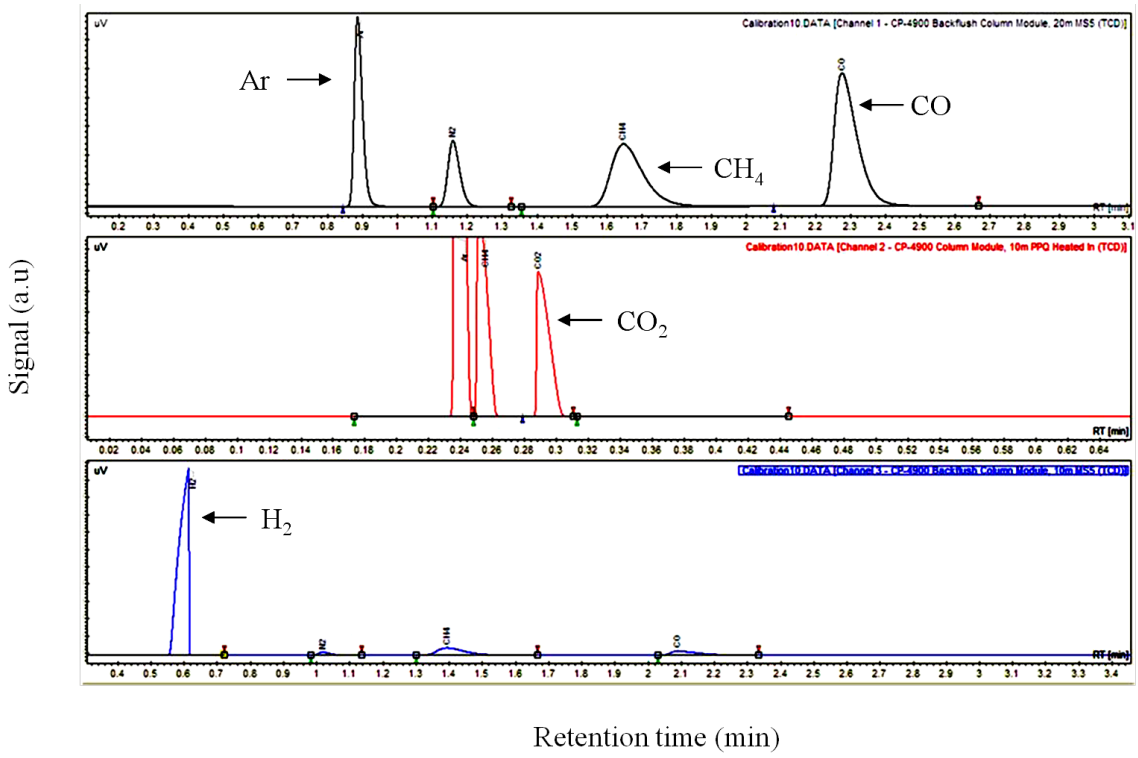

Figure 4.1: A typical chromatogram obtained from the online GC-TCD analysis during Fischer-Tropsch synthesis (only peaks used in analysis are labeled)

4.7.1.1. Data work-up – Inorganic compound and methane

During Fischer-Tropsch synthesis, online samples were taken and analysed using GC-TCD. The molar flow rate of each species present was calculated using the peak area of the respective species present relative to the internal standard Ar. Since the flow rate of the internal gas standard (Ar) is fixed and known, the flow rates of the inorganic compounds and methane was then calculated from the known argon flow rate:.

$$\dot{n}_i = f_{TCD,i} \cdot \left(\frac{A_i}{A_{Ar}}\right) \cdot \dot{n}_{Ar,feed} \qquad (4.2)$$

Table 4.3: Conditions for the on-line gas chromatographic analysis using Thermal Conductivity Detectors (TCD)

Micro Gas Chromatograph Varian CP-4900	
	Channel A
Detector	Thermal Conductivity Detector
Column Type	Molsieve 5 Å Plot Column, 20 m
Carrier Gas	Hydrogen (H_2)
Analysis Temperature	80 ^oC
Analysis Pressure	150 kPa
Analysis Time	220 s
Gases selected	Argon (Ar), Methane (CH_4), Carbon monoxide (CO)
	Channel B
Detector	Thermal Conductivity Detector (TCD)
Column Type	Pora PLOT Q Column, 10m
Carrier Gas	Hydrogen (H_2)
Analysis Temperature	60 ^oC
Analysis Pressure	100 kPa
Analysis Time	220 s
Gases selected	Carbon dioxide (CO_2)
	Channel C
Detector	Thermal Conductivity Detector (TCD)
Column Type	Molecular sieve 5 PLOT, 10 m
Carrier Gas	Argon
Analysis Temperature	80 ^oC
Analysis Pressure	150 kPa
Analysis Time	220 s
Gases selected	Hydrogen (H_2)

Once the molar flow rates of the reactants and some of the products have been determined, the conversions of the reactants and selectivity of the compounds can be calculated.

The conversions (X_i) of a reactant i, is determined according to equation 4.3, below.

$$X_i = \frac{\dot{n}_{i,in} - \dot{n}_{i,out}}{\dot{n}_{i,in}} \quad (4.3)$$

with X_i : percentage conversion of compound i;
$\dot{n}_{i,in}$: feed gas molar flow rate of compound i;
$\dot{n}_{i,out}$: tail gas molar flow rate of compound i.

The yield and selectivity of compound i ($S_{i,C}$) on a carbon basis is calculated according to equation 4.4 and 4.5, respectively;

$$Y_{i,C} = \frac{\dot{n}_{i,out}}{\dot{n}_{co,in}} \quad (4.4)$$

$$S_{i,C} = \frac{Y_{i,C}}{X_{CO} - Y_{CO2}} \quad (4.5)$$

While the selectivity of carbon dioxide ($S_{CO_2,C}$), on a carbon basis is determined according to equation 3.6.

$$S_{CO2,C} = \frac{Y_{CO2,C}}{X_{CO}} \quad (4.6)$$

with $Y_{i,c}$: yield of compound i;
$S_{i,C}$: selectivity of compound i on a carbon basis;
X_{CO} : carbon monoxide (CO) conversion;
Y_{CO_2} : yield of carbon dioxide (CO_2).

The rate of the Fischer-Tropsch synthesis, i.e., the rate at which carbon is incorporated into organic product compounds, r_{FT}, is given by equation 4.7;

$$r_{FT} = \frac{\dot{n}_{CO,in} - \dot{n}_{CO,out} - \dot{n}_{CO2}}{SA_{total,FexC}} \quad (4.7)$$

with $n_{CO,in}$: molar flow rate of CO entering the reactor;
$n_{CO,out}$: molar flow rate of CO exiting the reactor;
n_{CO_2} : molar flow rate of CO_2 produced;
$SA_{total,FexC}$: total surface area of iron carbide in the spent catalyst.

$$SA_{total,FexC} = \frac{m_{spent\ cat.}}{SA_{FexC}} \quad (4.8)$$

Assuming that all Fe in spent catalysts is Mössbauer absorption spectroscopy visible, then the amount of iron carbide in the spent catalyst can be determined. The mole balance for iron yields:

$$n_{Fe,in} = n_{Fe,out}$$

with $n_{Fe,in}$: number of moles of iron in calcined catalyst;
$n_{Fe,out}$: number of moles of iron in spent catalyst.

Therefore:

$$\sum \dot{n}_{Fe,in\ phase\ i,out} = \sum \frac{m_{Fe,out,i}}{MM_{Fe,out,i}} \quad (4.9)$$

with $m_{Fe,in}$: mass of iron in calcined catalyst;
$MM_{Fe,in}$: molar mass of iron in calcined catalyst;
$m_{Fe,out}$: mass iron in spent catalyst;
$MM_{Fe,out}$: molar mass of iron in spent catalyst.

$$m_{\text{spent catalyst}} = \sum n_i \qquad (4.10)$$

with $m_{\text{spent catalysts}}$: mass of iron in calcined catalyst;

$\sum n_i$: sum of iron compound i.

The surface area (SA_{FexC}) is calculated according to equation relating to a sphere or a cube (equation 4.11). The crystallite diameter (nm) used to calculate the surface area is obtained from XRD analysis.

$$SA_{FexC} = \frac{6000}{(d_{XRD} \times \rho)} \qquad (4.11)$$

with $SA_{,FexC}$: surface area ($g.m^{-2}$);

d_{XRD} : average crystallite diameter (nm);

ρ : density ($g.cm^{-3}$).

4.7.2. Offline sampling technique

The offline product sampling was conducted using the glass ampoule sampling technique developed by Schulz and co-workers [9,10]. Glass ampoules were prepared from commercially available Pasteur pipettes, which were evacuated and subsequently sealed. During sampling the capillary end of the pre-evacuated gas ampoule was inserted through an airtight septum into a heated ampoule (Scheme 3.2). By breaking the end of the capillary, using the breaking fork, the volatile compounds were sucked into the ampoule. The capillary was then sealed immediately with a butane flame (ampoule sealer). These samples can be stored and then analysed using a special ampoule breaking device connected to a gas chromatography (GC) system with a flame ionization detector (FID) for the analysis of organic product compounds.

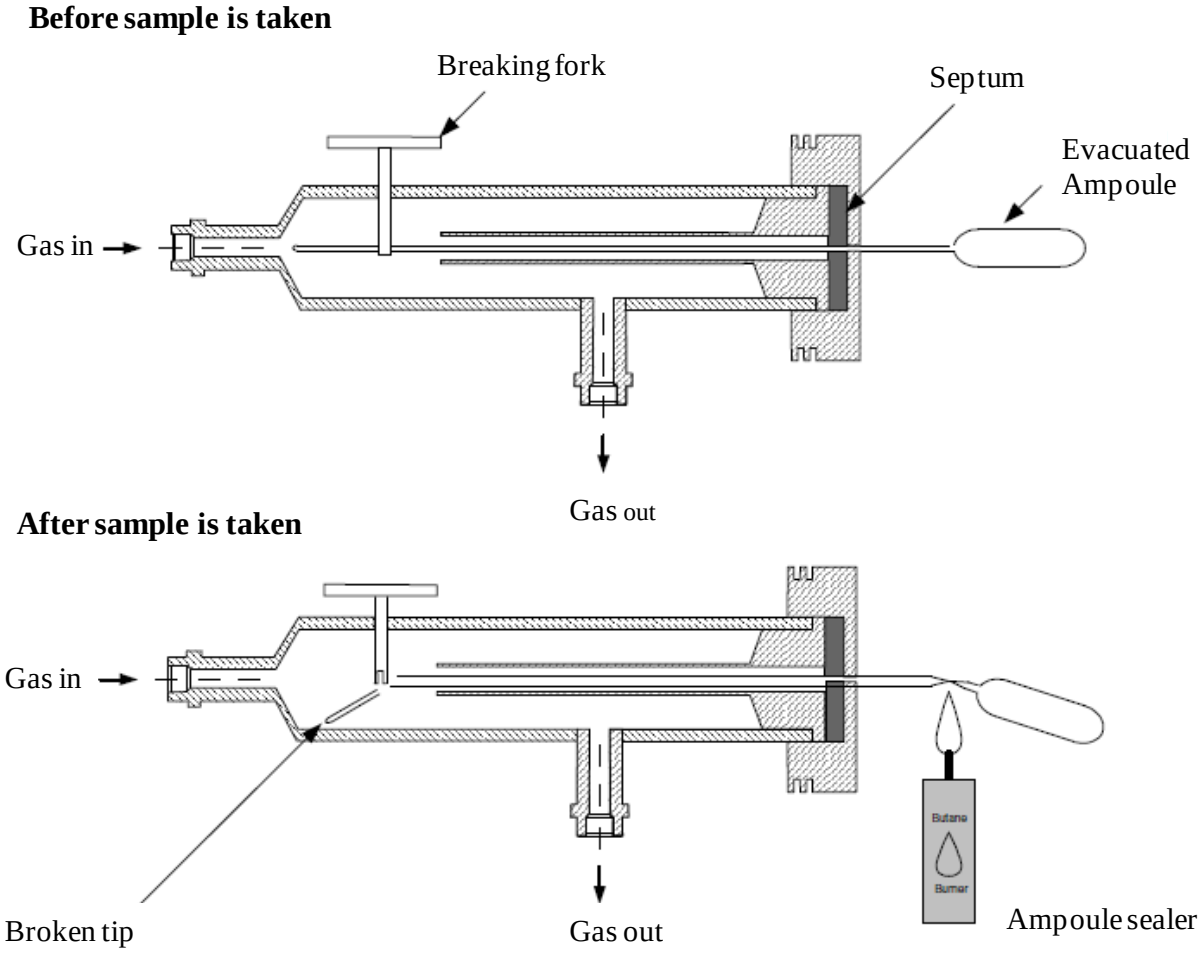

Scheme 4.2: Schematic drawing of the off-line ampoule sampling device

4.7.3. Analysis of organic product compounds

A gas chromatograph (GC) equipped with a flame ionization detector (FID) was used for offline analysis of organic products in the vapour phase under reaction conditions. The conditions under which the analysis took place are given in Table 4.4. A typical FID chromatogram of the Fischer-Tropsch synthesis products is shown in Figure 4.2.

The glass ampoule collected during the FTS run was placed into a heated ampoule breaker device where it was broken under a flow of nitrogen; this flow with the gas sample was then introduced into the split injector of the gas chromatograph through a system of valves, where the carrier gas was switched to hydrogen after 2 minutes.

The FID is carbon specific in its response, but the response of all carbon atoms is not equal. For example carbon atoms bonded to an oxygen atom gives a weaker response than other carbon atoms. To account for this variation in response, theoretical incremental response factors suggested by Kaiser et al. [11] are used. Using this approach, all carbon atoms not attached to an oxygen atom has a response factor of 1. For a carbon atom with a single bond to oxygen, the response factor is 0.55 and finally a carbon atom with a double bond to oxygen has no response. Therefore the response factor of a specific compound is calculated according to equation 4.12.

$$f_i = \left(\frac{N_{C,i}}{N_{C(noO)} + 0.55(N_{C(CO)})}\right) \qquad (4.12)$$

with f_i : response factor for compound i;
$N_{C,i}$: total number of carbon atoms;
$N_{C(noO)}$: number of carbon atoms not bonded to an oxygen atom;
$N_{C(CO)}$: number of carbon atoms with a single bond to oxygen.

The flow rate of the various organic product compounds can be obtained knowing the methane flow rate as obtained from the online GC-TCD analysis. The flow rate can be expressed as the molar flow rate of a product compound:

$$\dot{n}_{i,C} = \frac{f_{FID,i}}{N_{C,i}} \cdot \left(\frac{A_i}{A_{CH_4}}\right) \cdot \dot{n}_{CH_4} \qquad (4.13)$$

or as the molar flow rate of carbon in a product compound:

$$\dot{n}_{i,C} = f_{FID,i} \cdot \left(\frac{A_i}{A_{CH_4}}\right) \cdot \dot{n}_{CH_4} \qquad (4.14)$$

4.7.3.1. Data work-up – Organic compound

The selectivity (or molar content) of carbon within the fraction of carbon compounds ($S_{i,c,}$), can be expressed as in equation 4.15.

$$S_{i,c} = \frac{n_{i,c}}{\sum n_{i,c}} \qquad (4.15)$$

with $n_{i,c}$: molar fraction of compound i;

$\sum n_{i,c}$: sum of molar fraction of the carbon compounds.

This can be modified for carbon number specific selectivities. For example the selectivity (molar content) of linear olefins in linear hydrocarbon product for carbon number *x* would be as presented in equation 4.16:

$$(S_{lin.olefins})_{Cx} = \frac{(n_{lin.olefins})_{Cx}}{\sum(n_{lin.paraffins})_{Cx} + \sum(n_{lin.olefins})_{Cx}} \qquad (4.16)$$

Table 4.4: Conditions for the off-line gas chromatographic analysis using Flame Ionization Detector (FID)

Gas Chromatograph Varian CP-3800	
Detector	Flame Ionization Detector
Detector temperature	200 ^{o}C
Column type	25 m X 0.15 mm Capillary Column CP-SIL 5CB, 2 μm film thickness
Column pressure	1.72 bar
Carrier gas	H_2 (30 ml(STP).min^{-1})
Makeup gas	N_2 (25 ml(STP).min^{-1})
Oven Coolant	CO_2
	Temperature Program
	-55 ^{o}C, 1.50 min isothermal
	at 20 ^{o}C.min^{-1} to 0 ^{o}C, 0 min isothermal
	at 14 ^{o}C.min^{-1} to 100 ^{o}C, 0 min isothermal
	at 16 ^{o}C.min^{-1} to 280 ^{o}C, 22.36 min isothermal
Total time	20 min

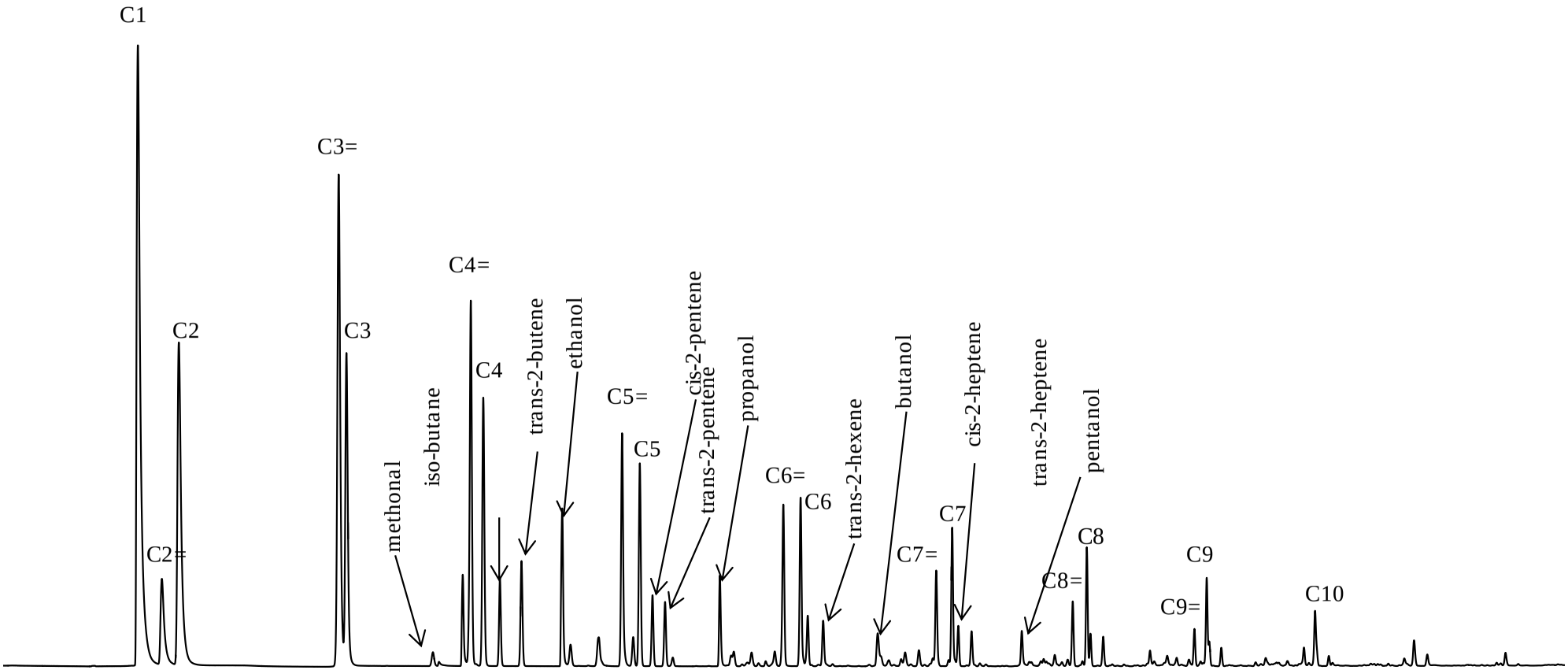

Figure 4.2: Typical FID chromatogram of the Fischer-Tropsch synthesis products

References

1. Sahoo, S.K., Agarwal, K., Singh, A.K., Polke, B.G. and Raha K.C. (2010), 'Characterization of γ-Fe_2O_3 and α-Fe_2O_3 nano powders synthesized by emulsion precipitation-calcination route and rheological behaviour of α-Fe_2O_3', *International Journal of Engineering, Science and Technology* **2**, 118.

2. Barbosa, A.L., Herguido, J. and Santamaria, J. (2001), 'Methane combustion over unsupported iron oxide catalysts', *Catalysis Today* **64**, 43.

3. Ramli, I., Muhamad, E.N., Abdullah, A.H., Taufiq-Yap, Y.H. and Hamid, S.B. (2004), 'Influnce of the number of washing on the characteristic of nanocrystalline copper oxide powders', *NSTI-Nanotechnology* **3**, 99.

4. Tao, S., Gao, F., Liu, X. and Sørensen, O.T. (2000), 'Preparation and gas-sensing properties of $CuFe_2O_4$ at reduced temperature', *Materials Science and Engineering B* **77**, 172.

5. Tsoncheva, T., Manova, E., Velinov, N., Paneva, D., Popova, M., Kunev, B., Tenchev, K. and Mitov, I. (2010), 'Thermally synthesized nanosized copper ferrites as catalysts for environment protection', *Catalysis Communications* **12**, 105.

6. Zhao, T., Hasegawa, M. and Takei, H. (1996), 'Crystal growth and characterization of cuprous ferrite ($CuFeO_2$)', *Journal of Crystal Growth* **166**, 408.

7. Krehula, S. and Musić, S. (2013), 'Formation of $AgFeO_2$, α-FeOOH, and Ag_2O from mixed $Fe(NO_3)_3$-$AgNO_3$ solutions at high pH', *Journal of Molecular Structure* **1044**, 221.

8. Murthy, Y.L.N., Rao, T.K., Kasiviswanath, I.V. and Singh, R. (2009), 'Synthesis and characterization of nano silver ferrite composite'. *Journal of Magnetism and Magnetic Materials* **322**, 2071.

9. Schulz, H. and Gökcebay, H. (1984), 'Fischer-Tropsch CO-hydrogenation as a means of linear olefins productions'. In: *Catalysis of organic Reactions*. (New

York) J.R. Kosak; M. Dekker, vol. 153, pp.153.

10. Schulz, H. and Nehren, S. (1986), 'Die Herstellung von Gas/Dampf - Eichgemischen für die Gaschromatographie', *Erdöl und Kohle - Erdgas – Petrochemie* **39**, 93.

11. Kaiser, R. (1969), *Chromatographie in der Gasphase*. Bibliographisches In-stitut, Mannheim, Germany.

Chapter 5

Characterization of the calcined model catalysts

This chapter discusses the results observed on the characterization of the calcined model catalysts.

5.1. Introduction

Copper has been added to iron-based FT catalysts as a reduction promoter [1,2,3,4]. However, in recent literature it has been observed to also influence the performance of the iron-based catalysts during Fischer-Tropsch synthesis. Earlier studies, conducted by Wachs et al. [5], in which copper- and silver- promoted iron-based catalysts were prepared by impregnation method, thereafter, used in the investigation of the promotional effect of copper and silver on iron-based FT catalysts. The results showed that copper acted as a reduction promoter, however, did not influence the performance of the iron-based catalysts during Fischer-Tropsch synthesis. On the other hand, silver did not act as a reduction promoter nor did it influence the performance of the iron-based catalyst during Fischer-Tropsch synthesis. These findings were attributed to the lack of intimate contact between the active phase (Fe) and the promoter (Cu or Ag) during the activation process as well as the Fischer-Tropsch synthesis. Therefore, the aim of this study is to gain better understanding on the promotional effect of copper and silver on the iron-based FT catalysts using ferrites as model catalysts. Herein, the observed characterization results of the calcined model catalysts are discussed.

5.2. Results and discussion

5.2.1. Experimental section

The maghemite (γ-Fe_2O_3) and hematite (α-Fe_2O_3) samples which were used as reference materials for the model systems were prepared using a precipitation method. The spinel copper ferrite ($CuFe_2O_4$), delaffosite copper ferrite ($CuFeO_2$) and silver ferrite ($AgFeO_2$) were prepared using a co-precipitation method. During the preparation of the spinel copper ferrite, sodium hydroxide (NaOH) was used as a precipitation agent instead of ammonium hydroxide (NH_4OH)

to avoid the formation of stable ammonium copper complexes thus ensuring optimal utilization of copper in the formation of copper ferrite systems.

The desired model catalysts (α-Fe_2O_3, $CuFe_2O_4$ and $CuFeO_2$) without any trace of impurities were obtained by calcining the model catalyst precursors at high temperature (950 ^oC). Attempts to prepare $CuFe_2O_4$ and $CuFeO_2$ by calcining at lower temperatures of 600 and 800 ^oC resulted in an incomplete transformation of the starting materials to the desired copper ferrite systems (see Appendix A1). Preparation of pure γ-Fe_2O_3 and $AgFeO_2$ involved calcining the model catalyst precursors at low temperature (350 and 400 ^oC, respectively). Attempts to prepare γ-Fe_2O_3 by calcining at higher temperature (above 500 ^oC) resulted in the formation of hematite (α-Fe_2O_3) as the final phase, while, exposure of the iron-silver precursor to higher temperature (above 500 ^oC), resulted in the segregation of the phases to α-Fe_2O_3 and Ag (see Appendix A2). Similar results have previously been reported [6].

The prepared model catalysts were characterized using atomic absorption spectroscopy (AAS), scanning electron microscopy - energy dispersive x-ray (SEM-EDX), x-ray diffraction (XRD), mössbauer absorption spectroscopy (MAS), infrared spectroscopy (IR), H_2-temperature-programmed reduction (H_2-TPR) and *in-situ* XRD techniques. A comprehensive discussion of the preparation and characterization techniques used, is given in Chapter 4.

5.2.2. X-ray diffraction (XRD)

The elemental composition as determined by SEM-EDX and AAS, phase(s) present, relative abundances and average crystallite sizes of the model catalysts (γ-Fe_2O_3, α-Fe_2O_3, $CuFe_2O_4$, $CuFeO_2$ and $AgFeO_2$) studied using the X-ray diffraction (XRD) are shown in Table 5.1. Figure 5.1 shows the XRD patterns of the calcined model catalysts. The experimental diffraction patterns of the various model catalysts were compared to their respective JCPDS database to confirm the formation of the desired phase. In all model catalysts successful preparation of the desired pure phase was observed.

The XRD patterns of maghemite (γ-Fe_2O_3) and hematite (α-Fe_2O_3) are shown in Figure 5.1 (a) and (b), respectively. An XRD pattern of the prepared γ-Fe_2O_3 showed diffraction peaks corresponding to maghemite and hematite phases. The relative abundances of the two phases were determined using Rietveld refinement Topas and were 98.7 and 1.3 wt-%, respectively. The broadness of the diffraction peaks showed that γ-Fe_2O_3 was formed in small average

crystallite sizes. Maghemite (γ-Fe_2O_3) is known to form at low temperatures and is stable in small crystallite sizes [7]. The phase transformation of the iron oxides during heating has been well documented [8], and has been shown to proceed via equation 5.1.

$$\gamma\text{-}Fe_2O_3 \xrightarrow{<400\,^{o}C} \alpha\text{-}Fe_2O_3 \qquad \text{Equation 5.1}$$

Figure 5.1 (b) shows narrow diffraction peaks corresponding to hematite (α-Fe_2O_3) phase of large crystallite sizes. Comparison of the diffraction peaks of the prepared α-Fe_2O_3 to the previously reported diffraction pattern for α-Fe_2O_3 [9,10], confirmed that pure α-Fe_2O_3 was formed.

Annealing the iron-copper oxide precursor at high temperature (950 ^{o}C), resulted in the formation of tetragonal $CuFe_2O_4$ as the dominant phase. Similar results have been previously reported by Yokoyama and co-workers [11,12]. However, $CuFe_2O_4$ is known to exhibit two different phases, the cubic (space group: *Fd3m*) and tetragonal (space group: *141/amd:2*), due to the temperature dependence of the formation of $CuFe_2O_4$ phases during preparation [13]. Although the XRD peaks of $CuFe_2O_4$ in a cubic phase overlap with those of the $CuFe_2O_4$ in a tetragonal phase (see Figure 5.1 (c)), Topas Rietveld refinement (a powerful tool) can be used to get an indication of the present phases and their relative abundances. The relative abundances of the cubic and tetragonal phases for the prepared $CuFe_2O_4$ were 18 and 82 wt-%, respectively. The XRD pattern of delafossite $CuFeO_2$ as shown in Figure 5.1 (d), confirmed the formation of a pure $CuFeO_2$ in a rhombohedral structure (space group: *R3m*). Furthermore, the diffraction pattern of α-Fe_2O_3, $CuFe_2O_4$ and $CuFeO_2$ showed sharp and symmetric peaks; this is indicative of large average crystallite sizes and high crystallinity. The observed peak shape is in accordance with the obtained large average crystallite sizes.

The delaffosite silver ferrite ($AgFeO_2$) has been reported to crystallize as either rhombohedral *3R* (space group: *R3m*) [14] and/or hexagonal *2H* (space group: *$P6_3/mmc$*) [15,16] structures depending on the preparation conditions (see Figure 5.1(e)). Topas Rietveld refinement analysis showed the presence of rhombohedral and hexagonal phases in relative abundances of 75 and 15 wt-%, respectively. The observed broad diffraction peak in the XRD pattern of $AgFeO_2$ is indicative of small average crystallite sizes. The average crystallite sizes of α-Fe_2O_3, $CuFe_2O_4$ and $CuFeO_2$ as determined by Topas Rietveld refinement were in the range of 90-110 nm, while those of γ-Fe_2O_3 and $AgFeO_2$ were 9 and 7 nm, respectively.

Table 5.1: Physiochemical characteristics of model catalysts, γ-Fe_2O_3, α-Fe_2O_3, $CuFe_2O_4$, $CuFeO_2$ and $AgFeO_2$

Sample	**γ-Fe_2O_3**	**α-Fe_2O_3**	**$CuFe_2O_4$**	**$CuFeO_2$**	**$AgFeO_2$**
Fe/Me[a], mol/mol	-	-	2.53±0.03	1.15±0.01[a]	1.91±0.20[a]
					1.91±0.06[b]
Na, wt.-%			<0.01	<0.01	<0.01
Phases[a]	98.7 %, γ-Fe_2O_3	100 %, α-Fe_2O_3	18 %, *c*-$CuFe_2O_4$	100 %, $CuFeO_2$	75 %, *3R*-$AgFeO_2$
	1.3 , α-Fe_2O_3		82 %, *t*-$CuFe_2O_4$		25 %, *2H*-$AgFeO_2$
d, nm[a]	9 (γ-Fe_2O_3)	110	16 (*c*-$CuFe_2O_4$)	109	7 (*3R*-$AgFeO_2$)
	14 (α-Fe_2O_3)		90 (*t*-$CuFe_2O_4$)		- (*2H*-$AgFeO_2$)

[a] Elemental composition as determined using EDX;
[b] Elemental composition as determined using AAS;
[c] phase composition and average crystallite size as determined using using Rietveld refinement of XRD pattern.

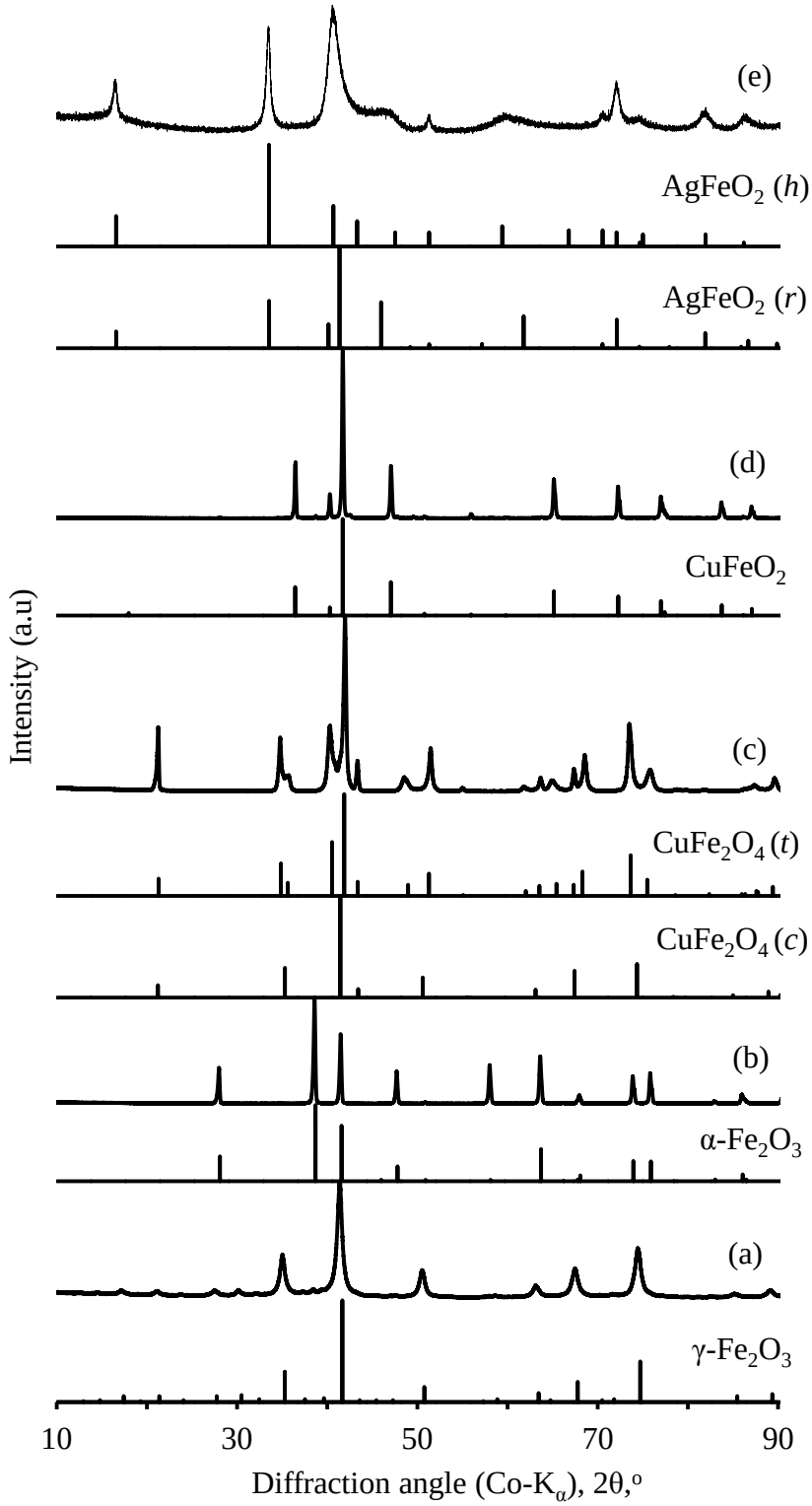

Figure 5.1: XRD patterns of (a) γ-Fe_2O_3, (b) α-Fe_2O_3, (c) $CuFe_2O_4$, (d) $CuFeO_2$ and (e) $AgFeO_2$ after calcination

5.2.3. Mössbauer absorption Spectroscopy (MAS)

The present phase(s), relative abundance and oxidation states of the compounds in the model catalysts (γ-Fe_2O_3, α-Fe_2O_3, $CuFe_2O_4$, $CuFeO_2$ and $AgFeO_2$) were determined using Mössbauer absorption spectroscopy. In order to obtain the most accurate Mössbauer results, the model catalysts were analysed at room temperature (298 K), liquid helium temperature (4.2 K) and liquid helium temperature (4.2 K) in an applied magnetic field of 10 T parallel to the direction of γ-rays.

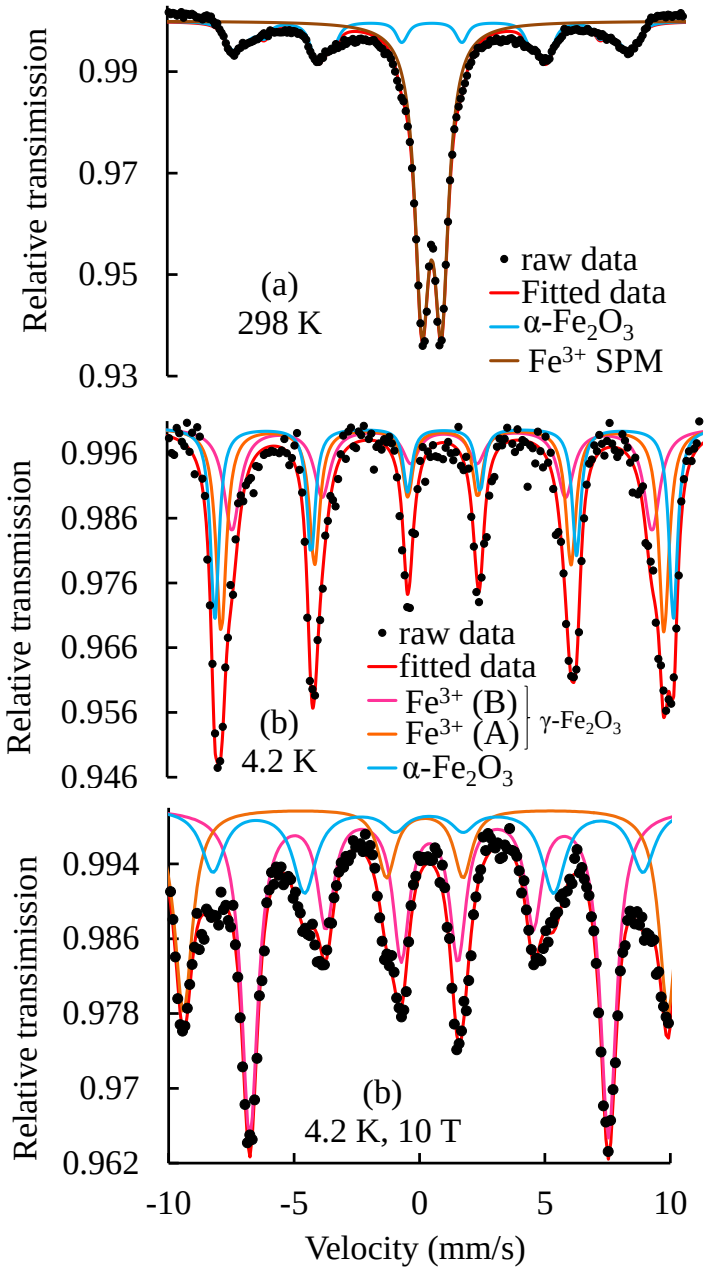

Figure 5.2: Mössbauer spectra γ-Fe_2O_3, recorded at (a) 298 K, (b) 4.2 K and (c) 4.2 K, 10 T

The Mössbauer spectra of the model catalysts are shown in Figures 5.2-5.6. The hyperfine parameters of the model catalysts are given in Table 5.2 and Table 5.3. Figure 5.2 (a), (b) and (c) shows the MAS spectra of γ-Fe_2O_3 recorded at room temperature, liquid helium temperature and liquid helium temperature with an applied magnetic field of 10 T, respectively. The MAS spectrum recorded at room temperature was fitted with a quadrupole doublet and a sextet. The hyperfine parameters of the sextet corresponded to α-Fe_2O_3, with relative abundance of 29 %, while, the observed doublet is ascribed to SPM species, suggesting that 71 % of the Fe is in the form of small crystallites sizes of less than ±10 nm (superparamagnetic). The MAS of the sample analysed at 4.2 K showed three well resolved sextets, two of the sextets related to Fe^{3+} (A) and Fe^{3+} (B) of γ-Fe_2O_3 and other sextet was typical of α-Fe_2O_3. The relative abundance of γ-Fe_2O_3 and α-Fe_2O_3 were 70 and 30 %, respectively. The MAS spectrum obtained at 4.2 K in the presence of the magnetic field (10 T), showed an almost cancelation of the lines 2 and 5^1 in the one sextet on the B sites while a small contribution subsists on the A sites. This is probably due to the presence of defects and vacancies that prevent the spins from being fully aligned with the applied magnetic field, which is expected in ferromagnetic materials. Similar behaviour has also been reported by Linderoth [17]. The obtained hyperfine parameters were related to Fe^{3+} (A) and Fe^{3+} (B) of γ-Fe_2O_3 as well as Fe^{3+} of α-Fe_2O_3. The relative abundance of the γ-Fe_2O_3 and α-Fe_2O_3 was 67 and 33 %, respectively.

The MAS results agree well with the XRD results. The Mössbauer spectrum of α-Fe_2O_3, recorded at 298 K was fitted with a magnetic sextet. The hyperfine parameters of the fitted sextet are consistent with the previously reported values for α-Fe_2O_3 [18]. The observation of the sextet at room temperature suggests the existence of large average crystallite sizes of α-Fe_2O_3, in accordance with the XRD results (see in Table 5.1).

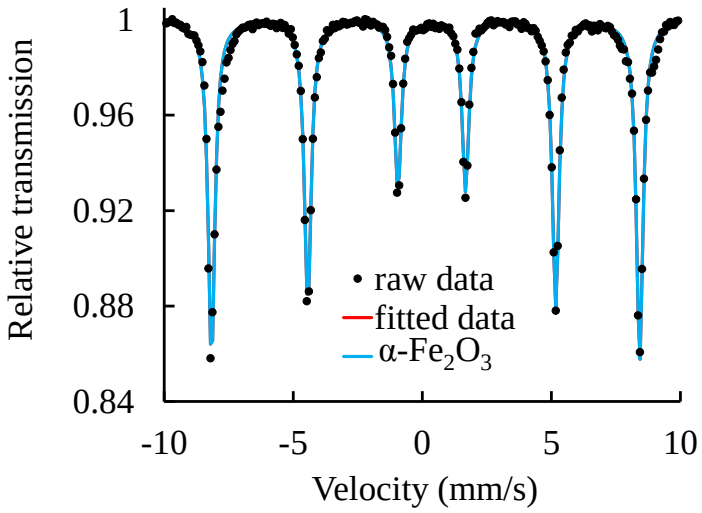

Figure 5.3: Mössbauer spectrum of α-Fe_2O_3 recorded at 298 K

Copper ferrite, $CuFe_2O_4$, is unique among the spinels for two reasons. Firstly, its cation distribution over the non-equivalent sites is variable and strongly dependent on the temperature. Secondly, the presence of Cu^{2+} ions leads to severe Jahn-Teller type distortions of the sites. For this reason, the non-equivalent sites are more distinct than in other spinels. It is to be expected that due to these two facts a study of a number of copper ferrite phases at different temperatures might be fruitful for a more detailed analysis of the Mössbauer spectra of spinels. Therefore, the MAS spectra of $CuFe_2O_4$ were recorded at 298 K (a), at 4.2 K (b) and at 4.2 K in an applied magnetic field 10 T (c). All the spectra are fitted with two sextets. The observed magnetically well split spectrum at room temperature (298 K) indicates the existence of large average crystallite sizes in good agreement with the observed XRD results (see Table 5.1).

The hyperfine parameters of the two sextets observed at different MAS analyses conditions are consistent with those of $CuFe_2O_4$, which correspond to the two Fe^{3+} ions present in the octahedral and tetrahedral sites of the $CuFe_2O_4$ structure [19,20,21,22]. The high values of the hyperfine induction ($ß_{hf}$) observed are ascribed to the Fe^{3+} ions in the octahedral (B) sites, while the low values were ascribed to Fe^{3+} ions in the tetrahedral (A) sites. This assignment is attributed to the stronger hyperfine interaction of A-O-C (where A = Cu and C = Fe) and the lower covalency of the Fe^{3+}-$O^{=}$ bond for Fe^{3+} ions in the octahedral site (B site) [23]. The distribution of cations over the two sites is approximately 56 % of Fe^{3+} ions on the A sites and 44 % of Fe^{3+} ions on the B sites yielding a Fe^{3+}(A)/Fe^{3+}(B) ratio of 1.27, or Fe^{3+}(A):Fe^{3+}(B) ratio of 1:0.79. This value differs slightly from the stoichiometric ratio of 1:1. Non-stoichiometric

ratios of 1.18 [19] and 1.32 [24] have previously been reported for $CuFe_2O_4$. The ratio found in this study yields cation distributions for the $CuFe_2O_4$ sample:

$$(Cu_{0.06}^{2+}Fe_{0.94}^{3+})_A[Cu_{0.96}^{2+}Fe_{1.06}^{3+}]_BO_4$$

This cation distribution together with the observed hyperfine parameters for the prepared $CuFe_2O_4$ agrees well with the previously reported values, which are related to the inverse spinel structure (tetragonal phase) [19,24]. It can thus be concluded that the prepared $CuFe_2O_4$ is in the tetragonal phase.

Furthermore, the MAS spectrum recorded at 4.2 K in the presence of the applied magnetic field, showed an almost cancelation of the lines 2 and 5^1 in the two sextets on the B sites while a small contribution subsists on the A sites. This is probably due to the presence of defects and vacancies that prevent the spins from being fully aligned with the applied magnetic field, which is expected in ferromagnetic materials. A similar behaviour has also been reported for γ-Fe_2O_3 with the vacancies being located rather on the B sites [25]. The hyperfine induction ($ß_{hf}$) value of the A sites of the sextet recorded at 4.2 K in the presence of the applied magnetic field (10 T) show a shrinkage as compared to those recorded in the absence of the applied magnetic field, which is consistent with the ferromagnetic nature of the inverse spinel structure of $CuFe_2O_4$.

The Mössbauer spectra of $CuFeO_2$ recorded at room temperature (298 K) and liquid helium temperature (4.2 K) are shown in Figure 5.5 (a) and (b), respectively. The MAS spectrum recorded at room temperature was fitted with a doublet. It should be noted that the existence of a doublet does not imply that the crystallite size is in a super-paramagnetic state (small average crystallite size), since the XRD results clearly showed an average crystallite size of 105 nm. The observed doublet is therefore, due to the fact that $CuFeO_2$ is paramagnetic at room temperature and the fitted doublet is, thus, related to the high spin Fe^{3+} ions located in octahedral site (B site) [26]. In this case the liquid helium temperature (4.2 K) Mössbauer analysis is important to obtain further information on the phase(s) present and relative abundance of the $CuFeO_2$. The spectrum recorded at 4.2 K was fitted with a single sextet corresponding to the high spin Fe^{3+} ions valence state; the spin structure of 4-Fe sublattice is totally collinear. The hyperfine parameters of the sextet are consistent with values previously reported for $CuFeO_2$ [21,27].

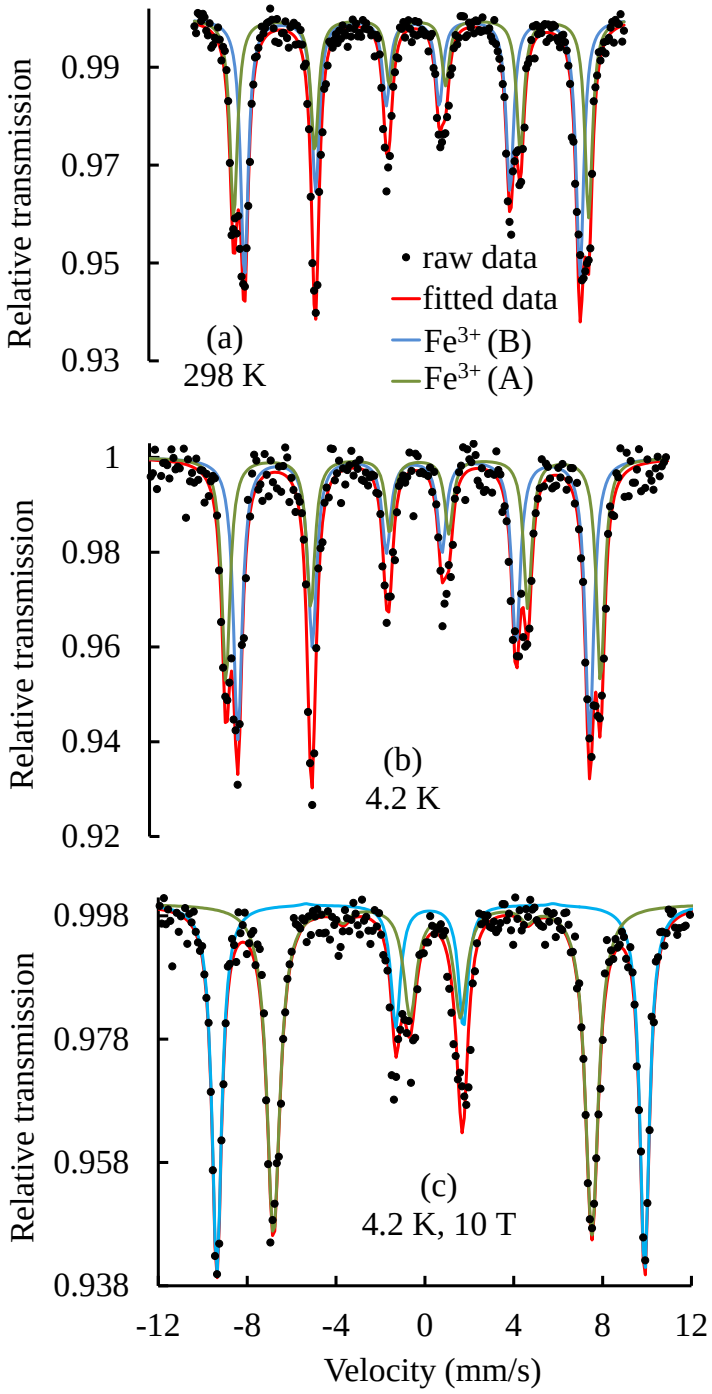

Figure 5.4: Mössbauer spectra $CuFe_2O_4$, recorded at (a) 298 K, (b) 4.2 K and (c) 4.2 K in 10 T (The six lines of a sextet are numbered from the outermost left (line 1) to the outermost right (line 6))

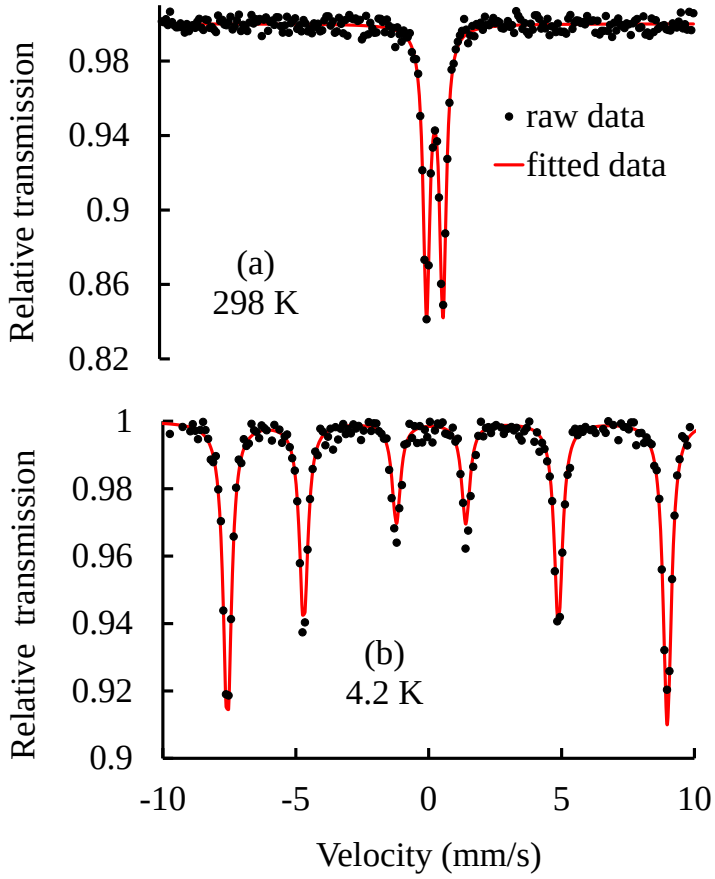

Figure 5.5: Mössbauer spectra $CuFeO_2$, recorded at (a) 298 K and (b) 4.2 K

The Mössbauer spectra of $AgFeO_2$ recorded at 298 K (a), at 4.2 K (b) and 4.2 K in an applied magnetic field B_{app} = 10 T (c), are shown in Figure 5.6 (a), (b) and (c), respectively. The MAS spectrum recorded at room temperature (Figure 5.6 (a)) was fitted with a quadrupole doublet superposed to a sextet. Similarly, to $CuFeO_2$, $AgFeO_2$ is known to be paramagnetic and therefore, the appearance of a quadrupole doublet may be related to the high spin Fe^{3+} species, as well as implies that the crystallites are in a superparamagnetic state (small average crystallite sizes) [21], in accordance with the XRD data of $AgFeO_2$ in which an average crystallite size of 9 nm was reported (see Table 5.1). The hyperfine parameter of the fitted sextet corresponded to the previously reported parameter values for the α-Fe_2O_3 [18].

The MAS spectra recorded at 4.2 K in the absence of an applied magnetic field (10 T) and 4.2 K in the presence of an applied magnetic field, shown in Figure 5.6 ((b) and (c)), were fitted with three sextets, respectively. The hyperfine parameters of one of the sextets corresponded to the parameter values of α-Fe_2O_3 [18], and the other two were attributed to the two structures of

$AgFeO_2$, i.e, rhombohedral $AgFeO_2$ (*r*) and hexagonal $AgFeO_2$ (*h*). The relative abundances of the two sextets were 32 and 38 % for the sextet with a smaller and a larger hyperfine induction (B_{hf}), respectively. However, due to the lack of tabulated MAS parameters for the two $AgFeO_2$ polytypes, it was not possible to distinguish which set of the MAS parameters corresponded to which structure.

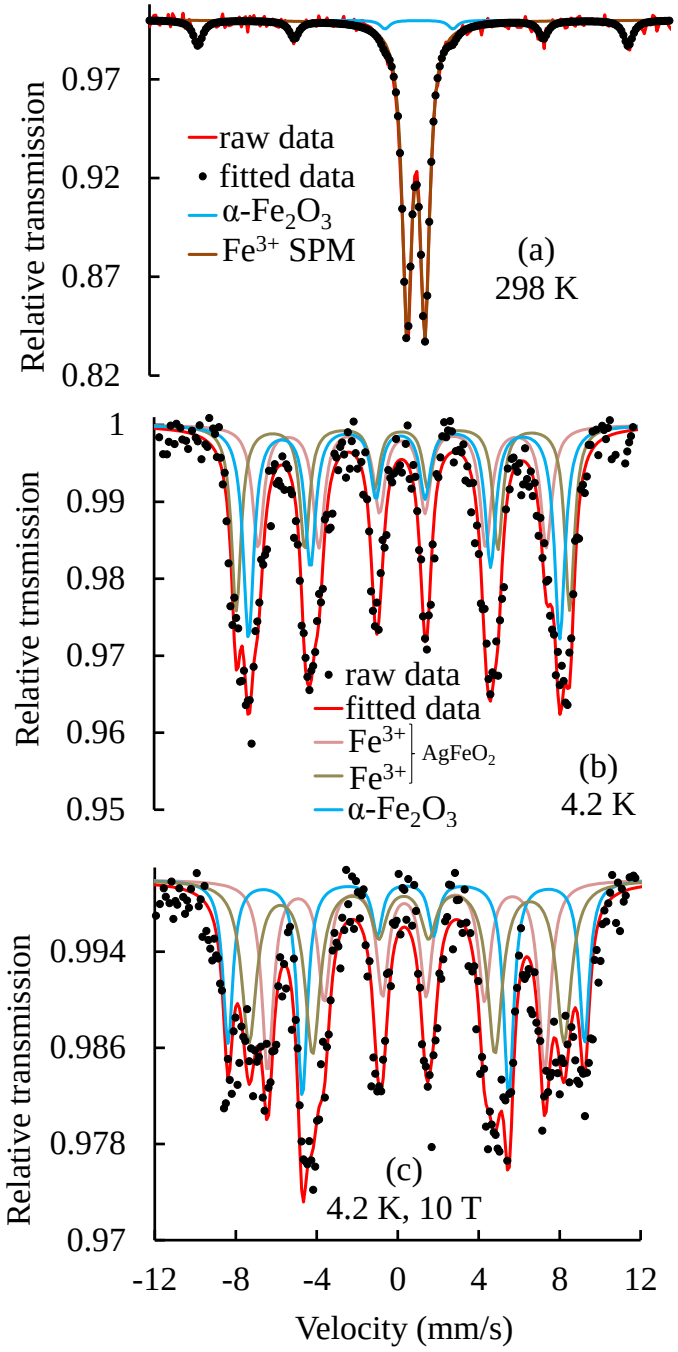

Figure 5.6: Mössbauer spectra $AgFeO_2$ recorded at (a) 298 K, (b) 4.2 K and (c) 4.2 K in 10 T

Table 5.2: Hyperfine parameters of the calcined γ-Fe_2O_3, α-Fe_2O_3 and $CuFe_2O_4$ obtained at 298 K, 4.2 K and 4.2 K in 10 T

δ – isomer shift, Δ - quadrupole splitting, **ß$_{hf}$** – hyperfine induction, **A** – relative area.

Model catalysts	**Temperature (K)**	**H_{app} (T)**	**MAS hyperfine parameters**			**Component**	**A (~2 %)**	**Phase**
			δ (~0.02 mm/s)	**Δ (~0.02 mm/s)**	**ß$_{hf}$ (~0.2 T)**			
γ-Fe_2O_3	298	0	0.35	0.01	-	doublet	29	Fe SPM
			0.34	0.75	46.2	sextet	71	Mixture γ-and α-Fe_2O_3
	4.2	0	0.44	-0.07	48.8	sextet	70	γ-Fe_2O_3
			0.43	-0.01	51.4	sextet		
			0.48	0.01	53.2	sextet	30	α-Fe_2O_3
	4.2	10	0.51	-0.02	44.3	sextet	67	γ-Fe_2O_3
			0.35	0.01	59.9	sextet		
			0.48	-0.05	53.2	sextet	33	α-Fe_2O_3
α-Fe_2O_3	298	0	0.36	-0.24	51.4	sextet	100	α-Fe_2O_3
$CuFe_2O_4$	298	0	0.27	-0.03	48.0	sextet (A)	56	$CuFe_2O_4$
			0.35	-0.29	50.8	sextet (B)	44	
	4.2	0	0.37	-0.02	50.5	sextet (A)	57	
			0.48	-0.28	53.8	sextet (B)	43	
	4.2	10	0.52	-0.12	44.4	sextet (A)	56	
			0.35	0.0581	59.7	sextet (B)	44	

Table 5.3: Hyperfine parameters of the calcined $CuFeO_2$ and $AgFeO_2$ obtained at 298 K, 4.2 K and 4.2 K in 10 T

δ – isomer shift, Δ - quadrupole splitting, $\boldsymbol{ß_{hf}}$ – hyperfine induction, **A** – relative area.

Model catalysts	**Temperature (K)**	**H_{app} (T)**	**MAS hyperfine parameters**			**Component**	**A (~2 %)**	**Phase**
			δ (~0.02 mm/s)	**Δ (~0.02 mm/s)**	**$ß_{hf}$ (~0.2 T)**			
$CuFeO_2$	298	0	0.38	0.61	-	doublet	100	$CuFeO_2$
	4.2	0	0.51	0.62	51.3	sextet	100	$CuFeO_2$
$AgFeO_2$	298	0	0.36	0.69	-	doublet	85	Fe SPM
			0.37	-0.22	51.3	sextet	15	α-Fe_2O_3
	4.2	0	0.47	-0.00	44.5	sextet	32	$AgFeO_2$
			0.47	0.18	48.0	sextet	38	
			0.46	0.08	51.5	sextet	30	α-Fe_2O_3
	4.2	10	0.49	0.09	42.4	sextet	33	$AgFeO_2$
			0.48	0.14	48.2	sextet	38	
			0.52	0.03	54.0	sextet	29	α-Fe_2O_3

5.2.4. Infrared spectroscopy (IR)

In all model catalysts two strong absorption bands in the range of 400-600 cm^{-1} typical for metal-metal and metal-oxygen bonds are observed. The IR spectra of the model catalysts are shown in Figure 5.7 (a-e) and absorption band wavenumbers are given in Table 5.4. The IR spectrum of γ-Fe_2O_3 showed a weak peak in the range of 400-800 cm^{-1}, corresponding to Fe-O stretching vibration mode, which may correspond to a partial vacancy ordering in the octahedral positions in the maghemite inverse spinel crystal structure [28,29,30,31]. The absorption bands of α-Fe_2O_3 were seen at υ_1 = 461.5 and υ_2 = 535.1 cm^{-1}, which are related to the lattice vibrations of the FeO_6 octahedron [22,32,33].

Two main broad metal oxygen bands are seen in the IR spectra of ferrites ($CuFe_2O_4$ and $CuFeO_2$), The IR spectrum of $CuFe_2O_4$ showed two absorption bands at approximately υ_1 = 582.9 and υ_2 = 419.1 cm^{-1}, which correspond to the intrinsic stretching vibrations of the Fe^{3+}-O^{2-} ions in the tetrahedral and octahedral sites [34,35,36,37,38,39,40], respectively. The different wavenumber values of the absorption peaks for tetrahedral and octahedral complexes of $CuFe_2O_4$ crystals have been attributed to the different values of Fe^{3+}-O^{2-} distances for tetrahedral and octahedral sites. The Cu^{2+} ions occupy mainly the octahedral sites, although a small fraction may be present in the tetrahedral sites. Accordingly, the broad tetrahedral vibration band accompanied with a shoulder can be attributed to the vibration of Cu^{2+}-O^{2-} in tetrahedral complexes. On the basis of the above discussion an inverse spinel structure (tetragonal phase) can be assigned to the $CuFe_2O_4$, and the cation distribution is suggested to be;

$$(Cu_y^{2+}Fe_{1-y}^{3+})_A[Cu_{1-2y}^{2+}Fe_{1+2y}^{3+}]_BO_4$$

these results agree well with the Mössbauer results in which a similar cation distribution was observed. The delafossite $CuFeO_2$ showed two bands at similar wavenumbers to those of $CuFe_2O_4$, a band at υ_1 = 595.2 cm^{-1} and at υ_2 = 436.9 cm^{-1}. To our knowledge, there have not been much IR studies conducted on the delafossite systems ($CuFeO_2$ and $AgFeO_2$), Bassaid et al., observed two absorption bands with the absorption band at higher wavenumber assigned to the linear sites of CuO_2^{3-} [41] and the absorption band at lower wavenumber related to the octahedral FeO_6 modes. Similar absorption band assignment may be given to the IR spectrum of $AgFeO_2$, with the absorption bands at higher wavenumber ascribed to the linear sites of AgO_2^{3-}.

Table 5.4: IR wavenumbers of γ-Fe_2O_3, α-Fe_2O_3, $CuFe_2O_4$, $CuFeO_2$ and $AgFeO_2$

M = metal (Fe or Cu or Ag)

Model catalysts	**Sites**	**Band**	**M-O^{2-}**	**Wavenumber (cm^{-1})**
γ-Fe_2O_3	Octahedral site		Fe^{3+}-O^{2-}	~737
α-Fe_2O_3	Octahedral site	υ_1	Fe^{3+}-O^{2-}	535.1
		υ_2		461.5
$CuFe_2O_4$	Tetrahedral sites (A)	υ_1	Fe^{3+}-O^{2-}	582.9
	Octahedral sites (B)		Cu^{2+}-O^{2-}	
		υ_2	Fe^{3+}-O^{2-}	419.1
$CuFeO_2$	Octahedral site	υ_1	Fe^{3+}-O^{2-}	595.2
		υ_2	Cu^{+}-O^{2-}	436.9
$AgFeO_2$	Octahedral site	υ_1	Fe^{3+}-O^{2}	595.2
		υ_2	Ag^{1+}-O^{2-}	436.8

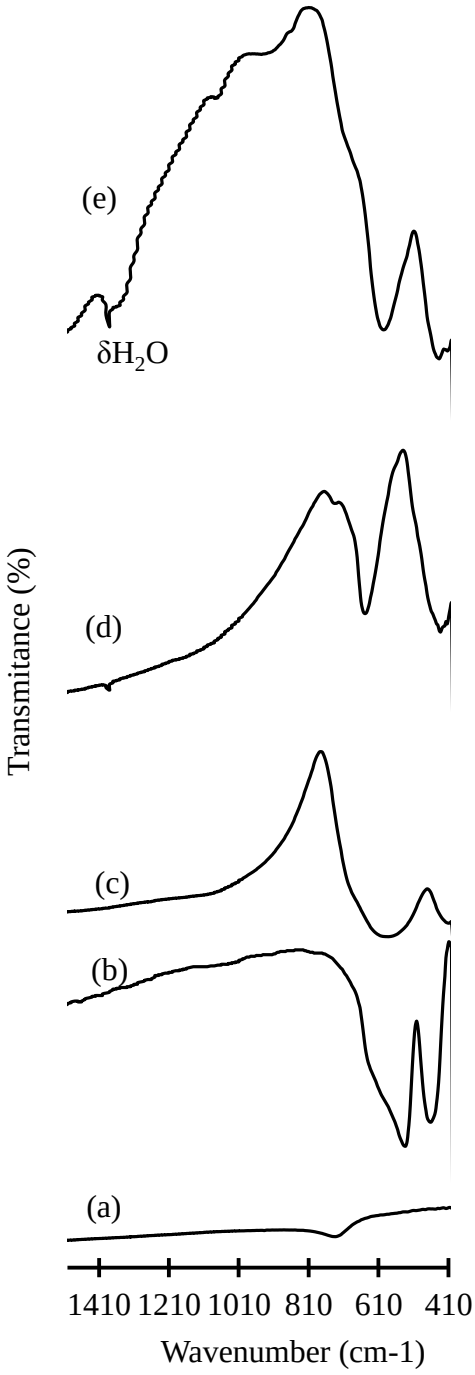

Figure 5.7: IR spectra of (a) γ-Fe_2O_3, (b) α-Fe_2O_3, (c) $CuFe_2O_4$, (d) $CuFeO_2$ and (e) $AgFeO_2$

5.3. Summary of the characterization results of the calcined model catalysts

The model catalysts were successfully prepared using the precipitation and co-precipitation method as confirmed by the various characterization results obtained. Characterization results from XRD, MAS and IR of the prepared spinel $CuFe_2O_4$ revealed the co-existance of the cubic and tetragonal phase with the tetragonal phase being the dominant phase. Similar results were

observed for the deloffisite $AgFeO_2$ which showed a co-existence of the two polytypes (rhombohedral and hexagonal crystal structure). However, it was difficult to distinguish between the two polytypes using MAS as well as XRD which was attributed to the small average crystallite size, thus limiting the detectability of the phases using the XRD analysis.

References

1. Dry, M. (1981), Catalysis-Science and Technology. In John R. Anderson and Michel Boudart (Ed.), Berlin Heidelburg:Springer-Verlag, vol. 1, pp. 159.

2. Wielers, A.F.H., Hop, C.E.C.A., van Beijnum, J., van der Kraan, A.M. and Geus, J.W. (1990), 'On the properties of silica-supported bimetallic Fe-Cu catalysts Part I. Preparation and characterization', *Journal of Catalysis* **121**, 364.

3. Luo, M., O'Brien, R.J. and Davis, B.H. (2004), 'Effect of Palladium on Iron Fischer-Tropsch Synthesis Catalysts', *Catalysis Letters* **98**, 17.

4. Grzybek, T., Klinik, J., Papp, H. and Baerns, M. (1990), 'Characterization of Cu and K containing Fe/Mn oxide catalysts for Fischer-Tropsch synthesis', *Chemical Engineering Technology* **13**, 156.

5. Wachs, I.E., Duyer, D.J. and Iglesia, E. (1984), 'Characterization of Fe, Fe-Cu and Fe-Ag Fischer-Tropsch Catalysts', *Applied Catalysis* **12**, 201.

6. Murthy, Y.L.N., Rao, T.K., Kasiviswanath, I.V. and Singh, R. (2009), 'Synthesis and characterization of nano silver ferrite composite', *Journal of Magnetism and Magnetic Materials* **322**, 2071.

7. Mogorosi, R.P., Fischer, N., Claeys, M. and van Steen, E. (2012), 'Strong-metal-support interaction by molecular design: Fe-silicate interactions in Fischer-Tropsch catalysts', *Journal of Catalysis* **289**, 140.

8. DeBoer, F.E. and Selwood, P.W. (1954), 'Activation energy for the solid state reaction γ-$Fe_2O_3 \rightarrow \alpha$-$Fe_2O_3$', *Journal of American Chemical Society* **76**, 3365.

9. Schimanke, G. and Martin, M. (2000), 'In situ XRD study of the phase transition of – nanocrystalline maghemite (γ-Fe_2O_3) to hematite (α-Fe_2O_3)', *Solid State Ionics* **136-137**, 1235.

10. Wang, X., Gao, L., Zheng, H., Ji, M., Shen, T. and Zhang, Z. (2004), 'Fabrication and electrochemical properties of α-Fe_2O_3 nanoparticles', *Journal of Crystal Growth* **269**, 489.

11. Yokoyama, M., Nakamura, A., Sato, T. and Haneda, K. (1998), 'Jahn-Teller effect in ultrafine copper ferrite particles', *Journal of the Magnetic Society of Japan* **22**, 243.

12. Deraz, N.M. (2008), 'Production and characterization of pure and doped copper ferrite nanoparticles', *Journal of Analytical and Applied Pyrolysis* **82**, 212.

13. Thapa, D., Kulkarni, N., Mishra, S.N., Paulose, P.L. and Ayyub, P. (2010), 'Enhanced magnetization in cubic ferromagnetic $CuFe_2O_4$ nanoparticles synthesized from a citrate precursor: the role of Fe^{2+}', *Journal of Physics D: Applied Physics* **43**, 195004.

14. Rogers, D.B., Shannon, R.D. and Prewitt, C.T. (1971), 'Chemistry of noble metal oxides. l. Syntheses and properties of ABO_2 delafossite compounds', *Inorganic Chemistry* **10**, 713.

15. Okamoto, S., Okamoto, I. and Ito, T. (1972), 'The crystal structure of a New Hexagonal Phase of $AgFeO_2$', *Acta Crystallography. B* **28**, 1774.

16. Nagarajan, R. and Tomar, N. (2009), 'Ultrasound assisted ambient temperatures synthesis of ternary oxides $AgMO_2$ (M = Fe, Ga), *Journal of Solids State Chemistry* **182**, 1283.

17. Linderoth, S., Hendriksen, P.V., Bødker, F., Wells, S., Davies, K., Charles, S.W. and Mørup, S. (1994), 'On spin-canting in maghemite particles', *Journal of Applied Physics* **75**, 6583.

18. Dyar, M.D., Agresti, D.G., Schaefer, M.W., Grant, C.A. and Sklute, E.C. (2006), 'Mössbauer Spectroscopy of Earth and Planetary Materials', *Annual Review of Earth and Planetary Sciences* **34**, 83.

19. Goya, G.F., Rechenberg, H.R. and Jiang, J.Z. (1998), 'Structural and magnetic properties of ball mill copper ferrite', *Journal of Applied Physics* **84**, 1101.

20. Evans, B.J. and Hafner, S. (1968), 'Mössbauer resonance of Fe^{57} in oxidic spinels containing Cu and Fe', *Journal of Physics and Chemistry of Solids* **29**, 1573.

21. Muir Jr.,A.H. and Wiedersich H. (1967), 'An investigation of $CuFeO_2$ by the Mössbauer effect', *Journal of Physics and Chemistry of Solids* **28**, 65.

22. Wang, X., Gao, L., Zheng, L. H., Ji, M., Shen. T. and Zhang, Z. (2004), 'Fabrication and electrochemical properties of α-Fe_2O_3 nanoparticles', *Journal of Crystal Growth* **269**, 489.

23. Selvan, R.K., Augustin, C.O., Oshtrakh, M.I., Miller, O.B. and Semionkin, V.A. (2005), 'Mössbauer and D.C magnetization studies of $(CuFe_2O_4)_{1-x}(SnO_2)_x$ (x = 0 and 5 wt%) nanocomposites, *Hyperfine Interactions* **165**, 231.

24. Jiang, J.Z., Goya, G.F. and Rechenberg, H.R. (1999), 'Magnetic properties of nanostructure $CuFe_2O_4$', *Journal of Physics: Condensed Matter* **11**, 4063.

25. Linderoth, S., Hendriksen, P.V., Bødker, F., Wells, S., Davies, K., Charles, S.W. and Mørup, S. (1994), 'On spin-canting in maghemite particles', *Journal of Applied Physics* **75**, 6583.

26. Sukeshini, A.M., Kobayashi, H., Tabuchi, M. and Kageyama, H. (2000), 'Physicochemical characterization of $CuFeO_2$ and lithium intercalation', *Solid State Ionics* **128**, 33.

27. Choi, D.H., Shim, I-B. and Kim, C.S. (2008), 'Mössbauer study of antiferromagnetic $CuFeO_2$', *Journal of Magnetism and Magnetic Material* **320**, 575.

28. Milan, A., Palacio, F., Falqui, A., Snoek, E., Serin, V., Bhattacharjee., Ksenofontov, V., Gütlich, P. and Gilbert, I. (2007), 'Maghemite polymer nanocomposites with modulated magnetic properties', *Acta Materialia* **55**, 2201.

29. Sahoo, S.K., Agarwal, K., Singh, A.K., Polke, B.G. and Raha K.C. (2010), 'Characterization of γ-Fe_2O_3 and α-Fe_2O_3 nano powders synthesized by emulsion

precipitation-calcination route and rheological behaviour of α-Fe_2O_3', *International Journal of Engineering, Science and Technology* **2**, 118.

30. de Faria, D.L.A., Silva, S.V. and de Oliveria, M.T. (1997), 'Raman microscopy of some iron oxides and oxyhydroxides', *Journal of Raman Spectroscopy* **28**, 873.

31. Kim I1. T., Nunnery, G.A., Jacob, K., Scwartz, J., Liu, X. and Tannenbaum. (2010), 'Synthesis, characterization, and alignment of magnetic carbon nanotubes tethered with maghemite nanoparticles', *Journal of Physical Chemistry. C* **114**, 6944.

32. Serna, C.J., Rendon, J.L. and Iglesias, J.E. (1982), 'Infrared surface modes in corundum type microcrystalline oxides', *Spectrochimica Acta Part A: Molecular Spectroscopy* **38**, 797.

33. Wang, X., Gao, L.S. and Zheng, H.G. (2004), 'Fabrication and electrochemical properties of α-Fe_2O_3 nanoparticles', *Journal of Crystal Growth* **269**, 489.

34. Selvan, R.K., Augustin, C.O., Berchmans, L.B. and Sarawathi. (2003), 'Combustion synthesis of $CuFe_2O_4$', *Material Research Bulletin* **38**, 41.

35. Berchmans,L.J., Selvan, R.K., Kumar, P.N.S., Augustin, C.O. (2004), 'Magneto-optical investigation of spinel ferrite $CuFe_2O_4$: observation of Jahn-Teller effect in Cu^{2+} ion', *Journal of Magnetism and Magnetic Materials* **279**, 173.

36. Laokul, P., Amornkitbamrung, V., Seraphin, S. and Maensiri, S. (2011), 'Characterization and magnetic properties of nanocrystalline $CuFe_2O_4$, $NiFe_2O_4$, $ZnFe_2O_4$ powders prepared by the Aloe vera extract solution', *Current Applied Physics* **11**, 101.

37. Selvan, R.K., Krishnan, V., Augustin, C.O., Bertagnolli, H., Kim, C.S. and Gedanken, A. (2008), 'Investigations on the structural, morphological, electrical, and magnetic properties of $CuFe_2O_4$-NiO nanocomposites', *Chemistry of Materials* **20**, 429.

38. Waldron, R.D. (1955), 'Infrared Spectra of Ferrites', *Physical Review* **99**, 1727.

39. Srinivasan, T.T., Srivastava, C.M., Venkataramani, N. and Patni, M. (1984), 'Infrared absorption in spinel ferrites', *Bulletin of Materials Science* **6**, 1063.

40. Gillot, B., Nivoix, V., Kester, O., Villette, C. and Rousset, A. (1997), 'Reactivity towards oxygen and cation distribution in copper-manganese ferrite spinels fine powders', *Materials Chemistry Physics* **48**, 111.

41. Bassaid, S., Chaib, M., Omeiri, Bouguelia, A. and Trari, M. (2009), 'Photocatalytic reduction of cadmium over $CuFeO_2$ synthesized by sol-gel', *Journal of Photochemistry and Photobiology A: Chemistry* **201**, 62.

Chapter 6

Effect of promoter on iron catalysts during H_2 and CO activation

This chapter is aimed at providing the reader with a better understanding on the reduction behavior, phase transformation as well as change in crystallite sizes of model catalysts during hydrogen (H_2) and carbon monoxide (CO) activation. In-situ experiments were conducted so as to gain better understanding on the phase transformation as well as change in average crystallite sizes.

6.1. Introduction

Prior to the Fischer-Tropsch synthesis, FT catalysts are subjected to activation treatment, whose purpose is to bring the catalysts to an active form for Fischer-Tropsch synthesis. The common activation gases employed in iron catalysts are H_2 [1,2], CO [3,4] or H_2/CO [5,6]. The extent of reduction is dependent on the activation temperature, duration of the activation experiment as well as the type of promoters added to the iron catalysts [3,7,8,9]. Industrial iron-based FT catalysts are promoted with copper to assist in the reduction of the iron catalysts during activation [10,11,12,13]. Copper acts as a reduction promoter during H_2 activation [14,15,16,17]. However, very little is known on the influence that metals (i.e., silver) in the same group as copper (in the periodic table) have on the reduction behaviour of the iron-based FT catalysts. Wachs et al. [18] studied the promotional effect of silver on an iron-based FT catalyst. They showed that silver did not act as a reduction promoter for the iron-based FT catalyst. This was attributed to the lack of intimate contact between Ag and Fe during the activation process. Since then no further study has been conducted on silver as a promoter for iron-based FT catalysts. Therefore, the aim of this present study is to gain better understanding on the promotional effect of copper and silver on the iron-based FT catalysts during H_2 and CO activation using the copper ferrites ($CuFe_2O_4$, $CuFeO_2$) and silver ferrite ($AgFeO_2$) as model catalysts.

The reduction behaviour, phase transformation and changes in the average crystallite sizes, were evaluated during and post H_2 and CO activation. These changes were subsequently compared to the bulk iron oxide (γ-Fe_2O_3 and α-Fe_2O_3). In an attempt to eliminate effects due to the

crystallite size, α-Fe_2O_3 (110 nm) was used as a reference material for copper incorporated iron catalysts ($CuFe_2O_4$ (90 nm), $CuFeO_2$ (106 nm)) and γ-Fe_2O_3 (9 nm) was used as a reference material for silver incorporated iron catalyst ($AgFeO_2$ (7 nm)). The activation of the model catalysts was characterized using H_2-Temperature-Programmed Reduction (H_2-TPR), *ex-situ* activation in a slurry reactor, Mössbauer absorption spectroscopy (MAS) and *in-situ* X-ray diffraction (XRD). The relative abundances of the α-Fe and Fe_xC were taken as measures of the extent of reduction for H_2 and CO activated samples, respectively. To note: the *ex-* and *in-situ* activated model catalysts were characterized using X-ray diffraction (XRD) and only the *ex-situ* model catalysts were characterized using Mössbauer absorption spectroscopy (MAS).

The major challenge with *ex-situ* characterization techniques is correlating the data to the Fischer-Tropsch activity and selectivity. Usually, numerous samples, at different times on stream, are required to formulate a plausible correlation to the Fischer-Tropsch synthesis performance of the catalyst. The general trend in literature is therefore to use *in-situ* methods. The benefit of using *in-situ* characterization as opposed to *ex-situ* is that an *in-situ* technique at realistic reaction conditions will provide more trustworthy results than the traditional *ex-situ* methods. *In-situ* measurements provide a deeper insight into the catalyst solid state system under operating conditions, thereby, providing valuable information on the structure of the bulk phase and its stability. For such an investigation, a set-up is used in which X-ray diffraction (XRD) measurements are taken from catalyst samples operated at close to real conditions in a miniature (small) reactor.

6.2. Mechanism of H_2-activation based on *in-situ* XRD

During H_2 activation the iron catalyst reduces from Fe_2O_3 to α-Fe [1,2]. The pathway of Fe_2O_3 reduction can be essentially different, involving a two-step ($Fe_2O_3 \rightarrow Fe_3O_4 \rightarrow$ α-Fe) [19,20,21] or a three-step ($Fe_2O_3 \rightarrow Fe_3O_4 \rightarrow FeO \rightarrow$ α-Fe) mechanism [22,23,24]. The metastable FeO phase can be stabilized on the support surface or with doping agents [25]. Depending on the extent of reduction either α-Fe or α-Fe and Fe_3O_4 or α-Fe, Fe_3O_4 and FeO may co-exist after H_2 activation. However, to gain better understanding on the phase transition and change in the average crystallite sizes during H_2 activation, *in-situ* XRD studies were conducted on the X-ray diffraction (XRD) instrument using a Bruker D8 Advanced X-ray diffractometer, mimicking typical Fischer-Tropsch activation conditions. The model catalyst (0.60 g) was loaded onto an sample holder into the *in-situ* XRD chamber; a reducing gas of 60 ml(STP).min^{-1} was flowed

through the sample. The sample was heated up from 60 to 270 ^{o}C at a heating rate of 1 ^{o}C.min^{-1}; once at 270 ^{o}C, the temperature was held there for 16 hours. The XRD data was acquired throughout the activation experiment. Detailed activation conditions are discussed in Chapter 4 (section 4.4.6).

The reduction behaviour during *in-situ* H_2 activation of γ-Fe_2O_3, α-Fe_2O_3, $CuFe_2O_4$, $CuFeO_2$ and $AgFeO_2$ are shown in Figure 6.1, 6.2, 6.3, 6.4 and 6.5, respectively. The reduction mechanism, temperature (^{o}C), time (min) at which the respective phase transformation occurs as well as relative abundances of the phase(s) present after H_2 activation are given in Table 6.1. Figure 6.1 (a) shows the 3D view of the diffraction pattern of γ-Fe_2O_3 during H_2 activation, while (b) shows the phase transformation of γ-Fe_2O_3 during H_2 activation. The initial appearance of diffraction peaks corresponding to Fe_3O_4 at 270 ^{o}C (393 minutes) confirmed the start of the first reduction step attributed to γ-Fe_2O_3 → Fe_3O_4. The second reduction step ascribed to Fe_3O_4 → α-Fe, was confirmed by the appearance of the diffraction peaks corresponding to α-Fe at 270 ^{o}C (530 minutes). The phases present after activation was Fe_3O_4 and α-Fe, with relative abundances of 46 and 54 mol-%, respectively. The growth in the average crystallite size of the phases as a function of time is shown in Figure 6.1 (c). A gradual increase in the average crystallite sizes of the Fe_3O_4 and α-Fe of up to ~25 and 44 nm, respectively, was observed.

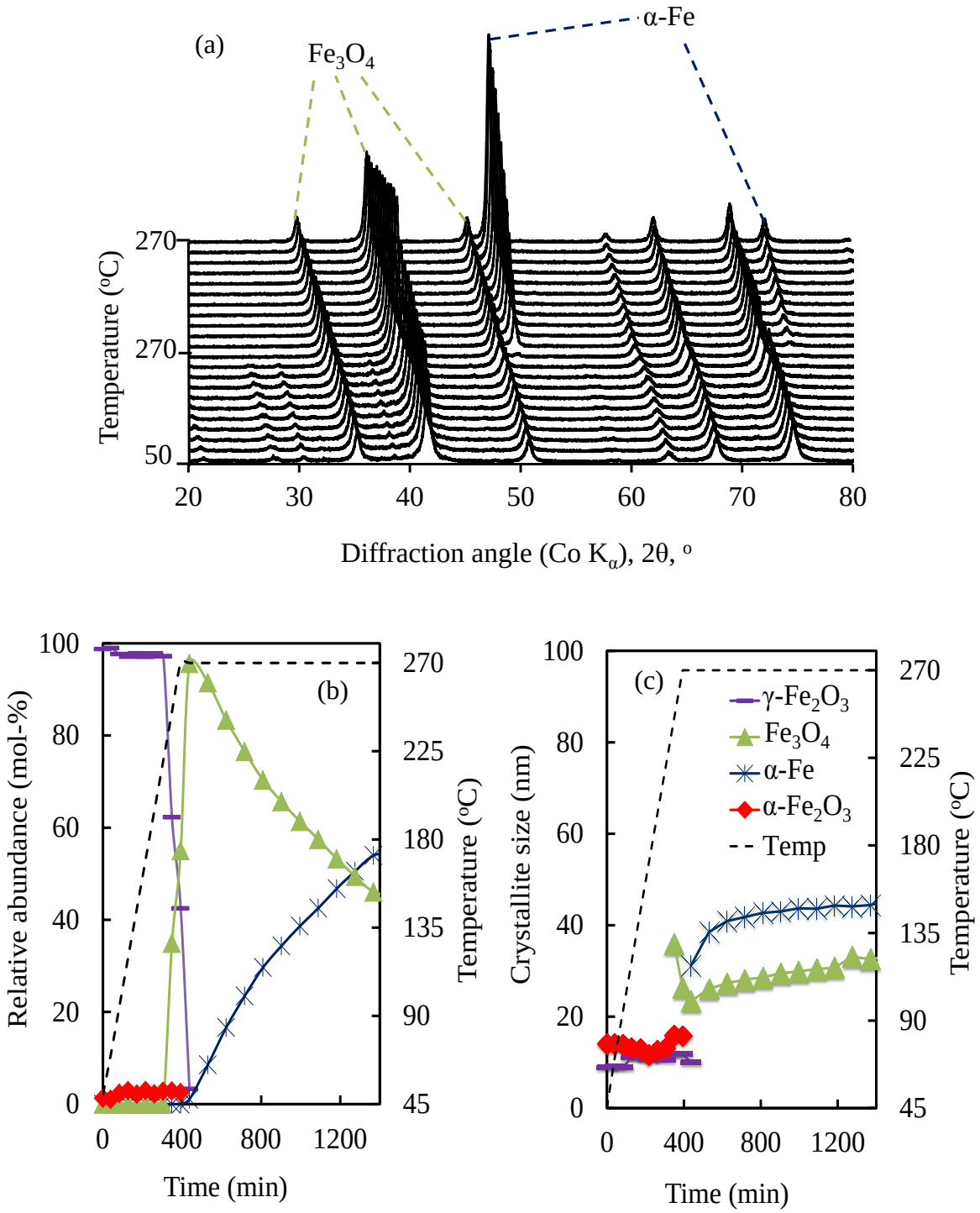

Figure 6.1: Phase analysis of γ-Fe_2O_3 during H_2-activation using *in-situ* XRD: (a) diffraction pattern, 3D view, (b) phase transformation of γ-Fe_2O_3 and (c) evolution of the average crystallite size (nm) during H_2-activation as a function of time (min)

Figure 6.2 shows the reduction behaviour during H_2 activation of α-Fe_2O_3. The phase transformation of α-Fe_2O_3 → Fe_3O_4 and Fe_3O_4 → α-Fe was confirmed by the initial appearance of diffraction peaks corresponding to Fe_3O_4 and α-Fe observed at 270 °C (438 minutes) as

shown in Figure 6.2 (a). Simultaneous reduction process of α-Fe_2O_3 → Fe_3O_4 → α-Fe postulated from the H_2-TPR results is confirmed by the occurrence of the phase transformation of α-Fe_2O_3 → Fe_3O_4 and Fe_3O_4 → α-Fe at the same temperature and time. The phase(s) present after H_2 activation were α-Fe_2O_3, Fe_3O_4 and α-Fe, with relative abundances of 2, 59 and 39 mol-%. Figure 6.2 (b), shows the evolution of the average crystallite size during H_2 activation. The average crystallite size of α-Fe_2O_3, Fe_3O_4 and α-Fe after H_2 activation was 78, 40 and 44 nm, respectively. A decrease in the average crystallite size of α-Fe_2O_3 was observed with time on stream (min), while the average crystallite size of Fe_3O_4 and α-Fe remained more or less the same (~40 nm). Furthermore, the on-set of the reduction of γ-Fe_2O_3 is only at a slightly lower temperature (260 °C) than the on-set of the reduction of α-Fe_2O_3 (270 °C). The minimal effect of the crystallite size on the reduction of iron(III)oxide implies that the reduction process is not dominated by bulk properties of the material, but rather by a surface phenomenon e.g., the hydrogen activation on the surface of the oxide.

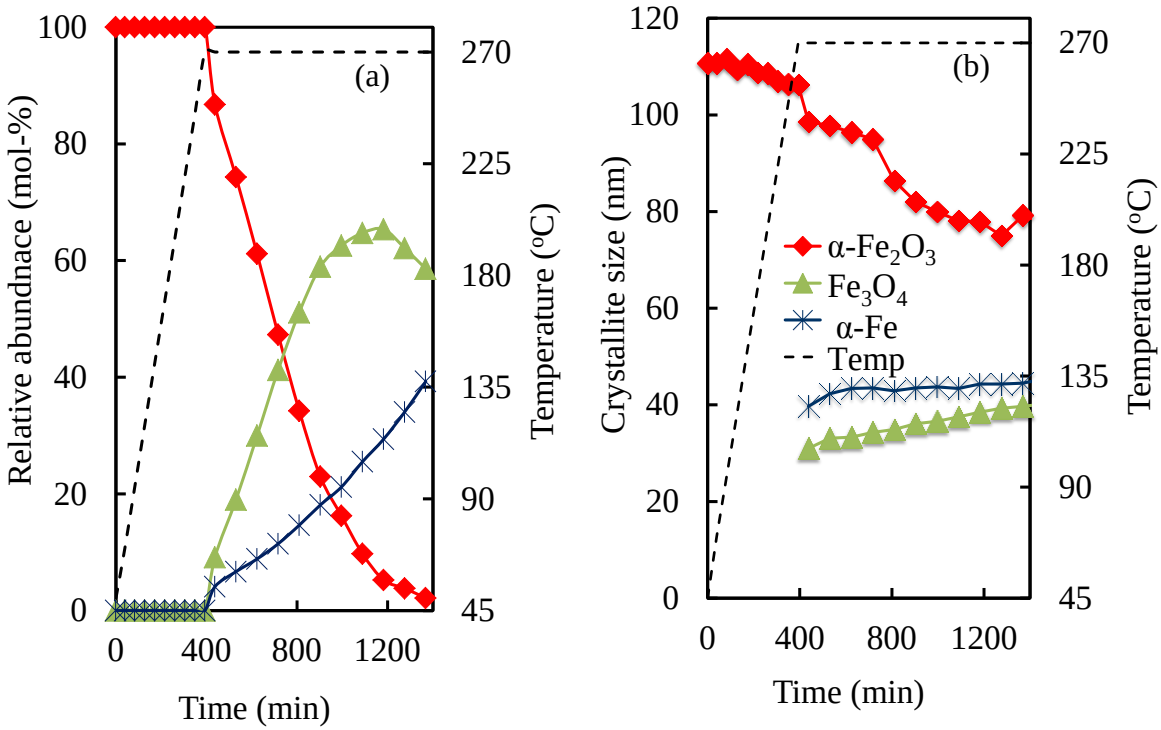

Figure 6.2: Phase analysis of α-Fe_2O_3 during H_2 activation using *in-situ* XRD: (a) phase transformation of α-Fe_2O_3 and (b) evolution of the average crystallite size (nm) during H_2-activation as a function of time (min)

The phase transformations as well as the average crystallite sizes of $CuFe_2O_4$ and $CuFeO_2$ during H_2 activation are shown in Figure 6.3 and 6.4, respectively. The reduction process occurred in a two-step reduction process; the first step corresponding to the decomposition of the copper ferrites to Cu and Fe_3O_4. This was confirmed by the appearance of diffraction peaks corresponding to Cu and Fe_3O_4 observed at 170 ^oC for $CuFe_2O_4$ (Figure 6.3 (a)) and 245 ^oC for $CuFeO_2$ (Figure 6.4 (a)). The initial appearance of diffraction peaks typical of α-Fe deemed the start of the second reduction step ascribed to $Fe_3O_4 \rightarrow$ α-Fe was observed at 270 ^oC (438 minutes) for $CuFe_2O_4$ and 270 ^oC (393 minutes) for $CuFeO_2$. The on-set of the reductive decomposition for $CuFe_2O_4$ and $CuFeO_2$ occurs at a slightly lower temperature than the reduction of γ-Fe_2O_3 with a similar size. Furthermore, a faster rate of reduction for the first reduction step (copper ferrite $\rightarrow$ Cu + Fe_3O_4) was observed in spinel $CuFe_2O_4$ as compared to the delafossite $CuFeO_2$.

These results may be related to the relative structural stability of delafossite. The phases present after H_2 activation were Fe_3O_4, α-Fe and Cu, with a normalized relative abundance of 11, 58 and 31 mol-%, respectively. After H_2 activation the $CuFeO_2$ sample showed diffraction peaks corresponding to α-Fe and Cu with relative abundance were 51 and 49 mol-%, respectively. This results are in accordance with previously reported results which showed that an increase in copper loadings on iron-based catalysts, enhanced reduction to metallic phases [26,27]. Moreover, metallic copper content in $CuFe_2O_4$ and $CuFeO_2$ after H_2 activation was 31 and 49 mol-%, respectively.

The change in the average crystallite sizes as a function of time during H_2 activation is shown in Figure 6.3 (b) and 6.4 (b) for $CuFe_2O_4$ and $CuFeO_2$, respectively. The spinel $CuFe_2O_4$ showed an increase in crystallite size of Fe_3O_4 until 48 nm, and thereafter, decreased to 34 nm. On the other hand, the average crystallite size of α-Fe showed gradual increase up to 37 nm. The average crystallite size of Cu showed a gradual increase to 21 nm, and thereafter stabilized. The stabilization of the average crystallite sizes of Cu after 400 minutes may be attributed to minimal or no water vapour formation during reduction which may promote sintering. Change in the average crystallite size during H_2 activation of $CuFeO_2$ is shown in Figure 6.4 (b). $CuFeO_2$ results showed a similar trend to those of the observed $CuFe_2O_4$, a gradual increase in the average crystallite size of Fe_3O_4 up to 48 nm was observed, while the average crystallite sizes of the α-Fe and Cu stabilized at ~38 and 32 nm, respectively. Incorporation of copper in iron oxide

seemed to assist in the reduction of the average crystallite size of the α-Fe after H_2 activation as compared to the observed average crystallite of α-Fe (45 nm) in the un-promoted iron oxide. Similar results have been reported by Cairns [27].

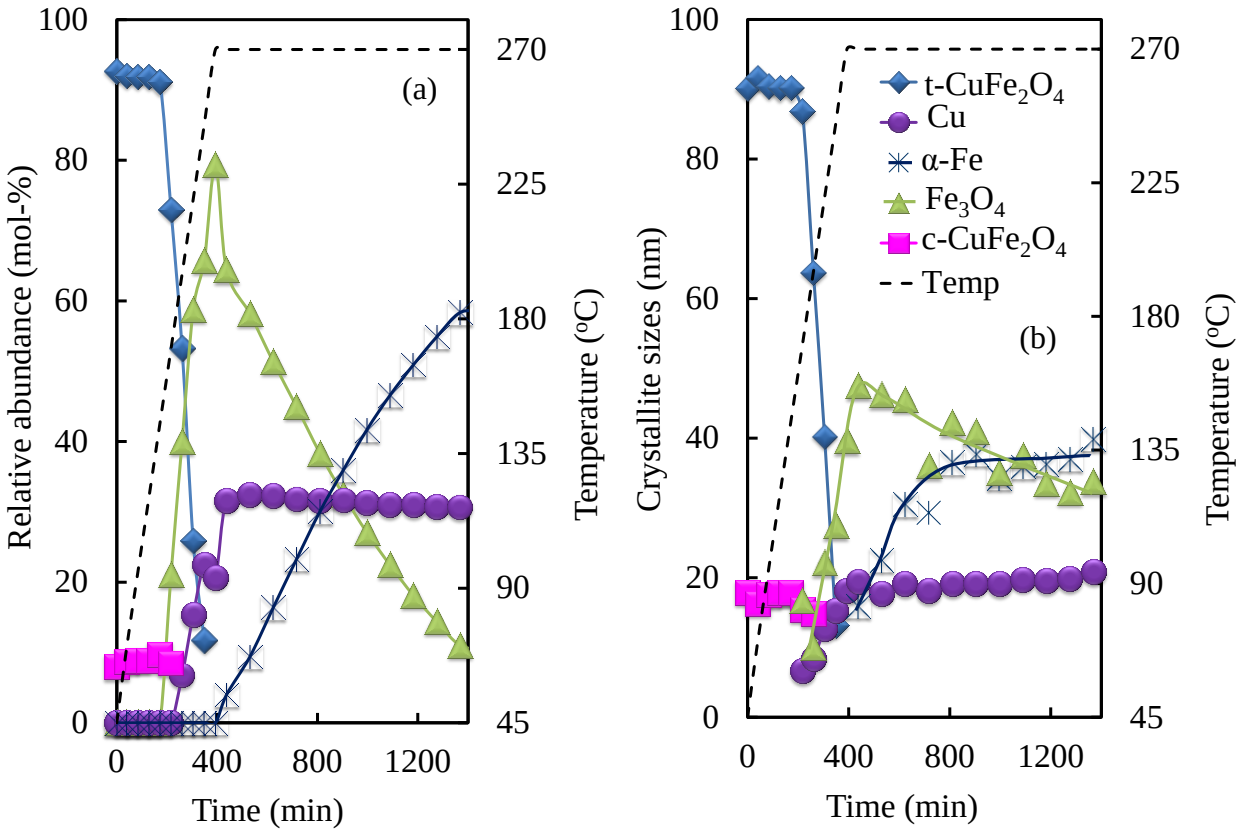

Figure 6.3: Phase analysis of $CuFe_2O_4$ during H_2 activation using *in-situ* XRD: (a) phase transformation of $CuFe_2O_4$ and (b) evolution of the average crystallite size (nm) during H_2-activation as a function of time (min)

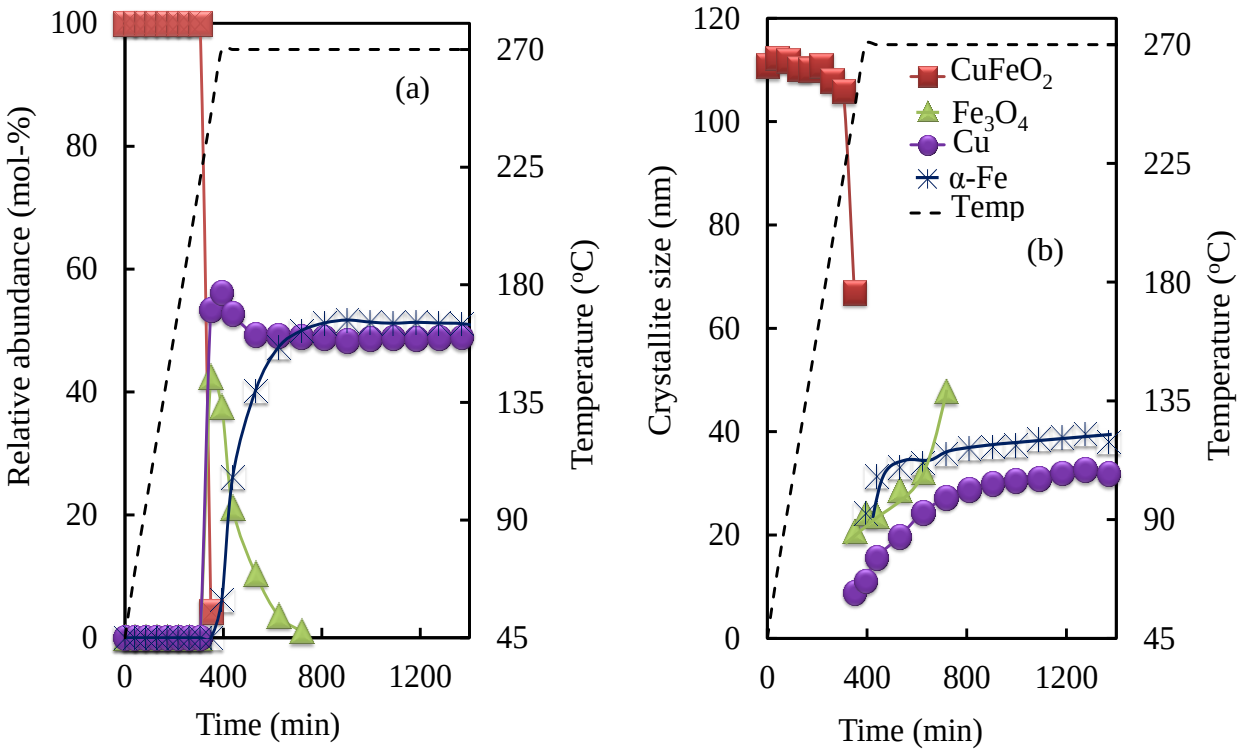

Figure 6.4: Phase analysis of $CuFeO_2$ during H_2 activation using *in-situ* XRD: (a) phase transformation of $CuFeO_2$ and (b) evolution of the average crystallite size (nm) during H_2-activation as a function of time (min)

The phase transformation and average crystallite size during H_2 activation of the incorporation silver in the iron oxide ($AgFeO_2$) is shown in Figure 6.5 (a) and (b), respectively. The reduction of $AgFeO_2$ occurred via a two-step reduction process; the first reduction step was ascribed to the decomposition of $AgFeO_2$ to Ag and Fe_3O_4 and was confirmed by the appearance of diffraction peaks corresponding to Ag and Fe_3O_4 at a temperature as low as ~80 ^oC. The reductive decomposition of silver ferrite starts at very low temperature, which cannot solely be attributed to the small average crystallite size of this material, since the reduction of maghemite (9 nm) starts at only slightly lower temperatures than the reduction of hematite (110 nm). Hence, the ease of reduction must be attributed to either the structural instability of this phase in hydrogen or the ability of this material to activate hydrogen. The initial appearance of diffraction peaks corresponding to α-Fe at 270 ^oC (393 minutes) deemed the start of the second reduction step, which was attributed to the phase transformation of $Fe_3O_4 \rightarrow$ α-Fe. The phases present after H_2 activation were α-Fe and Ag, constituting 62 and 38 mol-%, respectively. The change in the average crystallite sizes of the present phases are shown in Figure 6.5 (b). Average crystallite sizes of 57 and 25 nm were observed for α-Fe and Ag, respectively.

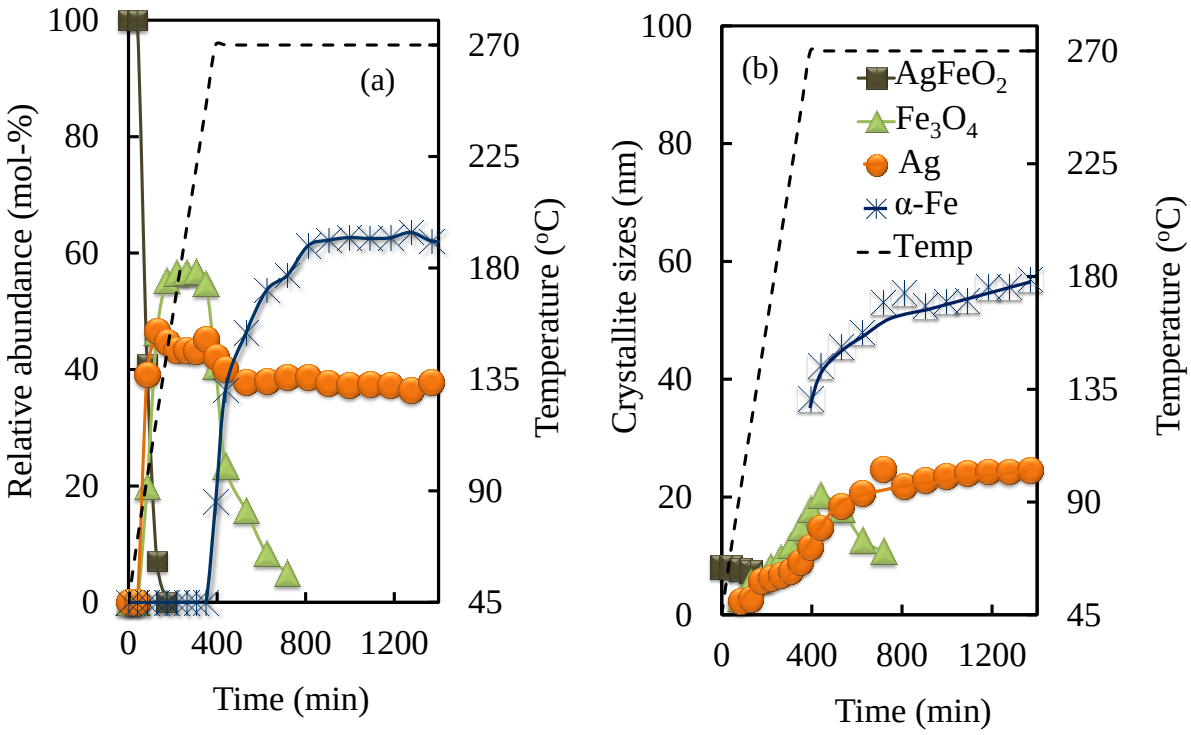

Figure 6.5: Phase analysis of $AgFeO_2$ during H_2 activation using *in-situ* XRD: (a) phase transformation of $AgFeO_2$ and (b) evolution of the average crystallite size (nm) during H_2 activation as a function of time (min)

The *in-situ* H_2 activation study of all the promoted model catalysts seems to indicate that copper and silver facilitates the second step reduction process (Fe_3O_4 to α-Fe). The formation of α-Fe took place for all the model catalysts under essentially isothermal conditions at 270 °C. Figure 6.6 shows the rate of formation of α-Fe as a function of the amount of iron present as Fe_3O_4. The rate of reduction of Fe_3O_4 in the sample *ex* maghemite is virtually indistinguishable from the rate in the sample *ex* hematite. This is not surprising seeing the similarity in the average crystallite size of magnetite in these samples (23-32 nm for the sample γ-Fe_2O_3 (ex) and 30-38 nm for the α-Fe_2O_3 (ex)). The rate of formation of α-Fe from Fe_3O_4 was previously described using a random nucleation model [28,29,30,31]. However, close inspection of the dependency of the rate of α-Fe formation as a function of the amount of Fe present as Fe_3O_4 shows a positive deviation from this model at a high content of α-Fe as Fe_3O_4, i.e., the rate of reduction is faster than predicted by this model when a large amount of Fe is present as Fe_3O_4. These observations may be attributed to hydrogen spill-over from metallic copper and silver to the magnetite phase when in close proximity [32].

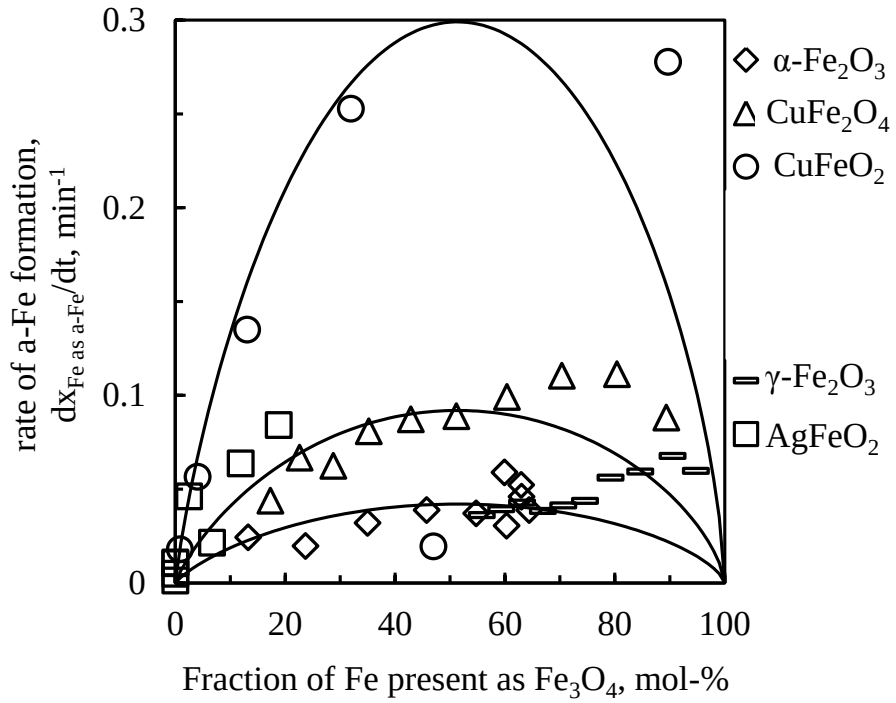

Figure 6.6: Rate of α-Fe formation during *in-situ* H_2 activation at 270 ^oC as a function of the Fe present as Fe_3O_4 (solid lines represent model fit to a three dimensional nucleation model)

6.2.1. H_2-Temperature programmed reduction (H_2-TPR)

H_2-Temperature programmed reduction (H_2-TPR) was used to study the reduction behaviour of the model catalysts under H_2 atmosphere. The H_2-TPR profiles of model catalysts are shown in Figure 6.7. The H_2-TPR profile of α-Fe_2O_3 showed numerous unresolved reduction peaks, attributed to the large average crystallite size (110 nm), which may be assigned to the simultaneous reduction of α-Fe_2O_3 → Fe_3O_4 → FeO → α-Fe. The temperature maxima of the reduction peaks ranged from 450 to 950 ^oC. These results are in accordance with the results observed during the *in-situ* XRD activation, in which a simultaneous reduction of α-Fe_2O_3 to α-Fe was observed.

Two distinctive reduction peaks were observed for the spinel copper ferrite ($CuFe_2O_4$). The first reduction peak appearing at 327 ^oC was attributed to the reduction of $CuFe_2O_4$ to Cu and Fe_3O_4, and a similar reduction process has been reported by Faungnawakij et al. [33]. The second reduction peak appearing at 585 ^oC was attributed to the reduction of Fe_3O_4 to α-Fe [34,35,36]. The reduction of delafossite $CuFeO_2$ occurred in a three reduction step process, confirmed by the appearance of three distinctive reduction peaks at 374, 526 and 833 ^oC.

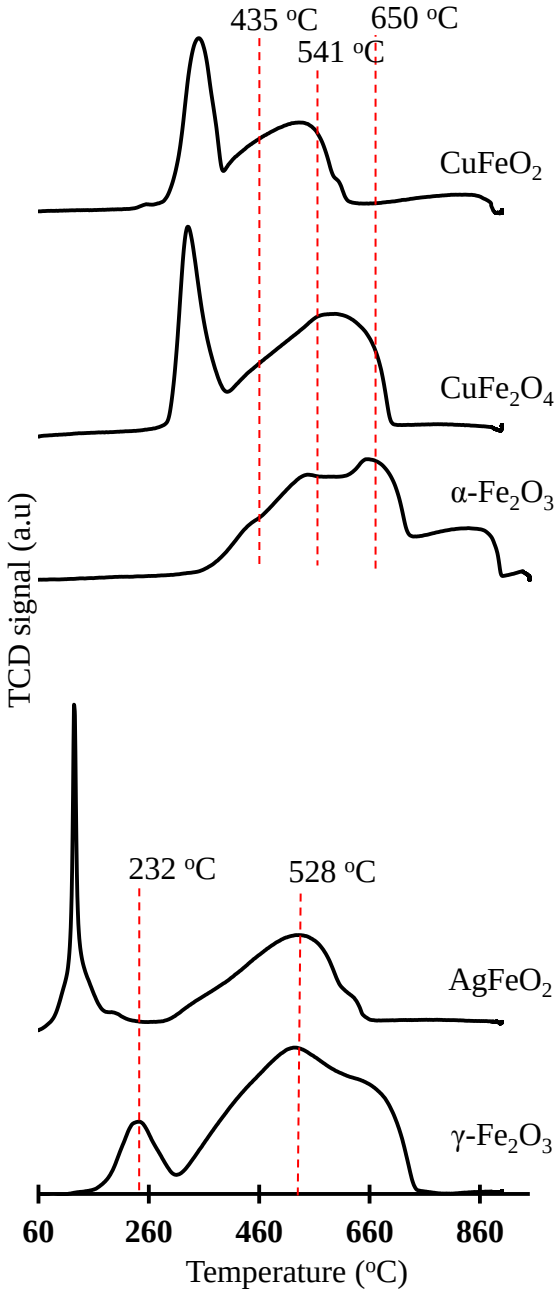

Figure 6.7: H_2-TPR profiles of the model catalysts

The first reduction peak appearing at lower temperature was attributed to the reduction of $CuFeO_2$ to Cu and Fe_3O_4, the second reduction peak was attributed to the reduction of Fe_3O_4 to α-Fe [37] and the third shoulder reduction peak was ascribed to the reduction of FeO to α-Fe, FeO has been reported to be stable at temperatures >600 °C [38,39,40,41]. Similarly, Maiti et al. [42] noted the formation of FeO as an intermediate phase during the reduction of the co-precipitated mixed oxides and suggested that the stability of the FeO phase results was due to

incorporation of an appreciable amount of Mn^{2+} ions into the lattice. The H_2-TPR profile of the Cu incorporated iron oxide systems ($CuFe_2O_4$ and $CuFeO_2$) compared to α-Fe_2O_3, showed that the presence of Cu shifted the first reduction peak temperature maximum towards lower temperature implying greater ease of reduction. This is known to occur through the initial facile reduction of copper oxide to copper at lower temperature [43], which is then able to assist in the hydrogen dissociation thus providing a source of atomic hydrogen to assist in the reduction of the iron oxide to metallic iron at relatively lower temperatures [11,10], a type of hydrogen spill-over. Similar results have previously been reported [44,13,45,46,47,48].

Two reduction peaks were observed in the H_2-TPR profile of maghemite (γ-Fe_2O_3). The first reduction peak appearing at 232 ^oC was attributed to the reduction of γ-Fe_2O_3 → Fe_3O_4. The second reduction peak appearing at 528 ^oC was attributed to the reduction of Fe_3O_4 → α-Fe [49]. Comparison of the reduction behaviour of α-Fe_2O_3 (110 nm) and γ-Fe_2O_3 (9 nm), revealed that average crystallite size played a role in the reduction behaviour of the model catalyst. The small average crystallite size sample (γ-Fe_2O_3) showed better reducibility than the sample with large average crystallite size (α-Fe_2O_3) [50]. The reduction of $AgFeO_2$ occurred in a two-step reduction process, confirmed by the appearance of the two distinctive reduction peaks in the H_2-TPR profile. The first reduction peak appearing at 124 ^oC was ascribed to the reduction of $AgFeO_2$ to Ag and Fe_3O_4 and the second reduction peak appearing at 535 ^oC was ascribed to the reduction of Fe_3O_4 to α-Fe. The silver incorporated iron oxide ($AgFeO_2$) showed ease of reducibility as compared to γ-Fe_2O_3, the first reduction peak of $AgFeO_2$ appear at lower temperature than that of γ-Fe_2O_3. From these results it was concluded that silver in intimate contact with iron enhances the reducibility of the iron catalyst, and thus acts as a reduction promoter. The importance of the intimate contact between the iron oxide and the promoter (i.e copper) is further shown in Figure B.1 (Appendix B). The H_2-TPR result of the physically mixed CuO and α-Fe_2O_3 sample is compared to those observed for the pure CuO and α-Fe_2O_3. The H_2-TPR profile of the physically mixed CuO and α-Fe_2O_3 shows similar reduction behaviour to the TPR profile of pure CuO and α-Fe_2O_3. No shift in the reduction peak temperatures of the physically mixed CuO and α-Fe_2O_3 sample were observed as compared to that of CuO and α-Fe_2O_3.

6.3. Mechanism of CO activation based on *in-situ* XRD

Carbon monoxide (CO) activation of iron-based catalysts has been reported to occur through the reduction and/or carburization of Fe_2O_3 to Fe_xC via Fe_3O_4 [51]. A number of study have shown

similar phase transformation using Temperature-Programmed EXAFS/XANES characterization technique [52]. Carburization has been defined as the transformation of an iron oxide to iron carbide during CO activation and/or Fischer-Tropsch synthesis.

Depending on the activation conditions as well as the presence of promoters, a number of iron carbides may be formed; these include the hexagonal – O-carbides (έ-$Fe_{2.2}C$, ε-Fe_2C) and trigonal prismatic – TP-carbides (Fe_7C_3, χ-Fe_5C_2, and θ-Fe_3C) [53].

The reduction behaviour of γ-Fe_2O_3, α-Fe_2O_3, $CuFe_2O_4$, $CuFeO_2$ and $AgFeO_2$ during the CO activation is shown in Figure 6.8, 6.9, 6.10, 6.11 and 6.12, respectively. Table 6.2 shows the relative abundances of the phases present and the average crystallite sizes post CO activation. The XRD pattern of the CO activated γ-Fe_2O_3 is shown in Figure 6.8. The appearance of initial diffraction peaks corresponding to Fe_3O_4 at 170 ^oC confirmed the phase transformation of γ-Fe_2O_3 → Fe_3O_4. Diffraction peaks corresponding to FeO at 245 ^oC deemed the start of the subsequent reduction step which was attributed to Fe_3O_4 → FeO transition. As the diffraction peaks of FeO disappeared, diffraction peaks corresponding to χ-Fe_5C_2, θ-Fe_3C, ε-carbide and Fe_7C_3 appeared at 270 ^oC (438 minutes), as shown in Figure 5.8 (a) and (b). A further phase transformation to Fe_7C_3 was observed at 270 ^oC (530 minutes). The phases present after CO activation were Fe_3O_4, χ-Fe_5C_2, θ-Fe_3C, ε-carbide and Fe_7C_3 with relative abundances of 9, 52, 21, 1 and 17 mol-%, respectively. The changes in the average crystallite size of the phases during the progression of CO activation are shown in Figure 6.8 (c). The average crystallite sizes of the phases present after CO activation were 26, 16, 11, 17 and 17 nm, for Fe_3O_4, χ-Fe_5C_2, θ-Fe_3C, ε-carbide and Fe_7C_3, respectively.

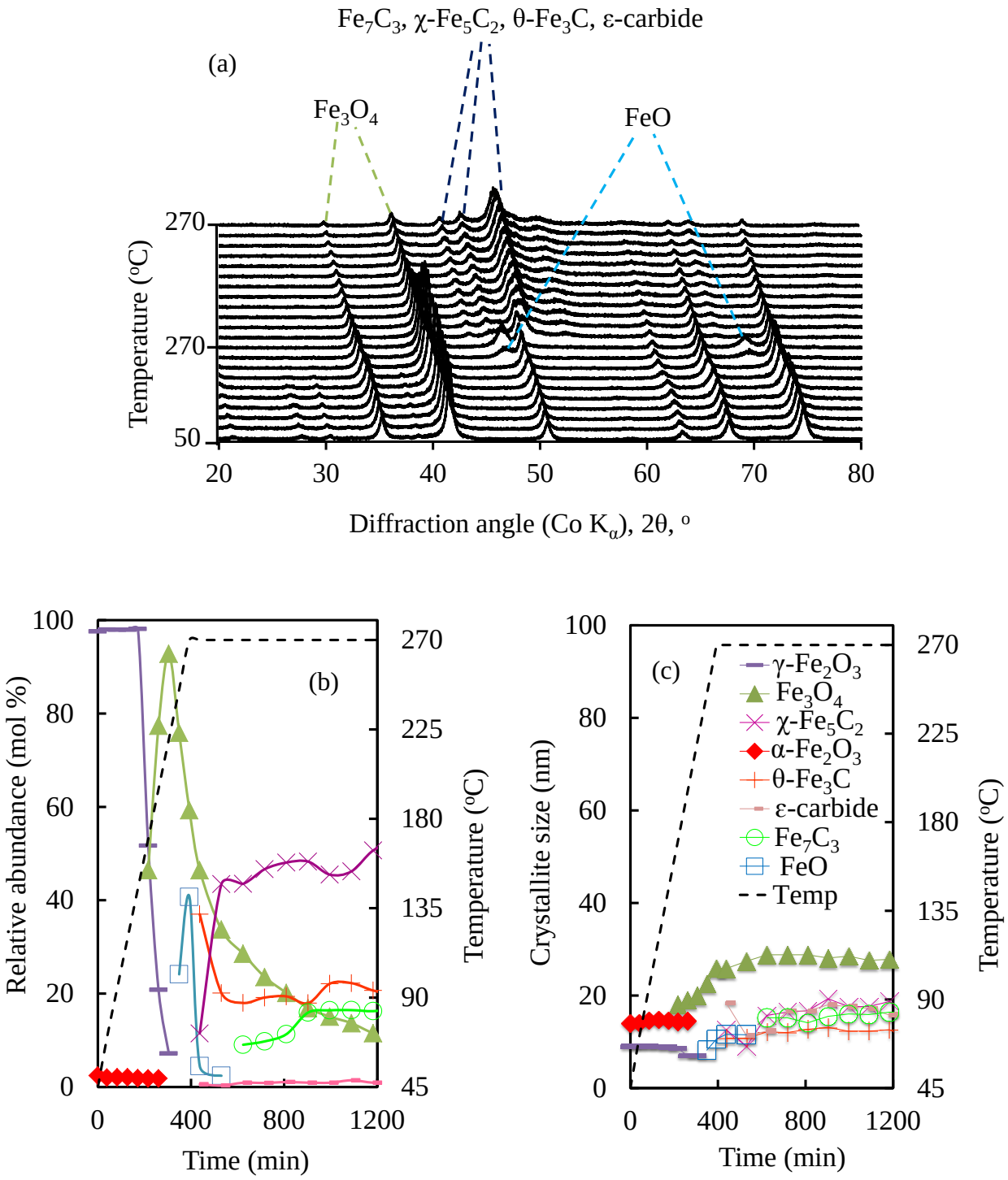

Figure 6.8: Phase analysis of γ-Fe_2O_3 during CO activation using *in-situ* XRD: (a) diffraction pattern, 3D view, (b) phase transformation of γ-Fe_2O_3 and (c) evolution of the average crystallite size (nm) during CO activation as a function of time (min)

The phase transformation of α-Fe_2O_3 during CO activation is shown in Figure 6.9. The first reduction step attributed to α-Fe_2O_3 → Fe_3O_4 was confirmed by the initial appearance of diffraction peaks corresponding to Fe_3O_4 at 270 ^oC (393 minutes) as shown in Figure 6.9 (b) [54,55]. The subsequent reduction step attributed to the carburization of Fe_3O_4 observed at 270^oC (530 minutes), was confirmed by the appearance of the diffraction peaks corresponding to χ-Fe_5C_2. The phases present after CO activation was Fe_3O_4 and χ-Fe_5C_2, with relative abundances of 15 and 85 mol-%, respectively. The final average crystallite sizes of Fe_3O_4 and χ-Fe_5C_2 were 28 and 10 nm, respectively (Figure 6.9 (b)). The initial reduction of α-Fe_2O_3 to magnetite during CO activation results in the formation of magnetite crystalline domains with a size similar to the size obtained with H_2-activation (~31 nm), but in contrast to H_2-activation do not grow (possibly due to the lack of water in case of CO activation, which may accelerate the sintering process [56,57]. The carburization of Fe_3O_4 (*ex*-hematite), results in the cleavage of small χ-Fe_5C_2 crystallites (~10 nm) due to the difference in the skeletal density [58].

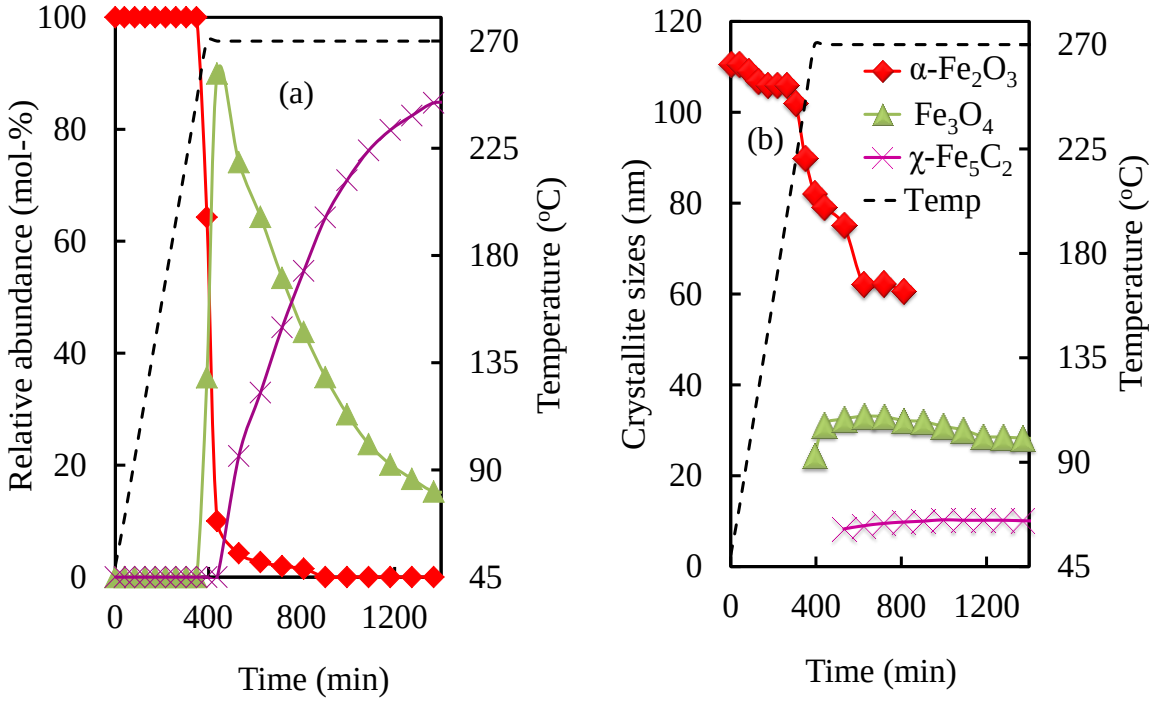

Figure 6.9: Phase analysis of α-Fe_2O_3 during CO activation using *in-situ* XRD: (a) phase transformation of α-Fe_2O_3 and (b) evolution of the average crystallite size (nm) during CO activation as a function of time (min)

The phase transformation of the spinel $CuFe_2O_4$ during CO activation is shown in Figure 6.10. The decomposition of $CuFe_2O_4$ → Cu + Fe_3O_4 was confirmed by the appearance of diffraction

peaks at 245 °C and the initial appearance of diffraction peaks corresponding to χ-Fe_5C_2, θ-Fe_3C and ε-carbide at 270 °C (438 minutes), deemed the start of carburization of Fe_3O_4.

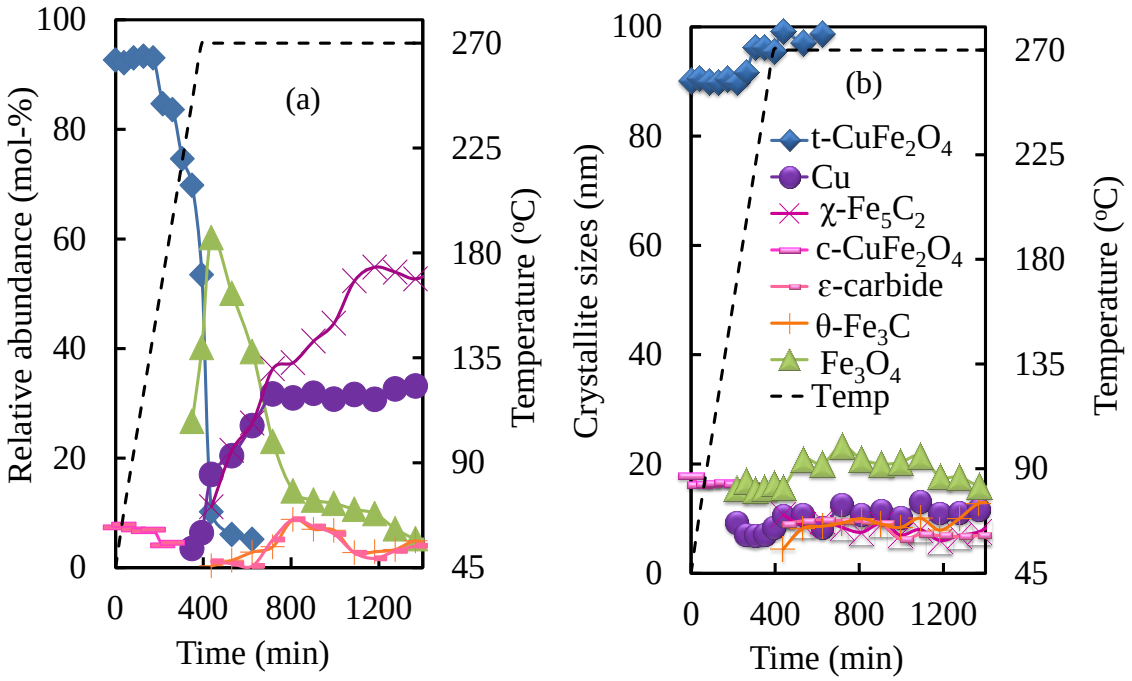

Figure 6.10: Phase analysis of $CuFe_2O_4$ during CO activation using *in-situ* XRD: (a) phase transformation of $CuFe_2O_4$ and (b) evolution of the average crystallite size (nm) during CO activation as a function of time (min)

The phases present after CO activation were Fe_3O_4, χ-Fe_5C_2, θ-Fe_3C, ε-carbide and Cu with normalized relative abundances of 5, 54, 5, 3 and 32 mol-%, respectively (Figure 6.10 (a)). The average crystallite sizes of these iron containing phases present after CO activation, Fe_3O_4, χ-Fe_5C_2, θ-Fe_3C, ε-carbide and Cu were 18, 13, 10, 13, 7 and 12 nm, respectively (Figure 6.10 (b)). The phase transformation of $CuFeO_2$ during CO activation (Figure 6.11) followed a similar trend to that of $CuFe_2O_4$ (Figure 6.10). The initial reduction step attributed to the decomposition of $CuFeO_2$ to Cu and Fe_3O_4 was confirmed by the initial appearance of diffraction peaks corresponding to Cu and Fe_3O_4 at 270 °C (393 minutes). The average crystallite size of these phases changes only slightly with increasing activation time in contrast to what was observed during the activation in H_2. It might thus be concluded that the extent of sintering/crystal growth is less for the activation in CO compared to the activation in H_2. The reduced extent of crystal growth might be linked to an inhibition of the crystal growth process by e.g., amorphous carbon deposited during the CO activation, which may act as a spacer, the passivation of the copper surface with CO_2 generated during CO activation and/or the possible role of product water in

this process. The subsequent reduction step $Fe_3O_4 \rightarrow \chi\text{-}Fe_5C_2$ was confirmed by the appearance of diffraction peaks corresponding to $\chi\text{-}Fe_5C_2$ which were observed at the same temperature and time as the previous step (Figure 6.11 (a)). As the activation experiment progressed diffraction peaks corresponding to $\theta\text{-}Fe_3C$ appeared at 270 ^oC (903 minutes), suggestive of the transformation of $\chi\text{-}Fe_5C_2 \rightarrow \theta\text{-}Fe_3C$. De Smit et al. [36] pointed out that the transformation between the carbide phases is dependent on the chemical potential of carbon imposed by the surrounding gas environment. The chemical potential of carbon imposed by the gas environment changes during CO activation, since the amount of CO_2 formed varies. It might be concluded that the initially formed $\chi\text{-}Fe_5C_2$ is transformed into $\theta\text{-}Fe_3C$ and ε-carbide due to the lowering of the chemical potential of carbon (induced by the conversion of CO into CO_2 at this stage) [32]. Towards the end of the CO activation step, the chemical potential of carbon increases favouring the re-formation of $\chi\text{-}Fe_5C_2$. Similar iron carbide phase transformations were reported by Sirimanothan et al. [59]. The phases present after CO activation were Fe_3O_4, $\chi\text{-}Fe_5C_2$, $\theta\text{-}Fe_3C$ and Cu. The normalized relative abundance of Fe_3O_4, $\chi\text{-}Fe_5C_2$, $\theta\text{-}Fe_3C$ and Cu were 4, 43, 7 and 46 mol-%, respectively. The average crystallite sizes of Fe_3O_4, $\chi\text{-}Fe_5C_2$, $\theta\text{-}Fe_3C$ and Cu were 17, 5, 13 and 22 nm, respectively.

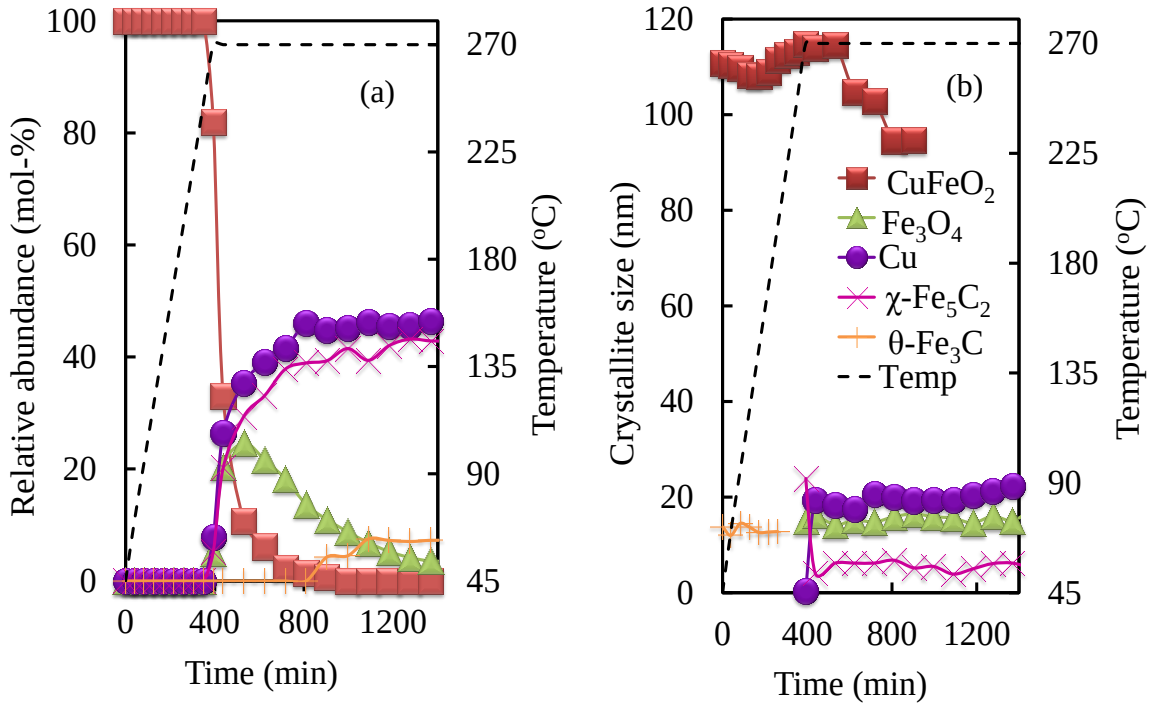

Figure 6.11: Phase analysis of $CuFeO_2$ during CO activation using *in-situ* XRD: (a) phase transformation of $CuFeO_2$ and (b) evolution of the average crystallite size (nm) during CO activation as a function of time (min)

Figure 6.12 shows the reduction behaviour of $AgFeO_2$ during CO activation. The initial reduction step is attributed to the simultaneous decomposition of $AgFeO_2$ to Ag and Fe_3O_4, and the reduction of $Fe_3O_4 \rightarrow \chi\text{-}Fe_5C_2$. The reduction steps were confirmed by the initial appearance of diffraction peaks corresponding to Ag, Fe_3O_4 and $\chi\text{-}Fe_5C_2$ observed at 95 ^oC (Figure 6.12 (a)). The subsequent reduction step was attributed to the phase transformation to $\theta\text{-}Fe_3C$ 170^oC, confirmed by the initial appearance of diffraction peaks corresponding to $\theta\text{-}Fe_3C$. Diffraction peaks corresponding to ε-carbide appeared at 270 ^oC (349 minutes). The phases present after CO activation were Fe_3O_4, $\chi\text{-}Fe_5C_2$, $\theta\text{-}Fe_3C$, ε-carbide and Ag with normalized relative abundances of 13, 40, 26, 1 and 21 mol-%, respectively. The average crystallite sizes of Fe_3O_4, $\chi\text{-}Fe_5C_2$, $\theta\text{-}Fe_3C$, ε-carbide and Ag were 19, 11, 11, 9 and 14 nm, respectively.

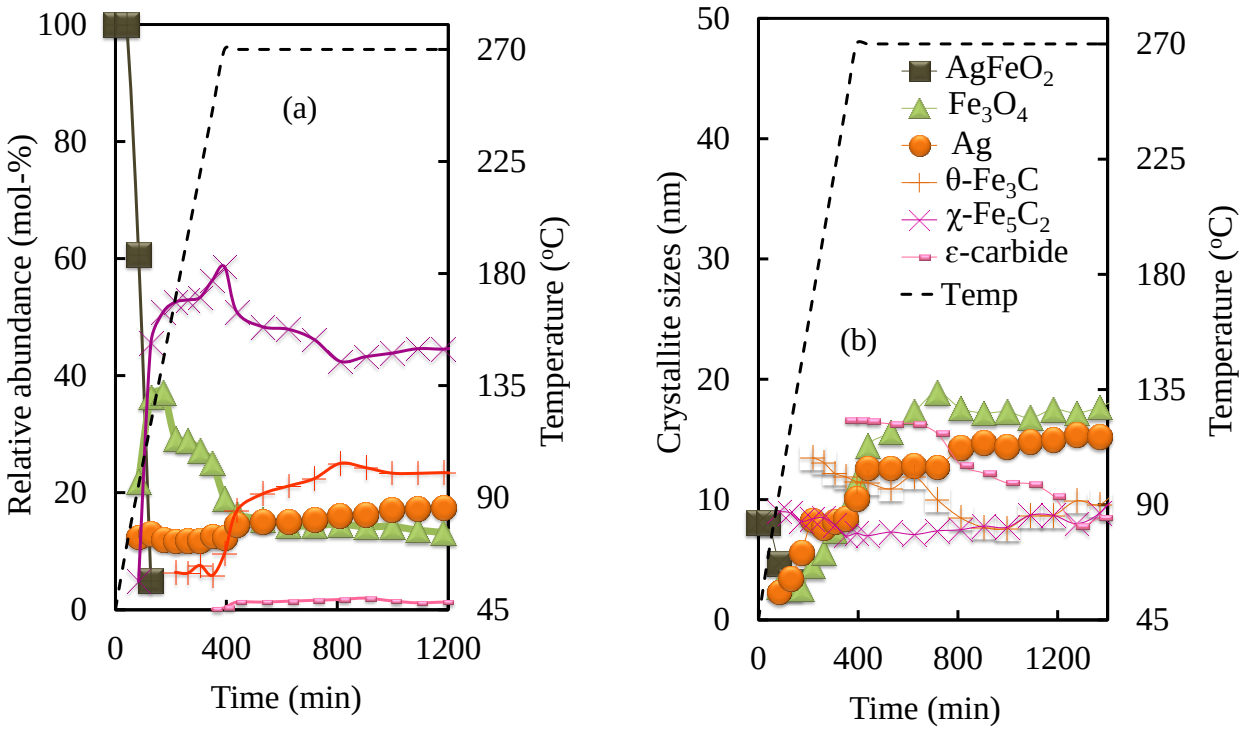

Figure 6.12: Phase analysis of $AgFeO_2$ during CO activation using *in-situ* XRD: (a) phase transformation of $AgFeO_2$ and (b) evolution of the average crystallite size (nm) during CO activation as a function of time (min)

Figure 6.13 shows the rate of iron carbide formation during CO activation as a function of the fraction of Fe in Fe_3O_4. It has been proposed that CO may spillover from copper to a closely associated iron oxide phase [32]. This spillover may assist in the rate of carburization of magnetite to the carbide phase(s) in a similar manner as hydrogen spillover assists the reduction of magnetite to metallic iron. However, the rate of iron carbide formation does not appear to be

strongly influenced by the presence of metallic copper or silver in its vicinity as shown in Figure 6.13. The rate of formation of iron carbide in the CO-activated sample ex hematite, α-Fe_2O_3, as a function of the fraction of Fe present as Fe_3O_4 can be modelled as a 1st order reaction (reaction order 1.03 ± 0.43; rate constant (0.29 ± 0.10).10^{-2} min^{-1}). The data points for the promoted iron catalysts do not deviate much from the obtained correlation for the transformation of magnetite to iron carbide for the un-promoted iron catalysts, except for the data points representing the initial conversion of magnetite ex spinel copper ferrite, $CuFe_2O_4$. This suggests that spill-over of carbon monoxide to magnetite is kinetically not relevant for its carburization. In general, the rate of spill-over, i.e., the rate of transport, is controlled by the surface diffusion of the adsorbed species and the driving force to move onto the surface of the other phase. The mobility of CO and H on Cu(111) is similar [60]. The driving force to spill-over onto the other phase is for atomic H higher (based on DFT-calculations [61,62]) larger than for CO (based on comparison of CO-TPD from Cu(111) [63] and from Fe_3O_4(111) [64]), since the difference in the strength of adsorption of H on these two phases is less than the difference in the strength of adsorption of CO on these phases.

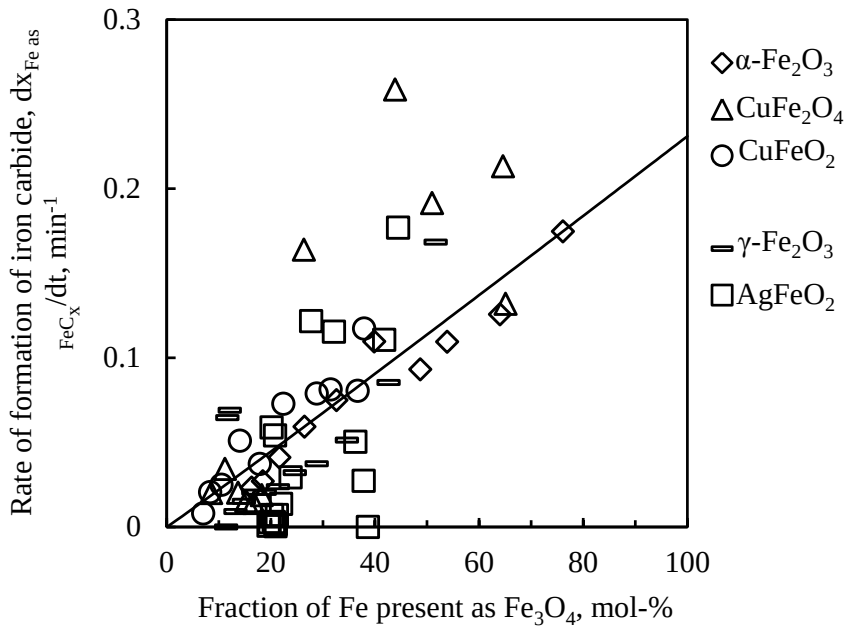

Figure 6.13: Rate of iron carbide (predominantly χ-Fe_5C_2) formation during *in-situ* CO activation at 270 ^oC as a function of the Fe present as Fe_3O_4 (solid lines represent model fit to a first order rate with respect to the fraction of Fe present as Fe_3O_4 for the sample hematite)

The importance of the role of spill-over is however not only determined by the mobility of the species and the driving force for spill-over to the other phase, but also by the rate of its competing reaction, viz. the direct activation of the species on the other phase. The activated H_2-chemisorption on Fe_3O_4 can be expected to be more difficult than on Cu(111), due to its surface geometry [[65]42], whereas chemisorption of CO is expected to be non-activated on these surfaces. Hence, hydrogen spill-over may become important, because it competes with the relatively slow dissociative H_2-chemisorption on the oxide. It should be further realized that the effect of spill-over can only be observed if the arrival of the reducing agent at the reactive site is controlling the rate of activation. Furthermore, a thorough kinetic comparison of the rate of carburization of the sample *ex* silver ferrite is not possible, since the carburization takes place mainly at temperatures lower than 270 ^oC. However, the low rate of carburization obtained at 270 ^oC indicates that silver, just like copper, does not facilitate the carburization of magnetite.

6.4. Characterization of *ex-situ* activated samples

Model calcined catalyst precursor (5.00 g) was added to molten wax in a slurry reactor, while increasing temperature to 270 ^oC at a heating rate of 1 $^oC.min^{-1}$, under argon flow, at a pressure of 1 bar. Once the reactor temperature was at 270 ^oC and atmospheric pressure, the argon gas flow was switched to the reducing gas at a flow rate of 500 ml (STP).min^{-1}. The activation experiment was carried out for 16 hours. Detailed activation conditions are included in Chapter 4 (Section 4.4.6). The activated model catalysts embedded in wax were characterized using X-ray diffraction (XRD) and Mössbauer absorption spectroscopy (MAS). The specific iron phase content (determined by XRD) present after activation of the promoted model catalysts was normalized to the total iron content in the activated catalyst.

6.4.1. H_2-activation studies

6.4.1.1. X-ray diffraction (XRD)

The XRD patterns of the H_2 activated γ-Fe_2O_3, α-Fe_2O_3, $CuFe_2O_4$, $CuFeO_2$ and $AgFeO_2$ are shown in Figure 6.14 (a), (b), (c), (d) and (e), respectively. The relative abundance (mol-%) of the phases present as well as the average crystallite sizes (nm) are given in Table 6.1. The H_2 activated γ-Fe_2O_3, showed diffraction peaks corresponding to Fe_3O_4 and α-Fe, with normalized relative abundances of 77 and 23 mol-%, respectively. The iron phases present after the H_2 activation of α-Fe_2O_3 were α-Fe_2O_3, Fe_3O_4, FeO and α-Fe with relative abundances of 58, 18, 20 and 4 mol-%, respectively. The presence of the starting material (α-Fe_2O_3) and the low α-Fe

content clearly shows the difficulty in the reducibility of α-Fe_2O_3 which may be attributed to the large crystallite size. These results are in accordance with the results observed in H_2 *in-situ* XRD as well as the H_2-TPR analysis. The H_2 activated $CuFe_2O_4$ showed diffraction peaks corresponding to Fe_3O_4, α-Fe and Cu. The normalized relative abundances of Fe_3O_4, α-Fe and Cu were 30, 42 and 28 mol-%, respectively. The present phases Fe_3O_4, α-Fe and Cu showed average crystallite sizes of 23, 23 and 15 nm, respectively. The diffraction peaks observed after H_2 activation of $CuFeO_2$ corresponded to Fe_3O_4, α-Fe and Cu with relative abundance of 2, 50 and 48 mol-%, respectively. The average crystallite size of Fe_3O_4, α-Fe and Cu were 12, 21 and 20 nm, respectively. The high α-Fe content obtained in the H_2 activated copper incorporated iron oxide systems as compared to α-Fe_2O_3 confirmed the ease of reduction of the iron oxide in the presence of copper, as reported by de Smit [66].

The XRD pattern of the activated $AgFeO_2$ showed diffraction peaks corresponding to Fe_3O_4, α-Fe and Ag. The normalized relative abundance of Fe_3O_4, α-Fe and Ag were 12, 54 and 34 mol-%, respectively. The average crystallite sizes of Fe_3O_4, α-Fe and Ag, were 23, 18 and 11 nm, respectively. The relative abundance of Ag was less than the expected theoretical value. The deviance in the experimental value versus the theoretical value may be attributed to the instrumental (XRD) average crystallite size limitations as observed in the copper incorporated iron oxide systems. Comparison of the α-Fe content in the H_2 activated $AgFeO_2$ and γ-Fe_2O_3, showed that the presence of silver resulted in a higher α-Fe content, confirming that the presence of Ag assists in the reduction of iron oxide; hence Ag acts as a reduction promoter during H_2 activation. Furthermore, the average crystallite size of α-Fe was smaller for the promoted iron catalysts as compared to the un-promoted iron catalysts, as shown in Table 6.1, suggesting that the presence of a promoter reduces the average crystallite size of α-Fe. Similar results have shown that the presence of copper increases the rate of reduction of the iron oxide component in iron-based catalyst, thus leads to smaller crystallite sizes [27,44].

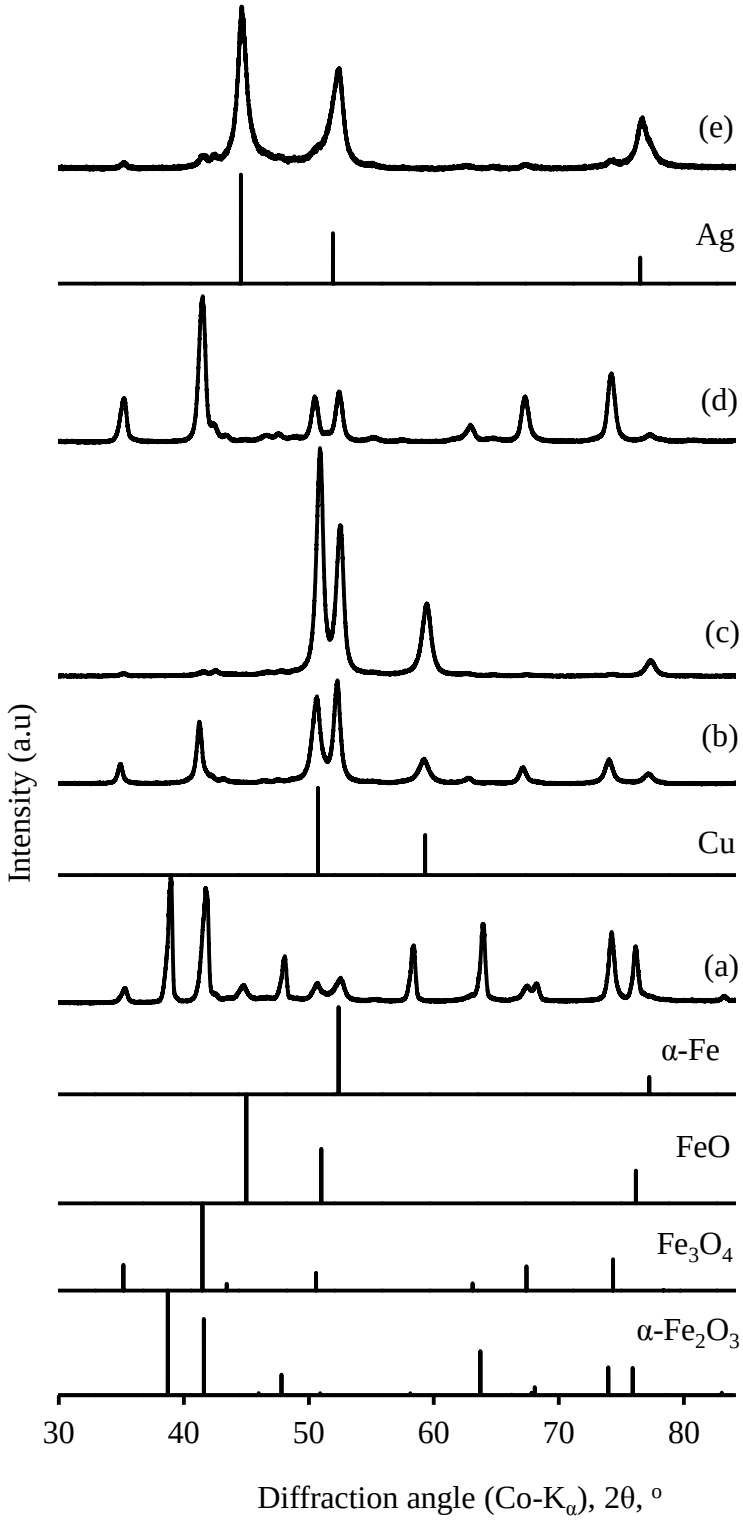

Figure 6.14: XRD pattern of the samples after *ex-situ* H_2 activation at 270 ^oC for 16 hrs: (a) α-Fe_2O_3 (b) $CuFe_2O_4$, (c) $CuFeO_2$ (d) γ-Fe_2O_3 and (e) $AgFeO_2$

Table 6.1: Physio-chemical characteristics of the wax embedded model catalyst after activation in H_2 at 270 ^oC for 16 hrs in a slurry reactor

Sample		**γ-Fe_2O_3**	**α-Fe_2O_3**	**$CuFe_2O_4$**	**$CuFeO_2$**	**$AgFeO_2$**
Phases[a]	Fe_2O_3		58 (86)			
	Fe_3O_4	77 (39)	18 (32)	30 (23)	2 (12)	12 (23)
	FeO		20 (5)			
	α-Fe	23 (32)	4 (67)	42 (23)	50 (21)	54 (18)
	Cu/Ag			28 (15)	48 (20)	34 (11)
Fe/Me[b]**, mol/mol**				2.50	1.08	1.93

where: Me = Cu or Ag

[a] phase composition in mol-% Me (in brackets the average crystallite size in nm) as determined using using Rietveld refinement of XRD-pattern;

[b] molar ratio of copper in the metal phase relative to iron in the detected iron phases as determined using Rietveld refinement of XRD-pattern.

6.4.1.2. Mössbauer absorption spectroscopy (MAS)

The Mössbauer absorption spectra of H_2 activated γ-Fe_2O_3, α-Fe_2O_3, $CuFe_2O_4$, $CuFeO_2$ and $AgFeO_2$ are shown in Figure 6.15, 6.16, 6.17 (a) and (b) and 6.18, respectively. The MAS hyperfine parameters of all model catalysts are given in Table 6.2 and 6.3, with **δ** – isomer shift, Δ - quadrupole splitting, $\boldsymbol{ß_{hf}}$ – hyperfine induction, **A** – relative area.

The MAS spectrum of the H_2 activated γ-Fe_2O_3 (Figure 6.15) was fitted with three sextets superimposed to a quadrupole doublet. The hyperfine parameters corresponded to Fe_3O_4 (two sextets) and α-Fe (single sextet). The quadrupole doublet has hyperfine parameters consistent with Fe^{3+} SPM. The relative abundances of Fe_3O_4, α-Fe and Fe^{3+} SPM are 80, 18 and 2 %, respectively. Similarly, to α-Fe_2O_3 results, the MAS results of γ-Fe_2O_3 were less than those observed in the XRD results. From the observed results it can be concluded that un-promoted iron oxide tends to re-oxidise to a larger extent as compared to the promoted catalysts.

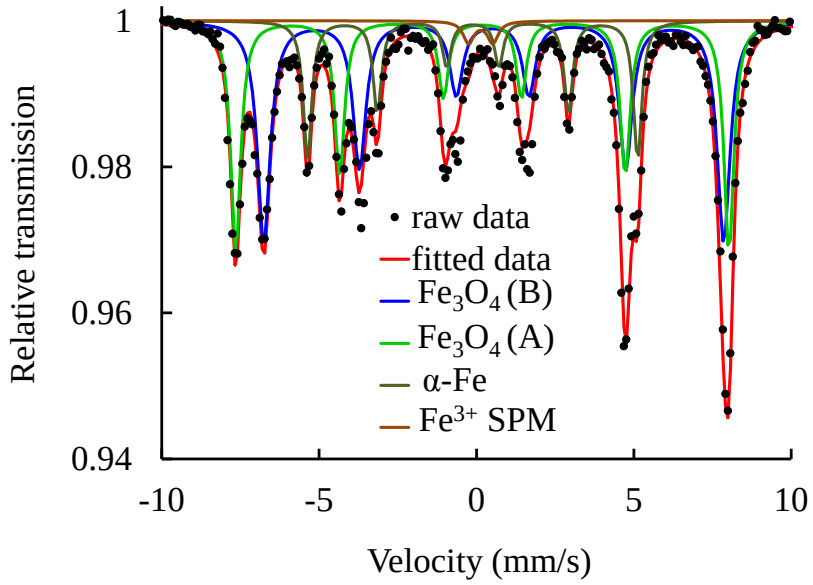

Figure 6.15: Mössbauer spectrum of γ-Fe_2O_3 (recorded at 298 K) after activation in H_2 at 270 ^oC for 16 hrs

The MAS spectrum of the H_2 activated α-Fe_2O_3 (Figure 6.16), was fitted with five sextets; with hyperfine parameters corresponding to α-Fe_2O_3 (single sextet), Fe_3O_4 (two sextets), α-Fe (single sextet) and Fe^{3+} SPM (single sextet). The two sextets observed for Fe_3O_4, arises from the inverse spinel structure of Fe_3O_4 having to different sites (A and B), the site with the large hyperfine induction corresponds to the Fe^{3+} on the tetrahedral (A) site whilst the site with a small hyperfine induction corresponds to a mixture of Fe^{3+} and Fe^{2+} on the octahedral (B) site. The proximity of the divalent and trivalent cations on the B sites frequently results in the electrons being thermally delocalised over the Fe^{2+} and Fe^{3+} cations [67]. Therefore, due to electron delocalisation, the sextets corresponding to Fe^{3+} and Fe^{2+} are not separated and appear as broad lines. The MAS parameters corresponding to the B sites are therefore intermediate between Fe^{3+} and Fe^{2+}, which is often referred to as $Fe^{2.5+}$. The relative abundances of the present phases were 52, 41, 1 and 6 %, respectively. Comparison of the present phase content determined by MAS to the XRD results showed a deviance in the relative abundances, which may be attributed to the re-oxidation of the iron oxide (FeO) to Fe_3O_4 upon exposure to air during MAS characterization.

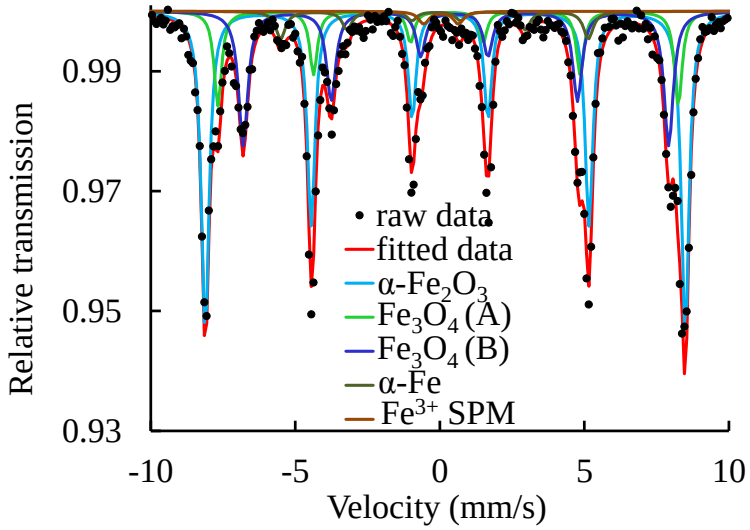

Figure 6.16: Mössbauer spectrum of α-Fe_2O_3 (recorded at 298 K) after activation in H_2 at 270 ^{o}C for 16 hrs

The MAS spectra of the H_2 activated $CuFe_2O_4$ and $CuFeO_2$ shown in Figure 6.17 (a) and (b), respectively, were fitted with three sextets and one quadrupole doublet. The hyperfine parameters of the sextets corresponded to Fe_3O_4 (two sextets), α-Fe (single sextet) and the hyperfine parameter of the quadrupole doublet corresponded to Fe^{3+} species in a superparamagnetic state (SPM), with relative abundances of 55, 42 and 3 %, respectively, for $CuFe_2O_4$ and 6, 87 and 7 %, respectively. Higher α-Fe content was observed for $CuFe_2O_4$ and $CuFeO_2$ as compared to the bulk iron oxide, in accordance with XRD results.

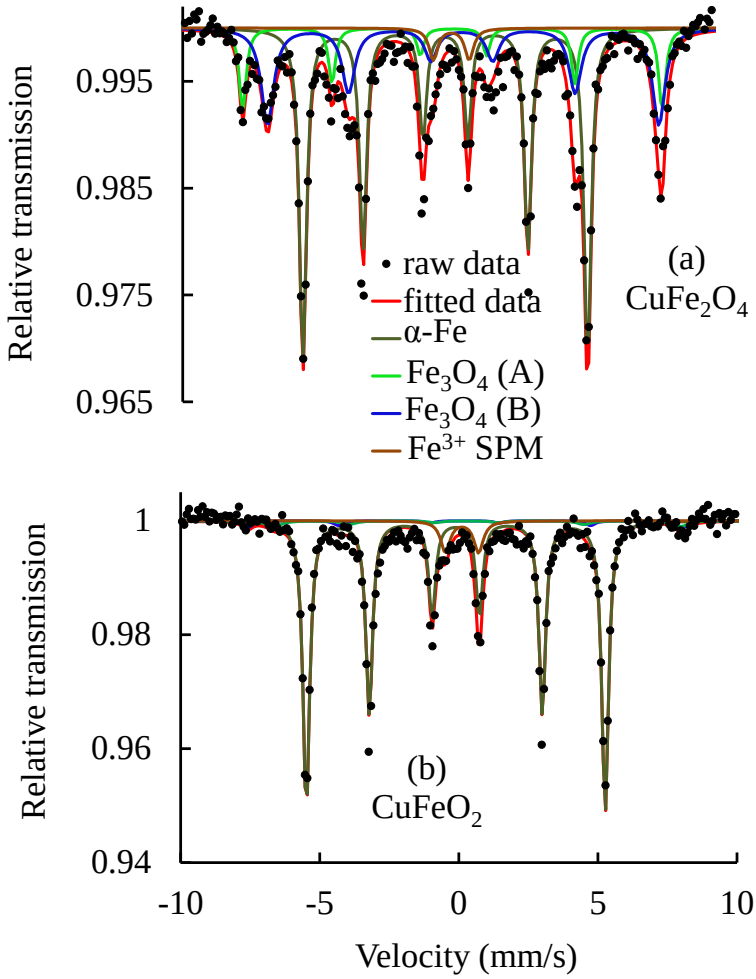

Figure 6.17: Mössbauer spectra of (a) $CuFe_2O_4$ and (b) $CuFeO_2$ after activation in H_2 at 270 ^oC for 16 hrs

The MAS spectrum of the H_2 activated $AgFeO_2$ shown in Figure 6.18 was fitted with three sextets and a quadrupole doublet. The hyperfine parameters were consistent with Fe_3O_4 (two sextets) and α-Fe (single sextet), constituting 17 and 76 %, respectively. The quadrupole doublet has hyperfine parameters consistent with Fe^{3+} SPM, constituting 7 % of the total iron content, in accordance with the XRD results, yet again, confirming less re-oxidation occurs in the presence of a promoter. Comparison of the α-Fe content obtained after H_2 activation of $AgFeO_2$ and γ-Fe_2O_3 showed a higher α-Fe content for $AgFeO_2$ (76 %) as compared to γ-Fe_2O_3 (18 %), in accordance with XRD results. Moreover, the promoted model catalysts further showed a higher content of the superparamagnetic Fe^{3+} ions than that of the bulk iron oxide model catalysts, indicating that the average crystallite sizes of the promoted model catalysts were reduced [38,68].

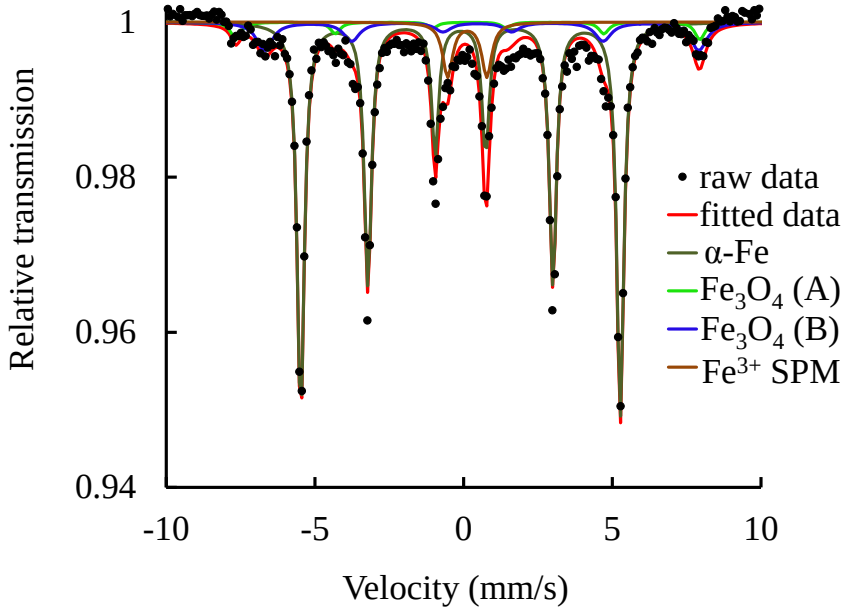

Figure 6.18: Mössbauer spectrum of $AgFeO_2$ after activation in H_2 at 270 ^oC for 16 hrs

Table 6.2: Mössbauer hyperfine parameters of model catalysts (γ-Fe_2O_3, α-Fe_2O_3 and $CuFeO_2$) after *ex-situ* H_2 activation at 270 ^oC for 16 hrs

δ – isomer shift, Δ - quadrupole splitting, $\boldsymbol{ß_{hf}}$ – hyperfine induction, **A** – relative area.

Model catalysts	**Temperature (K)**	**H_{app} (T)**	**MAS hyperfine parameters**			**Component**	**A (~2 %)**	**Phase** (after activation)
			δ (~0.02 mm/s)	**Δ (~0.02 mm/s)**	**B_{hf} (~0.2 T)**			
γ-Fe_2O_3	298	0	0.30	-0.01	48.6	sextet (A)	80	Fe_3O_4
			0.64	0.04	45.3	sextet (B)		
			0.01	-0.01	32.5	sextet	18	α-Fe
			0.25	0.77	-	doublet	2	Fe^{3+} SPM
α-Fe_2O_3	298	0	0.38	-0.17	51.5	sextet	52	α-Fe_2O_3
			0.27	0.04	49.4	sextet (A)	41	Fe_3O_4
			0.64	0.06	45.6	sextet (B)		
			0.00	-0.06	33.0	sextet	6	α-Fe
			0.15	1.20	-	doublet	1	Fe^{3+} SPM
$CuFe_2O_4$	298	0	0.29	-0.04	49.0	sextet (A)	55	Fe_3O_4
			0.65	0.05	45.7	sextet (B)		
			0.00	0.01	33.2	sextet	42	α-Fe
			0.22	1.35	-	doublet	3	Fe^{3+} SPM

Table 6.3: Mössbauer hyperfine parameters of model catalysts ($CuFeO_2$ and $AgFeO_2$) after *ex-situ* H_2 activation at 270 ^oC for 16 hrs

δ – isomer shift, Δ - quadrupole splitting, $\boldsymbol{ß_{hf}}$ – hyperfine induction, **A** – relative area.

Model catalysts	**Temperature (K)**	**H_{app} (T)**	**MAS hyperfine parameters**			**Component**	**A (~2 %)**	**Phase** (after activation)
			δ (~0.02 mm/s)	**Δ (~0.02 mm/s)**	**B_{hf} (~0.2 T)**			
$CuFeO_2$	298	0	0.33	0.02	48.5	sextet (A)	6	Fe_3O_4
			0.60	0.04	45.3	sextet (B)		
			0.06	0.00	33.3	sextet	87	α-Fe
			0.23	1.19	-	doublet	7	Fe^{3+} SPM
$AgFeO_2$	298	0	0.33	0.02	48.5	sextet (A)	17	Fe_3O_4
			0.60	0.04	45.3	sextet (B)		
			0.06	0.00	33.3	sextet	76	α-Fe
			0.23	1.19	-	doublet	7	Fe^{3+} SPM

6.4.2. CO activation studies

6.4.2.1. X-ray diffraction (XRD)

The XRD patterns of the CO activated γ-Fe_2O_3, α-Fe_2O_3, $CuFe_2O_4$, $CuFeO_2$ and $AgFeO_2$ are shown in Figure 6.19 (a), (b), (c), (d) and (e), respectively. The relative abundances of the phases present as well as the average crystallite sizes post CO activation are given in Table 6.4. The XRD pattern of γ-Fe_2O_3 after CO activation showed diffraction peaks corresponding to Fe_3O_4, FeO, χ-Fe_5C_2, θ-Fe_3C and ɛ́-$Fe_{2.2}C$/ε-Fe_2C (Figure 6.19 (a)), with relative abundances of 48, 12, 31, 8 and 1 mol-%, respectively. The observed average crystallite sizes of Fe_3O_4, FeO, χ-Fe_5C_2, θ-Fe_3C and ɛ́-$Fe_{2.2}C$/ε-Fe_2C were 25, 12, 9, 25 and 25 nm, respectively. The presence of FeO phase suggests that the reduction process may also occur via FeO to the iron carbide phases. Similar type of reduction mechanism was also reported by de Smit [66], in which they attributed their findings to the presence of the small crystallite sizes in the starting material. It is very difficult to distinguish between ε-Fe_2C and ɛ́-$Fe_{2.2}C$ using XRD, since the diffraction peaks of ε-Fe_2C and ɛ́-$Fe_{2.2}C$ are observed at very similar angles [69,70], therefore, the term ε-carbide will be used in reference to ɛ́-$Fe_{2.2}C$/ε-Fe_2C.

The XRD pattern of the CO activated α-Fe_2O_3 (Figure 6.19 (b)), showed diffraction peaks corresponding to Fe_3O_4 and χ-Fe_5C_2 constituting 75 and 25 mol-%, respectively. The average crystallite of Fe_3O_4 and χ-Fe_5C_2 was 38 and 10 nm, respectively. Figure 6.19 (c) shows the XRD pattern of the CO activated $CuFe_2O_4$ with diffraction peaks corresponding to Fe_3O_4, Fe_5C_2, θ-Fe_3C, ε-carbide and Cu. The normalized relative abundances of the iron containing species (Fe_3O_4, χ-Fe_5C_2, θ-Fe_3C and ε-carbide) were 49, 23, 7 and 1 mol-%, respectively. The observed average crystallite sizes were 20, 7, 15 and 16 nm for Fe_3O_4, χ-Fe_5C_2, θ-Fe_3C and ε-carbide, respectively. The relative abundance of Cu was 19 mol-%, with an average crystallite size of 12 nm. While, the XRD pattern of the CO activated $CuFeO_2$ revealed diffraction peaks corresponding Fe_3O_4, χ-Fe_5C_2, ε-carbide and Cu. The normalized relative abundances of Fe_3O_4, χ-Fe_5C_2 and ε-carbide were 17, 40 and 1 mol-%, respectively. The observed iron containing phases Fe_3O_4, χ-Fe_5C_2 and ε-carbide showed average crystallite sizes of 14, 6 and 15 nm, respectively. Metallic copper (Cu) constituted 42 mol-% and an average crystallite size of 11 nm. The copper incorporated iron oxide systems showed higher total Fe_xC content as compared to α-Fe_2O_3, confirming that the presence of copper assists in the reduction of the iron oxide during CO activation, in accordance with previous results reported by Hayakawa et al. [71], which showed that the presence of copper in the iron-based catalysts enhanced the formation of

iron carbide. Furthermore, $CuFe_2O_4$ and $CuFeO_2$ showed Cu content less than the expected theoretical value. The deviance in the experimental value versus the theoretical value may be attributed to the instrumental (XRD) average crystallite size limitations. Small crystallite sizes are not detectable using the XRD, the average crystallite size as determined by Topas Rietveld refinement was 12 and 11 nm, respectively. Diffraction peaks corresponding to Fe_3O_4, χ-Fe_5C_2, θ-Fe_3C, ε-carbide and Ag were observed in the XRD pattern of the CO activated $AgFeO_2$ (Figure 6.19 (e)). The normalized relative abundances of the iron containing phases Fe_3O_4, χ-Fe_5C_2, θ-Fe_3C, ε-carbide were 4, 59, 8 and 2 mol-%, respectively. The relative abundance as well as the average crystallite size of Ag was 27 mol-% and 13 nm, respectively. The silver incorporated iron oxide ($AgFeO_2$) showed higher iron carbide content as compared to γ-Fe_2O_3. This result clearly show that in the presence of silver a facile reductive decomposition of $AgFeO_2$ to Ag and Fe_3O_4 is observed as compared to the decomposition of γ-Fe_2O_3 to Fe_3O_4. This is indicative of the effect/role of the promoter during the activation. It can be postulated that the higher iron carbide formation is as a consequence of the facile first reduction step process ($AgFeO_2$ to Ag and Fe_3O_4). The silver content was less than the expected theoretical value which may be attributed to the instrumental limitations, as observed in the copper incorporated iron oxide systems.

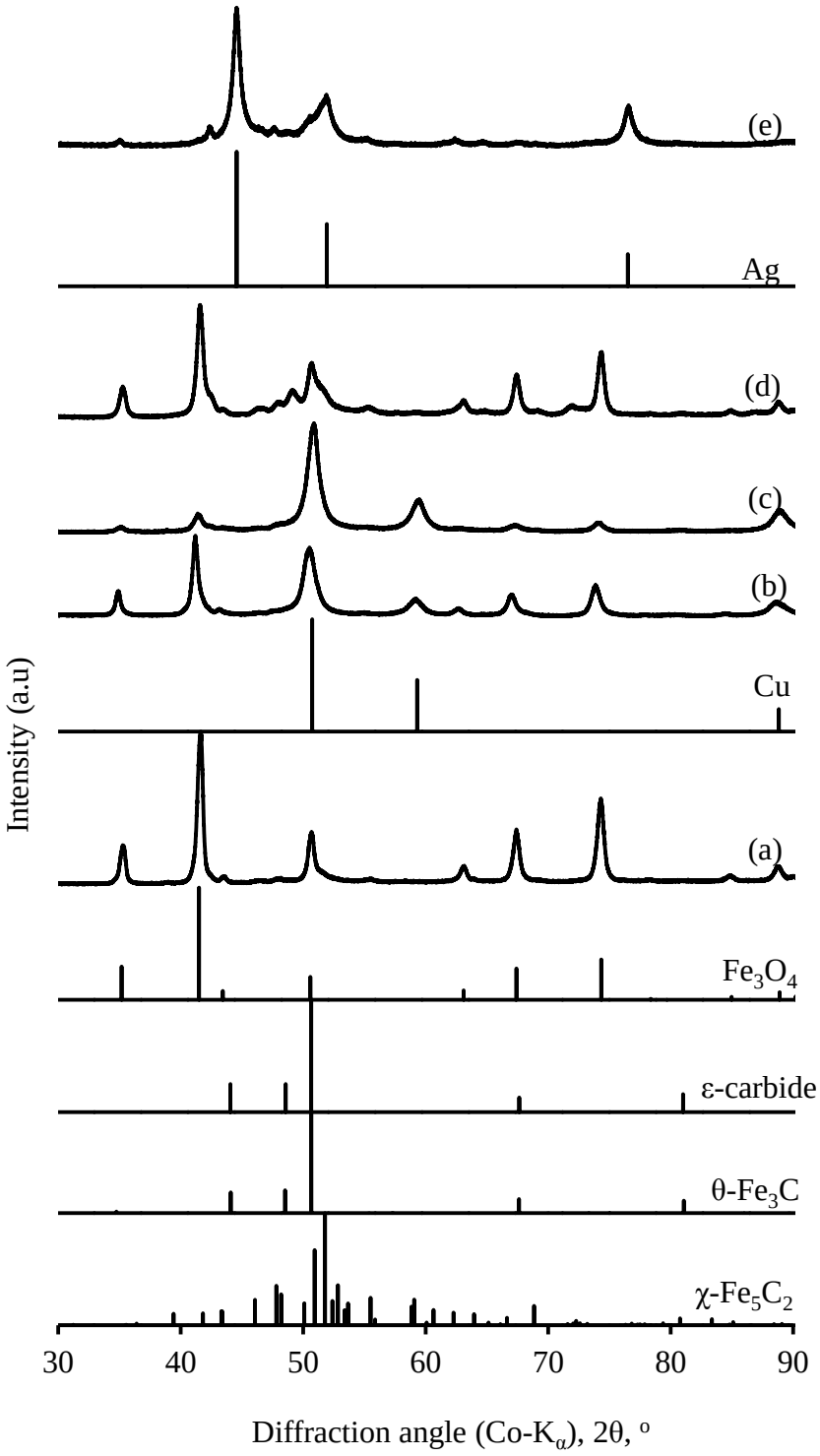

Figure 6.19: XRD pattern of the samples after *ex-situ* CO activation at 270 ^{o}C for 16 hrs: (a) α-Fe_2O_3, (b) $CuFe_2O_4$, (c) $CuFeO_2$ (d) γ-Fe_2O_3 and (e) $AgFeO_2$

Table 6.4: Physio-chemical characteristics of the wax embedded model catalyst after activation in CO at 270 ^{o}C for 16 hrs in a slurry reactor

Sample		**γ-Fe_2O_3**	**α-Fe_2O_3**	**$CuFe_2O_4$**	**$CuFeO_2$**	**$AgFeO_2$**
Phases[a]	Fe_3O_4	48 (25)	75 (38)	49 (20)	17 (14)	4 (35)
	FeO	12 (14)				
	χ-Fe_5C_2	31 (9)	25 (10)	23 (7)	40 (6)	59 (8)
	θ-Fe_3C	8 (25)		7 (15)	1 (15)	8 (22)
	ε-carbide	1 (25)		1 (16)		2 (12)
	Cu/Ag			19 (12)	42 (11)	27 (13)
Fe/Me[b]**, mol/mol**				4.20	1.39	2.64

where: Me = Cu or Ag

[a] phase composition in mol-% Me (in brackets the average crystallite size in nm) as determined using using Rietveld refinement of XRD-pattern;

[b] molar ratio of copper in the metal phase relative to iron in the detected iron phases as determined using Rietveld refinement of XRD-pattern;

6.4.2.2. Mössbauer absorption spectroscopy (MAS)

The Mössbauer absorption spectra of the CO activated γ-Fe_2O_3, α-Fe_2O_3, $CuFe_2O_4$, $CuFeO_2$ and $AgFeO_2$ are shown in Figure 6.20, 6.21, 6.22, 6.23, 6.24 and 6.25, respectively. The hyperfine parameters of the model catalysts are given in Table 6.5 and 6.6, with **δ** – isomer shift, Δ - quadrupole splitting, $\boldsymbol{ß_{hf}}$ – hyperfine induction, **A** – relative area. Figure 6.20 shows the MAS spectrum of the CO activated γ-Fe_2O_3, which revealed seven sextets superimposed to two quadrupole doublets. The hyperfine parameters corresponded to Fe_3O_4 (two sextets), χ-Fe_5C_2 (three sextets), θ-Fe_3C (single sextet) and ε-$Fe_{2.2}C$ (single sextet), with relative abundances of 54, 32, 5 and 2 %, respectively. One of the quadrupole doublets was ascribed to Fe carbide in a SPM state, while the other doublet was ascribed to FeO, with relative abundances of 2 and 5 %, respectively.

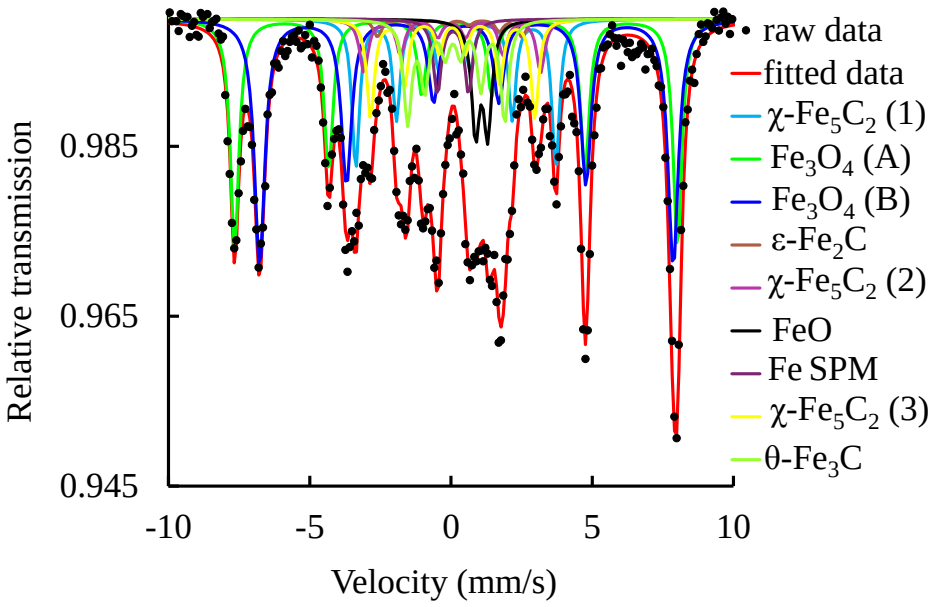

Figure 6.20: Mössbauer spectrum of γ-Fe_2O_3 (recorded at 298 K) after CO activation at 270 ^{o}C for 16 hrs

The MAS spectrum of the CO activated α-Fe_2O_3 was fitted with five sextets is shown in Figure 6.21; the hyperfine parameters corresponded to Fe_3O_4 (two sextets) and χ-Fe_5C_2 (three sextets) with relative abundances of 76 and 24 %, respectively.

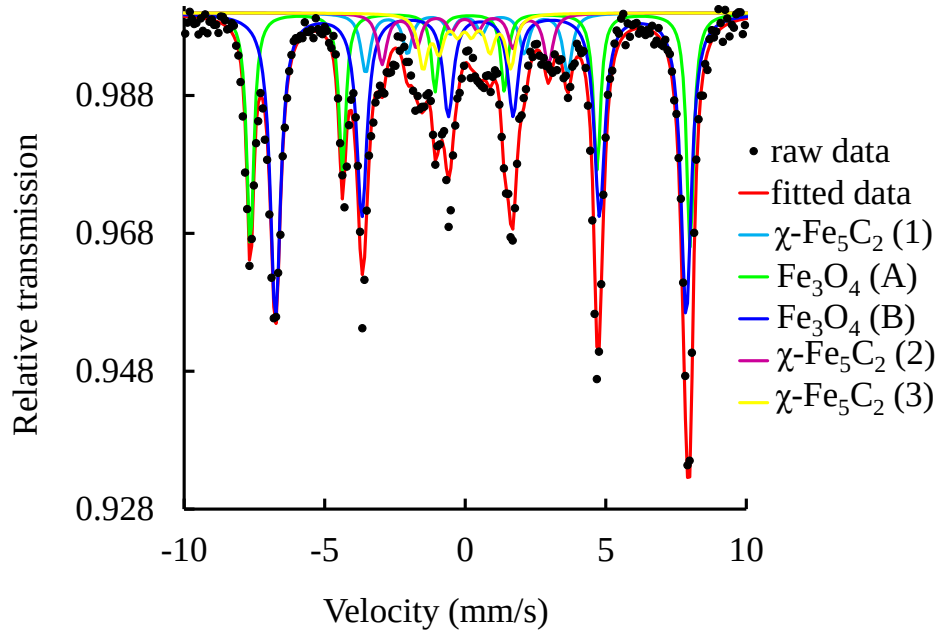

Figure 6.21: Mössbauer spectra of α-Fe_2O_3 (recorded at 298 K) after CO activation at 270 ^{o}C for 16 hrs

Figure 6.22 (a), shows the MAS spectrum of the CO activated $CuFe_2O_4$ fitted with eight sub-spectra: seven sextets and a quadrupole doublet, with hyperfine parameters corresponding to Fe_3O_4 (two sextets), χ-Fe_5C_2 (three sextets), θ-Fe_3C (single sextet), ε-Fe_2C (single sextet) and Fe^{3+} SPM. The relative abundances of the present phases were 77, 14, 5, 2 and 2 %, respectively. While the MAS spectrum of the CO activated $CuFeO_2$ (Figure 6.22 (b)) was fitted with six sextets and one quadrupole doublet, the hyperfine parameters were consistent with Fe_3O_4 (two sextets), χ-Fe_5C_2 (three sextets) and έ-$Fe_{2.2}C$ (single sextet), with relative abundance of 34, 48 and 14 %, respectively. The quadrupole doublet was ascribed to Fe carbide SPM species yielding 4 % of the total iron carbide content.

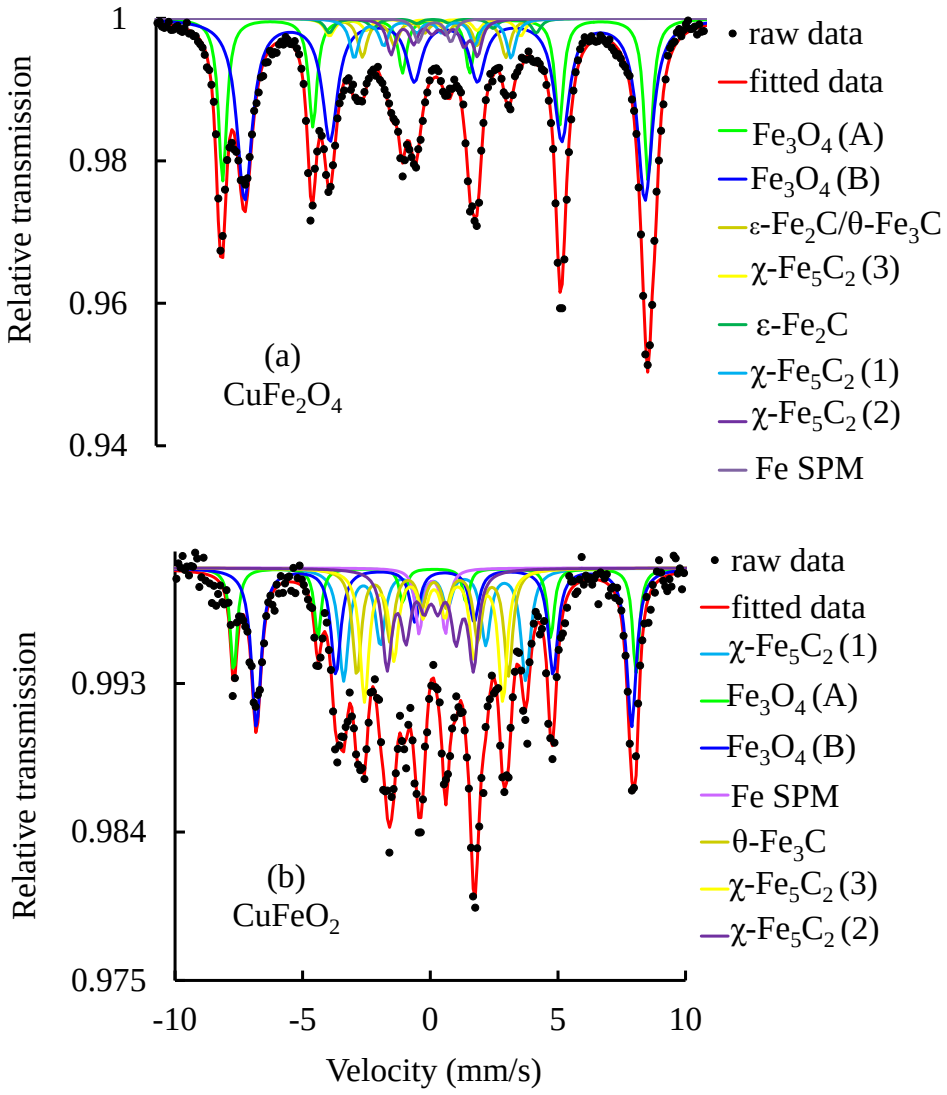

Figure 6.22: Mössbauer spectra of (a) $CuFe_2O_4$ and (b) $CuFeO_2$ (recorded at 298 K) after CO activation at 270 ^oC for 16 hrs

The MAS spectrum of the CO activated $AgFeO_2$ (Figure 6.23) was fitted with seven sextets superimposed to a quadrupole doublet. The hyperfine parameters are typical of Fe_3O_4 (two sextet), χ-Fe_5C_2 (three sextet), θ-Fe_3C (single sextet) and $\acute{\varepsilon}$-$Fe_{2.2}C$ (single sextet), with relative abundances of 6, 62, 12 and 6 %, respectively. The quadrupole doublet was ascribed to Fe carbide SPM, constituting 14 % of the total iron content. The iron containing phases present after CO activation of γ-Fe_2O_3, α-Fe_2O_3, $CuFe_2O_4$, $CuFeO_2$ and $AgFe_2$ as determined using MAS were in accordance with the XRD results.

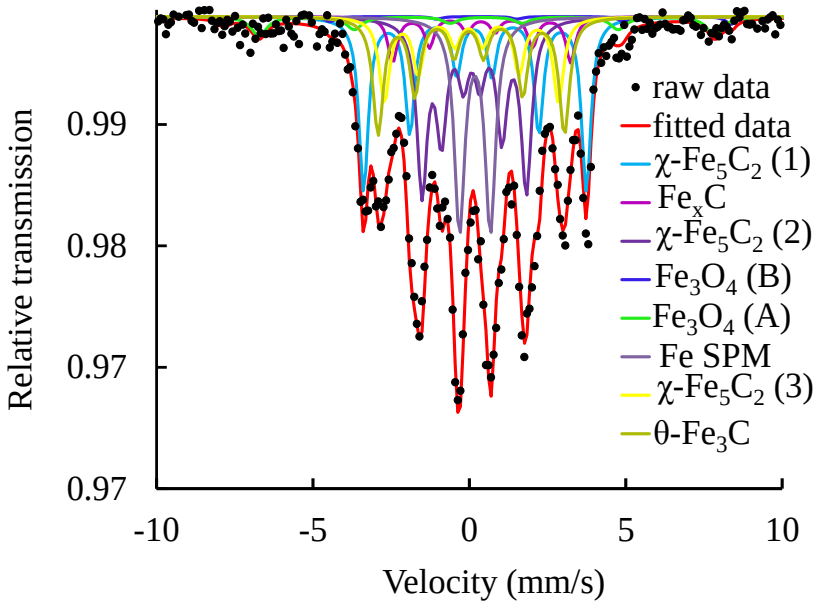

Figure 6.23: Mössbauer spectrum of $AgFeO_2$ after activation in CO at 270 ^oC for 16 hrs

Table 6.5: Mössbauer hyperfine parameters of model catalysts (γ-Fe_2O_3, α-Fe_2O_3 and $CuFe_2O_4$) after *ex-situ* CO activation at 270 ^oC for 16 hrs

δ – isomer shift, Δ - quadrupole splitting, $\boldsymbol{ß_{hf}}$ – hyperfine induction, **A** – relative area.

	Temperature (K)	**H_{app} (T)**	**MAS hyperfine parameters**			**Components**	**A (~2 %)**	**Phase** (after activation)
			δ (~0.02 mm/s)	**Δ (~0.02 mm/s)**	**B_{hf} (~2 T)**			
γ-Fe_2O_3	298	0	0.31	-0.03	48.6	sextet (A)	54	Fe_3O_4
			0.66	0.01	45.4	sextet (B)		
			0.26	0.05	22.0	sextet	32	χ-Fe_5C_2
			0.17	0.02	18	sextet		
			0.24	0.12	10.7	sextet		
			0.15	0.02	19.4	sextet	5	θ-Fe_3C
			1.19	0.43	-		5	FeO
			0.19	1.11	-	doublet	2	Fe^{3+} SPM
			0.21	-0.27	15.9	sextet	2	$\acute{\varepsilon}$-$F_{2.2}C$
α-Fe_2O_3	298	0	0.28	0.02	48.5	sextet (A)	76	Fe_3O_4
			0.67	0.00	45.3	sextet (B)		
			0.15	0.02	22.3	sextet	24	χ-Fe_5C_2
			0.10	0.02	18.3	sextet		
			0.13	0.09	9.7	sextet		
$CuFe_2O_4$	298	0	0.30	-0.02	48.0	sextet (A)	77	Fe_3O_4
			0.65	-0.04	45.2	sextet (B)		
			0.24	-0.06	21.6	sextet	14	χ-Fe_5C_2
			0.12	0.03	17.8	sextet		
			0.23	-0.12	9.8	sextet		
			0.27	-0.06	19.2	sextet	5	θ-Fe_3C
			0.19	0.02	23.4	sextet	2	ε-Fe_2C
			0.26	1.18	-	doublet	2	Fe^{3+} SPM

Table 6.6: Mössbauer hyperfine parameters of model catalysts ($CuFeO_2$ and $AgFeO_2$) after *ex-situ* CO activation at 270 ^oC for 16 hrs

δ – isomer shift, Δ - quadrupole splitting, $\boldsymbol{ß_{hf}}$ – hyperfine induction, **A** – relative area.

	Temperature (K)	**H_{app} (T)**	**MAS hyperfine parameters**			**Components**	**A (~2 %)**	**Phase** (after activation)
			δ (~0.02 mm/s)	**Δ (~0.02 mm/s)**	**B_{hf} (T)**			
$CuFeO_2$	298	0	0.28	0.02	48.9	sextet (A)	34	Fe_3O_4
			0.66	-0.02	45.6	sextet (B)		
			0.25	0.07	22.1	sextet	48	χ-Fe_5C_2
			0.23	-0.05	18.4	sextet		
			0.13	-0.03	10.5	sextet		
			0.26	-0.01	16.8	sextet	14	ε-$Fe_{2.2}C$
			0.19	1.03	-	sextet t	4	Fe^{3+} SPM
$AgFeO_2$	298	0	0.33	0.00	49.2	sextet (A)	6	Fe_3O_4
			0.65	0.05	45.5	sextet (B)		
			0.28	0.02	22.1	sextet	62	χ-Fe_5C_2
			0.20	0.02	18.5	sextet		
			0.18	0.08	10.3	sextet		
			0.14	0.02	19.2	sextet	12	θ-Fe_3C
			0.28	0.02	16.8	sextet	6	ε-$Fe_{2.2}C$
			0.27	0.99	-	doublet	14	Fe^{3+} SPM

6.5. Summary of the characterization results of the H_2 and CO activated model catalysts

6.5.1. H_2 activated model catalysts

The presence of copper and silver in the iron oxide ($CuFe_2O_4$, $CuFeO_2$ and $AgFeO_2$) showed a more facile reductive decomposition of the iron oxide as compared to the un-promoted iron catalysts (γ-Fe_2O_3 and α-Fe_2O_3) of similar crystallite sizes as observed from H_2-TPR, *in-situ* XRD as well as *ex-situ* XRD results. Copper does also promote the consecutive reduction step (magnetite to α-Fe) during H_2-activation possibly by H_2-spill-over. Moreover, both silver and copper accelerate the rate of reduction of magnetite to α-Fe.

6.5.2. CO activated model catalysts

The *in-situ* XRD results of the CO activated model catalysts showed an enhanced iron carbide formation in the presence of the promoter (copper and silver). Similar results were observed in the *ex-situ* XRD results. The carburization of magnetite in the absence of hydrogen was not facilitated by copper indicating that either CO does not spill-over or that spill-over of CO is kinetically irrelevant for the carburization process. It is thus speculated that the enhanced iron carbide formation in the presence of a promoter is ascribed to the facile reduction of the first reduction step process (reductive decomposition of the ferrite to the metal and Fe_3O_4).

References

1. Dry, M.E, in: J.R.Anderson, M. Boudart (Eds.), Catalysis-Science and Technology, Springer-Verlang, New York, 1981, pp. 59.

2. Herranz, T., Rojas, S., Pérez-Alonso, S., Ojeda, F.J., Terreros, M. Fierro, J.L.G. (2006), 'Genesis of iron carbides and their role in the synthesis of hydrocarbons from synthesis gas', *Journal of Catalysis* **243**, 199.

3. O'Brien, R.J., Xu, L.G., Spicer, R.L. and Davis, B.H. (1996), 'Activation study of precipitated iron Fischer-Tropsch catalysts', *Energy and Fuels* **10**, 921.

4. Bukur, D.B., Koranne, M., Lang, X., Rao, K.R.P.M. and Hwang, J.S. (1995), 'Pretreatment effect studies with a precipitated iron Fischer-Tropsch catalyst', *Applied Catalysis A: General* **126**, 85.

5. Kölbel, H. and Ralek, M. (1980), 'The Fischer-Tropsch Synthesis in the liquid phase', *Catalysis Reviews: Scientific Engineering* **21**, 225.

6. Bukur, D.B., Lang, X.S. and Ding, Y.J. (1999), 'Pretreatment effect studies with a precipitated iron Fischer-Tropsch catalyst in a slurry reactor', *Applied Catalysis A: General* **186**, 255.

7. Rao, K.R.P.M., Huggins, F.E., Huffman, G.P., Gormley, R.J., O'Brien, R.J. and Davis, B.H. (1996), 'Mössbauer study of iron Fischer-Tropsch catalysts during activation and synthesis', *Energy and Fuel* **10**, 546.

8. Luo, M. and Davis, B.H. (2003), 'Fischer-Tropsch synthesis : activation of low-alpha potassium promoted iron catalysts', *Fuel Processing Technology* **83**, 49.

9. Hao, Q.L., Liu, F.X, Wang, H., Chang, J., Zhang, C.H., Bai, L., Xiang, H.W., Li, Y.W., Yi, F. and Xu, B.F. (2007), 'Effect of reduction temperature on a spray-dried catalyst for slurry Fischer-Tropsch synthesis', *Journal of Molecular Catalysis A* **261**, 104.

10. Li, S., Li, A., Krishnamoorthy, S. and Iglesia, E. (2001), 'Effects of Zn, Cu, and K promoters on the structure and on the reduction, carburization, and catalytic behaviour of iron-based Fischer-Tropsch synthesis catalysts', *Catalysis Letters* **77**, 197.

11. Jin, Y. And Datye, A. (2000), 'Phase transformations in iron Fischer-Tropsch catalysts during Temperature-programmed reduction', *Journal of Catalysis* **107**, 219.

12. Anderson R B. The Fischer-Tropsch Synthesis. Orlando: Academic Press, 1984.

13. Dry M E. In: Anderson J R, Boudart M eds. Catalysis-Science and Technology. New York: Springer-Verlag, 1981, 15.

14. Bartholomew C H. Recent Developments in Fischer-Tropsch Catalysis, New Trends in CO Activation, Studies in Surface Science and Catalysis. Amsterdam: Elsevier, 1991.

15. Kölbel, H. and Ralek, M. (1980), 'The Fischer-Tropsch Synthesis in the Liquid Phase', *Catalysis Reviews-Science and Engineering* **21**, 225.

16. van der Laan, G.P. and Beenackers, A.A.C.M. (1999), 'Kinetics and Selectivity of the Fischer-Tropsch Synthesis: A Literature Review', *Catalysis Reviews-Science and Engineering* **41**, 225.

17. Rogatis, L.D. (2009), 'Methane partial oxidation on NiCu-based catalysts', *Catalysis Today* **145**, 176.

18. Wachs, I.E., Duyer, D.J. and Iglesia, E. (1984), 'Characterization of Fe, Fe-Cu and Fe-Ag Fischer-Tropsch Catalysts', *Applied Catalysis* **12**, 201.

19. Lin, H.Y., Chen, Y.W. and Li, Ch. (2003), 'The mechanism of reduction of iron oxide by hydrogen', *Thermochimica Acta* **400**, 61.

20. Munteanu, G., Ilieva, L. and Andreeva, D. (1997), 'Kinetic parameters obtained from TPR data for α-Fe_2O_3 and Auα-Fe_2O_3 systems', *Thermochimica Acta* **291**, 171.

21. Lebedeva, O. and Sachtler, W.H.M. (2000), 'Enhanced reduction of Fe_2O_3 caused by migration of TM ions out of Zeolite Channels', *Journal of Catalysis* **191**, 364.

22. Baranski, A., Lagan, J.M., Pattek, A. and Reizer, A. (1982), 'The simultaneous effect of promoters and water on the reduction of an iron catalyst for ammonia synthesis', *Applied Catalysis* **3**, 207.

23. Unmuth, E.E., Schwartz, L.H. and Butt, J.B. (1980), 'Iron alloy Fischer-Tropsch catalysts: I: Carburization studies of the Fe-Ni system', *Journal of Catalysis* **63**, 404.

24. Slagtern, A., Swaan, H.M., Olsbye, U., Dahl, I.M. and Mirodatos, C. (1998), 'Catalytic partial oxidation of methane over Ni-, Co-, and Fe-based catalysts', *Catalysis Today* **46**, 107.

25. Chen, K. and Yan, Q. (1997), 'CO hydrogenation over zircornia supported iron catalysts promoted with rare earth oxides', *Applied Catalysis A: General* **158**, 215.

26. Hexana, W.M., A systematic study of the effect of chemical promoters on the precipitated Fe-based Fischer-Tropsch synthesis catalyst, PhD Thesis, University of the Witwatersrand, Johannesburg, 2009.

27. Cairns,P., Oxygenates in Iron Fischer-Tropsch Synthesis: is Copper a selectivity promoter?, PhD Thesis, University of Cape Town, Cape Town, 2008.

28. Chonco, Z.H., Lodya, L., Claeys, M. and van Steen, M. (2013), 'Copper ferrites: a model for investigating the role of copper in the dynamic iron-based Fischer-Tropsch catalyst', *Journal of Catalysis*, **308**, 363.

29. Chonco, Z.H., Ferreira, A., Lodya, L., Claeys, M. and van Steen, M. (2013), 'Ferrites - a model structure to study group 11 promoters in Fe-based Fischer-Tropsch catalysts', *Journal of Catalysis* **307**, 283.

30. Wimmers, O.J., Arnoldy, P. and Moulijn, J.A. (1986), 'Determination of the reduction mechanism by temperature-programmed reduction: application to small iron oxide (Fe_2O_3)

particles', *Journal of Physical Chemistry* **90**, 1331.

31. Tiernan, M.J., Barnes, P.A. and Parkes, G.M.B. (2001), 'Reduction of iron oxide catalysts: The investigation of kinetic parameters using rate perturbation and linear heating thermoanalytical techniques', *Journal of Physical Chemistry B* **105**, 220.

32. E. de Smit, F.M.F. de Groot, R. Blune, M. Hävecker, A. Knop-Gericke, B.M. Weckhuysen (2010), 'The role of Cu on the reduction behaviour and surface properties of Fe-based Fischer-Tropsch catalysts', *Physical Chemistry Chemical Physics* **12**, 667.

33. Faungnawakij, K., Kikuchi, R., Fukunaga, T. and Eguchi, K. (2009), 'Stability enhancement in Ni-promoted Cu-Fe spinel catalysts for dimethly ether steam reforming', *Journal of Physical Chemistry Letters C* **113**, 18455.

34. Faungnawakij, K., Tanaka, Y., Shimoda, N., Fukunaga, T., Kikuchi, R. and Eguchi, K. (2007), 'Hydrogen production from dimethyl ether stream reforming over composite catalysts of copper ferrite spinel and alumina', *Applied Catalysis. B: Environmental* **74**, 144.

35. Faungnawakij, K., Kikuchi, R., Fukunaga, T. and Eguchi, K. (2008), 'Catalytic hydrogen production from dimethyl ether over $CuFe_2O_4$ spinel-based composites: Hydrogen reduction and metal dopant effects', *Catalysis Today* **138**, 157.

36. Kameoka, S., Tanabe, T. and Tsai, A. (2005), 'Spinel $CuFe_2O_4$: a precursor for copper catalyst with high thermal stability and activity', *Catalysis Letters* **100**, 89.

37. Kato, S., Fujimaki, R., Ogasawara, M., Wakabayashi, T., Nakahara, Y. and Nakata, S. (2009), 'Oxygen storage capacity of $CuMO_2$ (M = Al, Fe, Mn, Ga) with a delafossite-type structure', *Applied Catalysis B: Environmental* **89**, 183.

38. Mogorosi, R.P., Fischer, N., Claeys, M. and van Steen, E. (2012), 'Strong-metal-support interaction by molecular design: Fe-silicate interactions in Fischer-Tropsch catalysts', *Journal of Catalysis* **289**, 140.

39. Zhang, C.H., Yang, Y., Teng, B.T., Li, T.Z., Zheng, H.Y. and Xiang, H.W. (2006), 'Study of an iron-manganese Fischer-Tropsch synthesis catalyst promoted with copper', *Journal of Catalysis* **237**, 405.

40. Kock, A.J.H.M., Fortuin, H.M. and Geus, J,W. (1985), 'The reduction behavior of supported iron catalysts in hydrogen or carbon dioxide atmospheres', *Journal of Catalysis* **96**, 261.

41. Yang, Y., Xiang, H.W., Tian, L., Wang, H., Zhang, C.H. and Tao, Z.C. (2005), 'Structure and Fischer-Tropsch performance of iron-manganese catalyst incorporated with SiO_2 ', *Applied Catalysis A: General* **284**, 105.

42. Maiti, G.C., Malessa, R. and Baerns, M. (1983), 'Iron/manganese oxide catalysts for Fischer-Tropsch synthesis: Part I: structural and textural changes by calcination, reduction and synthesis', *Applied Catalysis* **5**, 151.

43. Li, S., Krisyhnamoorthy, S., Li, A., Meitzner, G.D. and Iglesia, I. (2002), 'Promoted iron-based catalysts for the Fischer-Tropsch synthesis: design, synthesis, site densities and catalytic properties', *Journal of Catalysis* **206**, 202.

44. Wan, H., Wu, B., Zhang, C., Xiang, H. and Li, Y. (2008), 'Promotional effects of Cu and K on precipitated iron-based catalysts for Fischer-Tropsch synthesis', *Journal of Molecular Catalysis A: Chemical* **283**, 33.

45. Anderson R B. The Fischer-Tropsch Synthesis. Orlando: Academic Press, 1984.

46. Bartholomew C H. Recent Developments in Fischer-Tropsch Catalysis, New Trends in CO Activation, Studies in Surface Science and Catalysis. Amsterdam: Elsevier, 1991.

47. Kölbel, H. and Ralek M. (1980), 'The Fischer-Tropsch Synthesis in the Liquid Phase', *Catalysis Reviews-Science and Engineering* **21**, 225.

48. van der Laan G.P. and Beenackers A.A.C.M. (1999), 'Kinetics and Selectivity of the

Fischer-Tropsch Synthesis: A Literature Review', *Catalysis Reviews-Science and Engineering* **41**, 225.

49. Bukur, D.B., Okabe, K., Rosynek, M.P., Li, C., Wang, D., Rao, K.R.P.M. and Huffman, G.P.(1995), 'Activation studies with a precipitated iron catalyst for Fischer-Tropsch synthesis', *Journal of Catalysis* **155**, 353.

50. Leith, L.R and Howden, M.G. (1988), 'Temperature programmed reduction of mixed iron-manganese oxide catalysts in hydrogen and carbon monoxide', *Applied Catalysis* **37**, 75.

51 . Luo, M., Handeh, H. and Davis. B.H. (2009), 'Fischer-Tropsch synthesis: Catalyst activation of low alpha iron catalyst', *Catalysis Today* **140**, 127.

52. B. H. Davis, Mario L. Occelli, Advances in Fischer-Tropsch Synthesis, Catalysts, and Catalysis, page 128

53. Emmett P.D. (Ed), Crystalline Phase and their relationship to Fischer-Tropsch Catalysis, Reinhold, New York, 1956, pp. 407.

54. Zhang, C.H., Yang, Y., Teng, B.T., Li, T.Z., Zheng, H.Y., Xiang, H.W. and Li, Y.W. (2006), 'Study of an iron-manganese Fischer-Tropsch synthesis catalyst promoted with copper', *Journal of Catalysis* **237**, 405.

55. Luo, M., O'Brien, R.J., Bao, S. and Davis, B.H. (2003), 'Fischer-Tropsch synthesis: Induction and steady state activity of high alpha potassium promoted iron catalysts', *Applied Catalysis A: General* **239**, 111.

56. Anderson, P.J. and Morgan, P.L. (1964), 'Effect of water vapour on sintering of MgO', *Transactions of the Faraday Society* **60**, 930.

57. Borgwardt. R.H. (1989), 'Calcium oxide sintering in atmosphere containing water and carbon dioxide', *Industrial Engineering Chemistry Research* **28**, 493.

58. Li, S., Ding, W., Meitzner, G.D. and Iglesia, E. (2002), 'Spectroscopic and transient kinetic studies of site requirements in rron-catalyzed Fischer−Tropsch synthesis', *Journal of Physical Chemistry B* **106**, 85.

59. Sirimanothan, N., Hamdeh, H.H., Zhang, Y. and Davis, B.H. (2002), 'Fischer-Tropsch synthesis: changes in phase and activity during use', *Catalysis Letters* **82**, 181.

60. Barth, J.V. (2000), 'Transport of adsorbate at metal surfaces: From thermal migration to hot precursors', *Surface Science Report* **40**, 75.

61. Hammer,B., Scheffler, M., Jacobsen, K.W. and J.K. Nørskov, J.K. (1994), 'Multidimensional potential energy surface for H_2 dissociation over Cu(111)', *Physical Review Letters* **73**, 1400.

62. Sun, X., Kurahashi, M., Pratt, A. and Yamauchi, Y. (2011), 'First-principles study of atomic hydrogen adsorption on Fe_3O_4 (100)', *Surface Science* **605**, 1067.

63. Greeley, J., Gokhale, A.A., Kreuser, J., Dumesic, J. A., Topsøe, H., Topsøe, N. –Y. and Mavrikakis, M. (2003), 'CO vibrational frequencies on methanol synthesis catalysts: a DFT study', *Journal Catalysis* **213**, 63.

64. Lemire, C., Meyer, R., Henrich, V.E., Shaikhutdinov, Sh. and Freund, H.-J. (2004), 'The surface structure of Fe_3O_4 (111) films as studied by CO adsorption', *Surface Science* **572**, 103.

65. Huang, W. and Ranke, W. (2006), 'Autocatalytic partial reduction of FeO(111) and Fe_3O_4 (111) films by atomic hydrogen', *Surface Science* **600**, 793.

66. de Smit., Iron-based Fischer-Tropsch Synthesis: New Insights from *in-situ* (Micro) spectroscopy, Diffraction and Theory, PhD, University of Utrecht, Nederlands, 2010.

67. Murad E. and Johnston J.H., Iron Oxides and Oxyhydroxides, in Mössbauer Spectroscopy Applied to Inorganic Chemistry. Ed. Gary J. Long, Plenum Press, New York, 1987.

68. Wan , H.J., Wu, B.S., Zhang, C.H., Teng, B.T., Tao, Z.C., Yang, Y., Zhu, Y.L., Xiang, H.W. and Li, Y.W. (2006), 'Effect of Al_2O_3/SiO_2 ratio on iron-based catalysts for Fischer-

Tropsch synthesis', *Fuel* **85**, 1371.

69. Le Caër, G., Dubois, J.M., Pijolat, M., Perrrichon, V. and Bussiére, P. (1982), 'Characterization by Moessbauer spectroscopy of iron carbides formed by Fischer-Tropsch synthesis', *Journal of Physical Chemistry* **86**, 4799.

70. Niemantsverdriet, J.W., van der Kraan, A.M., van Dijk, W.L. and van der Baan, (1980), 'Behavior of metallic iron catalysts during Fischer-Tropsch synthesis studied with Mossbauer spectroscopy, x-ray diffraction, carbon content determination, and reaction kinetic measurements', *Journal of Physical Chemistry* **84**, 3363.

71. Hayakawa, H., Tanaka, H. and Fujimoto, K. (2006), 'Studies on precipitated iron catalysts for Fischer-Tropsch synthesis', *Applied Catalysis A: General* **310**, 24.

Chapter 7

Fischer-Tropsch synthesis performance of the model catalysts

This chapter aims to provide the reader with the results observed on the promotional effect of copper and silver on iron-based catalysts during the Fischer-Tropsch synthesis. Prior to the Fischer-Tropsch synthesis the model catalysts were activated in hydrogen (H_2) and carbon monoxide (CO). Herein, the observed FTS results of the promoted iron catalysts are compared to the un-promoted iron catalysts.

7.1. Introduction

Copper has traditionally been added to the iron-based FT catalysts to enhance the rate of reduction of iron oxide [1,2,3,4]. Additionally, a number of studies have also shown an increase in the FT performance with copper promotion [5,6,7,8,9]. O'Brien et al. [10], studied the effect of copper on iron catalysts during Fischer-Tropsch synthesis, the catalysts were activated under different activation conditions (H_2, CO, H_2/CO). The results showed an increase in the activity with copper promotion irregardless of the activation gas used. Wachs et al. [11] investigated the promotional effect of copper and silver on the performance of iron catalysts during the Fischer-Tropsch synthesis. The results showed that the addition of copper and silver to the iron catalyst had no effect on the FT performance; this was ascribed to the lack of intimate contact between the iron and promoter (Cu, Ag) during the Fischer-Tropsch synthesis.

Promotion of iron catalyst with copper has been shown to affect the performance of iron-based catalysts during the Fischer-Tropsch synthesis [10] however; the reasons for the observed changes remain elusive. To this day, there is still no clear understanding as to how the presence of copper in iron-based FT catalysts may influence the performance of iron catalysts during Fischer-Tropsch synthesis. To our knowledge no other studies have been conducted on the promotional effect of silver on iron-based Fischer-Tropsch catalysts. Therefore, an understanding of the effect of copper on the iron-based FT catalysts may give an insight into the role of other metals (e.g., silver) in the same group as copper (in the periodic table) during Fischer-Tropsch synthesis.

7.2. Characterization of the spent model catalysts

7.2.1. Hydrogen (H_2) activated model catalysts

7.2.1.1. X-ray diffraction (XRD)

XRD patterns of the model catalysts activated in H_2 at 270 ^oC, thereafter, exposed to FTS conditions at 250 ^oC for 48 hrs are shown in Figure 7.1 (a) γ-Fe_2O_3 (ex), (b) α-Fe_2O_3 (ex), (c) $CuFe_2O_4$ (ex), (d) $CuFeO_2$ (ex) and (e) $AgFeO_2$ (ex). The phase(s) present, relative abundance (mol-%) and the average crystallite sizes (nm) are given in Table 7.1, which were estimated using Topas Rietveld refinement. In all the spent catalysts, the presence of either iron oxide (i.e., magnetite) and/or iron carbides were observed as expected for iron catalysts under Fischer-Tropsch synthesis conditions [12,13]. Moreover, XRD pattern of the copper- or silver-promoted iron catalysts showed XRD pattern of copper and silver present in its metallic phase. The XRD pattern of γ-Fe_2O_3 (ex) (Figure 7.1 (a)), showed diffraction peaks corresponding to magnetite (Fe_3O_4) and Hägg carbide (χ-Fe_5C_2), constituting 68 and 32 mol-%, respectively. The average crystallite sizes of Fe_3O_4, χ-Fe_5C_2 after FTS was 48 and 16 nm, respectively. Figure 7.1 (b) shows the XRD pattern of α-Fe_2O_3 (ex), with XRD diffraction peaks corresponding to Fe_3O_4 and χ-Fe_5C_2 constituting 90 and 10 mol-%, respectively. The observed average crystallite size of Fe_3O_4 and χ-Fe_5C_2 was 45 and 14 nm, respectively. The XRD pattern of the $CuFe_2O_4$ (ex) is shown in Figure 7.1 (c), with diffraction peaks corresponding to Fe_3O_4, χ-Fe_5C_2, θ-Fe_3C and Cu. The relative abundance of the phases, Fe_3O_4, χ-Fe_5C_2, θ-Fe_3C and Cu were 37, 40, 8 and 16 mol-%, respectively. The phases present, Fe_3O_4, χ-Fe_5C_2, θ-Fe_3C and Cu had average crystallite sizes 34, 10, 14 and 22 nm, respectively. Figure 7.1 (d) shows the XRD pattern of $CuFeO_2$ (ex), diffraction peaks corresponding to Fe_3O_4, χ-Fe_5C_2 and metallic Cu were observed. The normalized relative abundance of the phases was 26, 45 and 29 mol-% for Fe_3O_4, χ-Fe_5C_2 and Cu, respectively. The phases Fe_3O_4, χ-Fe_5C_2 and Cu had average crystallite sizes of 19, 9 and 18 nm, respectively. Diffraction peaks corresponding to Fe_3O_4, χ-Fe_5C_2 and Ag were observed in the XRD pattern of $AgFeO_2$ (ex) as shown in Figure 7.1 (e). The normalized relative abundance of Fe_3O_4, χ-Fe_5C_2 and Ag phases was 2, 83 and 15 mol-%, respectively. After FTS average crystallite sizes of 12, 20 and 11 nm were observed for Fe_3O_4, χ-Fe_5C_2 and Ag, respectively. The promoted iron-catalysts showed an enhanced iron carbide formation as compared to the un-promoted iron catalysts. Similar results were reported by Rao et al. [14]. Furthermore, the addition of Cu or Ag to the iron catalyst seemed to reduce the average crystallite size of the χ-Fe_5C_2 as compared to the un-promoted iron catalysts, given in Table 7.1.

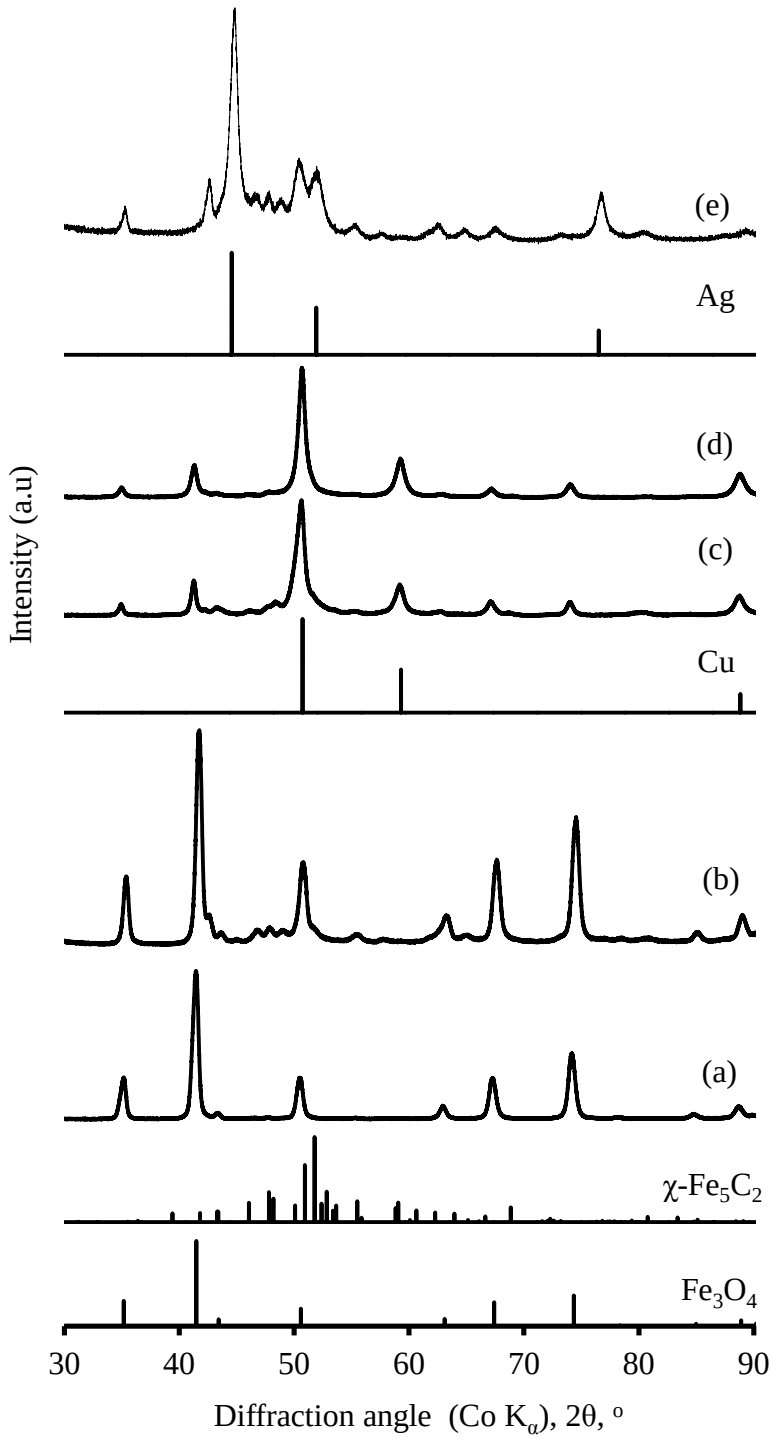

Figure 7.1: X-ray diffractograms of the samples (a) γ-Fe_2O_3 (ex), (b) α-Fe_2O_3 (ex), (c) $CuFe_2O_4$ (ex), (d) $CuFeO_2$ (ex) and (e) $AgFeO_2$ (ex) after activation in H_2 (270 ^oC for 16 hrs) and exposure to Fischer-Tropsch conditions (250 ^oC, 20 bars for 48 hrs)

Similar results were observed by Cairns [15]. They reported that although it is unclear how, it was evident that copper played a role on the resulting χ-Fe_5C_2 average crystallite size. An

oxidation study of the model catalysts was conducted by re-analysis of the spent catalysts after 10 months of storage in wax. The samples were analysed using XRD (the results are shown in Appendix B). The storage procedure leads to some oxidation. The extent of oxidation is small and not an obvious function of the copper content in the catalyst. In particular the metastable phase FeO is prone to oxidation.

Table 7.1: Physio-chemical characteristics of the model compounds after activation in H_2 (270 ^oC for 16 hrs) and exposure to Fischer-Tropsch conditions (250 ^oC, 20 bars for 48 hrs)

Sample		**γ-Fe_2O_3 (ex)**	**α-Fe_2O_3 (ex)**	**$CuFe_2O_4$ (ex)**	**$CuFeO_2$ (ex)**	**$AgFeO_2$ (ex)**
Fe/Me[a], mol/mol		-	-	2.75±0.28	1.18±0.13	1.75
Phases[b]	Fe_3O_4	68 (45)	90 (48)	30 (19)	26 (19)	2 (12)
	χ-Fe_5C_2	32 (14)	10 (16)	40 (10)	45 (9)	83 (20)
	θ-Fe_3C			8 (14)		
	Cu/Ag			16 (22)	29 (18)	15 (11)
Fe/Me[c], mol/mol				4.8	2.4	5.5

where Me = Cu or Ag

[a] Phase composition using EDX

[b] phase composition in mol-% Me (in brackets the average crystallite size in nm) as determined using using Rietveld refinement of XRD-pattern

[c] molar ratio of copper in the metal phase relative to iron in the detected iron phases as determined using Rietveld refinement of XRD-pattern.

7.2.1. Mössbauer absorption spectroscopy (MAS)

Mössbauer spectra of the H_2 activated model catalysts after the Fischer-Tropsch synthesis are shown in Figure 7.2-7.4. The MAS hyperfine parameters are given in Table 7.2 and 7.3. All the Mössbauer spectra were recorded at room temperature (298 K) and only the sample of $AgFeO_2$ (ex) was further recorded at liquid helium (4.2 K). All the activated model catalysts showed the presence of magnetite (Fe_3O_4) and iron carbide as final phases. The promoted iron catalysts further revealed an iron phase in superparamagnetic material (related to the presence of iron in small magnetic domains). Figure 7.2 (a) and (b) shows the MAS spectra of γ-Fe_2O_3 (ex) and α-Fe_2O_3 (ex), respectively. The spectra were fitted with hyperfine parameters similar to Fe_3O_4 and iron carbide (Fe_xC), constituting 80 and 20 %, respectively, for γ-Fe_2O_3 (ex) and 96 and 4 %, respectively, for α-Fe_2O_3 (ex). Due to the small quantities of the iron carbide phase present in the spent catalyst, it was difficult to obtain accurate data as which iron carbide was present,

therefore, the iron carbide is denoted as Fe_xC. The relative abundance of the phases present is in agreement with the XRD results (XRD studies discussed in section 7.2.1.1).

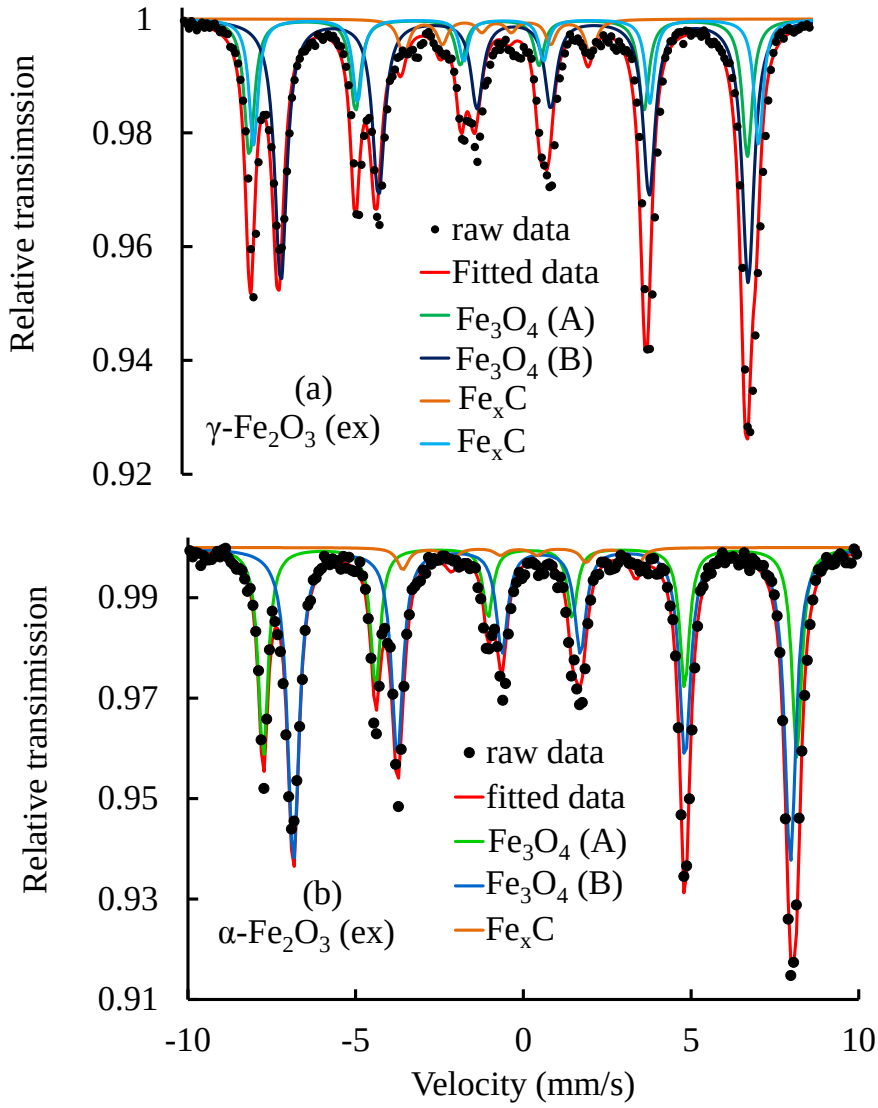

Figure 7.2: Mössbauer spectra of γ-Fe_2O_3 (ex) and α-Fe_2O_3 (ex) after activation in H_2 (270 ^oC for 16 hrs) and exposure to Fischer-Tropsch conditions (250 ^oC, 20 bars for 48 hrs)

The MAS spectra of the copper promoted iron catalysts ($CuFe_2O_4$ (ex) and $CuFeO_2$ (ex)) are shown in Figure 7.3 (a) and (b), respectively. The MAS spectra were fitted with five sextets and a quadrupole doublet. Two of the sextets had MAS hyperfine parameters similar to Fe_3O_4 and three of the sextets are typical of the Hägg carbide (χ-Fe_5C_2). The quadrupole doublet was attributed to Fe species in SPM state. The relative abundances of the Fe_3O_4 and χ-Fe_5C_2 phases in $CuFe_2O_4$ (ex) were 46 and 49 %, respectively, and the quadrupole doublet constituted 5 % of

the total Fe content. While, in $CuFeO_2$ (ex) the relative abundances of Fe_3O_4 and χ-Fe_5C_2 phases were 17 and 76 %, respectively, and the quadrupole doublet constituted 7 % of the total iron content. Comparison of the MAS results with the XRD results showed discrepancies which may be attributed to the presence of Fe in SPM material due to the presence of small crystallite sizes, which creates difficulties in quantifying the sample using XRD or MAS technique.

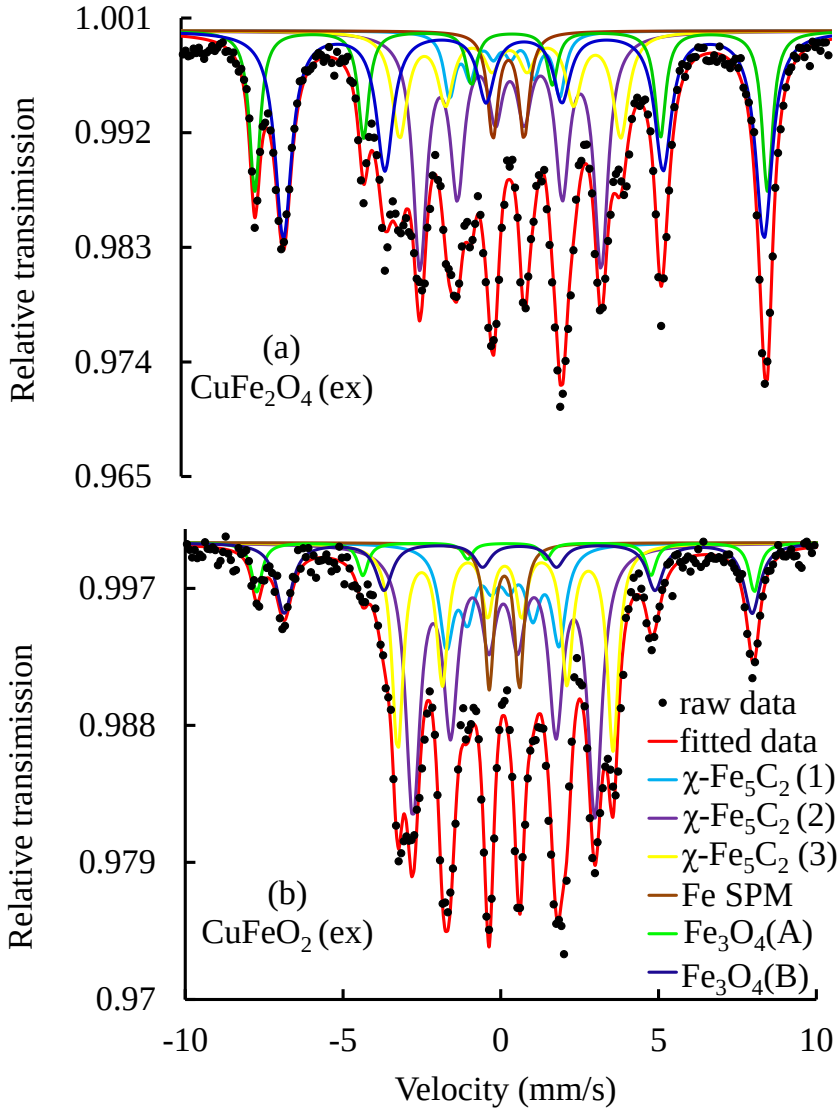

Figure 7.3: Mössbauer spectra of (a) $CuFe_2O_4$ (ex) and (b) $CuFeO_2$ (ex) after activation in H_2 (270 ^oC for 16 hrs) and exposure to Fischer-Tropsch conditions (250 ^oC, 20 bars for 48 hrs)

Figure 7.4 (a) and (b) shows the MAS spectra of $AgFeO_2$ (ex) recorded at room temperature and liquid helium, respectively. The MAS spectrum recorded at room temperature was fitted with four sextets and a quadrupole doublet. Two of the sextets had hyperfine parameters

corresponding to Fe_3O_4, while, the other two sextets had hyperfine parameters typical of χ-Fe_5C_2. The quadrupole doublet was ascribed to the Fe in SPM state. The relative abundances of the Fe_3O_4, χ-Fe_5C_2 and quadrupole doublet were 6, 69 and 26 %, respectively. H_2 activated $AgFeO_2$ was further analysed at liquid nitrogen. The MAS spectrum recorded at liquid helium showed the disappearance of the quadrupole doublet which was attributed to Fe in SPM. The MAS spectrum was fitted with five sextets; three of the sextets had hyperfine parameters similar to Fe^{3+} and Fe^{2+} in B-site and Fe^{3+} in A-site of the Fe_3O_4, while, the two sextets had hyperfine parameters typical of the χ-Fe_5C_2. The relative abundances of Fe_3O_4 and χ-Fe_5C_2 were 33 and 69 %, respectively. The disappearance of the quadrupole doublet as well as the increase in the relative abundance of Fe_3O_4 in the MAS results recorded at liquid helium suggested that the Fe in SPM state (observed in the MAS spectrum recorded at room temperature) was attributed to the presence of Fe_3O_4 in small crystallite sizes. The promoted iron catalysts showed enhanced iron carbide formation as compared to the un-promoted iron catalysts. Moreover, the promoted iron catalyst recorded at room temperature showed smaller average crystallite size of the iron carbide as compared to the un-promoted iron catalyst (confirmed by the appearance of superparamagnetic material in the promoted iron catalysts). These results corresponded well with the observed XRD results and were similar to the results previously reported by Cairns [15].

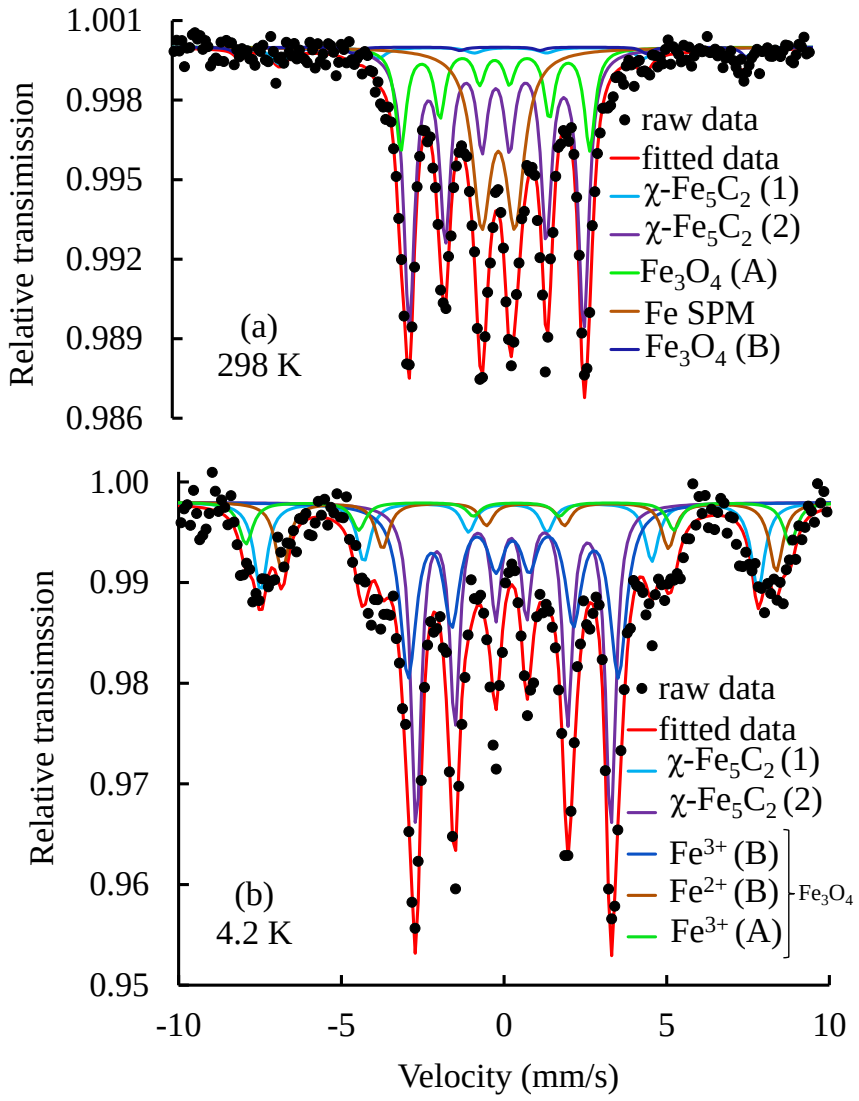

Figure 7.4: Mössbauer spectra of $AgFeO_2$ (ex) recorded at (a) 298 K and (b) 4.2 K, after activation in H_2 (270 ^oC for 16 hrs) and exposure to Fischer-Tropsch conditions (250 ^oC, 20 bars for 48 hrs)

Table 7.2: Mössbauer hyperfine parameters of γ-Fe_2O_3 (ex), α-Fe_2O_3 (ex), $CuFe_2O_4$ (ex) and $CuFeO_2$ (ex) activation in H_2 (270 ^oC for 16 hrs) and exposure to Fischer-Tropsch conditions (250 ^oC, 20 bars for 48 hrs)

δ – isomer shift, Δ - quadrupole splitting, $\boldsymbol{ß_{hf}}$ – hyperfine induction, **A** – relative area.

Model catalysts	**Temperature (K)**	**H_{app} (T)**	**MAS hyperfine parameters**			**Components**	**A (~2 %)**	**Phase**
			δ (~0.02 mm/s)	**Δ (~0.02 mm/s)**	**B_{hf} (~2 T)**			
γ-Fe_2O_3 (ex)	298	0	0.33	0.01	49.4	sextet (A)	93	Fe_3O_4
			0.66	-0.01	46.0	sextet (B)		
			0.82	0.02	17.9	sextet	7	Fe_xC
α-Fe_2O_3 (ex)	298	0	0.32	-0.04	49.3	sextet (A)	96	Fe_3O_4
			0.63	0.02	45.9	sextet (B)		
			-0.02	0.02	21.5	sextet	4	Fe_xC
$CuFe_2O_4$ (ex)	298	0	0.29	-0.25	48.9	sextet (A)	46	Fe_3O_4
			0.67	-0.99	45.9	sextet (B)		
			-0.64	0.02	10.5	sextet	49	χ-Fe_5C_2
			0.25	0.08	17.3	sextet		
			0.24	0.02	21.1	sextet		
			0.95	0.96	-	doublet	5	Fe SPM

Table 7.3: Mössbauer hyperfine parameters of $CuFeO_2$ (ex) and $AgFeO_2$ (ex) activation in H_2 (270 ^oC for 16 hrs) and exposure to Fischer-Tropsch conditions (250 ^oC, 20 bars for 48 hrs)

δ – isomer shift, Δ - quadrupole splitting, $\boldsymbol{ß_{hf}}$ – hyperfine induction, **A** – relative area.

Model catalysts	**Temperature (K)**	**H_{app}**	**MAS hyperfine parameters**			**Components**	**A (~2 %)**	**Phase**
			δ (~0.02 mm/s)	**Δ (~0.02 mm/s)**	**B_{hf} (~2 T)**			
$CuFeO_2$ (ex)	298	0	0.29	-0.04	48.9	sextet (A)	17	Fe_3O_4
			0.69	-0.05	45.9	sextet (B)		
			0.33	0.08	11.1	sextet	76	χ-Fe_5C_2
			1.01	0.02	17.9	sextet		
			0.25	0.02	21.2	sextet		
			0.23	0.95	-	doublet	7	Fe SPM
$AgFeO_2$ (ex)	298	0	0.27	-0.02	49.2	sextet (A)	6	Fe_3O_4
			0.67	-0.05	44.5	sextet (B)		
			0.25	0.02	16.9	sextet	69	χ-Fe_5C_2
			0.22	0.08	18.3	sextet		
			0.32	1.04	-	doublet	25	Fe SPM
	4.2	0	0.25	0.05	47.4	sextet (A)	33	Fe_3O_4
			0.83	0.11	47.1	sextet (B)		
			0.52	0.05	51.9	sextet		
			0.37	0.07	18.5	sextet	67	χ-Fe_5C_2
			0.39	0.02	20.0	sextet		

Moreover, comparison of the XRD results to those obtained from Mössbauer analysis shows that the XRD-analysis seems to underestimate the amount of iron present as Fe_3O_4 in the sample significantly for the model compounds $CuFeO_2$ (ex) and $AgFeO_2$ (ex), due to the large amount of superparamagnetic iron present in these samples as shown in Figure 7.5. Hence, the use of a single technique to estimate the phases present in the catalyst may lead to erroneous interpretation of the results. The samples *ex* delafossite contain large amounts of super-paramagnetic iron. Small domains of magnetite may be formed upon oxidation of nano sized crystallites of Hägg iron carbide with the product water. A thermodynamic driving force for this reaction under the conditions of the Fischer-Tropsch synthesis applied in this study is only present if small magnetite clusters are cleaved off from the carbide crystallites [16]. The sample $AgFeO_2$ (ex) contains after the Fischer-Tropsch synthesis much more superparamagnetic iron than the sample $CuFeO_2$ (ex) implying some role of the promoter element on the transformation of iron in this sample.

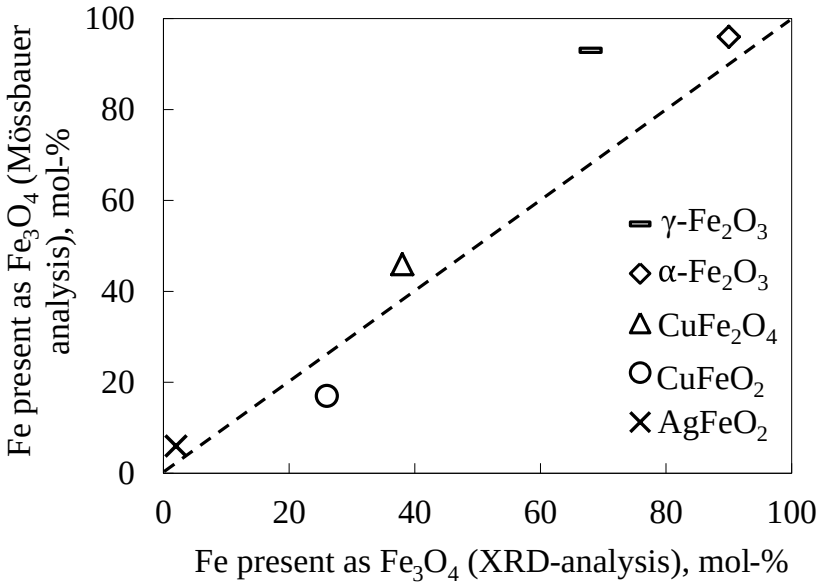

Figure 7.5: Correlating the amount of oxidic iron determined using Mössbauer absorption spectroscopy and the using XRD (amount of Fe_3O_4 as determined using mössbauer at 298 K)

7.2.2. Fischer-Tropsch synthesis (FTS) activity

The FT performance (activity and selectivity) of the model catalysts were measured in a slurry reactor. The model catalysts (5.00 g) were slowly added to 300 g of molten wax (H1-hardened Sasolwax) in the 1 dm^{-3} slurry reactor. The reaction conditions were: T = 250 ^oC, P = 20 bar, a

synthesis gas comprising of H_2 and CO with an effective partial pressure of 16.8 bar. Argon was used as an internal reference. The ratio of H_2: CO: Ar is 2.1: 1: 0.6. The FT reaction was carried out for 48 hrs. Prior to the Fischer-Tropsch synthesis the model catalysts were activated at 270 ^oC for 16 hrs in either pure H_2 or CO gas (500 ml(STP).min^{-1}). Furthermore, a control experiment was performed, in which the separate particles of CuO and α-Fe_2O_3 were loaded into the reactor to evaluate the effect of separate copper particles present during the Fischer-Tropsch synthesis. Detailed Fischer-Tropsch synthesis conditions are discussed in Chapter 4 (Section 4.5.3.2).

The FT activity is expressed as carbon conversion (sum of carbon monoxide and carbon dioxide conversions) as a function of time on stream (hr). Figure 7.6 shows the steady state carbon conversions of γ-Fe_2O_3 (ex), α-Fe_2O_3 (ex), $CuFe_2O_4$ (ex), $CuFeO_2$ (ex) and $AgFeO_2$ (ex). The FT activity was between of 5 to 30 C-%. The promoted iron catalysts showed higher activity as compared to the un-promoted iron catalysts. Similar results have previously been reported by Kölbel [17], Bukur [18] and Deckwer [19]. The observed higher activity for the promoted iron catalysts may be ascribed to the enhanced formation of the iron carbide phase, which has been reported as the possible catalytically active phase for the Fischer-Tropsch synthesis [20,21]. It is a known concept that under Fischer-Tropsch synthesis conditions the iron phase(s) may transform from one phase to the other (i.e., iron oxide (Fe_3O_4) to various iron carbides or vice versa). Van Steen et al. [22] suggested that this may occur via the oxidation of the iron carbide(s) in the presence of H_2O to form iron oxide (Fe_3O_4), which may subsequently undergo sintering in the presence H_2O, thereby resulting in large crystallites of Fe_3O_4. These large crystallites of Fe_3O_4 may further undergo reductive carburization with simultaneous crystallite break-up as shown in Scheme 7.1.

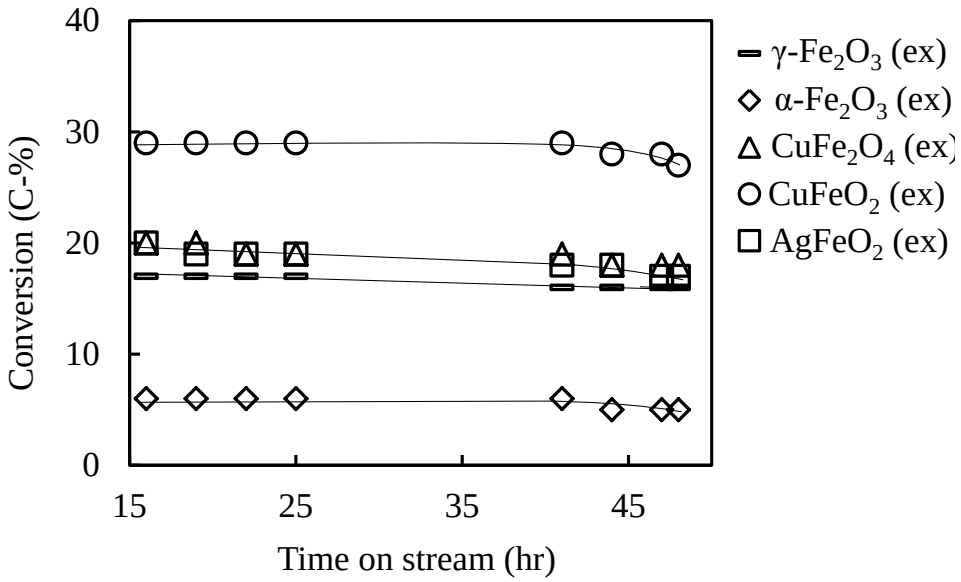

Figure 7.6: Carbon conversion of γ-Fe_2O_3 (ex), α-Fe_2O_3 (ex), $CuFe_2O_4$ (ex), $CuFeO_2$ (ex) and $AgFeO_2$ (ex) as a function of time on stream (hr) after activation in H_2 (270 ^oC, 16 hrs) and exposure to Fischer-Tropsch conditions (270 ^oC, 48 hrs)

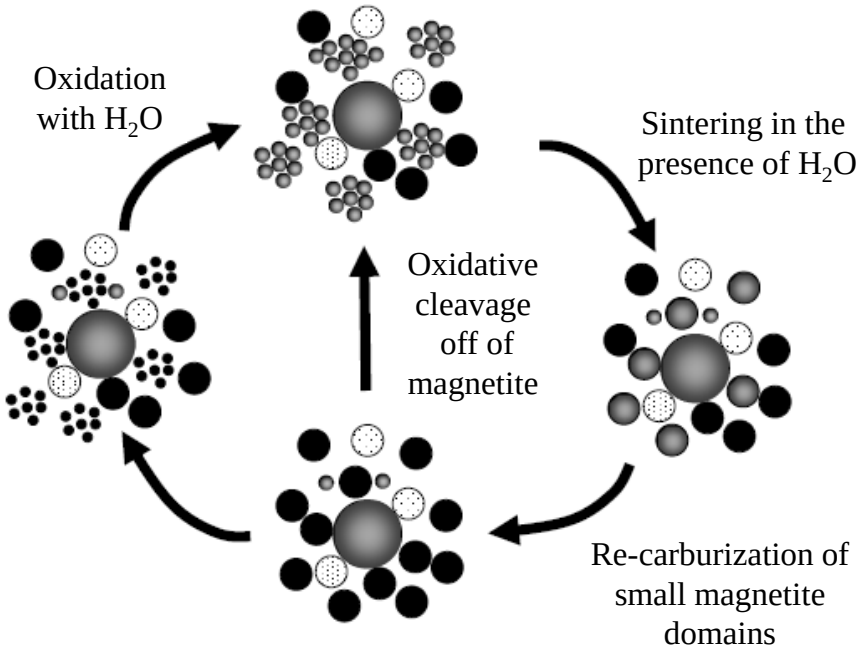

Scheme 7.1: Schematic representation of the transformations with an iron-based Fischer-Tropsch catalyst in the presence of a group 11 metal (black: iron carbide; grey: magnetite; dotted: group 11 metal).

It is suspected that the enhanced formation of iron carbide as well as smaller average crystallite sizes observed in the promoted iron catalysts as compared to the un-promoted iron catalysts may possibly be attributed to the presence of the promoter. It is, therefore, speculated that the promoter (copper or silver) in close proximity with the iron enhances the rate of the iron carbide formation in the cycle (see Scheme 7.1). Various mechanisms may contribute to an enhance carbide formation. For instance H_2-spillover to Fe_3O_4 under Fischer-Tropsch conditions may accelerate the carburization process via a partial reduction of Fe_3O_4 to α-Fe and thus resulting in enhanced carbide formation. Alternatively, the well dispersed promoter may prevent magnetite from sintering. This may lead to an enhanced rate of carburization, if the rate of carburization of magnetite is dependent on the size of magnetite. Similar results were reported by Li et al. [23], in which they suggested that the smaller active domains lead to shorter diffusion paths and to a larger number of sites for CO adsorption/dissociation in the Fischer-Tropsch synthesis.

7.2.3. Product formation

7.2.3.1. Carbon dioxide (CO_2) formation

Carbon dioxide is one of the many products formed during Fischer-Tropsch synthesis. Iron catalysts are reported to be active for CO_2-formation via the water-gas shift reaction (WGS). Carbon dioxide can be formed in the removal of adsorbed oxygen (formed by the dissociation of CO) from the catalytically active surface, carburization of the iron oxide in the catalyst and the water-gas shift activity. The latter is the typical explanation given for the origin of CO_2 in iron-based Fischer-Tropsch synthesis. In a study conducted by Estralla et al. [24], in which they studied the behaviour of similar catalysts systems as in the present study, $CuFe_2O_4$ and Cu/Fe_3O_4 catalysts, under WGS reaction conditions, using *in-situ* characterization, it was shown that at temperature below 350 ^oC, the CO_2 formed was ascribed to the partial reduction of the oxide sample by reaction with CO (the only product being CO_2). While, at temperature above 350 ^oC a simultaneous evolution of the WGS products (H_2 and CO_2) was observed. Furthermore, magnetite has been reported as the active phase for the WGS reaction [25,26,27,28,29,30]. In the present study the sample $AgFeO_2$ (ex) contains less magnetite (according to the XRD-measurement) than the sample $CuFeO_2$ (ex), but the selectivity for the conversion of CO into CO_2 is much higher. These samples further show a higher content of superparamagnetic iron representing magnetite in small domains. The rate of CO_2-formation can be reasonably correlated with the amount of superparamagnetic iron in the catalyst sample as determined by Mössbauer absorption spectroscopy at room temperature as shown in Figure 7.7.

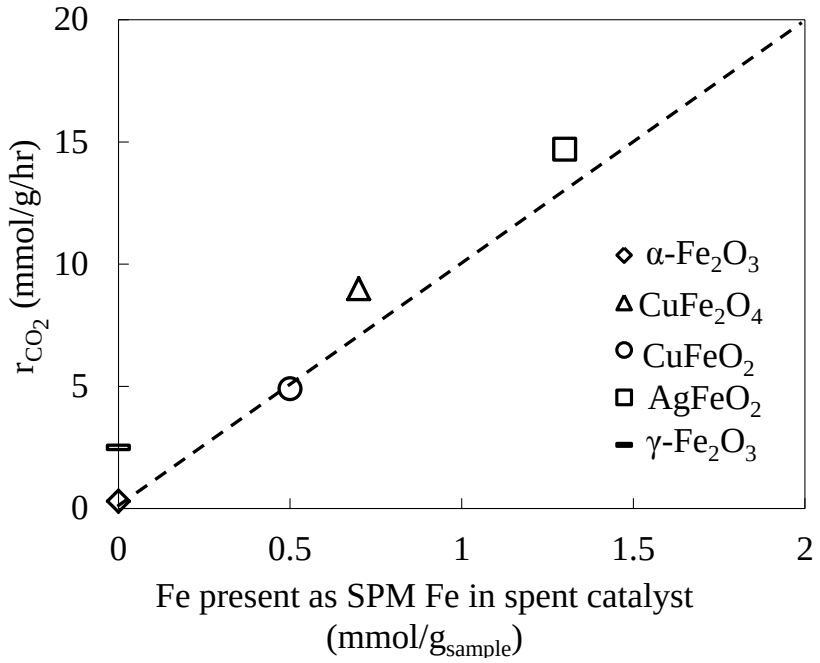

Figure 7.7: Correlating the rate of CO_2-formation in the Fischer- Tropsch synthesis with the amount of superparamagnetic iron as determined by room temperature Mössbauer absorption spectroscopy for H_2 activated model catalysts

The correlation of the rate of CO_2-formation with the amount of superparamagnetic iron implies that small domains of Fe_3O_4 are involved in the formation of CO_2. It might be argued that the surface of these crystallites catalyses the water-gas shift reaction. Based on the study by Estralla et al. [24], water gas shift activity over magnetite is not expected at the conditions employed here. Carburization of superparamagnetic iron may occur under Fischer-Tropsch conditions (as shown by the CO pretreatment of the catalyst at slightly higher temperatures), and is thought to be the main origin of CO_2-formation over the promoted catalysts.

7.2.4. Formation of organic products

7.2.4.1. Methane (CH_4) formation chain growth probability (α)

Methane is thermodynamically the most stable Fischer-Tropsch synthesis product [31], but not a desired product. Therefore, it must be kept as low as possible. Methane is formed through the associative desorption of methyl species and surface hydrogen. The methyl species can alternatively act as a chain starter and undergo chain growth (Scheme 7.2).

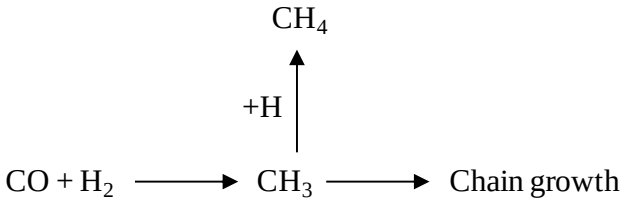

Scheme 7.2: Schematic presentation of methane formation

The methane selectivity is determined by the likelihood that the carbon containing monomer for the Fischer-Tropsch synthesis is converted into a surface methyl species and the likelihood that the surface methyl species desorbs by hydrogen addition. Hence, the methane selectivity in C-% is related to the chain growth of the FT hydrocarbon product. The obtained methane selectivities in C-% are low, as expected for iron catalysed Fischer- Tropsch synthesis. It can be noted that the methane selectivity is lower for the promoter containing catalysts (Table 7.4). These catalysts also showed a higher activity and selectivity for the formation of CO_2. The observed change in the methane selectivity might be related to the reduction of the CO partial pressure which reduces the inhibition of the Fischer-Tropsch synthesis by adsorbed CO. As outlined by van Santen et al. [32], a high coverage of the catalytically active surface with CO will yield methane. Hence reducing the surface coverage of the catalytically active surface with CO may result in a reduction in the methane selectivity if the surface coverage with CO is initially high. The methane selectivity will pass a minimum upon further lowering of the CO-coverage. The introduction of copper in the hydrogen activated model systems results in a decrease in the selectivity for light hydrocarbons (C_1-C_4) and an increase in the desired product (long chain) for the low temperature Fischer-Tropsch synthesis (C_{5+}) (see Table 7.4).

Table 7.4: Selectivities of the model catalysts after activation in H_2 (270 ^oC for 16 hrs) and exposure to Fischer-Tropsch conditions (250 ^oC, 20 bars for 48 hrs)

	γ-Fe_2O_3 (ex)	**α-Fe_2O_3 (ex)**	**Cu/α-Fe_2O_3**	**$CuFe_2O_4$ (ex)**	**$CuFeO_2$ (ex)**	**$AgFeO_2$ (ex)**
S_{CH_4}[a], C-%	4	4	4	3	2	1
$S_{C_2\text{-}C_4}$[a], C-%	9	10	11	6	5	4
S_{C5+}[a], C-%	87	86	85	92	93	95

[a] Content of the various product fractions in the fraction of organic product compounds

Similarly, to the copper, the presence of silver in close proximity of the catalytically active phase seems to enhance the formation of long chain hydrocarbons. This might be attributed to an increased surface concentration of the monomer. However, the C_{5+} selectivity cannot be linked to the re-adsorption of olefins, since the olefin content over the silver containing samples is higher than over the other model catalysts. It has been noted previously that iron-based catalysts do not re-incorporate olefins to a large extent [34]. Furthermore, a control experiment was performed, in which the separate particles of CuO and α-Fe_2O_3 were loaded into the reactor to evaluate the effect of separate copper particles present during the Fischer-Tropsch synthesis. The results observed were comparable to the un-promoted iron catalyst (α-Fe_2O_3).

7.2.5. Olefin formation

During Fischer-Tropsch synthesis the main primary organic products formed are the olefins [33]. According to the alkyl mechanism olefins, are formed via dissociative desorption of growing surface alkyl species. Alternatively, paraffin can be formed via hydrogen addition to the alkyl species. 1-olefin can further re-adsorb non-terminally to the catalyst surface and upon desorption form olefins with internal double bonds (this secondary reaction is known as the double bond shift isomerisation) or may be re-incorporated for further chain growth or get hydrogenated to the corresponding paraffin as shown in Scheme 7.3. The double bond isomerisation shift reaction is more pronounced on hydrogen rich metal surfaces. In the case of no or minimal secondary reactions, the hydrogenation of alkyl species to paraffin is strongly subdued resulting in the formation of up to 70-90 mol-% of olefins [33,34].

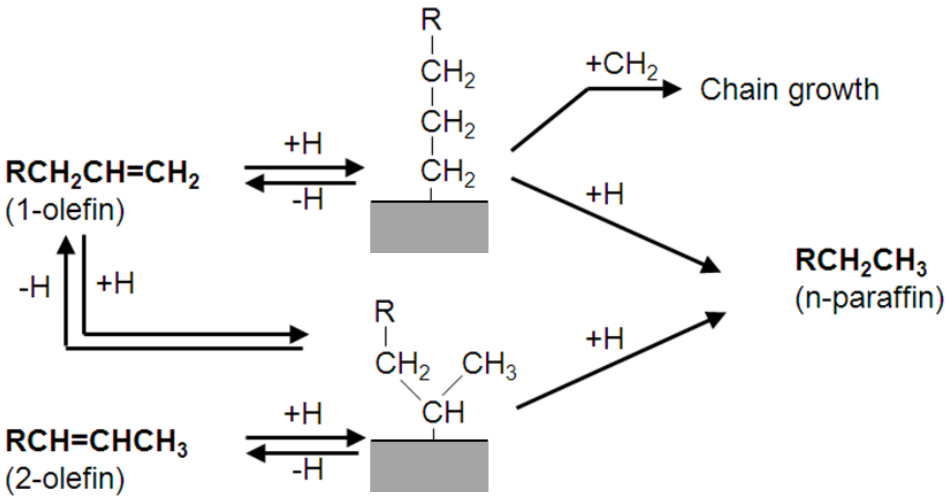

Scheme 7.3: Proposed chain termination steps in the Fischer-Tropsch synthesis, forming the primary products (α-olefins and n-paraffins) and the adsorption of 1-olefin and subsequent double bond isomerisation reaction

The extent of secondary reactions can be determined by plotting the mole fraction of olefins in the corresponding linear hydrocarbon (HCN) as a function of carbon number as shown in Figure 7.8. An increase in the olefin in linear HCN from C_2 to C_3 was observed; a maximum value was reached at C_3 and then decreased with increasing carbon number. The lower C_2 olefin content reflects preferred secondary conversion of ethene (C_2) and long chain olefin. The lower ethane (C_2) content in C_2-hydrocarbond observed for the copper promoted iron as compared to the un-promoted iron catalysts was indicative of a preferred secondary hydrogenation. The highest olefin content in the C_2 fraction was observed for the silver promoted iron catalyst, in conjunction with high 1-olefin content. This implies that secondary olefin conversion over this catalyst is limited. This might be attributed to the low activity of silver for the hydrogenation of the C=C-bond [35].

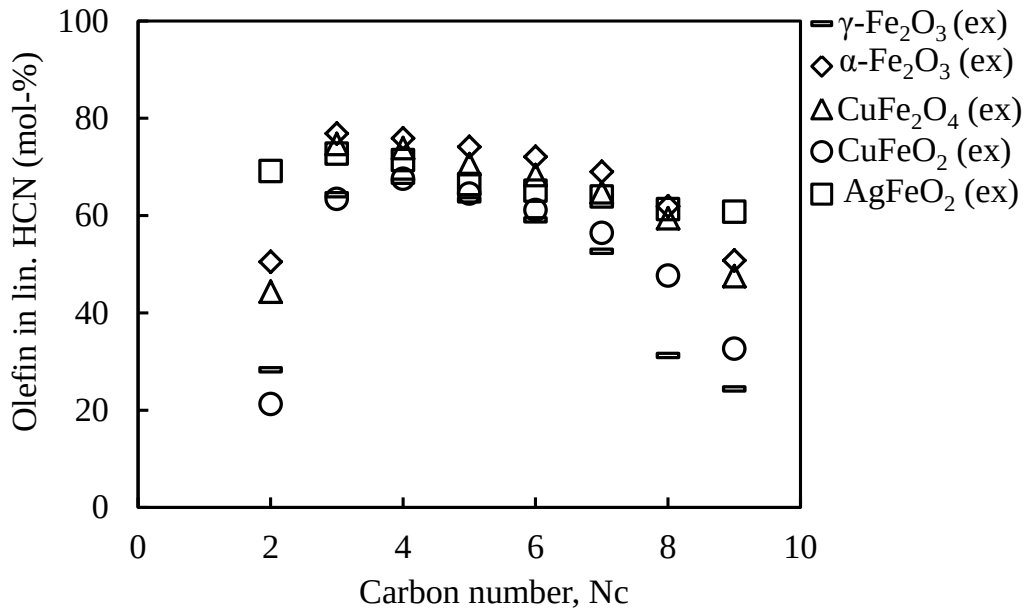

Figure 7.8: Mole fraction of olefins in linear HCNs of the model catalysts as a function of carbon number after activation in H_2 (270 ^{o}C for 16 hrs) and exposure to Fischer-Tropsch conditions (250 ^{o}C, 20 bars for 48 hrs)

The olefin content in C_5-hydrocarbon olefin was further used to investigate the olefin selectivity. The extent of the isomerization reaction (double bond shift reaction) was estimated by investigating the changes in the olefin content (of a particular carbon number) with the changes in the CO-conversion as given in Table 5. The extent of secondary reactions typically increases with increasing conversion [36]. This may possibly be ascribed to the enhancement of the catalytic activity, further enhanced by the relative enrichment of the gas atmosphere with hydrogen (due to the CO_2-formation). Moreover, the control experiment, in which CuO and α-Fe_2O_3 were added to the reactor as separate particles, showed only a marginal difference in the CO conversion in comparison with the CO conversion over the sample *ex*-hematite, which might be related to the slight difference in the conditions during the reduction process.

Table 7.5: Olefin content in C_5-HC olefin and the CO-conversion of the model catalysts after activation in H_2 (270 ^oC for 16 hrs) and exposure to Fischer-Tropsch conditions (250 ^oC, 20 bars for 48 hrs)

	γ-Fe_2O_3 (ex)	**α-Fe_2O_3 (ex)**	**Cu/α-Fe_2O_3**	**$CuFe_2O_4$ (ex)**	**$CuFeO_2$ (ex)**	**$AgFeO_2$ (ex)**
CO-conversion (%)	19	6	9	25	31	29
Olefin content in C_5-HC[a] olefin, mol-%	63	74	71	71	65	66
1-olefin content in C_5-olefin[b], mol-%	60	89	85	90	66	98

[a] Amount of olefins in the fraction of linear hydrocarbons with a particular number of carbon atoms

[b] Amount of linear 1-olefins in the fraction of linear olefins with a particular number of carbon atoms

7.2.6. Oxygenate products formation

Oxygenates constitute a small amount of the Fischer-Tropsch synthesis product. These are mainly made up of alcohols, aldehydes and ketones. The pathway for the formation of oxygenates during the Fischer-Tropsch is not well described in the literature, however, Pichler and Schulz [37] proposed that oxygenates are either formed through CO-insertion into an alkyl-metal bond. Alternatively formed through addition of an OH group to an adsorbed alkylidene species as proposed by Johnston and Joyner [38] (see Scheme 7.4).

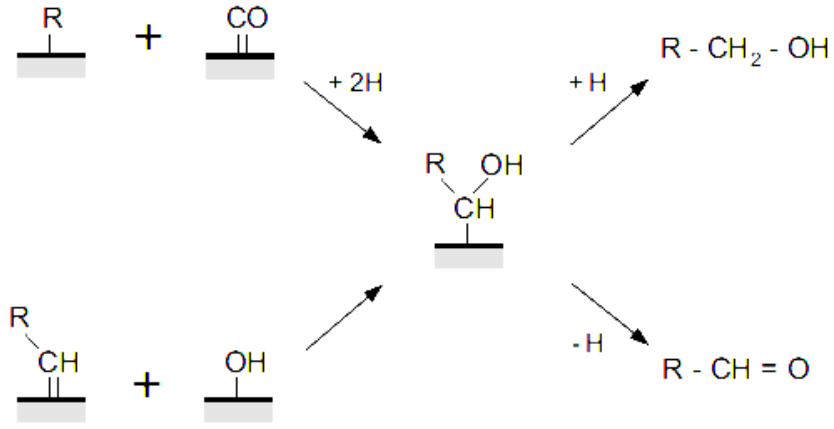

Scheme 7.4: Proposed routes of oxygenates formation

Previous studies have shown that the addition of copper to the iron catalyst enhances oxygenate formation [15,39]. However, the copper promoted iron catalysts showed similar C_5-alcohol

content results as compared to the un-promoted iron catalysts while an increase in the C_5 alcohol content was observed for the silver promoted iron catalyst as given in Table 7.6.

Table 7.6: Mole fraction of the total C_5 oxygenates in linear hydrocarbon (HCN) products after activation in H_2 (270 ^oC for 16 hrs) and exposure to Fischer-Tropsch conditions (250 ^oC, 20 bars for 48 hrs)

	γ-Fe_2O_3 (ex)	**α-Fe_2O_3 (ex)**	**$CuFe_2O_4$ (ex)**	**$CuFeO_2$ (ex)**	**$AgFeO_2$ (ex)**
C_5 oxygenates in linear C_5 product compounds, mol-%	8	8	9	6	14

7.2.7. Branched products formation

In addition to linear products, branched products are also found in small amounts in the Fischer-Tropsch synthesis products. The branched products can be formed primarily, involving the reaction of a surface alkylidine species with a surface methyl species [40,41] or by re-adsorption of α-olefins and successive chain growth [42] as shown in Scheme 7.5.

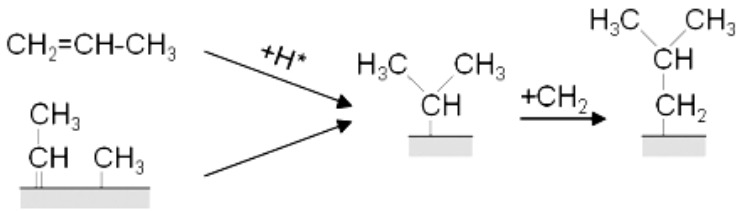

Scheme 7.5: Proposed formation routes of branched hydrocarbons

The molar ratio of methyl branched to linear hydrocarbon in the C_5 fraction is given in Table 7.7. The copper promoted iron catalyst ($CuFeO_2$ (ex)) showed lower branched product formation as compared to the un-promoted catalyst (α-Fe_2O_3 (ex)). The formation of branched product compounds is related to the relative hydrogen availability on the catalyst surface [43], with increasing hydrogen availability the primary formation of branched product compounds decreases and the secondary formation of this class of products increases.

Table 7.7: Molar ratio of iso (branched) to n (straight) compounds in the C_5 hydrocarbon fraction after activation in H_2 (270 ^oC for 16 hrs) and exposure to Fischer-Tropsch conditions (250 ^oC, 20 bars for 48 hrs)

	γ-Fe_2O_3 (ex)	**α-Fe_2O_3 (ex)**	**Cu/α-Fe_2O_3**	**$CuFe_2O_4$ (ex)**	**$CuFeO_2$ (ex)**	**$AgFeO_2$ (ex)**
iso-C_5/n-C_5, mol/mol	0.16	0.26	0.23	0.08	0.20	0.35

7.3. Characterization of the spent catalysts

7.3.1. Carbon monoxide activated catalysts

7.3.1.1. X-ray diffraction (XRD)

The XRD patterns of the model catalysts that were activated in CO at 270 ^oC, thereafter, exposed to FTS conditions (250 ^oC 20 bars, 48 hrs and H_2: CO: Ar ratio of 2: 1: 0.6) are shown in Figure 7.9 (a) γ-Fe_2O_3 (ex), (b) α-Fe_2O_3 (ex), (c) $CuFe_2O_4$ (ex), (d) $CuFeO_2$ (ex) and (e) $AgFeO_2$ (ex). The phase(s) present, relative abundance (mol-%) and average crystallite sizes (nm) are given in Table 7.8. Iron oxide (magnetite) and iron carbide were observed as the final phase(s) in all the model catalysts. The metallic copper and silver phases were further observed in the XRD pattern of the copper and silver promoted iron catalysts after the Fischer-Tropsch synthesis.

The XRD pattern of γ-Fe_2O_3 (ex) (Figure 7.9 (a)), showed XRD diffraction peaks corresponding to Fe_3O_4, FeO and χ-Fe_5C_2, constituting 72, 6 and 22 mol-%, respectively. The average crystallite sizes of the phases Fe_3O_4, FeO and χ-Fe_5C_2 were 43, 9 and 26 nm, respectively. The XRD pattern of α-Fe_2O_3 (ex) (Figure 7.9 (b)), revealed diffraction peaks corresponding to Fe_3O_4 and χ-Fe_5C_2, constituting 83 and 17 mol-%, respectively. The average crystallite sizes of Fe_3O_4 and χ-Fe_5C_2 were 42 and 10 nm, respectively. Figure 7.9 (c) showed the XRD pattern of the $CuFe_2O_4$ (ex), diffraction peaks corresponded to Fe_3O_4, χ-Fe_5C_2 and Cu with the normalized relative abundance of 55, 29 and 16 mol-%, respectively were observed. The average crystallite of Fe_3O_4, χ-Fe_5C_2 and Cu was 30, 12 and 16 nm, respectively. Diffraction peaks corresponding to Fe_3O_4, χ-Fe_5C_2 and Cu (Figure 7.9 (d)) were observed in the XRD pattern of $CuFeO_2$ (ex). The normalized relative abundance of the phases Fe_3O_4, χ-Fe_5C_2 and Cu was 28, 48 and 24 mol-%, respectively. The average crystallite sizes of Fe_3O_4, χ-Fe_5C_2 and Cu were 26, 9 and 20 nm, respectively. Diffraction peaks corresponding to Fe_3O_4, FeO, χ-Fe_5C_2 and Ag were observed in

the XRD pattern of $AgFeO_2$ (ex) as shown in Figure 7.9 (e). The normalized relative abundance of Fe_3O_4, FeO, χ-Fe_5C_2 and Ag was 4, 13, 67 and 16 mol-%, respectively. The average crystallite sizes of Fe_3O_4, FeO, χ-Fe_5C_2 and Ag were, n/a, 14, 9 and 13 nm, respectively. The promoted iron catalysts showed an enhanced iron carbide formation as compared to the un-promoted iron catalysts. Furthermore, the average crystallite sizes of the iron carbide phase were in a range of 9-14 nm as given in Table 7.8. The Cu and Ag fraction that could not be accounted for maybe present in the spent catalyst in small average crystallite sizes; this would thus result in difficulty in analyses with the XRD technique. An oxidation study of the model catalysts was conducted by re-analysis of the spent catalysts after 10 months of storage in wax. The samples were analysed using XRD (the results are shown in Appendix B). The storage procedure leads to some oxidation. The extent of oxidation is small and not an obvious function of the copper content in the catalyst. In particular the metastable phase FeO is prone to oxidation.

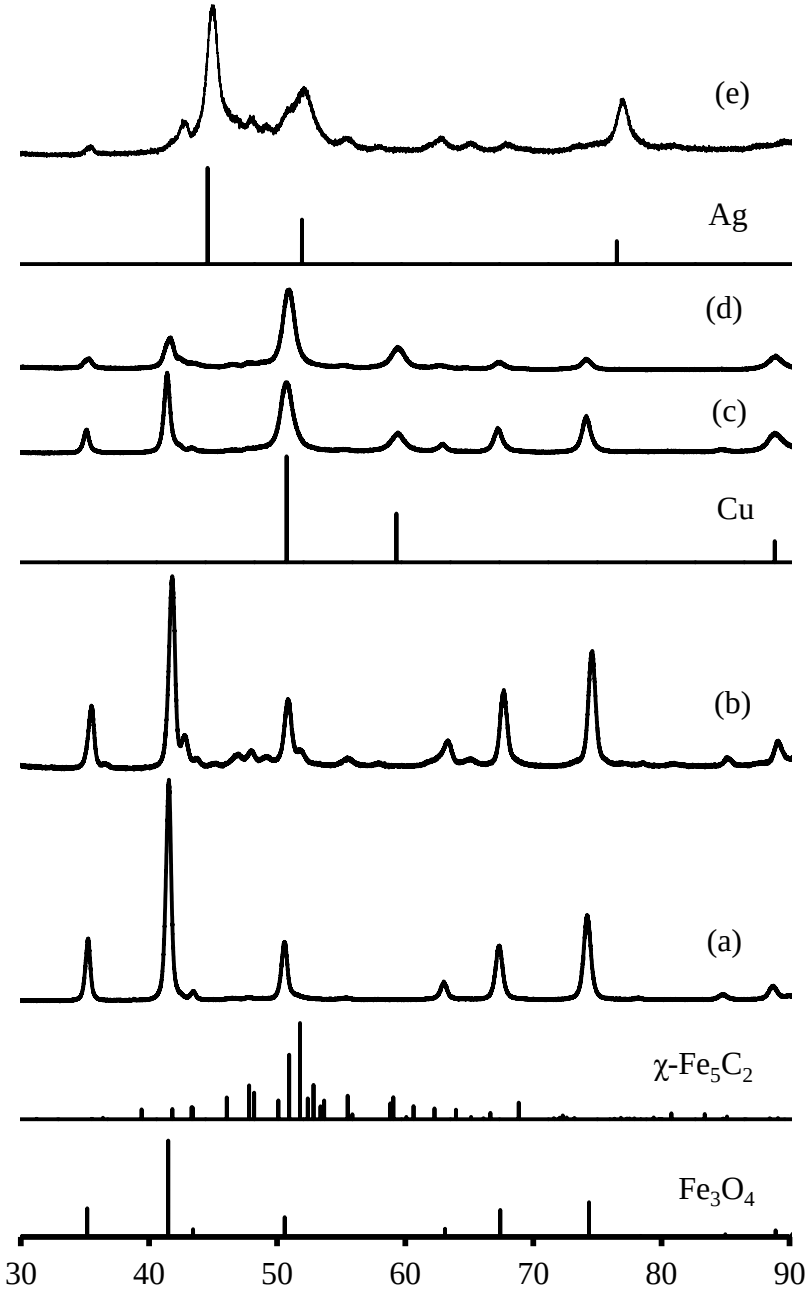

Figure 7.9: X-ray diffractograms of the model catalysts after activation in CO (270 ^{o}C for 16 hrs) and exposure to Fischer-Tropsch conditions (250 ^{o}C, 20 bars for 48 hrs (a) γ-Fe_2O_3 (ex), (b) α-Fe_2O_3 (ex), (c) $CuFe_2O_4$ (ex), (d) $CuFeO_2$ (ex) and (e) $AgFeO_2$ (ex)

Table 7.8: Physio-chemical characteristics of the model compounds after activation in CO (270 ^{o}C for 16 hrs) and exposure to Fischer-Tropsch conditions (T = 250 ^{o}C, 20 bars for 48hrs)

Sample		**γ-Fe_2O_3 (ex)**	**α-Fe_2O_3 (ex)**	**$CuFe_2O_4$ (ex)**	**$CuFeO_2$ (ex)**	**$AgFeO_2$ (ex)**
Fe/Me[a], mol/mol		-	-	2.29±0.10	1.21±0.17	1.76±0.25
Phases[b]	Fe_3O_4	72 (43)	83 (17)	55 (30)	28 (26)	4 (-)
	FeO	6 (9)				13 (14)
	χ-Fe_5C_2	22 (26)	17 (10)	29 (12)	48 (9)	67 (9)
	Cu/Ag			16 (16)	24 (20)	16 (13)
Fe/Me[c], mol/mol				5.2	3.2	6.0

where Me = Cu or Ag

[a] Phase composition using EDX

[b] phase composition in mol-% Me (in brackets the average crystallite size in nm) as determined using Rietveld refinement of XRD-pattern

[c] molar ratio of copper in the metal phase relative to iron in the detected iron phases as determined using Rietveld refinement of XRD-pattern.

7.3.1.2. Mössbauer absorption spectroscopy (MAS)

Mössbauer spectra of the CO activated model catalysts after the Fischer-Tropsch synthesis are shown in Figure 7.10-7.12. The MAS hyperfine parameters are given in Table 7.9 and 7.10. All the Mössbauer spectra were recorded at room temperature (298 K) and only the sample of *ex*-$AgFeO_2$ was further recorded at liquid helium (4.2 K). In all the model catalysts the presence of magnetite (Fe_3O_4) and iron carbide were observed as final phases. While, the promoted iron catalysts also revealed an iron phase in superparamagnetic material (related to the presence of iron material in small crystallite size). The MAS spectra of γ-Fe_2O_3 (ex) and α-Fe_2O_3 (ex) are shown in Figure 7.10 (a) and (b), respectively. The MAS spectrum showed three sextets. Two of the sextets had hyperfine parameters similar to Fe_3O_4 and one of the sextets had hyperfine parameters typical of iron carbide (Fe_xC). The relative abundance of Fe_3O_4 and Fe_xC were 92 and 8 %, respectively. The MAS spectrum of the γ-Fe_2O_3 (ex) as shown in Figure 7.10 was fitted with four sextets, two of the sextets had hyperfine parameters similar to Fe_3O_4 and the other two were typical of iron carbide (Fe_xC). The relative abundances of the Fe_3O_4 and Fe_xC were 88 and 12 %, respectively. These results are in agreement with the previously discussed XRD results (XRD studies discussed in section 7.3.1.1).

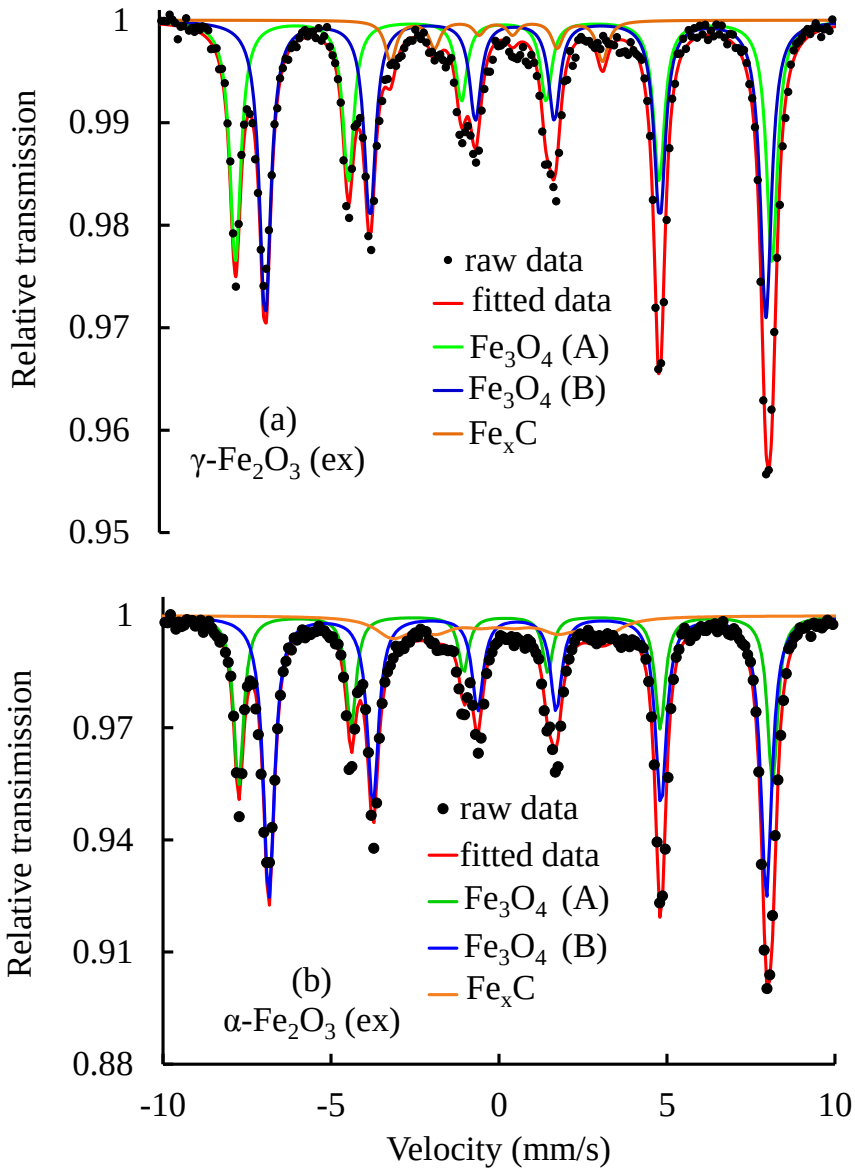

Figure 7.10: Mössbauer spectra of γ-Fe_2O_3 (ex) and α-Fe_2O_3 (ex) after activation in CO (270 ^oC, 16 hrs) and exposure to Fischer-Tropsch conditions (250 ^oC, 20 bars for 48 hrs)

Figure 7.11 (a) and (b) show the MAS spectra of $CuFe_2O_4$ (ex) and $CuFeO_2$ (ex), respectively. The MAS spectra were fitted with five sextets and a quadrupole doublet, two of the sextets had MAS hyperfine parameters similar to Fe_3O_4, while, three of the sextets are typical of χ-Fe_5C_2. The quadrupole doublet was attributed to Fe species in SPM state. The relative abundances of the Fe_3O_4 and χ-Fe_5C_2 phases for the spent catalyst of $CuFe_2O_4$ (ex) were 70 and 23 %, respectively, and the quadrupole doublet constituted 7 % of the total Fe content. In the spent catalyst of $CuFeO_2$ (ex), the relative abundances of the Fe_3O_4 and χ-Fe_5C_2 phases were 56 and 38 %, respectively, and the quadrupole doublet constituted 6 % of the total iron content.

Comparison of the MAS and XRD results of $CuFe_2O_4$ (ex) and $CuFeO_2$ (ex) revealed a slight discrepancy in the results; this difference may be attributed to the presence of small average crystallite sizes (confirmed by the quadrupole doublet in MAS results) that are not XRD detectable.

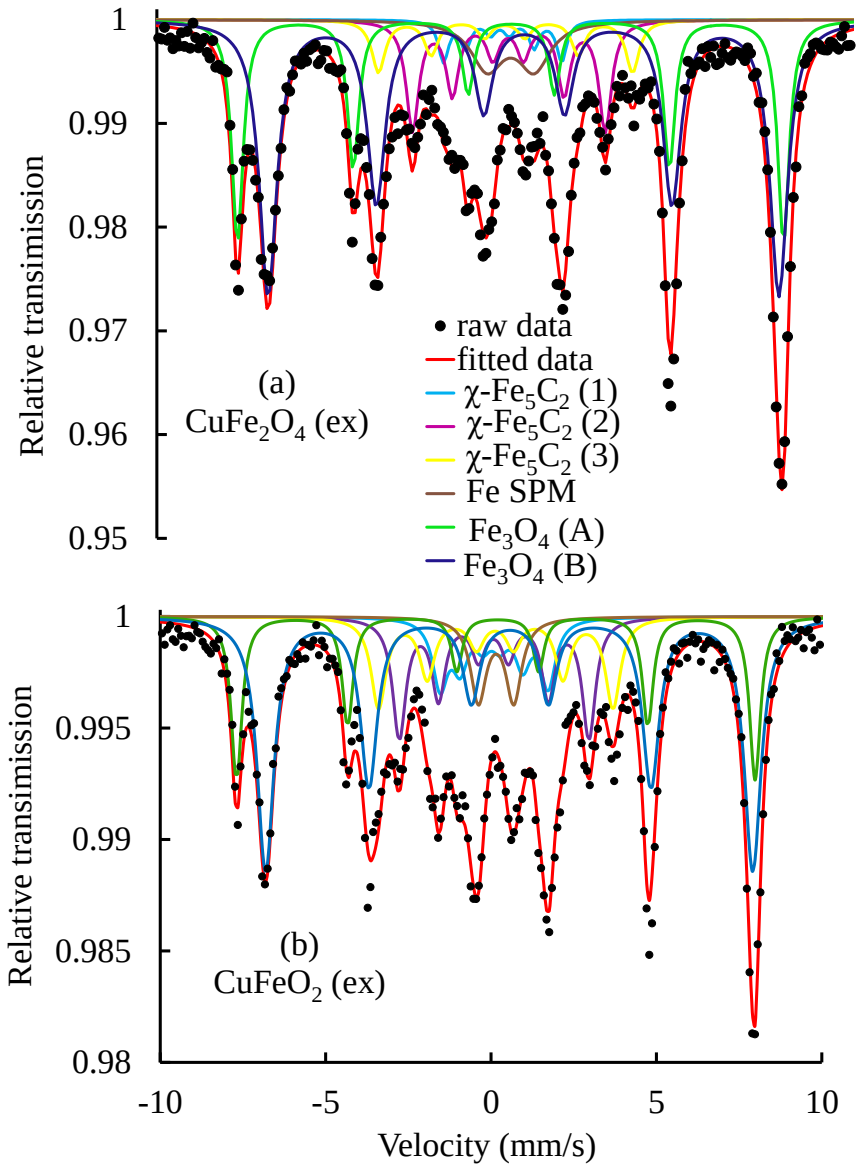

Figure 7.11: Mössbauer spectra of (a) $CuFe_2O_4$ (ex) and (b) $CuFeO_2$ (ex) after activation in CO (270 ^oC, 16 hrs) and exposure to Fischer-Tropsch conditions (250 ^oC, 20 bars for 48 hrs)

The MAS spectra of $AgFeO_2$ (ex) were recorded at room temperature and liquid helium as shown in Figure 7.12 (a) and (b), respectively. The MAS spectrum recorded at room temperature was fitted with five sextets and a quadrupole doublet. Two of the sextets had hyperfine

parameters corresponding to Fe_3O_4, while, the other three sextets had hyperfine parameters typical of the χ-Fe_5C_2 phase. The quadrupole doublet was attributed to the Fe in SPM state. The relative abundances of the Fe_3O_4, χ-Fe_5C_2 and quadrupole doublet were 10, 56 and 34 %, respectively. The MAS spectrum recorded at liquid helium resulted in the disappearance of the quadrupole doublet which was attributed to Fe in SPM. The MAS spectrum was fitted with six sextets; three of the sextets had hyperfine parameters similar to Fe^{3+} and Fe^{2+} in B-site and Fe^{3+} in A-site of the Fe_3O_4 phase, while, the other three sextets had hyperfine parameters typical of the χ-Fe_5C_2 phase.

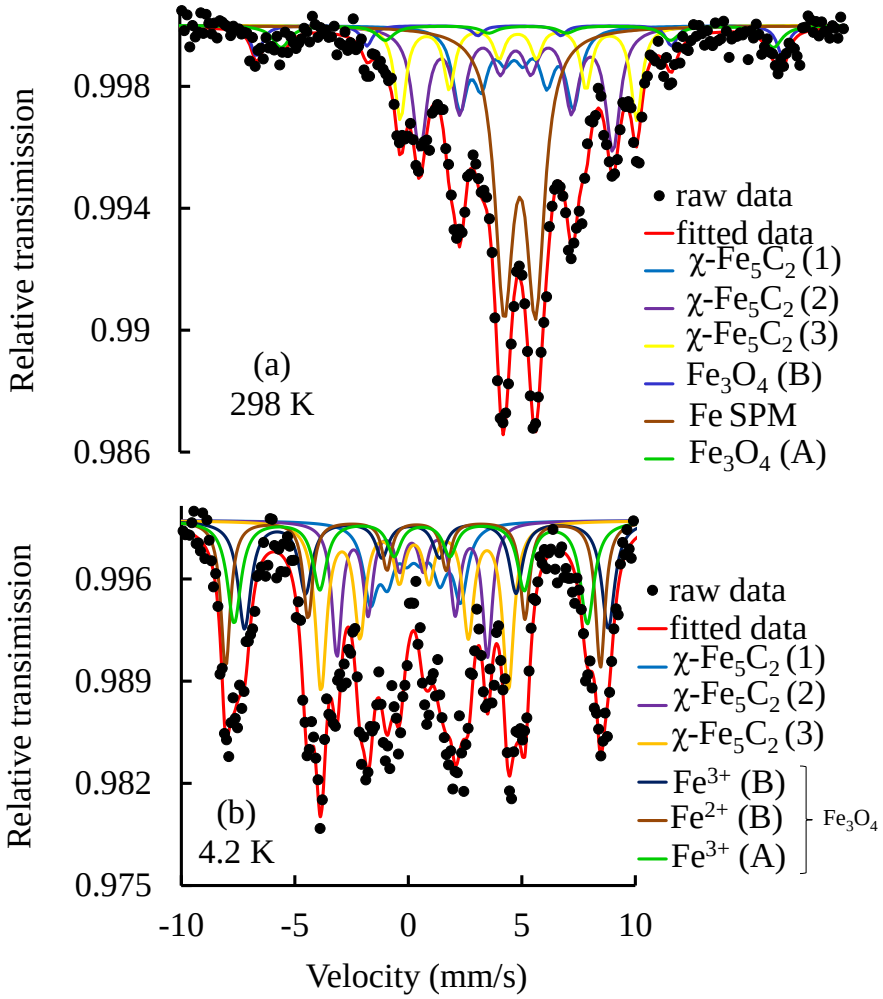

Figure 7.12: Mössbauer spectra of $AgFeO_2$ (ex) recorded at (a) 298 K and (b) 4.2 K, after activation in CO (270 ^oC, 16 hrs) and exposure to Fischer-Tropsch conditions (250 ^oC, 20 bars for 48 hrs)

The relative abundances of Fe_3O_4 and χ-Fe_5C_2 were 48 and 52 %, respectively. The disappearance of the quadrupole doublet as well as the increase in the relative abundance of

Fe_3O_4 in the MAS results recorded at liquid helium (as compared to the room temperature recorded results) suggested that the Fe in SPM state was ascribed to the presence of Fe_3O_4 in small crystallite sizes.

Table 7.9: Mössbauer hyperfine parameters of γ-Fe_2O_3 (ex), α-Fe_2O_3 (ex), $CuFe_2O_4$ (ex) and $CuFeO_2$ (ex) after activation in CO (270 ^oC, 16 hrs) and exposure to Fischer-Tropsch conditions (250 ^oC, 20 bars for 48 hrs)

δ – isomer shift, Δ - quadrupole splitting, $\boldsymbol{ß_{hf}}$ – hyperfine induction, **A** – relative area.

	Temperature (K)	$\mathbf{H_{app}}$	**MAS hyperfine parameters**			Components	**A (~2 %)**	**Phase** (after FTS)
			δ (mm/s)	**Δ (mm/s)**	$\boldsymbol{B_{hf}}$ **(T)**			
γ-Fe_2O_3 (ex)	298	0	0.31	-0.02	49.3	sextet (A)	88	Fe_3O_4
			0.66	0.01	45.9	sextet (B)		
			0.06	0.02	19.3	sextet	12	Fe_xC
α-Fe_2O_3 (ex)	298	0	0.32	-0.03	49.3	sextet (A)	92	Fe_3O_4
			0.66	-0.01	46.0	sextet (B)		
			0.08	0.02	19.5	sextet	8	Fe_xC
$CuFe_2O_4$ (ex)	298	0	0.30	-0.02	48.7	sextet (A)	70	Fe_3O_4
			0.67	-0.02	45.5	sextet (B)		
			0.02	0.08	10.5	sextet	23	χ-Fe_5C_2
			0.23	0.02	17.2	sextet		
			0.13	0.02	22.7	sextet		
			0.29	1.35	-	doublet	7	Fe SPM
$CuFeO_2$ (ex)	298	0	0.29	-0.06	48.6	sextet (A)	56	Fe_3O_4
			0.67	-0.02	45.7	sextet (B)		
			0.17	0.08	10.1	sextet	38	χ-Fe_5C_2
			0.20	0.02	17.8	sextet		
			0.25	0.02	21.9	sextet		
			0.27	1.07	-	doublet	6	Fe SPM

Table 7.10: Mössbauer hyperfine parameters of $AgFeO_2$ (ex) after activation in CO (270 ^oC, 16 hrs) and exposure to Fischer-Tropsch conditions 250 ^oC, 20 bars for 48 hrs)

δ – isomer shift, Δ - quadrupole splitting, $\boldsymbol{ß_{hf}}$ – hyperfine induction, **A** – relative area.

	Temperature (K)	**H_{app}**	**MAS hyperfine parameters**			**Component**	**A (~2 %)**	**Phase**
			δ (mm/s)	**Δ (mm/s)**	**B_{hf} (T)**			
$AgFeO_2$ (ex)	298	0	0.32	0.01	49.0	sextet (A)	10	Fe_3O_4
			0.56	-0.02	45.9	sextet (B)		
			0.20	0.08	10.6	sextet	56	χ-Fe_5C_2
			0.22	0.02	17.9	sextet		
			0.28	0.02	22.0	sextet		
			0.33	0.95	-	doublet	34	Fe SPM
	4.2	0	0.57	0.69	49.7	sextet (B)	48	Fe_3O_4
			0.40	-0.16	51.2	sextet (B)		
			0.47	-0.49	48.3	sextet (A)		
			0.39	0.08	12.3	sextet	52	χ-Fe_5C_2
			0.27	0.02	20.6	sextet		
			0.38	0.02	25.6	sextet		

It has been argued [16] that copper in iron-based catalysts may facilitate carburization of the magnetite phase, although it does not facilitate carburization in the absence of hydrogen (vide supra). Copper may activate hydrogen under Fischer-Tropsch conditions. Hydrogen spilled over to the magnetite surface may partially reduce its surface and thereby accelerating its carburization. The acceleration of the carburization process will lead to a reduced average crystallite size of the magnetite phase. Furthermore, the relative abundance of the other phases, viz. iron carbide and superparamagnetic iron, will increase (Figure 7.13).

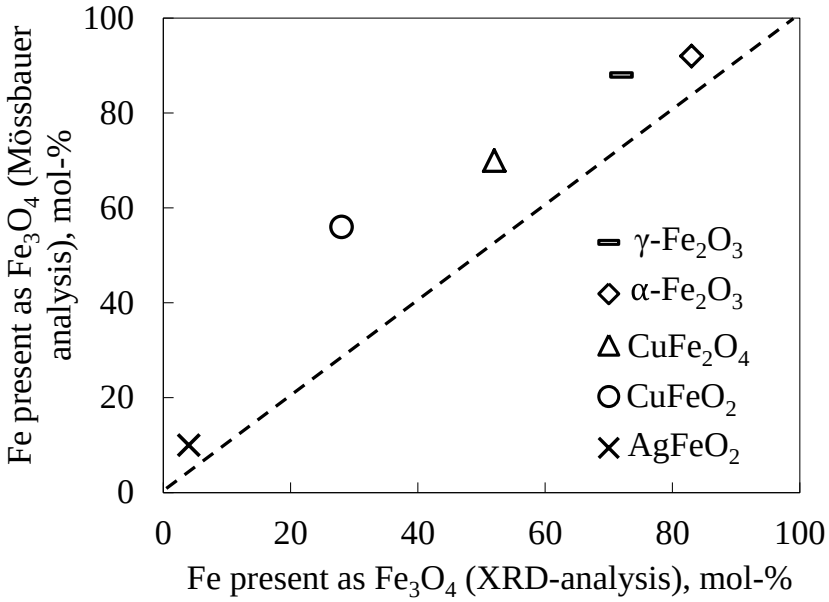

Figure 7.13: Correlating the amount of oxidic iron determined using Mössbauer absorption spectroscopy and the using XRD-analysis (amount of Fe_3O_4 as determined using Mössbauer at 298 K)

7.3.2. Fischer-Tropsch synthesis (FTS) activity

The FT activity of the model catalysts, expressed as conversion (C-%) as a function of time on stream (hr) is shown in Figure 7.14. The promoted iron catalysts showed higher activity as compared to the un-promoted iron catalysts. The observed high activity was consistent with high iron carbide (χ-Fe_5C_2) content as shown in XRD and MAS results; this observed activity trend is similar to that of the H_2 activated model catalysts. The average crystallite size of the χ-Fe_5C_2 was in a similar range (9-14 nm) in all the model catalyst, therefore, the crystallite size effect on the FT activity may be eliminated.

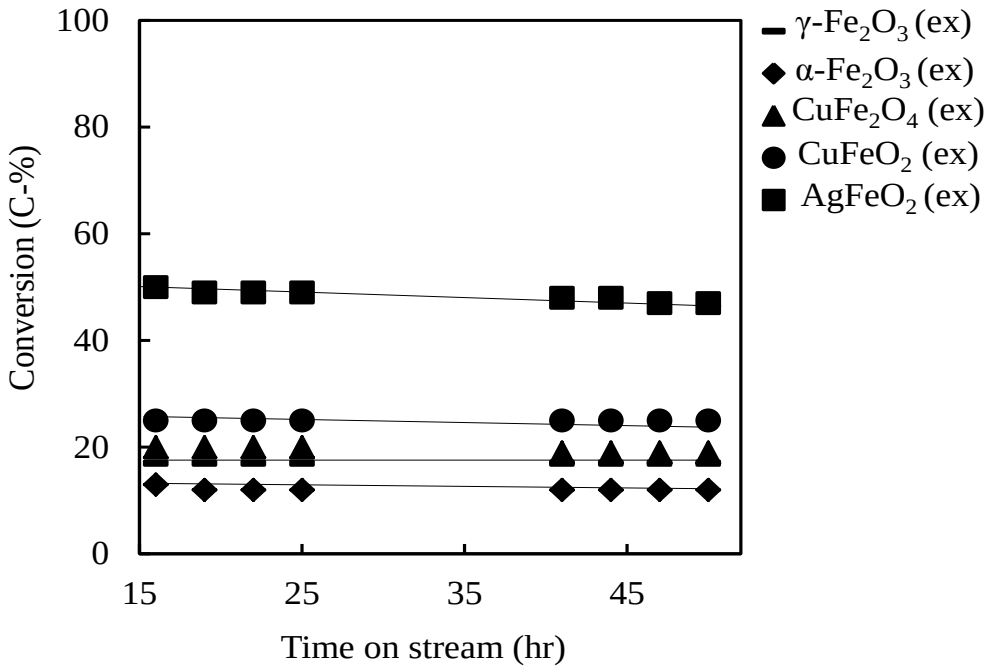

Figure 7.14: Carbon conversions of the model catalyst as a function of time on stream (hr) after activation in CO (270 ^{o}C for 16 hrs) and exposure to Fischer-Tropsch condition (270 ^{o}C, 20 bars for 48 hrs)

7.3.3. Product formation

7.3.3.1. Carbon dioxide (CO_2) formation

Figure 7.15 shows the rate of CO_2-formation as a function of Fe present as SPM Fe in spent catalyst. Similarly to the H_2 activated model catalysts, the CO activated model catalysts (promoted iron catalysts) showed a higher rate of CO_2. The silver promoted iron catalyst shows the highest rate of CO_2 as compared to the copper promoted as well as un-promoted iron catalyst. This results may be explained by correlating the rate of CO_2-formation with the amount of superparamagnetic iron, which implies that the small domains of Fe_3O_4 are susceptible to re-carburization and the rate of carburization of large magnetite crystallites is relatively slow, being too slow to significantly form CO_2. The samples *ex* hematite and *ex* maghemite do not contain superparamagnetic iron. Carbon dioxide formed over these samples may originate from oxygen removal adsorbed on the catalytically active carbide surface. This implies that oxygen in carbon monoxide used for the formation of organic product compounds is under the applied conditions for ca. 10% removed as CO_2 (and the balance as water).

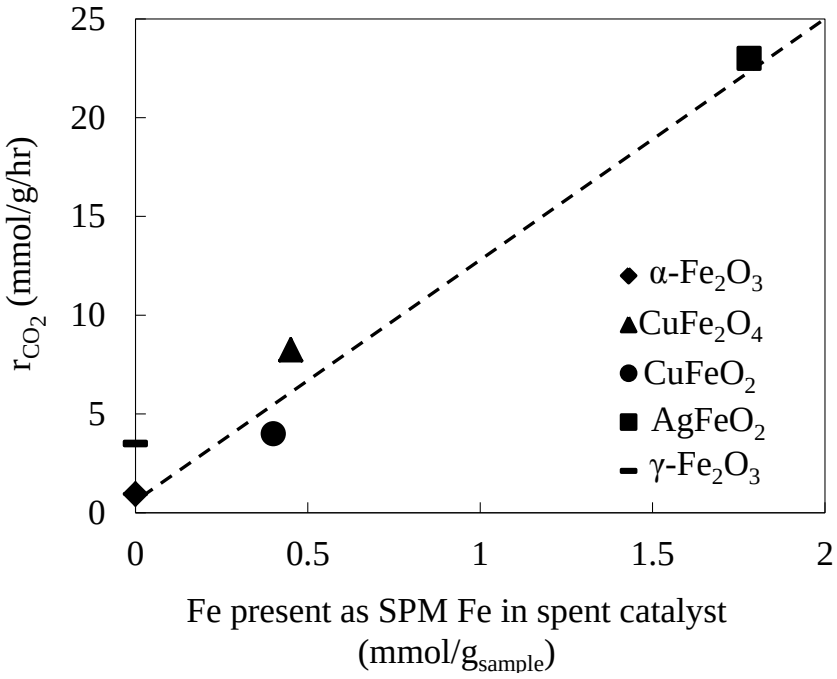

Figure 7.15: Correlating the rate of CO_2-formation in the Fischer- Tropsch synthesis with the amount of superparamagnetic iron as determined by room temperature Mössbauer absorption spectroscopy for CO activated model catalysts

7.3.4. Formation of organic products

7.3.4.1. Methane (CH_4) formation and chain growth probability (α)

Table 7.11 shows the methane selectivity of the model catalysts. Copper promoted iron catalysts showed higher CH_4 selectivity as compared to the un-promoted iron catalysts while the lowest CH_4 selectivity was observed for silver promoted iron catalyst. The expected inverse relationship between CH_4 selectivity and the chain growth probability was observed. Similarly, to the H_2 activated model catalysts, promoted iron catalysts showed higher C_{5+} selectivity as compared to the un-promoted iron catalysts (see Table 7.11). Furthermore, higher C_{5+} values (>90 C-%) were observed for H_2 activated promoted model catalysts as compared to the CO activated promoted model catalysts.

Table 7.11: Selectivities of the model catalysts after activation in H_2 (270 ^oC for 16 hrs) and exposure to Fischer-Tropsch conditions (250 ^oC, 20 bars for 48 hrs)

	γ-Fe_2O_3 (ex)	**α-Fe_2O_3 (ex)**	**$CuFe_2O_4$ (ex)**	**$CuFeO_2$ (ex)**	**$AgFeO_2$ (ex)**
S_{CH_4}[a], C-%	3	3	4	5	2
$S_{C_2\text{-}C_4}$[a], C-%	9	8	7	10	8
S_{C5+}[a], C-%	88	89	89	85	90

[a] Content of the various product fractions in the fraction of organic product compounds

7.3.5. Olefin formation

Figure 7.16 shows the mole fraction of the total olefin content of the model catalysts in linear hydrocarbons (HCNs) as a function of carbon number. A slight decrease in the olefin content was observed for the copper promoted iron catalysts as compared to the un-promoted iron catalysts. The un-promoted iron catalysts as well as the silver promoted iron catalyst were in the same range.

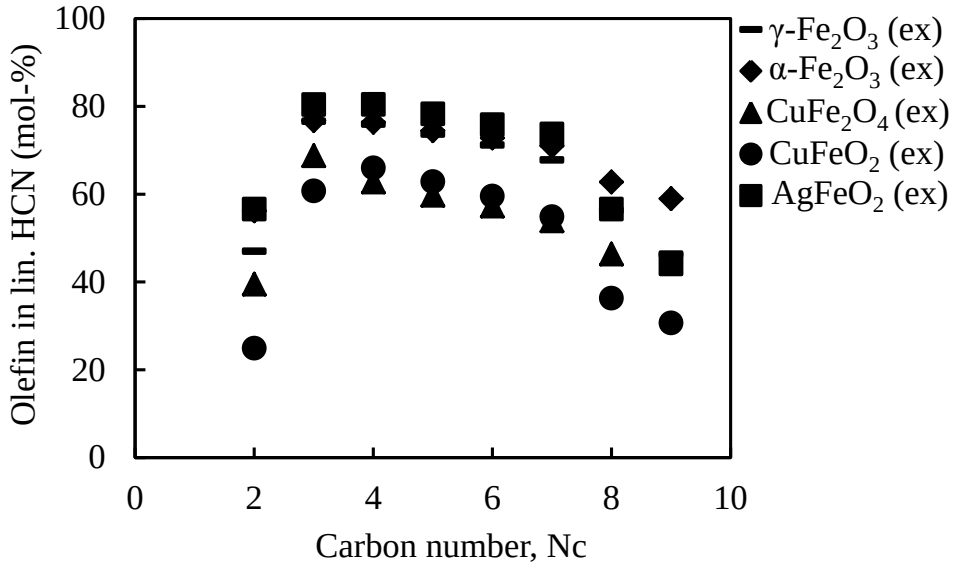

Figure 7.16: Mole fraction of olefins in linear HCNs of the model catalysts as a function of carbon number after activation in CO (270 ^oC, 16 hrs) and exposure to Fischer-Tropsch conditions (250 ^oC, 20 bars for 48 hrs)

The olefin selectivity was further investigated using olefin fraction C_5 fraction in their corresponding C-fraction. The observed mole percent of the olefins in their corresponding C-fraction and the CO-conversion are given in Table 7.12.

Table 7.12: Olefin content in C_5-HC olefin and the CO-conversion of the model catalysts after activation in CO (270 ^oC for 16 hrs) and exposure to Fischer-Tropsch conditions (250 ^oC, 20 bars for 48 hrs)

	γ-Fe_2O_3 (ex)	**α-Fe_2O_3 (ex)**	**$CuFe_2O_4$ (ex)**	**$CuFeO_2$ (ex)**	**$AgFeO_2$ (ex)**
CO-conversion (%)	23	12	20	21	66
Olefin content in C_5-HC[a] olefin, mol-%	74	67	67	63	78
1-olefin content in C_5-olefin[b], mol-%	85	89	87	63	90

[a] Amount of olefins in the fraction of linear hydrocarbons with a particular number of carbon atoms
[b] Amount of linear 1-olefins in the fraction of linear olefins with a particular number of carbon atoms

7.3.6. Oxygenate products formation

Table 7.13 shows the C_5 alcohol fraction in linear C_5 HCN products taken after 48 hrs time on stream. The copper promoted iron catalysts showed no significant effect on the C_5-alcohol content as compared to the un-promoted iron catalysts, while, an increase in the C_5 alcohol content was observed for the silver promoted iron catalyst. Comparison of these results to those observed after H_2 activation showed no significant differences (see Table 7.6).

Table 7.13: Mole fraction of the total C_5 oxygenates in linear hydrocarbon (HCN) products after activation in CO at 270 ^oC for 16 hrs and exposure to Fischer-Tropsch conditions (250 ^oC, 20 bars for 48 hrs)

	γ-Fe_2O_3 (ex)	**α-Fe_2O_3 (ex)**	**$CuFe_2O_4$ (ex)**	**$CuFeO_2$ (ex)**	**$AgFeO_2$ (ex)**
C_5 oxygenates in linear C_5 product compounds, mol-%	7	7	9	8	14

7.3.7. Branched products formation

The molar ratio of methyl branched to linear hydrocarbons in the C_5 fraction is shown in Table 7.14. The copper incorporated iron catalysts showed lower branching C_5 selectivity than the un-

promoted iron catalysts. The silver incorporated iron catalyst shows similar branching results to that of the un-promoted iron catalyst.

Table 7.14: Molar ratio of iso (branched) to n (straight) compounds in the C_5 hydrocarbon fraction of the model catalysts after activation in CO at 270 ^oC for 16 hrs and exposure to Fischer-Tropsch conditions (250 ^oC, 20 bars for 48 hrs)

	γ-Fe_2O_3 (ex)	**α-Fe_2O_3 (ex)**	**$CuFe_2O_4$ (ex)**	**$CuFeO_2$ (ex)**	**$AgFeO_2$ (ex)**
iso-C_5/n-C_5, mol/mol	0.19	0.20	0.11	0.17	0.19

7.4. Summary of the Fischer-Tropsch synthesis performance of the H_2 and CO activated model catalysts

An increase in the FT activity of the promoted iron catalysts as compared to the un-promoted iron catalysts was observed for the H_2 and CO activated catalysts. The enhanced FT activity for the promoted iron catalysts may be ascribed to the higher carbide content. The promoted iron catalysts showed a higher CO_2-selectivity, which is attributed to the carburization of superparamagnetic iron (mainly as magnetite) during the Fischer-Tropsch synthesis. The rate of formation of CO_2 correlates with the amount of superparamagnetic iron present in the sample, although some carbon dioxide is formed in the oxygen removal from the catalytically active surface as well. This implies that the iron-based catalyst is a dynamic catalyst system, in which phase transformations are taking place on the time scale of the catalytic reaction. Furthermore, the copper promoted iron catalysts showed a reduction in the olefin selectivity due to secondary hydrogenation. While, the silver promoted iron catalysts showed a high olefin content (in particular for the most reactive olefin, ethene) in conjunction with a high 1-olefin content. This implies that secondary olefin conversion over this catalyst is limited. This might be attributed to the low activity of silver for the hydrogenation of the C=C-bond [35].

References

1. Bartholomew C H. Recent Developments in Fischer-Tropsch Catalysis, New Trends in CO Activation, Studies in Surface Science and Catalysis. Amsterdam: Elsevier, 1991.

2. Kölbel, H. and Ralek, M. (1980), 'The Fischer-Tropsch Synthesis in the Liquid Phase', *Catalysis Reviews-Science and Engineering* **21**, 225.

3. van der Laan, G.P. and Beenackers, A.A.C.M. (1999), 'Kinetics and Selectivity of the Fischer-Tropsch Synthesis: A Literature Review', *Catalysis Reviews-Science and Engineering* **41**, 225.

4. Rogatis, L.D. (2009), 'Methane partial oxidation on NiCu-based catalysts', *Catalysis Today* **145**, 176.

5. Bukur, D.B., Mukesh, D. and Patel, S.A. (1990), 'Promoters effects on precipitated iron catalysts for Fischer-Tropsch synthesis', *Industrial and Engineering Chemistry Research* **29**, 194.

6. Wielers, A.F.H., Koebrugge, G.W. and Geus, J.W. (1990), 'On the properties of silica-supported bimetallic Fe-Cu catalysts Part II. Reactivity in the Fischer-Tropsch synthesis', *Journal of Catalysis* **121**, 375.

7. Li, S., Li, A., Krishnamoorthy, S. and Iglesia, E. (2001), 'Effects of Zn, Cu, and K promoters on the Reduction, Carburization, and Catalytic Behaviour of Iron-Based Fischer-Tropsch Synthesis Catalysts', *Catalysis Letters* **77**, 197.

8. O'Brien, R.J. and Davis, B.H. (2004), 'Impact of Copper on an Alkali Promoted Iron Fischer-Tropsch Catalyst', *Catalysis Letters* **94**, 1.

9. Zhang, C.H., Yang, Y., Teng, B.T., Li, T.Z., Zheng, H.Y., Xiang, H.W. and Li, Y.W. (2006), 'Study of an iron-manganese Fischer-Tropsch synthesis catalyst promoted with copper', *Journal of Catalysis* **237**, 405.

10. O'Brien, R.J., Xu, L., Spicer, R.L., Bao, S., Milburn, D.R. and Davis, B.H. (1997), 'Activity and selectivity of precipitated iron Fischer-Tropsch catalysts', *Catalysis Today* **36**, 325.

11. Wachs, I.E., Duyer, D.J. and Iglesia, E. (1984), 'Characterization of Fe, Fe-Cu and Fe-Ag Fischer-Tropsch Catalysts', *Applied Catalysis* **12**, 201.

12. Anderson, R.B. (1984), *The Fischer-Tropsch Synthesis*, Academic press, inc., Orlando.

13. Dry, M. (1981), Catalysis - Science and Technology. In John R. Anderson and Michel Boudart (Ed.), *Volume 1*, (pp. 159-255). Berlin Heidelburg:Springer-Verlag.

14. Rao, K.R.P.M., Huggins, F.E., Huffman, G.P., Gormly, R.J., O'Brien, R.J. and Davis, B.H. (1996), 'Mössbauer study of iron Fischer-Tropsch catalysts during activation and synthesis', *Energy and Fuels* **10**, 546.

15. Cairns,P., Oxygenates in Iron Fischer-Tropsch Synthesis: is Copper a selectivity promoter?, PhD Thesis, University of Cape Town, Cape Town, 2008.

16. Chonco, Z. H., Lodya, L., M. Claeys and van Steen, E. (2013), ''Copper ferrites: a model for investigating the role of copper in the dynamic iron-based Fischer-Tropsch catalyst', *Journal of Catalysis* **308**, 363.

17. Kölbel, H., Ackerman, P., Ruschenburg, E., Langheim, R. and Engelhardt, F. (1951), 'Beitrag zur Fischer-Tropsch Synthese on Eisenkontakten', *Chemie Inenieur Technik* **23**, 153.

18. Bukur, D.B., Mukesh, D. and Patel, S.A. (1990), 'Promoter effects on precipitated iron catalysts for Fischer-Tropsch synthesis', *Industrial Engineering Chemistry Research* **29**, 194.

19. Deckwer, W.D., Serpemen, Y., Ralek, M. and Schmidt, B. (1982), 'Fischer-Tropsch synthesis in the Slurry phase on Mn/Fe catalysts', *Industrial and Engineering Chemistry Process Design and Development* **21**, 222.

20. Shroff, M.D., Kalakkad, D.S., Sault, A.G. and Datye, A.K. (1995), 'Activation of

precipitated iron Fischer-Tropsch synthesis catalysts', *Journal of Catalysis* **156**, 185.

21. Dictor, R.A. and Bell, A.T. (1986), 'Fischer-Tropsch synthesis over reduced and unreduced iron oxide catalysts', *Journal of Catalysis* **97**, 121.

22. van Steen, E. and Claeys, M. (2008), 'Fischer-Tropsch catalysts for Biomass-to-Liquid (BTL) process', *Chemical Engineering & Technology* **31**, 655.

23. Li, S., Li, A., Krishnamoorthy, S., Meitzner, G.D. and Iglesia, E. (2002), 'Promoted iron-based catalysts for the Fischer-Tropsch synthesis: design, synthesis, site densities and catalytic properties', *Journal of Catalysis* **206**, 202.

24. Estrella, M., Barrio, L., Zhou, G., Wang, X., Wang, Q., Wen, W., Hanson, J.C., Frenkel, A.I. and Rodriguez, J.A. (2009), 'In situ characterization of CuFe2O4 and Cu/Fe3O4 Water-Gas Shift catalysts', *Journal of Physical Chemistry C* **113**, 14411.

25. Newsome, D.S. (1980), 'The water-gas shift reaction', *Catalysis Reviews Science and Engineering* **21**, 275.

26. Rethwisch, D.G. and Dumenic J.A. (1986), 'Adsorptive and catalytic properties od supported metal oxides. III. Water-gas shift over supported iron and zinc oxides', *Journal of Catalysis* **101**, 35.

27. Zhang, H.B. and Schrader, G.L. (1985), 'Characterization of a fused iron catalyst for Fischer-Tropsch synthesis by in situ laser Raman spectroscopy', *Journal of Catalysis* **95**, 325.

28. Rao, K.R.P.M., Huggins, F.E., Mahajan, V., Huffman, G.P., Rao, V.U.S., Bhatt, B.L., Bukur, D.B., Davis, B.H. and O'Brien, R.J. (1995), 'Mössbauer spectroscopy study of iron-based catalysts used in Fischer-Tropsch synthesis', *Topics in Catalysis* **2**, 71.

29. Rhodes, C., Hutchings, G.J., and Ward, M.A. (1995), 'Water-gas shift reaction: finding the mechanistic boundary', *Catalysis Today* **23**, 43.

30. Andreeva, D., Idakiev, V., Tabakova, T., Andreeva, A. and Giovanoli, R. (1996), 'Low-

temperature water-gas shift reaction Au/α-Fe_2O_3 catalysts', *Applied Cataysis A General* **134**, 275.

31. Anderson, R. B.: 1984, *The Fischer-Tropsch Synthesis*. Academic Press, New York.

32. van Santen, R.A., Ciobica, I. M., van Steen, E. and Ghouri, M.M. (2011), 'Chapter 3-Mechanistic issues in Fischer-Tropsch catalysis', *Advances in Catalysis* **54**, 127.

33. Schulz, H. and Claeys, M. (1999), 'Reactions of α-olefins of different chain length added during Fischer-Tropsch synthesis on a cobalt catalyst in a slurry reactor', *Applied Catalysis A: General* **186**, 71.

34. Claeys, M. and van Steen, E. (2004), 'Fischer-Tropsch Technology', *Studies in Surface Science and Catalysis* **152**, 601.

35. Ponec, V. and Bond, G.C. (1995), 'Chapter 11: 'Catalytic hydrogenation and dehydrogenation', *Studies in Surface Science and Catalysis* **95**, 477.

36. Bukur, B.D., Pan, Z., Ma, W., Jacobs, G. and Davis, B.H. (2012), 'Effect of CO conversion on the product distribution of a Co/Al_2O_3 Fischer-Tropsch synthesis catalyst using a Fixed bed reactor', *Catalysis Letters* **142**, 1382.

37. Pichler, H. and Schulz, H. (1970), 'Neue Erkenntnisse auf dem Gebiet der Synthese von Kohlenwasserstoffen aus CO und H_2', *Chemical Engineering and Technology* **42**, 1162.

38. Johnston, P., Joyner, R.W. and Guczi, F.S,L. (1993), 'Structure function relationships in heterogeneous catalysis: the embedded surface molecule approach and its applications', *Studies in Surface Science and Catalysis* **75**, 165.

39. Ma, W., Kugler, E.L. and Dadyburjor, D.B. (2011), 'Promotional effect of copper on activity and selectivity to hydrocarbons and oxygenates for Fischer-Tropsch synthesis over potassium promoted iron catalysts supported on activated carbon', *Energy Fuels* **25**, 1931.

40. Lee, C.B. and Anderson, R.B, Proceedings of the 8th International Congress on Catalysis, Bruxelles, Belgium, (1984) vol. 2, pp.15.

41. Schulz, H., Erich, E., Gorre, H. and van Steen, E. (1990), 'Regularities of selectivity as a key for discriminating FT-surface reactions and formation of the dynamic system', *Catalysis Letters* **7**, 157.

42. Schulz, H., Rao, B.R. and Elstner, M. (1970), '14C-Studien zum Reactionsmechanismus der Fischer-Tropsch Synthese', *Erdöl Kohle, Erdgas, Petrochemie* **23**, 651.

43. Schulz, H., van Steen, E. and Claeys, M. (1994), 'Selectivity and mechanism of Fischer-Tropsch synthesis with iron and cobalt catalysts', *Studies in Surface Science and Catalysis* **81**, 455.

Chapter 8

General conclusions

This chapter is aimed at providing the reader with overall conclusions on the promotional effect of copper and silver on iron-based Fischer-Tropsch catalysts. These results are compared to the un-promoted iron oxide. Full summaries are supplied after every section in the preceding chapter. However, the major observations and conclusions will be discussed here again.

The model catalysts were successfully prepared via the co-precipitation method. Calcination at high temperature (950 ^{o}C) of the copper incorporated iron catalysts resulted in the formation of the desired copper ferrite phases (i.e., spinel $CuFe_2O_4$ and $CuFeO_2$) with large average crystallite sizes. Hematite (α-Fe_2O_3) of similar crystallite size was used as reference material. Silver incorporated iron catalyst ($AgFeO_2$) was prepared at 400 ^{o}C; attempts to prepare it at high temperature (950 ^{o}C) resulted in the segregation of the iron-silver precursor to metallic silver and iron oxide (α-Fe_2O_3); maghemite (γ-Fe_2O_3) of similar crystallite size was used as reference material. Characterization of the model catalysts using XRD, MAS, IR, SEM-EDX and AAS collectively confirmed the successful preparation of the model catalysts.

The reduction behaviour as well as the reducibility of the model catalysts was evaluated using *in-situ* XRD and *ex-situ* XRD experiments. The phase transformation and changes in the average crystallite sizes during H_2 and CO activation were evaluated via an *in-situ* XRD experiment, in an attempt to gain better understanding of the phase transformation and the changes in the average crystallite sizes during activation. In this experiment, activation conditions similar to those used prior to the FTS were mimicked. The first phase transformation observed during H_2 and CO activation of the promoter incorporated iron catalyst was observed at lower temperature as compared to the un-promoted iron catalysts confirming ease of reduction in the presence of promoter (Cu, Ag) in close proximity to the iron. Promoted iron catalysts also showed higher α-Fe (during H_2 activation) and Fe_xC (during CO-activation) formation. The observed results correlated with the results observed during *ex-situ* XRD (H_2 and CO activation studies). Furthermore, the presence of Cu or Ag in close proximity to the iron surface was observed to enhance the rate of the α-Fe formation during the second reduction step ($Fe_3O_4 \rightarrow \alpha$-Fe). This is postulated to occur via the H_2-spillover by copper/silver acting as the hydrogen activator, the

hydrogen spill-over to the magnetite thereby enhancing the rate of α-Fe formation [1]. The carburization of magnetite in the absence of hydrogen is not facilitated by copper or silver indicating that either CO does not spill-over or that spill-over of CO is kinetically irrelevant for the carburization process.

The Fischer-Tropsch synthesis of the model catalysts was conducted at T = 250 ^{o}C, P_{total} = 20 bar over 48 hrs on line stream (at steady state) in a slurry bed reactor. The performance of the model catalysts was monitored using an online TCD and offline FID. An increase in the activity of the promoted iron catalysts as compared to the un-promoted iron catalysts was observed. The enhanced FT activity for the promoted iron catalysts is ascribed to the higher carbide content. The rate of formation of CO_2 correlates with the amount of superparamagnetic iron present in the sample, although some carbon dioxide is formed in the oxygen removal from the catalytically active surface as well. This implies that the iron-based catalyst is a dynamic catalyst system, in which phase transformations are taking place on the time scale of the catalytic reaction. Furthermore, the copper promoted iron catalysts showed a reduction in the olefin selectivity due to secondary hydrogenation, while the silver promoted iron catalysts showed a high olefin content (in particular for the most reactive olefin, ethane (C_2)) in conjunction with a high 1-olefin content. This implies that secondary olefin conversion over this catalyst is limited. This might be attributed to the low activity of silver for the hydrogenation of the C=C-bond [2].

Future work

- Surface characterization of the model catalysts during or after H_2 and CO activation and Fischer-Tropsch synthesis to investigate the location of the copper or silver on the iron catalyst.
- Activation of the model catalysts under synthesis gas, for comparison of the results with those done under H_2 and CO. How does the promoter behave under such conditions?
- Evaluate the effect of gold (Au) as a promoter for the iron-based Fischer-Tropsch catalysts. Investigating the similarities and differences in the promotional effect of Au as compared to Cu and Ag.

References

1. de Smit, E., de Groot, F.M.F., Blune, R., Hävecker, M., Knop-Gericke, A. and Weckhuysen, B.M. (2010), 'The role of Cu on the reduction behaviour and surface properties of Fe-based Fischer-Tropsch catalysts', *Physical Chemistry Chemical Physics* **12**, 667.

2. Ponec, V. and Bond, G.C. (1995), 'Chapter 11: Catalytic hydrogenation and dehydrogenation', *Studies in Surface Science and Catalysis* **95**, 477.

Appendix

A: Preparation method

A.1. Preparation of delaffosite copper ferrite ($CuFeO_2$)

Figure A.1, shows the phase(s) transformation during heating at 950 ^oC, in an attempt to prepare a pure phase of $CuFeO_2$.

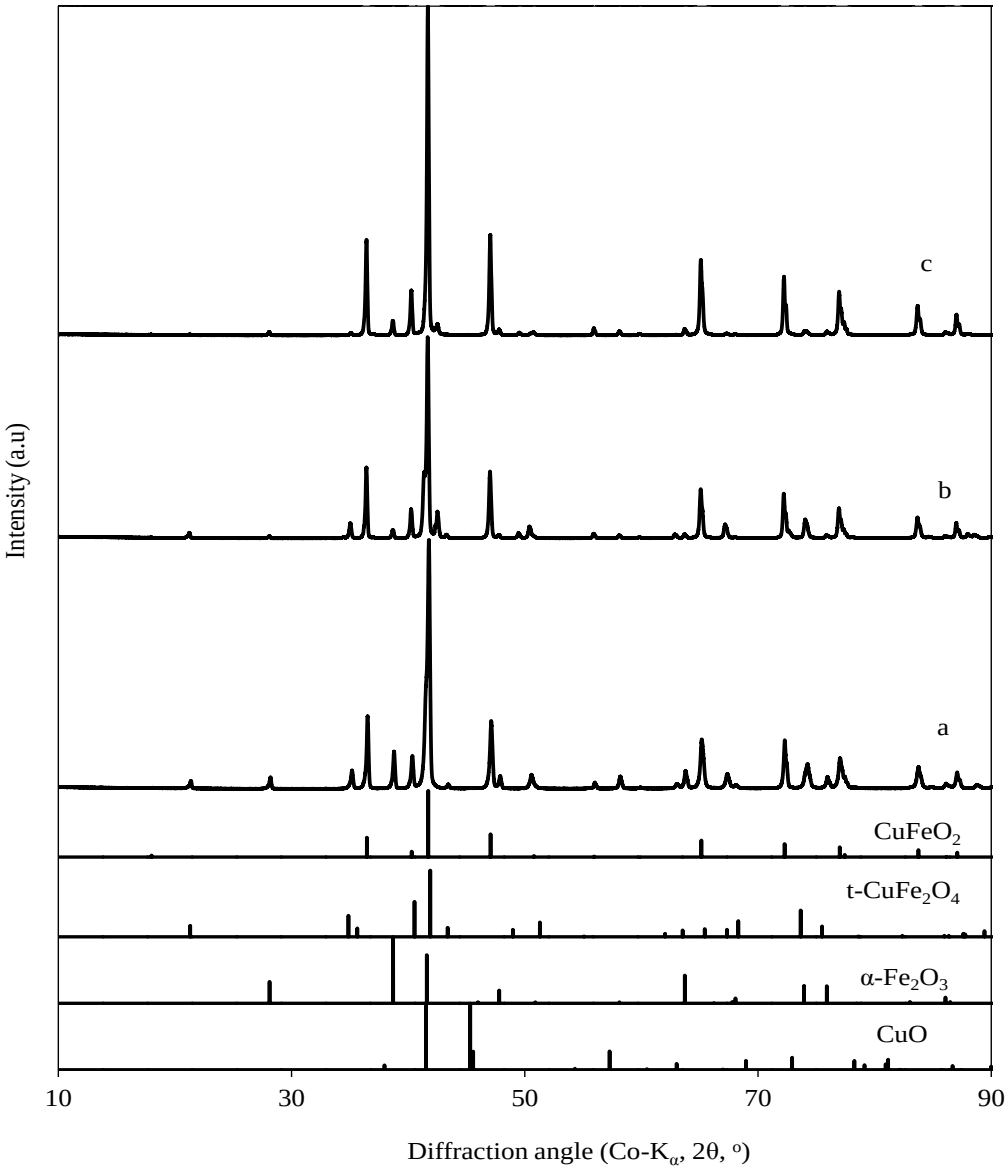

Figure A1: Preparation of $CuFeO_2$

A.2. Preparation of delaffosite silver ferrite ($AgFeO_2$)

Attempts made to prepare silver ferrites of large crystallites by calcining at high temperature (700 ^oC), resulted in the formation of α-Fe_2O_3 and metallic silver as the final phase(s). The diffraction patterns of the sample calcined at 400 and 700 ^oC, respectively, are shown in Figure A1.

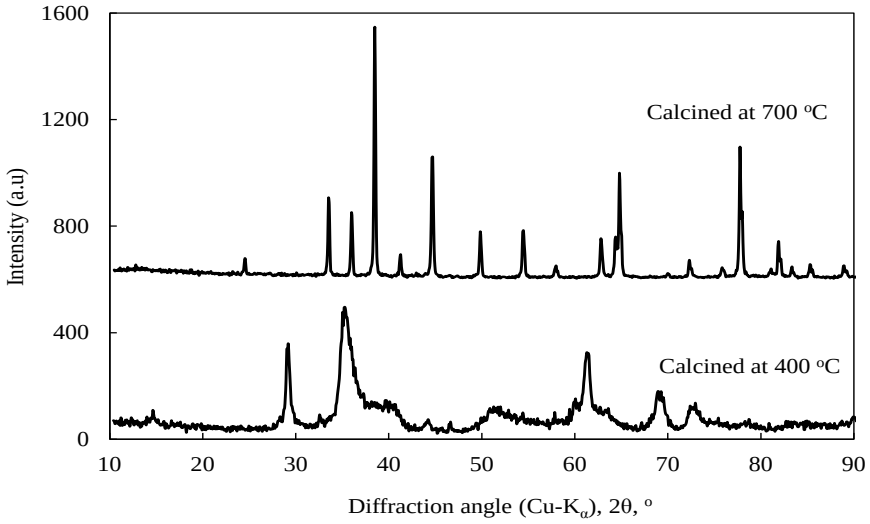

Figure A2: Preparation of $AgFeO_2$ by calcination at 400 ^oC and 700 ^oC

B: Activation studies

B.1. H_2 -TPR studies: Intimate contact

Pure α-Fe_2O_3, CuO and physically mixed CuO/α-Fe_2O_3 samples were used to study the effect of intimate contact between promoter and the active phase during H_2 reduction. Preliminary results reveal that the physically mixed sample (CuO/α-Fe_2O_3) showed three reduction peaks. The first reduction peaks appearing at a similar position to that of CuO was ascribed to the reduction of CuO to Cu. The second and third reduction peak appear at the same position as the reduction peaks of α-Fe_2O_3 and were thus attributed to the reduction of Fe_2O_3 to Fe_3O_4 and Fe_3O_4 to Fe, respectively. Comparison of the H_2-TPR profiles of the samples (CuO, α-Fe_2O_3, CuO/α-Fe_2O_3) revealed no differences, therefore no promotional effect of copper to the iron. Intimate contact was required for any promotional effect to occur.

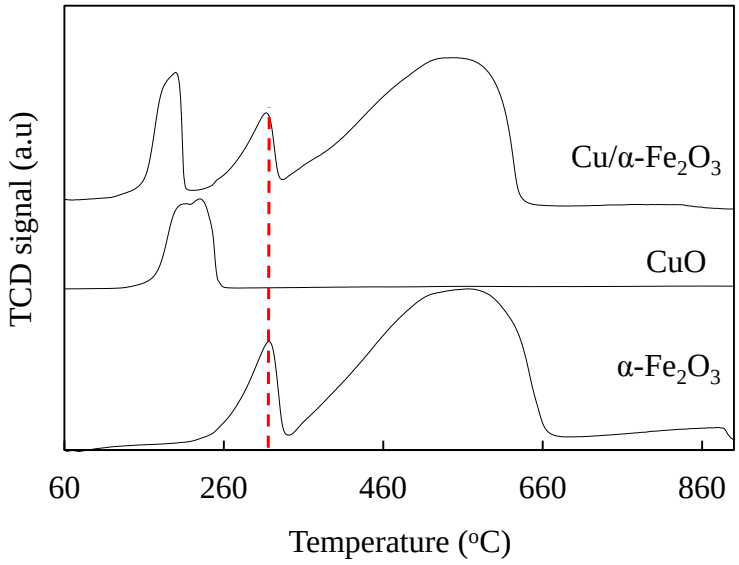

B.2. *In-situ* XRD H_2 activation studies:

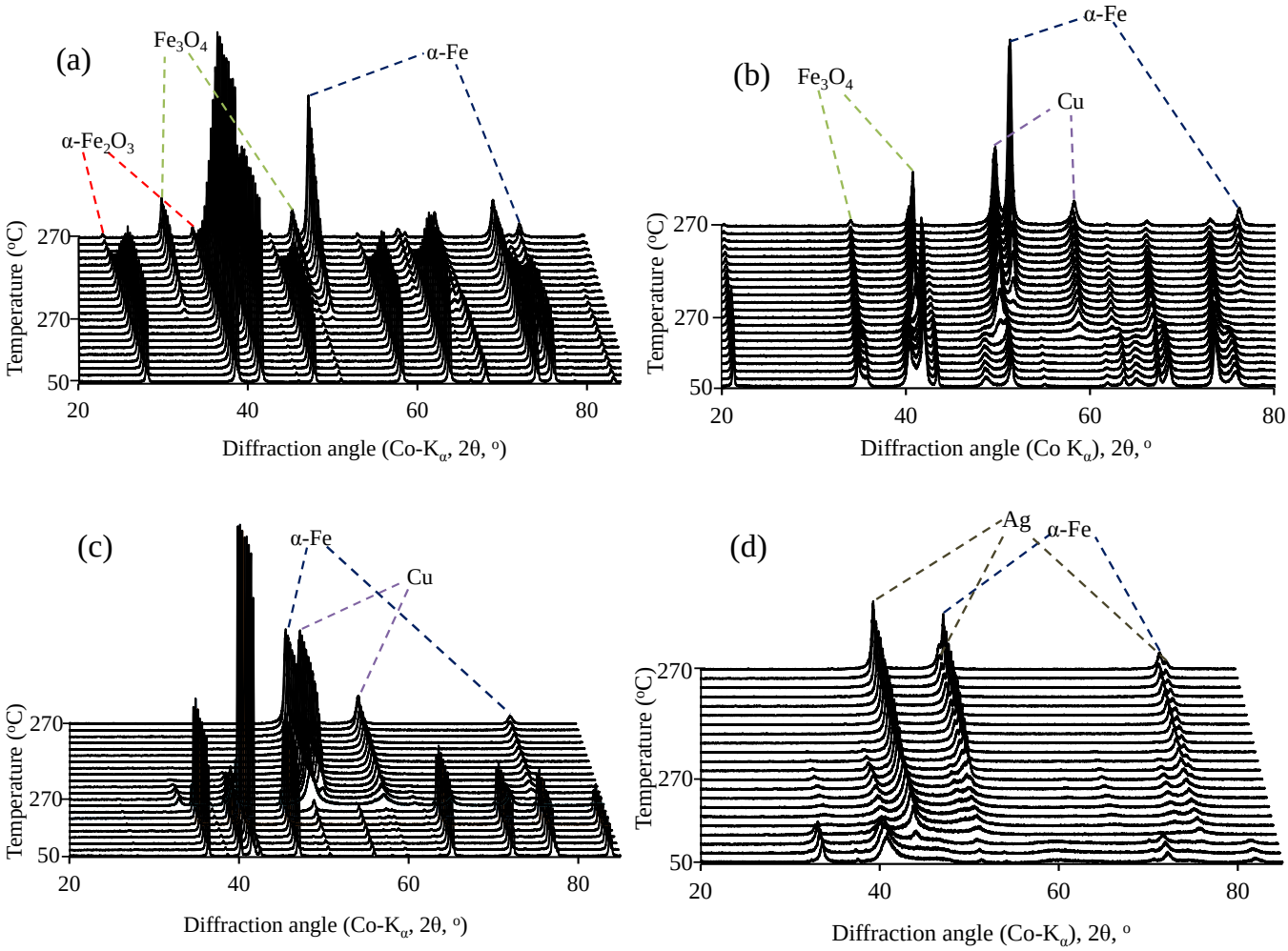

Figure B1: *In-situ* XRD 3D view of H_2 activated model catalysts, (a) α-Fe_2O_3, (b) $CuFe_2O_4$, (c) $CuFeO_2$ and (d) $AgFeO_2$

B.3 *In-situ* XRD CO activation studies:

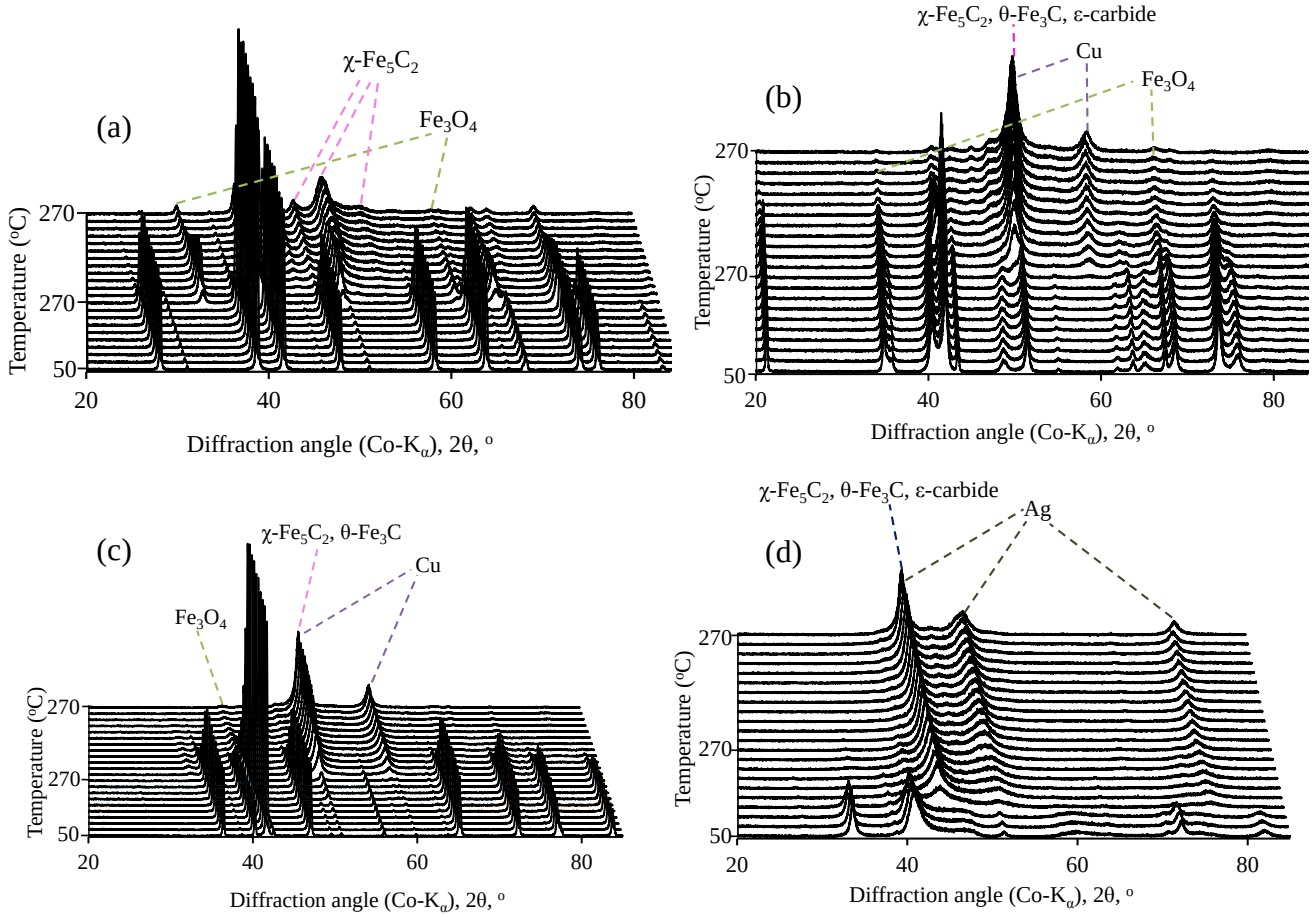

Figure B3: *In-situ* XRD 3D view of CO activated model catalysts, (a) α-Fe_2O_3, (b) $CuFe_2O_4$, (c) $CuFeO_2$ and (d) $AgFeO_2$

C. Oxidation studies: Storage of samples

The effect of oxidation within the spent sample was investigated by re-analysing the wax embedded spent catalyst after 10 months of storage. The storage procedure leads to some oxidation. The samples activated in H_2 and CO are given in Table B.1 and B.2, respectively. The extent of oxidation is small and not an obvious function of the copper content in the catalyst. In particular the metastable phase FeO is prone to oxidation.

Table C1. Physio-chemical characteristics of the model compounds after H_2-activation in slurry reactor (T = 270°C, p = 1 bar, pure H_2, for 16hr) and exposure to Fischer-Tropsch conditions (T = 250°C; p_{H_2} = 10.1-11.1 bar; p_{CO} = 4.3-5.2 bar; p_{H2O} = 0.3-1.4 bar; p_{CO2} = 0.03-0.5 bar) for 48hr

		Analyzed immediately after Fischer-Tropsch synthesis					**Analyzed 10 months later**				
Samples		γ-Fe_2O_3	α-Fe_2O_3	$CuFe_2O_4$	$CuFeO_2$	$AgFeO_2$	**γ-Fe_2O_3**	**α-Fe_2O_3**	**$CuFe_2O_4$**	**$CuFeO_2$**	**$AgFeO_2$**
Phase[a]	Fe_3O_4	73 (45)	92 (48)	37 (34)	30 (19)	2 (12)	**77 (45)**	**94 (48)**	**41 (33)**	**29 (19)**	**3 (12)**
	χ-Fe_5C_2	27 (14)	8 (16)	40 (10)	42 (9)	73 (21)	**23 (14)**	**6 (16)**	**41 (10)**	**32 (11)**	**65 (20)**
	θ-Fe_3C			8 (14)							
	Cu			16 (22)	28 (18)	25 (11)			**18 (22)**	**39 (36)**	**32 (11)**

[a] Phase composition in wt.-% (in brackets the average crystallite size in nm) as determined using determined using Rietveld refinement of XRD-pattern

Table C2. Physio-chemical characteristics of the model compounds after CO-activation in slurry reactor (T = 270°C, p = 1 bar, pure H_2, for 16hr) and exposure to Fischer-Tropsch conditions (T = 250°C; p_{H_2} = 10.1-11.1 bar; p_{CO} = 4.3-5.2 bar; p_{H_2O} = 0.3-1.4 bar; p_{CO_2} = 0.03-0.5 bar) for 48hr

		Analyzed immediately after Fischer-Tropsch synethsis					**Analyzed 10 months later**				
Samples		γ-Fe_2O_3	α-Fe_2O_3	$CuFe_2O_4$	$CuFeO_2$	$AgFeO_2$	**γ-Fe_2O_3**	**α-Fe_2O_3**	**$CuFe_2O_4$**	**$CuFeO_2$**	**$AgFeO_2$**
Phase[a]	Fe_3O_4	76 (43)	86 (42)	50 (30)	26 (19)	5 (-)	**85 (43)**	**89 (42)**	**55 (30)**	**34 (26)**	**5 (-)**
	FeO	6 (9)		2 (10)		14 (14)					
	χ-Fe_5C_2	18 (26)	14 (10)	28 (12)	45 (9)	59 (9)	**15 (10)**	**11 (10)**	**29 (12)**	**35 (9)**	**67 (9)**
	θ-Fe_3C			7 (21)							
	Cu			14(16)	29 (20)	22 (13)			**18 (22)**	**31 (20)**	**28 (13)**

[a] Phase composition in wt.-% (in brackets the average crystallite size in nm) as determined using determined using Rietveld refinement of XRD-pattern